Investigating

Cetyltrimethylammonium Bromide (CTAB)

Reverse Microemulsions using

Nuclear Magnetic Resonance

By

Amanda Jayne Mills

A thesis submitted to the

University of Birmingham

For the degree of

DOCTOR OF PHILOSOPHY

School of Chemistry

College of Engineering and Physical Sciences

University of Birmingham

September 2015

Abstract

This thesis investigates CTAB/alcohol/hexane/water reverse micelles, where the alcohol is butanol, pentanol, hexanol and heptanol, through the use of nuclear magnetic resonance (NMR). Diffusion and relaxation measurements showed the alcohol is distributed between the reverse micelle (RM) interface and the continuous phase, and exchanges between these two environments. The exchange of pentanol in the CTAB/pentanol/hexane/water RM was investigated using 2D relaxation exchange spectroscopy (REXSY), and was determined to be on the order of milliseconds. The proportion of alcohol in the interface was determined for all microemulsions which decreases as a function of increasing alcohol size. Each microemulsion was investigated by molecular simulations which produced oblate shaped droplets, which was associated with a non-homogeneous distribution of alcohol in the interface.

CTAB was determined to be present in solely the interface of the microemulsions with the exception of the CTAB/pentanol/hexane/water RM. The CTAB/pentanol/hexane/water RM behaves differently as initially the CTAB was distributed between the RM and the continuous phase but, after time, the surfactant is re-distributed so that CTAB is present in only the interface. The RM sizes were determined using the CTAB diffusion coefficients. The droplet sizes decreased as a function of alcohol chain length, with the exception of the CTAB/pentanol/hexane/water RM which, after time, gave the largest droplet of all the microemulsions.

With love to my future husband, Timothy Snell

Acknowledgments

Firstly, I would like to say a huge thank you to my supervisor Melanie Britton, who has given me continued support and encouragement throughout the past four years. She has not only been a great teacher, she has always believed in my abilities, even when I have doubted myself. I have enjoyed working with Melanie, and I admire her passion for research and her excited cheer when research breakthroughs are made. I would like to thank Sue and Matt for the journey we have gone on together throughout our undergraduate degree and PhD, particularly Sue for her long discussions on microemulsions. I would also like to thank Antoine for his help at the beginning of my PhD, Catherine for being my office neighbour and listening to all my ramblings, Emma for our long conversations with Catherine and Josh for his love of my northern accent. A special thanks must go to Heather, for her cheerful, bubbly personality who was a welcome presence in the office, and brought a welcome distraction from my work. I would also like to thank John Wilkie, who supported me in performing the molecular simulations in this thesis.

Above all I would like to thank my future husband, Tim, whose continued, undoubted support and belief in me has given me the ability to complete this PhD, I would not have been able to do it without him by my side. I cannot thank him enough for his support and love, not only throughout my PhD, but in our life together so far. I thank him for his ability to make me smile and laugh every single day. I would also like to thank my parents, who supported me throughout my life at university and for the knowledge that I can always count on them to help me in times of need, my sister Lisa and her husband Tom for the evenings spent drinking and for gifting me with my beautiful niece Harriet. Lastly, I would like to thank my future in-laws Helen and Andrew, who have taken me into their family and treated me like their daughter, Amy, who is like another sister to me, and Adam.

Table of Contents

List of Figures

List of Tables

1. Introduction

It is well known that oil and water are immiscible and a clear phase separation can be seen when they are mixed together; however, in the presence of surfactant molecules a thermodynamically stable isotropic mixture is formed. These clear, thermodynamically stable mixtures of oil, water and surfactants are known as microemulsions. Microemulsions typically consist of surfactant aggregates in the form of micelles (oil-in-water droplets) or reverse micelles (water-in-oil droplets), Figure 1.1. Reverse micelles (RMs) consist of nanometre size water droplets surrounded by a surfactant monolayer in an oil continuous phase, and have a wide range of unique properties and applications. Their thermodynamic stability is a great advantage over other macro emulsions and suspensions, which are kinetically stable but thermodynamically unstable.[1] The most attractive property of RMs is the ability to solubilise aqueous entities in a hydrophobic environment which has led to their use in many different applications.
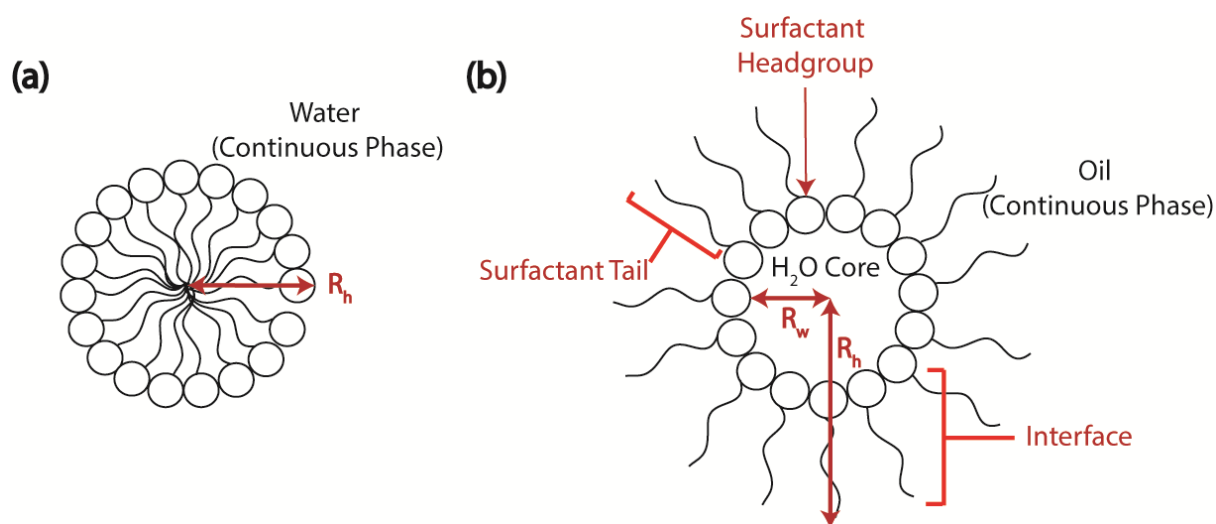
Figure 1.1: (a) A schematic of a micelle where the continuous phase is water and (b) A schematic of a reverse micelle (RM) with a water core and an oil continuous phase. The interface, surfactant tails and headgroups, the water core radius, R_w, and the hydrodynamic radius, R_h are labelled.

1

RMs are frequently used as templates in the synthesis of nanoparticles[2-7] and as reactors for chemical and enzymatic reactions.[8-10] Reverse micelles are dynamic systems and move in a random fashion, leading to regular droplet collisions which is the basic mechanism for nanoparticle synthesis and chemical reactions in RMs. Droplet collisions can lead to coalescence, where two droplets mix, and then break apart again, after having exchanged reverse micelle contents. Exchange of RM contents in this way has enabled some aqueous chemical reactions to take place in hydrophobic environments, which can overcome problems with reactant solubility.[11] The ability of RMs to host chemical reactions in nanometre size structures makes them ideal reactors for nanoparticle synthesis.[12] The RM cores provide an ideal template for synthesis of nanoparticles due to the dispersed nature of the droplets preventing nanoparticle aggregation, which is a common problem in other nanoparticle synthesis techniques.[13]

In addition to uses in chemical reactions and nanoparticle synthesis, RMs have applications as drug delivery and biomolecule carriers.[14-16] RMs became attractive as drug delivery carriers due to their ease of preparation, long shelf-life, low toxicity and very small droplet size.[14] The small droplet size increases the chance of adhesion to membranes and allows drug transport in a more controlled fashion.[14] In addition, RMs allow sustained drug release into the body,[17] as when RMs come into contact with aqueous environments the RM core grows and transforms into a liquid crystalline phase, which reduces drug release.[18] Moreover, RMs have been used in the encapsulation of biomolecules[15,16] such as enzymes and proteins. It has been found that the reactivity and conformation of these biomolecules in the water core of RMs depends on the specific properties of the RM such as the water content.[3,15] Some RMs have been used as models for cell membranes,[19,20] and therefore can provide vital information on the possible interactions of the biomolecules in confined water and with the cell membrane.[15] As a consequence of the wide range of applications of RMs, there is a significant need to understand the formation, microstructure, size, shape and chemical properties of these surfactant aggregates.

1.1 Reverse Micelles

The formation of RMs is driven by the amphiphilic nature of the surfactant molecules;[21] the

RM structures are stabilised by the favourable interactions between polar parts of the surfactants.[21]

The surfactant molecules organise so that the hydrophobic tail is directed towards the oil and the

hydrophilic headgroup interacts with the water, minimising the unfavourable oil and water

interactions and reducing the interfacial tension between the two liquids. RMs form at a specific

surfactant concentration known as the critical micelle concentration (cmc).[22] The composition of RMs

consisting of surfactant, oil and water is defined by two important parameters: the water to

surfactant ratio, ω_0, Equation 1.1 and the volume droplet fraction, ϕ_d, which give a measure of

droplet concentration, Equation 1.2.

$$\omega_0 = \frac{[\mathrm{H_2O}]}{[\mathrm{surfactant}]} \qquad \qquad \text{Equation 1.1}$$

$$\phi_d = \frac{V_{\mathrm{droplet}}}{V_{\mathrm{total}}} = \frac{V_{\mathrm{H_2O}} + V_{\mathrm{surfactant}}}{V_{\mathrm{H_2O}} + V_{\mathrm{surfactant}} + V_{\mathrm{oil}}} \qquad \qquad \text{Equation 1.2}$$

Here, [$\mathrm{H_2O}$] and [surfactant] are the concentrations of water and surfactant respectively, and $V_{\mathrm{H_2O}}$,

$V_{\mathrm{surfactant}}$ and V_{oil} are the volumes of water, surfactant and oil, respectively.

CTAB Reverse Micelles

Although the most common and widely studied surfactant used in RM formation is sodium

bis(2-ethylhexyl) sulfosuccinate (AOT), there is interest in RMs formed with cetyltrimethylammonium

bromide (CTAB). CTAB is particularly interesting as a surfactant for RMs because the headgroup is

similar to that of the lipid phosphatidylcholine.[19] Although phosphatidylcholine is zwitterionic, CTAB

is used as a model for this lipid as it is readily available, relatively cheap and contains the vital

trimethylammonium headgroup which is present in the lipid. Phosphatidylcholine is one of the most

abundant phospholipids in animals and plants,[23] as it is one of the major components of cell

membranes.[23] Therefore, CTAB RMs can be used to mimic cell membranes and determine the

microenvironment of biomolecules such as proteins within the cellular environment,[20] and any

possible interactions with the cell membrane. CTAB RMs have also been employed as a medium for

chemical reactions[9] and encapsulation of biomolecules.[15,16]
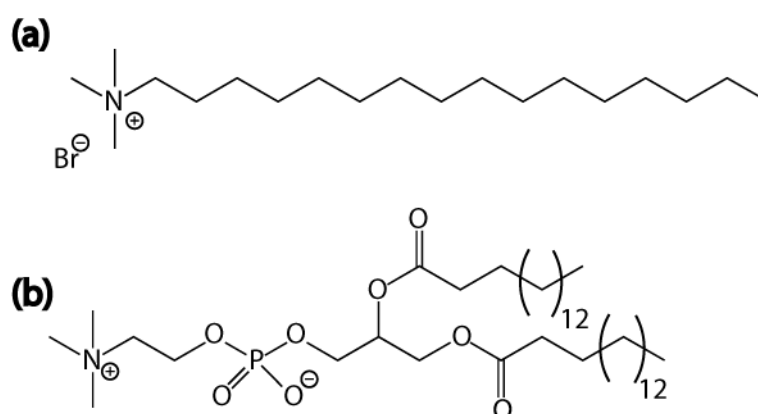
Figure 1.2: The structure of (a) cetyltrimethylammonium bromide (CTAB) and (b) a
phosphatidylcholine lipid found in cell membranes.

CTAB RMs have become particularly useful in the synthesis of nanoparticles and as reactors

for chemical reactions, as the long hydrophobic chain leads to a highly flexible surfactant film,[7]

increasing the fluidity of the interface and allowing greater intermicellar exchange.[5,7,11] All these

factors allow CTAB RMs to encapsulate high amounts of water[6] and therefore the reactant

concentration within the RM is increased, which in turn amplifies the chemical reaction rate.[24] As a

result, there is an increasing need to understand the physical parameters of the CTAB RMs to enable

their development in new and current applications. Some of these important parameters are

discussed below.

Shape

The shape of RM droplets is generally reported to be a spherical structure,[25-28] and is therefore the most commonly assumed.[11,25,29] When characterising RMs using techniques such as small angle neutron scattering (SANS),[30,31] small angle x-ray scattering (SAXS)[28,32] and dynamic light scattering (DLS),[33,34] prior knowledge of the droplet shape is required, and is often assumed to be spherical. However, reports suggest the shape of RM droplets deviate from spherical with changes in the microemulsion composition.[6,35] Deen et al.[36,37] tracked the shape of $C_{12}E_5$/water/1-chloroalkanes using SAXS and found the droplets become elongated as a function of the chloroalkane chain length. Deviation from spherical was also observed by Blochowicz et al.[38] when using SAXS to determine the effect of the polymer PEO(polyethylenoxide)-PI(polyisoprene)-PEO on AOT/decane/water reverse micelles. The shape deviation is more dramatic with changes in the water content of the RMs,[6,7,35] whereby an increased water content results in a deviation from spherical geometry. This was seen for CTAB RMs by Fang et al.[6] However, a contrasting trend was reported by Palazzo et al.[26] where the CTAB/pentanol/hexane/water reverse micelles remain spherical throughout all compositional changes, including an increase in water content. It is also reported that RMs with moderate tail length surfactants (C10 – C16), like CTAB, are thought to be spherical or nearly spherical at compositions close to the critical micelle concentration (cmc).[7] CTAB has a tail length of C16 and therefore lies on the boundary of this generalisation, thus, with the contrasting shape changes with CTAB RMs on increasing water content by Fang et al.[6] and Palazzo et al.,[26] some ambiguity lies in the shape of CTAB RMs.

Molecular modelling of RMs offers the ability to study the likely shape and structure of the droplets.[39] Extensive studies using molecular modelling have been performed on AOT RMs[12,40-44] with shape determination being one of the most important aspects of this work. Rodriguez et al.[45] performed molecular simulations on a benzylhexadecyldimethylammonium chloride (BHDC) RM which has the same headgroup as CTAB, and found the shape became elliptical. Recently, a

5

molecular simulation of the CTAB/chloroform/water RM system has been reported and indicates the droplet exhibits a prolate shape, particularly as the water pool size increases.[46] Simulations of the RM were performed at 273 K and 200 K to reveal the shape of the droplet becomes more spherical at lower temperatures.[46] Most RM simulations start from a pre-determined spherical geometry, as this considerably reduces the computational time and is the best approximation of the true shape. Vasquez et al.[42] showed that starting from a pre-determined spherical geometry or a random configuration has no effect on the resultant structure, provided sufficient simulation time was acquired (hundreds of nanoseconds). Previous RM simulations are generally in agreement that the RM deviates from spherical to an elliptical conformation.[40,42-45] However, Brodskaya et al.[41] and Graeve et al.[47] simulated AOT RMs and reported that the shape change from spherical became less pronounced as the reverse micelle size increased. Brodskaya et al.[41] stated that the mean shape of the micelles is an elongated ellipsoid where elongation decreases with increasing water content in the systems, which is in contrast to the findings by Fang et al.[6] for CTAB RMs.
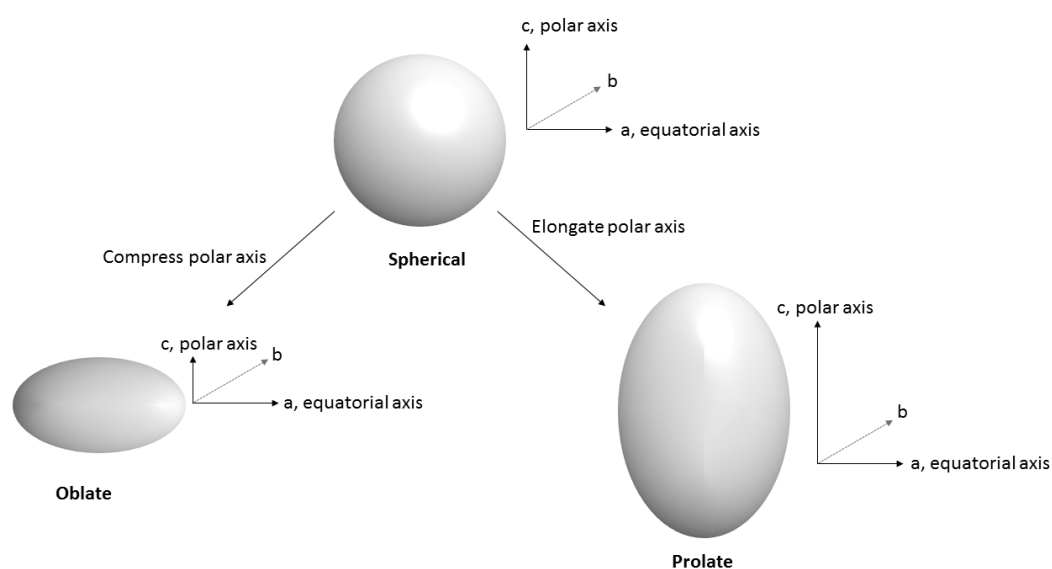
Figure 1.3: A schematic representation of spherical, oblate and prolate spheroids with labelling of the three semi-axes.

It is widely accepted, both experimentally and theoretically, that deviation from spherical results in ellipsoidal structures (oblate or prolate). These ellipsoidal structures are a result of compression (oblate) or elongation (prolate) along one axis of a sphere known as the polar axis, Figure 1.3. An oblate shape generally has a much shorter polar axis when compared to the equatorial axis which is at 90° to the polar axis, Figure 1.3, a prolate ellipsoid has a longer polar axis compared to the equatorial axis.

When employing molecular modelling, the shape of RMs can be determined by visual interpretation but a more accurate and quantitative method is to measure the three principal moments of inertia, I_1, I_2 and I_3. Using I_1, I_2 and I_3, the three semi-axes a, b and c, Figure 1.3, can be calculated[40] (Equation 1.3, Equation 1.4 and Equation 1.5), where M is the total mass.

$$I_1 = \frac{1}{5}M(a^2 + b^2)$$
<div align="right">Equation 1.3</div>

$$I_2 = \frac{1}{5}M(a^2 + c^2)$$
<div align="right">Equation 1.4</div>

$$I_3 = \frac{1}{5}M(b^2 + c^2)$$
<div align="right">Equation 1.5</div>

For spherical droplets $a = b = c$, for oblate droplets $a \approx b > c$ and for prolate droplets $a \approx b < c$. In addition, the eccentricity of the droplets can be determined using Equation 1.6. The eccentricity value gives a good approximation to the shape of the RM; when a droplet is spherical $e = 0$, whereas $e \rightarrow 1$ for an oblate or prolate shape.[40]

$$e = \sqrt{1 - \frac{c^2}{a^2}}$$
<div align="right">Equation 1.6</div>

Size

Measuring the three principal moments of inertia for molecular simulated droplets can also be employed to determine the size of molecular simulated RMs, and is the only method that can determine the length of each semi-axis, *a*, *b* and *c*. Experimental methods such as NMR,[26,48] DLS,[49-51] SAXS,[36,37,52] SANS,[30,53,54] fluorescence spectroscopy[55,56] and conductivity measurements[29,57,58] are used in RM size determination but require prior knowledge of the droplet shape. Therefore, they are often employed in conjunction with other techniques to determine the shape or, more commonly, the shape is assumed to be spherical. The sizes of RMs are affected by the amount of water inside the droplets.[25] As the amount of water increases, ω_0, more water is solubilised by the droplets and hence the RM size increases.

RM size analysis is most commonly performed by determining the diffusivity of the RM aggregate through dynamic light scattering (DLS) or nuclear magnetic resonance (NMR) measurements of diffusion. The diffusivity of the surfactant head group is of particular interest as it is a good representation of the RM diffusion,[59] which is vital in particle size analysis using diffusion NMR. The diffusion of the RM is related to the hydrodynamic radius, R_h, of the RMs using the Stokes-Einstein relationship when the continuous phase viscosity, η, is known, Equation 1.7, where *D* is the diffusion coefficient, k_B is the Boltzmann constant, *T* is temperature and η, is the dynamic viscosity of the continuous phase.

$$D = \frac{k_B T}{6\pi\eta R_h}$$
Equation 1.7

Particle size analysis via the Stokes-Einstein equation, Equation 1.7, is particularly accurate if the RM droplets are spherical,[60] which is often assumed. However, as discussed previously, RM droplets are not always spherical and can become ellipsoidal, either having an oblate or prolate shape. Determining the size of these oblate and prolate droplets requires the use of a modified Stokes-Einstein equation for non-spherical structures,[61,62] Equation 1.8, and incorporating shape

factors, f_{shape}, for prolate and oblate ellipsoids, Equation 1.9 and Equation 1.10, respectively.

Equation 1.8 enables the determination of R_H, the radius of a sphere with identical volume to the

ellipsoidal spheroid, by taking into account the different translational and rotational frictional

movement of the ellipsoidal structure when compared with that of a sphere of the same volume.[61-63]

In these shape factor equations $p = \frac{\text{polar radius,}c}{\text{equitorial radius,}a}$, thus for oblate ellipsoids $p < 1$ and prolate

ellipsoids $p > 1$.

$$R_{\text{H}} = \frac{k_{\text{B}}T}{6\pi\eta D f_{shape}}$$

Equation 1.8

$$f_{\text{prolate}} = \frac{\sqrt{p^2 - 1}}{p^{\frac{1}{3}}\ln\left[p + \sqrt{p^2 - 1}\right]}$$

Equation 1.9

$$f_{\text{oblate}} = \frac{\sqrt{\left(\frac{1}{p}\right)^2 - 1}}{\left(\frac{1}{p}\right)^{\frac{2}{3}}\arctan\left(\sqrt{\left(\frac{1}{p}\right)^2 - 1}\right)}$$

Equation 1.10

When determining the size of RM systems at high droplet fractions, ϕ_d, care must be taken

when using the Stokes-Einstein equation. The diffusion coefficient of the reverse micelles and solvent

may be reduced at higher droplet fractions due to obstruction of the diffusion pathway,[64,65] and

hence may limit the validity of the Stokes-Einstein equation, producing droplet radii larger than the

true value. This is known as the obstruction effect[64] or memory effect[66] and is related to the volume

droplet fraction and the shape of the obstructing particles.[64] The obstruction effect can be avoided

by performing diffusion measurements at low droplet fractions, which is known as infinite

dilution.[64,66] Measurements at infinite dilution is not always possible and therefore diffusion

measurements are performed along a dilution line (decreasing volume droplet fraction, ϕ_d) to obtain

multiple diffusion coefficients which can be extracted back to $\phi_d = 0$ to obtain the diffusion

coefficient at infinite dilution, D_0.[67] Alternatively, a correction can be applied[59,64,65,67-69] to adjust the

diffusion coefficient to take into account obstruction effects and determine D_0, Equation 1.11, where

α is the interaction coefficient and D_{obs} is the observed diffusion coefficient. For RMs, the droplet

interactions are usually attractive and therefore α is generally negative.[67] In the case of the hard

sphere model where there are no hydrodynamic interactions,[70] $\alpha = -2$. There are also variations of

this presented by Lindman et al.[65] that demonstrate the obstruction factor for non-spherical

particles.

$$D_{obs} = D_0(1 + \alpha\phi_d)$$
<div align="right">Equation 1.11</div>

CTAB RMs size have only been determined using a few techniques including electron

microscopy,[6] conductance measurements,[29] fluorescence spectroscopy[55,71] and NMR.[26] NMR

measurements of diffusion[26] for the CTAB/pentanol/hexane/water system measured droplet radii of

1 – 5 nm over a range of ω_0 values. Diffusion NMR was also employed by Law et al.[48] to determine

sizes of approximately 1 nm for the CTAB/hexanol/water RM system. The CTAB/hexanol/water

system was also studied by electron microscopy,[6] where much larger droplets were found ranging

between 10 and 150 nm. Conductance measurements[29] on the CTAB/heptane/butanol/ water

system gave droplet radii of 4.8 – 5.3 nm. Measurements by fluorescence spectroscopy have found

droplet radii of 4.0 – 4.5 nm for CTAB RMs in chloroform/iso-octane mixtures.[55,71] Although dynamic

light scattering is frequently used to determine the sizes of RMs,[49-51] it appears to be less utilized with

CTAB RMs.

Polydispersity

Polydispersity is a measure of the heterogeneity or distribution of the size of molecules, particles or surfactant aggregates in a solution. A solution consisting of uniformly sized particles or aggregates is known as monodisperse.[72] Polydispersity is measured on a scale of 0 to 1, where 0 is uniform, monodisperse droplets and 1 is polydisperse droplets.[30] Polydispersity values below 0.1 represent RMs where the size distribution is narrow; however, values above 0.7 are classified as having a broad size distribution (high degree of polydispersity).[73] The polydispersity of RM droplets has been measured with dynamic light scattering,[74,75] small angle neutron scattering,[76-78] diffusion NMR,[79] small angle x-ray scattering[80,81] (SAXS) and fluorescence spectroscopy.[82]

Typically, RMs exhibit a size polydispersity that is affected by water content, presence of additives, surfactant nature and temperature.[25] Measurements on the AOT/decane/water RMs with small angle neutron scattering (SANS) showed that the polydisperity increased as a function of temperature.[77] The polydispersity of AOT RMs is generally thought to be around 0.2;[80,83] however, Bhattacharya et al.[74] measured polydispersity values of $0.22 - 0.59$ for AOT RMs with DLS. CTAB RMs have been reported to have a high polydispersity,[84] Fang et al.[6] obtained RMs ranging in size from 100 to 1000 nm. A high degree of polydispersity of CTAB/chloroform/water RMs has been reported through the use of NMR diffusion ordered spectroscopy (DOSY),[79] where sizes of 8 nm, 11 nm and 22 nm were obtained. The polydispersity of CTAB/cyclohexane/butanol/water and CTAB/butanol/water RMs were studied by Begum et al.[73] using DLS. They reported polydispersity values of $0.1 - 0.35$ for the CTAB/cyclohexane/butanol/water and $0.23 - 0.5$ for the CTAB/butanol/water system. These CTAB RMs have polydispersity values similar to those of AOT RMs and hence are expected to have a similar degree of polydispersity.

Dynamics

So far the ability to quantify the size, shape and polydispersity of RMs has been discussed and the dynamics of RMs was briefly mentioned with respect to droplet size measurements. The constant random motion of the RM droplets inevitably leads to interdroplet collisions,[11,85] which can be in an elastic or inelastic fashion. An elastic collision is when two objects collide and they rebound off each other with no change in kinetic energy, each object has the same kinetic energy before and after the collision. An inelastic collision is one where kinetic energy is transferred during the collision and often leads to a reaction. If two reverse micelles collide in an inelastic fashion, the two droplets can coalesce to give a short lived dimer.[85] After a short period of time, these dimers separate to reform two RMs where the droplet cores are a mixture of the two original RMs contents prior to dimer formation,[9] as represented in Figure 1.4. Mixing of the droplet cores in this way allows micelle contents to move between droplets without entering the continuous phase, therefore allowing aqueous reactions to take place in hydrophobic environments. Reactions in RMs require the preparation of two different microemulsions, each containing one of the two reactants needed for the reaction to proceed, Figure 1.4. Once these two microemulsions are mixed, droplet collisions occur, resulting in exchange of RM core material (intermicellar exchange), producing RMs that contain a mixture of the two reactants which results in a reaction. The typical time for intermicellar exchange[5,11] is on the order of 10 μs to 1 ms.

The rate of reactions in RMs consists of a number of processes including the random motion of the droplets that leads to a collision, merging of two droplets to form a dimer, the chemical reaction and breakdown of the dimer to re-form two droplets.[7] The rate limiting step of this process is the fusion of droplets to form a dimer.[7,86] This process leads to a decrease in the interfacial area by either temporarily expelling surfactant molecules into the continuous phase or by forcing the surfactant molecules closer together to produce a more compact film.[86] Both these processes are unfavourable and hence the activation energy will be higher for this step.[7] The probability of dimer
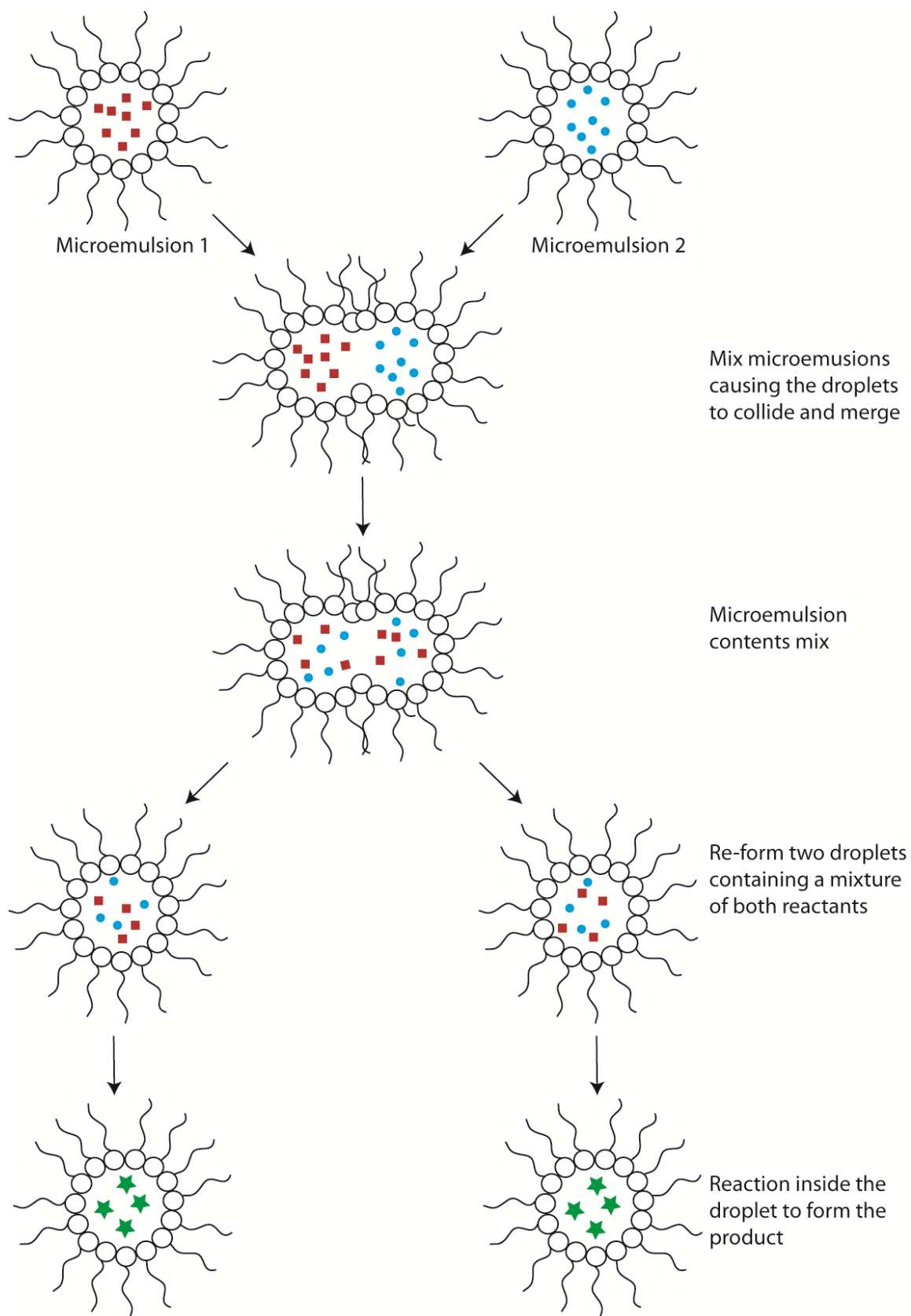
Figure 1.4: Schematic showing the processes involved in chemical reactions inside reverse micelles.

formation depends on the interfacial film flexibility;[7] a more flexible interfacial film produces more successful collisions for intermicellar exchange[11] and hence increases the rate of exchange. Only 1 in 1000 collisions leads to droplet fusion when RMs have rigid interfaces such as those consisting of AOT surfactant molecules,[11] whereas when the interface is more flexible, like those made of CTAB, the chance of dimer formation is more probable with 1 in 10 collisions leading to droplet fusion.[11] The increased chance of dimer formation of CTAB RMs leads to greater intermicellar exchange[5,7,11] which has led to their popularity as reactors for nanoparticle synthesis.[3,4,6,7]

In addition to dynamic droplets, the surfactant environment within the microemulsion is not static with molecular exchange occurring between the RM interface and the bulk organic continuous phase.[87] The exchange and micellisation mechanisms[88] are shown in equation 1.12, where k_F and k_D are the rate constants for micellisation and dissolution, respectively. The exchange process is represented by the rate constants k_1 and k_{-1}, which define the rate of association of a surfactant molecule into a micelle (k_1) and the dissociation of a surfactant molecule into the bulk (k_{-1}). These two processes have two different timescales, the exchange between aggregate and monomer is thought to be fast[25,88-90] whereas the micellisation-dissociation process is much slower.[88]

$$(n+1)\mathrm{A} \quad \underset{k_F}{\overset{k_D}{\leftrightharpoons}} \quad \mathrm{A}_n + \mathrm{A} \quad \underset{k_1}{\overset{k_{-1}}{\leftrightharpoons}} \quad \mathrm{A}_{n+1}$$

Equation 1.12
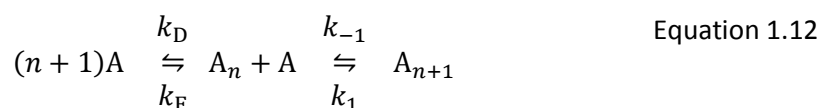
The exchange between monomer and aggregated surfactant molecules is diffusion-controlled with the average lifetime in a micelle[91] thought to be 10^{-6} s. Surfactant exchange in reverse micelles is generally expected to be fast,[90,92] with some lifetimes reported in the range of $10^{-6} - 10^{-3}$ s. There have been reports of slower surfactant exchange with fluorocarbon surfactants in the micellar systems with surfactants perfluoroheptanoic acid and perfluorooctanoic acid[91] and in some gemini surfactants.[89] Guo et al.[91] reported a slower exchange rate of some

fluorocarbon surfactants, with a lifetime of $0.1 - 1$ s, which was attributed to the formation of large surfactant aggregates which might phase separate and exist as dispersions. The aggregation of fluorocarbon surfactants is more likely than the conventional hydrocarbon surfactants due to the electron rich nature of fluorine producing stronger van der Waal forces,[91] particularly dispersion[93] and dipole-dipole interactions.

Co-surfactant

While the use of CTAB as a surfactant for RMs has favourable attributes related to the interface dynamics and fluidity, another key advantage of CTAB RMs is the requirement of an additional component in the form of a co-surfactant to enable RM formation.[5,19] Unlike some other surfactants, CTAB cannot form RMs without the aid of a co-surfactant, which is usually in the form of a medium chain alcohol.[5,19] The co-surfactant increases the stability of the RM by reducing the unfavourable interactions between the charged surfactant head groups.[7] The co-surfactant can act as the continuous oil phase, producing systems comprising three components, oil/co-surfactant, surfactant and water, known as tertiary microemulsions, which are characterised using ω_0, Equation 1.1, and ϕ_d, Equation 1.2. Alternatively, the co-surfactant can be in addition to the continuous phase;[3,26,55,94,95] these systems are known as quaternary systems. Quaternary microemulsions are characterised by ω_0, ϕ_d and an additional parameter to define the amount of co-surfactant present, P_0, Equation 1.13.

$$P_0 = \frac{[\text{co} - \text{surfactant}]}{[\text{surfactant}]} \qquad \text{Equation 1.13}$$

where [co-surfactant] is the concentration of the co-surfactant. In quaternary systems, the co-surfactant is thought to be distributed between the interphase and continuous oil phase.[26,96,97] The

attractive interaction of the alcohol tails and oil chains enables the alcohol to disperse in the oil continuous phase.[98] The alcohol also resides in the interface due to favourable interactions with the polar water core,[98] and the ability to stabilise the interface. Therefore, the determination of ϕ_d becomes more challenging because it requires the knowledge of the amount of pentanol in the RM interface, Equation 1.14.

$$\phi_d = \frac{V_{\text{droplet}}}{V_{\text{total}}} = \frac{V_{\text{H}_2\text{O}} + V_{\text{surfactant}} + V_{\text{co-surfactant in interface}}}{V_{\text{H}_2\text{O}} + V_{\text{surfactant}} + V_{\text{total co-surfactant}} + V_{\text{oil}}} \qquad \text{Equation 1.14}$$

The presence of alcohols has a dramatic effect on the properties of RMs including the fluidity of the interface,[99] mass transfer between the RM interface and continuous phase,[100] higher order structure and activity of solubilised enzymes[11,101] and the size and shape of synthesised nanoparticles.[3,4] The most significant effect of the addition of a co-surfactant is decrease in the RM interface rigidity[4,5,7,11] due to the re-organisation of surfactant to form a less compact film.[4] As a result, the kinetics for intermicellar exchange increases thus enabling reactions to occur within RMs more efficiently.[11] The packing of the co-surfactant and surfactant molecules in the interface affects the curvature of the droplets[102] and hence the addition of co-surfactants affects the droplet size.[5,7,11] Therefore, the addition of a co-surfactant to form quaternary microemulsions provides a useful additional parameter, P_0, by which the size, shape, and interface rigidity of the RM can be controlled.[2]

The choice of alcohol employed as a co-surfactant is particularly important as the chain length can affect the interfacial properties facilitating control of droplet size[95,103-105] and water solubilisation.[95,105-107] The droplet radius decreases with a reduction in the size of the co-surfactant due to the formation of more fluid interfaces.[103] More stable RMs are produced with a co-surfactant that forms the strongest van der Waal interactions with the surfactant molecules.[7] Thus, it was

reported by Bansal et al.[106] that more stable microemulsions with higher water solubilisation capacities are formed when the chain length of the alcohol co-surfactant and the oil continuous phase is approximately equal to the chain length of the surfactant molecules. The choice of co–surfactant has also been reported to affect the structure of solubilised enzymes. Naoe et al.[101] investigated the structure of *Mucor miehei* lipase solubilised in CTAB/iso-octane/alcohol/water where the alcohol was pentanol and hexanol. They reported the structure of the lipase is closest to its native structure when the co-surfactant was pentanol rather than hexanol. The effect of co-surfactant chain length on nanoparticles has been investigated by Chen et al.[3] They suggested pentanol is a better co-surfactant than butanol because more spherical monodispersed nanocrystals were formed in the CTAB/pentanol/hexane/water microemulsion, when compared with previous studies on the CTAB/butanol/octane/water microemulsion,[108] which produced polydisperse nanoparticles with a range of shapes.

The presence of an alcohol co-surfactant in the interface enables the alcohol hydroxyl to exchange with the water core.[94,109] This has been observed in the CTAB/hexanol/water[109] microemulsion as well as the *n*-octylribonamide/brine/decane/butanol[94] RM system and is common in water/alcohol mixtures.[110,111] The same interaction and exchange mechanisms found in water/alcohol mixtures can be applied to RM systems. The water and hydroxyl proton can form hydrogen bonds,[94,110,111] that facilitate proton exchange which has been found to be catalysed by acid or base.[109] NMR is a powerful tool in determining the presence of exchange and hydrogen bonds by simply monitoring changes in chemical shift, linewidth and lineshapes, due to their sensitivity to chemical environment and molecular interactions.[89,94] Hydrogen bonding can cause changes in the chemical shift of the hydroxyl alcohol and water protons.[94,111] An increase in hydrogen bonding will lead to a shift to lower field.[94] Proton exchange can also affect the position of the alcohol hydroxyl and water peaks. When exchange is slow[112] (> 0.1 s), two separate resonances are observed; however, when the exchange is fast[112] (< 0.001 s) these resonances coalesce representing an average

of the two resonances.[94] Halliday et al.[109] demonstrated how this exchange process is affected by the pH of the water core; they concluded that a more acidic water core leads to faster exchange. In addition to proton exchange, the co-surfactant undergoes molecular exchange[25,113-115] with co-surfactant molecules in the interface and continuous oil phase. This exchange has been reported to be fast[25] with an exchange rate of $< 10^{-4}$ s.

Composition

The presence of a co-surfactant, particularly in quaternary microemulsions, leads to RMs of greater complexity which makes characterisation more difficult. The exact distribution of the co-surfactant in RM systems is vital in size determination via the Stokes-Einstein equation, Equation 1.7. Determining droplet size using the Stokes-Einstein equation requires knowledge of the continuous phase viscosity, η, which is not as simple as assuming the viscosity of the oil is equal to the continuous phase viscosity. It is reported that the co-surfactant is distributed between the interface and the continuous phase,[26] thus, the continuous phase is a mixture of the oil and the co-surfactant. The presence of the more viscous alcohol co-surfactants in the continuous phase has a dramatic effect on its viscosity. Therefore, the exact composition of the continuous phase is vital to obtain the correct continuous phase viscosity and determine accurate droplet sizes via the Stokes-Einstein equation.

The composition of the continuous phase and interface can be determined using diffusion NMR.[26] Palazzo et al.[26,96,97] performed diffusion NMR measurements on the CTAB/hexane/pentanol/water RM system. They found that pentanol is distributed between the RM interphase and continuous phase and that exchange between these two regions was fast due to the presence of an averaged pentanol diffusion coefficient. With the use of the Lindman equation[116,117]

(Equation 1.15) the proportion of pentanol in the interface, P_{mic}, and the continuous phase, $1 - P_{\text{mic}}$, was possible.

$$D_{\text{obs}} = P_{\text{mic}}D_{\text{mic}} + (1 - P_{\text{mic}})D_{\text{bulk}}$$ Equation 1.15

Here, D_{obs} is the observed diffusion coefficient for pentanol, D_{mic} is the diffusion of the RM droplet and D_{bulk} is the diffusion coefficient of pentanol in the continuous phase (bulk). The Lindman equation is only valid for the fast exchange limit[116,117] and requires a priori knowledge of the diffusion of pentanol in the continuous phase, D_{bulk}, and the diffusion coefficient of CTAB as a measure of the RM diffusion coefficient, D_{mic}. From these studies Palazzo et al.[26] determined P_{mic} values ranging from 0.3 to 0.63 depending on the amount of CTAB and pentanol present in the system.

Diffusion NMR is not the only method of determining the interfacial composition of reverse micelles: previously a very simple method of dilution was used,[118] which also provides the thermodynamics of microemulsion formation,[119,120] and is still widely employed across the field. This is a relatively simple method where the microemulsion is diluted with oil until the microemulsion breaks down, then co-surfactant is added until the microemulsion reforms.[118] If this dilution method is repeated and the amount of oil and co-surfactant added at each step is recorded, the amount of co-surfactant in the interface can be determined[118-120] (see dilution method for more details). The validity of the dilution method was tested by Gustini et al.[118] by determining the interfacial composition of CTAB/hexane/pentanol/water RMs using both diffusion NMR and the dilution method. They found that both methods gave a similar portion of pentanol in the interfacial film and hence concluded that the dilution method can be used to successfully determine the interfacial composition.

In addition to experimental techniques, theoretical molecular modelling of RMs is also able to give vital information on the distribution of molecules throughout the system over the time of the

simulation. Rodriguez et al.[45] mapped the density profiles of the water oxygen, the surfactant headgroup, surfactant tail group and the centre of mass of the oil for the benzylhexadecyldimethylammonium chloride (BHDC)/water/benzene system which showed the benzene penetrated the BDHC surfactant layer. They also showed water penetration into the surfactant layer using accessible surface area of water calculations. Abel et al.[40] performed similar accessible surface area of water calculations on the AOT/octane/water system and found no water penetration into the surfactant layer. This demonstrates how use of different surfactants such as AOT, which is branched, and BDHC, which is linear, result in differences in the RM interface and interactions, simply by tracking the distribution of the water molecules.

Further to the vital understanding of the distribution of molecules, particularly the co−surfactant, throughout the sample, knowledge of the type of microemulsion present is important. This is particularly important when changing the composition of the microemulsion or when changing the temperature and/or the salinity of the aqueous phase,[26] as these can invoke phase changes e.g. transition from water-in-oil to oil-in-water. Diffusion NMR is a powerful tool in determining the type of microemulsion as the diffusive behaviour of each component in the system (surfactant, water and oil) can be determined individually within one experiment.[49,121] The multi-component diffusion studies enables one to determine whether a microemulsion consists of water-in-oil, oil-in-water or bi-continuous structures.[49,122] Components diffusing in the continuous phase should possess a diffusion coefficient similar to that of the pure solvent,[122] whereas components within the droplets experience some diffusive restriction, and hence the resultant diffusion coefficients are reduced, usually by an order of magnitude.[49,122] With this in mind, water-in-oil microemulsions are defined by $D_{water} \approx D_{surfactant} \ll D_{oil}$, oil-in-water microemulsion are represented by $D_{oil} \approx D_{surfactant} \ll D_{water}$ and $D_{oil} \approx D_{water} < D_{surfactant}$ for bicontinuous structures.[122]

The type of microemulsion present can also be determined by conductivity measurments.[49,57,123,124] Micelles have relatively high conductivity measurements[57] in the range of 10^{-6} to 10^{-5} S m^{-1}, whereas RMs give lower conductivity measurents[57] of 10^{-16} to 10^{-12} S m^{-1}. Due to the contrast in conductivity between the different phases, conductivity measurements have been used to track the changes in the AOT/heptane/water RM system as a function of water content (ω_0).[125] Initially, they found the conductivity to increase with ω_0 until a maximum was reached at ω_0 ≈ 20, the conductivity then decreased until approximately ω_0 = 70 where a sharp increase was observed. The sharp increase in conductivity at ω_0 = 70 is due to the onset of percolation,[57] where the RM droplets begin to merge to form infinite clusters and indicates, a phase change from the RM structure.

1.2 Reverse Micelle Characterisation Techniques:

The shape, size, polydispersity, dynamics and composition of RMs are vital in understanding microemulsions and their development in a wide range of applications, particularly in nanoparticle synthesis and drug delivery. The techniques used to characterise these properties were briefly mentioned in the previous section which included electron microscopy, fluorescence measurements, x-ray or neutron scattering, dynamic light scattering (DLS), nuclear magnetic resonance (NMR), molecular modelling, conductivity measurements and titration techniques. The following gives a brief overview of these techniques.

Electron Microscopy

Electron microscopy is a technique that allows direct visualisation of the microemulsion microstructure.[49] Transmission electron microscopy (TEM) and scanning electron microscopy (SEM) are the two main electron microscopy techniques.[126,127] Both these techniques involve the preparation of a thin layer of sample and firing a high energy electron beam at the sample under vacuum conditions. In TEM the electron beam is directed onto the sample so electrons can pass through; bright regions on a TEM image show areas where electrons have passed through the sample.[49] In SEM, the electron beam is scanned over the sample surface, which scatters the electron beam. The scattered electrons are detected and counted by the microscope to produce an image which can give information on the morphology, chemical composition and crystalline structure.[49] TEM and SEM initially suffered from many image artefacts due to the drying and fixation methods used to prepare samples.[49,128] Samples of aqueous nature, like microemulsions, do not withstand these drying or fixation procedures and water loss results. Retention of aqueous environments is vital in microemulsion investigations because water loss can lead to microstructure changes.[17] This has led to the development of new sample preparation techniques such as cryogenic and freeze-fracture techniques.

Cryogenic electron microscopy involves rapidly freezing the sample to cryogenic temperatures of around −150 °C by immersing in liquid nitrogen or ethane.[49,129] The freezing is so rapid the water forms vitreous (non-crystalline) ice; this enables visualisation of the sample in its hydrated state without dehydration and is the closest replica to solution state. Freezing has to occur at a specific rate[130] ($10^6 - 10^7$ K s^{-1}) and the sample has to be very thin,[128] $10 - 500$ nm, to avoid crystallisation.[129] It is important to note that cryogenic electron microscopy does lead to sample damage from the electron beam.[131] An additional sample preparation technique is freeze-fracture where the sample is rapidly frozen at cryogenic temperatures and fractured under vacuum to expose structural detail.[131] The fracture plane is usually along the hydrophobic domains.[49] Once fractured the

surface is coated in a platinum-carbon alloy and then a thin coating of carbon to produce a replica of the surface.[131,132] The replica of the fractured surface is released and cleaned for investigations by electron microscopy,[132] the quality of the image depends upon the quality of the fracture.[131] The introduction of these two methods has opened up the possibility of electron microscopy measurements on microemulsions and surfactant-based systems to gain information on the microstructure, shape, size and morphology. Care has to be taken as electron microscopy only produces information on a snapshot of the sample; to gain an accurate representation, analysis would have to be done on multiple regions.

Fluorescence

Fluorescence measurements are important in determining physical properties of RMs[56] such as surfactant aggregation number,[55,56] size,[55,56] and microviscosity.[133] Fluorescence spectroscopy requires the presence of a fluorophore[134], which is usually added as an additional component to the microemulsion, and is often known as a probe molecule. A fluorophore is a molecule that can be excited to a higher energy electronic state by absorbing photons from a photon beam passed through the sample. Eventually, the fluorophore returns to its ground state by emitting light of a characteristic wavelength and intensity, which is determined by the fluorophore structure and its chemical environment.[134] The emission is detected and its decay is monitored over time which enables the determination of physical properties of microemulsions.[55,135]

The determination of size and surfactant aggregation number requires the presence of a probe molecule (fluorophore) and a quencher. A quencher reduces the fluorescence intensity of the probe molecule when they are in close proximity.[136] An appropriate combination of probe and quencher must be obtained so that both the probe and the quencher are located in the same

environment within the microemulsion,[56] e.g. both are hydrophilic thus located in the water core. In determining the aggregation number and size, the fluorescence decay is measured according to:[55]

$$I(t) = I(0)e^{\left(-A_2 t - A_3\left(1-e^{-A_4 t}\right)\right)}$$
<div align="right">Equation 1.16</div>

where $A_2 = k_0$ (the rate constant of the fluorescence decay for the probe without a quencher), $A_4 = k_q$ (the pseudo 1ˢᵗ order rate constant for intermicellar quenching of the probe) and $A_3 = \frac{[Q]}{[M]}$, where [Q] is the quencher concentration and [M] is the concentration of micelles. The surfactant aggregation number, *N*, is determined using Equation 1.17, where *C* is the total surfactant concentration.[55] Calculating the surfactant aggregation using this method assumes all the surfactant molecules are in the RM interface.[55]

$$N = \frac{C}{[M]} = \frac{CA_3}{[Q]}$$
<div align="right">Equation 1.17</div>

With the knowledge of the surfactant aggregation, the radius of the water core can be determined via Equation 1.18, where ω_0 is the water to surfactant ratio and V_w is the volume of components in the water core, e.g. water, and, in the case of CTAB will require the volume of the bromide counterion.[55] Size determination by fluorescence assumes the RMs consist of a monolayer of surfactant molecules and are spherical and monodisperse.[55]

$$R_w = \left[\frac{3N(\omega_0 V_w)}{4\pi}\right]$$
<div align="right">Equation 1.18</div>

Conductivity

Electrical conductivity is a simple and inexpensive method of microemulsion characterisation.[49] Electrical conductivity is a measure of a materials ability to transport charge, thus, conductivity measurements of microemulsions provide information on how ions move through the aqueous environment of the microemulsion.[137] Conductivity is an ideal method for determining the onset of percolation, the point at which droplets merge to form infinite clusters, which is characterised by a large increase in conductivity[105] as the charge carriers are able to move through the clusters more easily.[125] The conductivity of RM droplets can be calculated using the relationship proposed by Eicke et al.[138] and was further developed by Kallay and Chittofrali,[139] Equation 1.19.

$$k = \frac{\varepsilon k_B T \phi_d R_w}{2\pi\eta R_h^4}$$

<div align="right">Equation 1.19</div>

where, k is the conductivity and ε is the solvent permittivity. The relationship in Equation 1.19 shows that the conductivity, k, depends on the droplet size, R_h, the concentration of the droplets, ϕ_d (volume droplet fraction) and the continuous phase viscosity, η.[57]

The size of RMs can be determined from conductivity measurements using Equation 1.19 and applying the charge fluctuation model proposed by Eicke et al.[138] to distinguish between R_w and R_h.[57] Alternatively, Bisal et al.[29] and Venable et al.[58] were able to use the effective medium theory (EMT) of conductance[140-142] to derive R_w and the interfacial ratio of co-surfactant to surfactant. However, this required several assumptions: the droplets are spherical, all the surfactant molecules are in the RM interface and the co-surfactant is distributed between all phases. The EMT is shape specific and therefore different variations are applied depending on the shape of the droplets, thus it is imperative the droplet shape is known to determine the droplet size using this method.[29]

There is a distinct trend in the conductivity of RMs with increasing droplet size and water content, ω_0. As the droplet size and hence ω_0 increases, the conductivity increases to a maximum, and then decreases.[143,144] The initial increase in conductivity is determined by the charge state of the droplets.[57,145] Charging of the droplets is easier with an increase in size and ω_0 therefore a greater number of charged droplets is obtained, increasing the conductivity.[145] The decrease in conductivity after the maximum is due to the motion of the droplets,[57] the droplets are larger, reducing the motion and hence the conductivity.[145]

Conductivity measurements can also be used to determine the ratio of co-surfactant to surfactant, r, in the interface by varying the amount of water in the microemulsion.[6,29] Changing the water content will lead to a change in the volume droplet fraction, ϕ, and hence a variation in the conductivity.[57] If the conductivity, k, is plotted against $(\phi - {}^1/_3)$ the value of r can be determined[58] by fitting the curve to Equation 1.20 where ϕ is represented by Equation 1.21. The fitting procedure is repeated for different values of r; the optimal r value is when the curve fitting passes though the origin.[58]

$$k = \frac{2}{3}\left(k_{\mathrm{d}}\left(\phi - \frac{1}{3}\right)\right)$$

<div align="right">Equation 1.20</div>

$$\phi = \frac{\rho_{\mathrm{m}}}{\rho_{\mathrm{d}}}\left[f_{\mathrm{surf}}\left(1 + r\frac{M_{\mathrm{co-surf}}}{M_{\mathrm{surf}}} + f_{\mathrm{water}}\right)\right]$$

<div align="right">Equation 1.21</div>

Where k_{d} is the conductivity of the dispersed phase, ρ_{m} is the density of the microemulsion system, ρ_{d} is the density of the dispersed phase, f_{surf} and f_{water} are the weight fractions of the surfactant and water and M_{surf} and $M_{\mathrm{co-surf}}$ are the molecular weights of the surfactant and co-surfactant molecules.

Dilution Method (Schulmans Titration)

In addition to conductivity, the determination of interfacial co-surfactant can be performed using a simple dilution method.[118-120] The dilution method, also known as the Schulmans titration, was introduced in 1955 by Bowcott and Schulman,[146] whereby a known amount of oil was added to a microemulsion of fixed water and surfactant concentration, ω_0. The addition of oil destabilises the microemulsion, invoking a transition from limpid to turbid,[118,119,147] by reducing the interfacial concentration of co-surfactant. The microemulsion is reformed by titrating the co-surfactant into the now turbid solution until the transition from turbid to limpid takes place.[118,119,147] After taking note of the volumes of oil and co-surfactant added, this process is repeated several times. When a co-surfactant is present in a microemulsion, there are three different regions it can reside, the interface, in the water core or in the continuous phase. Therefore the total co-surfactant concentration can be represented as:[119,120,148]

$$n_{cs} = n_{cs}^{i} + n_{cs}^{w} + n_{cs}^{o} \qquad \text{Equation 1.22}$$

Where n_{cs} is the total moles of co-surfactant, n_{cs}^{i} is the interfacial moles of co-surfactant, n_{cs}^{w} represents moles of co-surfactant in the water core and n_{cs}^{o} the co-surfactant in the oil phase. If the solubility of the co-surfactant in the oil phase is constant at a given temperature, as outlined by Birdi et al.,[149] the solubility can be represented in the form of Equation 1.23, with K the solubility constant of co-surfactant in oil and n_{o} the moles of oil.

$$K = \frac{n_{cs}^{o}}{n_{o}} \qquad \text{Equation 1.23}$$

If Equation 1.22 and Equation 1.23 are combined together and divided through by the number of surfactant moles, n_{s}, we obtain:

$$\frac{n_{cs}}{n_{s}} = \frac{n_{cs}^{i} + n_{cs}^{w}}{n_{s}} + \frac{Kn_{o}}{n_{s}} \qquad \text{Equation 1.24}$$

Most co-surfactants used in RM formation are medium to long chain alcohols which have negligible solubility in water and hence $n_{cs}^w = 0$. A plot of n_{cs}/n_s against n_o/n_s will yield a straight line with a gradient equal to the constant K and an intercept that represents n_{cs}^i/n_s.[119,120,148] Therefore, these dilution experiments also provide information on the solubility of co-surfactant in oil as well as the interfacial composition.[150]

Molecular Modelling

In addition to the wealth of experimental methods used to investigate reverse micelles, computer simulations have been employed to complement these findings and offer the ability to study the structure of RMs on a molecular level.[39] Molecular simulations offer the ability to model the interactions between molecules by evaluating the potential energies and intermolecular forces.[70] Molecular simulations of reverse micelles are usually only performed on one droplet and therefore inter-droplet exchange and interactions cannot be quantified;[39] however, intra-molecular interactions and the local microstructure of the droplet can be determined. One of the most important reverse micelle properties obtained using molecular modelling is the shape of the droplets. Experimental methods such as NMR, DLS, SAXS, SANS and conductivity require prior knowledge of the droplet shape, which is often assumed to be spherical, in order to measure the size of the droplets. More accurate droplet sizes can be obtained by combining experimental methods with the shape information from molecular simulations.

When performing molecular simulations of RMs or any chemical system, a force field needs to be applied. A force field uses a potential function to describe the interactions between atoms and define parameters such as bond lengths, partial charges, bond angles and van der Waals radii.[70] There are many different force fields currently in use with the most popular being AMBER[151] (Assisted Model Building with Energy Refinement), CHARMM[152] (Chemistry at Harvard

Macromolecular Mechanics) and GROMOS[153] (Groningen Molecular Simulation). These three force fields have been used in the simulation of RMs, and are often employed in the simulations of biomolecules.[154] All three of these force fields have been used in the simulation of AOT RMs,[12,40,42-44] whereas AMBER and GROMOS have been utilised for CTAB RMs.[46,155] The force fields also define how the atoms in a simulation are treated which can be either an all-atom, united-atom or coarse-grained approach. An all-atom approach provides parameters for all atoms in the simulation, including hydrogen,[42] while a united-atom approach treats hydrogens and the carbons associated with them as a united atom,[42] e.g. the methyl group in CTAB is treated as one united atom. In the coarse-grained approach groups of atoms are treated as one moiety and are therefore represented by one force interaction,[44] e.g. the surfactant tails.[70]

These different atom approaches have been applied to different components in a RM system by Vasquez et al.[42] who utilised an all-atom approach for the AOT surfactant and a united-atom approach for the solvent iso-octane. This allowed the iso-octane to be treated as 8 atoms instead of 26 which considerably reduced the required simulation time and computer power.[42,47] Some simulations of RMs have been performed in the absence of a solvent and hence no periodic boundaries.[156] This approach is unfavourable due to the termination of the simulation when water molecules escape the RM core, which limits the timescale of the simulation. The use of an all-atom solvent[40] is advantageous as it allows observation of molecule dynamics and distribution between the RM and the continuous phase.[70,155]

The CHARMM and GROMOS force fields were compared by Martinez et al.[43] by performing molecular simulations on the AOT/iso-octane/water RM system with both force fields and where the droplets are both spherically restrained and unrestrained. They found that the unrestrained droplets deviated from spherical when both force fields were employed. The RM droplet with the CHARMM force field deviated from spherical to rod-like, whereas the droplets simulated with the GROMOS

force field deviated to a disc from spherical geometry. This study demonstrates a dependence of the resultant shape of the RM on the type of force field utilised,[43,70] and how care must be taken when determining the type of force field to use in simulations of RMs.

X-ray and Neutron Scattering

Scattering techniques such as small angle x-ray scattering (SAXS) and small angle neutron scattering (SANS) have been used in the structural characterisation of many systems from soft matter, such as surfactant self-assemblies, to hard porous systems.[31] In these small angle scattering techniques an incident beam of radiation is directed at a sample. The sample scatters the beam of radiation and the intensity and angle of the scattered beam is recorded.[49] The scattered radiation produces an interference pattern which is Fourier transformed to produce an image.[25] Scattering arises from different entities depending on the technique used: SAXS uses x-rays which are scattered by regions of electron density, whereas SANS uses a neutron beam which is scattered by regions of different nuclear composition.[49] SAXS and SANS can give information on the shape, polydispersity and packing of microemulsion systems. However, only one of these characteristics can be found at any one time because two of these parameters must be known or assumed to gain information on the third.[32] It can usually be assumed that there is no packing in microemulsions at infinite dilution[32] therefore details of the shape or polydispersity are required.

Analysis of microemulsions using SANS requires selective deuteration of the different components to gain better contrast in the resultant images.[30,31] There is a high contrast between hydrogen rich material and deuterium rich material due to the difference in scattering lengths.[31] In addition, SANS requires a high powered source of which access is limited[31,49] and data acquisition is much longer than SAXS[49]. Nevertheless, SANS has a widespread use in microemulsion analysis and has been applied to tertiary[157] and quaternary[53] microemulsions. Freeman et al.[30] used SANS to track

the effect of bile salt on the size and polydispersity of the AOT/heptane/water reverse micelle system. SAXS measurements on microemulsions is less widespread than SANS due to the larger penetration depth and lack of sample damage in SANS.[31]

Dynamic Light Scattering (DLS)

Dynamic light scattering (DLS), also known as photon correlation spectroscopy (PCS) and quasi-elastic light scattering (QELS), is an easy non-invasive[33] method commonly employed in microemulsion systems to obtain size distributions from the determination of the hydrodynamic radius,[49] R_h. DLS involves directing a monochromatic, polarized laser light[17] through a dispersion of particles such as reverse micelles. The random motion of the RM droplets interacts with the laser light; as a consequence the light is scattered with random phase.[17,33] The sum of the scattered light from all the RMs in the solution gives regions of constructive and destructive interference leading to fluctuations in the scattered light intensity.[158] These fluctuations are sensitive to the motion of the particles:[48] smaller and rapid moving particles have fast fluctuations in intensity.[33] The detector monitors these fluctuations, which are processed to give an autocorrelation function[34] that gives information on the motion and size of the particles. Monodisperse, spherical particles with only translational motion will have an exponential decay in the autocorrelation function,[34] which, when analysed appropriately, gives the diffusion coefficient, D, of the diffusing particles.[17,34,48] For a polydisperse sample containing droplets of differing sizes, the autocorrelation function has a multi-exponential decay.[34]

The autocorrelation function decay can be converted into a distribution of decay rates by the use of the inverse Laplace transform (ILT).[70,159] The ILT converts time related data, usually a signal decay, into a probability distribution of the time related data.[160,161] See chapter 2 for more details on the ILT. The distribution of decay rates can be converted to a distribution of diffusion coefficients,[34,70]

and hence a distribution of droplet radius, R_h, by applying the Stokes-Einstein[25,33,34] equation, Equation 1.7, provided the viscosity, η, is known. DLS measures an intensity distribution and then converts to number and volume distributions.[34] The intensity distribution represents the contribution of each particle in relation to the intensity of scattered light from the particle. This is calculated directly from the autocorrelation function and requires no knowledge of the optical nature of the particles.[34] The intensity distribution can be converted into a number distribution, which represents the number of particles that give a specific observed intensity[34] by the application of Mie theory.[34] Mie theory provides methods of calculating how light is scattered from homogeneous spheres[70,162] and hence information about the scattering material is required, such as refractive index, to accurately determine the amount the material scatters. Often the refractive index of the droplets is not known; therefore an estimation is made,[34] which can generate errors in the number distributions.[48] Finally, the number distribution is converted into a volume distribution by multiplying the number of particles for a given size by the corresponding volume of a sphere. Both number and volume distributions will contain errors due to poor estimations of the refractive index of the droplet[34] causing errors to occur when applying Mie theory.[48] Errors are also amplified as a result of the application of Mie theory where small errors in the intensity distributions[70] lead to large errors in the number and volume distributions. Therefore, the use of number and volume distributions are discouraged but number distribution is the one typically reported,[48] so some caution needs to be taken when interpreting DLS data.

DLS is an advantageous method for microemulsion analysis as it is a cheap and easy method that does not require major operator training, which delivers immediate results.[33] There is no major sample preparation like deuteration as with SANS, and the technique provides particle size analysis for particles in the range of a few nanometres to 1 – 2 micrometres.[33] While there are many advantages to using DLS there are also some drawbacks that make particle size analysis of reverse micelles difficult. Samples for analysis by DLS must only scatter the light once between the light

source and the detector;[33] this is only achieved when samples are dilute and transparent.[17,33,49] The presence of dust in samples also causes issues for DLS and significant efforts need to be made to remove it, either by filtration or by extra data analysis.[48] DLS also requires the refractive index of the droplet and continuous phase to be different,[48] and assumes the particles are spherical. It has also been reported that weakly scattering particles of 50 nm or less are difficult to detect and the reproducibility of these data are poor.[34] Nevertheless, DLS has been widely used in determining the dynamics and sizes of reverse micelle systems.

Nuclear Magnetic Resonance (NMR)

Nuclear magnetic resonance (NMR) has been used to characterise the microstructure, size and dynamics of reverse micellar systems. NMR provides a non-invasive analysis of reverse micelle and allows measurements of optically opaque and turbid samples.[48] NMR does not require samples to have differences in refractive indices[48] or selective deuteration, NMR just requires the presence of NMR active nuclei such as ^{1}H, ^{19}F, ^{31}P, ^{13}C. NMR also has the ability to individually probe specific molecular species in the system and therefore can determine the different characteristics of each component in a reverse micelle system. NMR has become a powerful tool in investigating RM systems due to the ability to probe diffusion and relaxation processes as well as determining the presence of exchange. An outline of the theory of NMR can be found in the following chapter.

1.3 References

(1)   Tcholakova, S.; Denkov, N. D.; Ivanov, I. B.; Campbell, B. *Adv. Colloid Interface Sci.* **2006**, *123*, 259.

(2)   Capek, I. *Adv. Colloid Interface Sci.* **2004**, *110*, 49.

(3)   Chen, F. X.; Xu, G. Q.; Hor, T. S. A. *Mater. Lett.* **2003**, *57*, 3282.

(4)   Curri, M. L.; Agostiano, A.; Manna, L.; Della Monica, M.; Catalano, M.; Chiavarone, L.;

Spagnolo, V.; Lugara, M. *J. Phys. Chem. B* **2000**, *104*, 8391.

(5)   Eastoe, J.; Hollamby, M. J.; Hudson, L. *Adv. Colloid Interface Sci.* **2006**, *128*, 5.

(6)   Fang, X.; Yang, C. *J. Colloid Interface Sci.* **1999**, *212*, 242.

(7)   Uskokovic, V.; Drofenik, M. *Surf. Rev. Lett.* **2005**, *12*, 239.

(8)   Fendler, J. H. *Accounts Chem. Res.* **1976**, *9*, 153.

(9)   McIlwaine, R. E.; Fenton, H.; Scott, S. K.; Taylor, A. F. *J. Phys. Chem. C* **2008**, *112*, 2499.

(10)   Pileni, M. P. *J. Phys. Chem.* **1993**, *97*, 6961.

(11)   López-Quintela, M. A.; Tojo, C.; Blanco, M. C.; García Rio, L.; Leis, J. R. *Curr. Opin. Colloid

Interface Sci* **2004**, *9*, 264.

(12)   Graeve, O. A.; Fathi, H.; Kelly, J. P.; Saterlie, M. S.; Sinha, K.; Rojas-George, G.; Kanakala, R.;

Brown, D. R.; Lopez, E. A. *J. Colloid Interface Sci.* **2013**, *407*, 302.

(13)   Kowlgi, K.; Lafont, U.; Rappolt, M.; Koper, G. *J. Colloid Interface Sci.* **2012**, *372*, 16.

(14)   Kogan, A.; Garti, N. *Adv. Colloid Interface Sci.* **2006**, *123*, 369.

(15)   Luisi, P. L. *Angew. Chem., Int. Ed.* **1985**, *24*, 439.

(16)   Sharon, M.; Ilag, L. L.; Robinson, C. V. *J. Am. Chem. Soc.* **2007**, *129*, 8740.

(17)   Muller-Goymann, C. C. *Eur. J. Pharm. Biopharm.* **2004**, *58*, 343.

(18)   Muellergoymann, C. C.; Hamann, H. J. *J. Control. Release* **1993**, *23*, 165.

(19)   Crans, D. C.; Schoeberl, S.; Gaidamauskas, E.; Baruah, B.; Roess, D. A. *J. Biol. Inorg. Chem.*

2011, *16*, 961.

(20)   Marhuenda-Egea, F. C.; Piera-Velazquez, S.; Cadenas, C.; Cadenas, E. *Archaea* **2002**, *1*, 105.

(21)   Norde, W. *Colloids and Interfaces in Life Sciences and Bionanotechnology, Second Edition*;

Taylor & Francis, 2011.

(22)   Ruckenstein, E.; Nagarajan, R. *J. Phys. Chem.* **1975**, *79*, 2622.

(23)   Li, Z.; Agellon, L. B.; Allen, T. M.; Umeda, M.; Jewell, L.; Mason, A.; Vance, D. E. *Cell Maetab.*,

3, 321.

(24)   Yadav, T.; Tikariha, D.; Lakra, J.; Satnami, M. L.; Tiwari, A. K.; Saha, S. K.; Ghosh, K. K. *J. Mol.

Liq.* **2015**, *204*, 216.

(25)   Moulik, S. P.; Paul, B. K. *Adv. Colloid Interface Sci.* **1998**, *78*, 99.

(26)   Palazzo, G.; Lopez, F.; Giustini, M.; Colafemmina, G.; Ceglie, A. *J. Phys. Chem. B* **2003**, *107*,

1924.

(27)   Zulauf, M.; Eicke, H. F. *J. Phys. Chem.* **1979**, *83*, 480.

(28)   De, T. K.; Maitra, A. *Adv. Colloid Interface Sci.* **1995**, *59*, 95.

(29)   Bisal, S.; Bhattacharya, P. K.; Moulik, S. P. *J. Phys. Chem.* **1990**, *94*, 350.

(30)   Freeman, K. S.; Tan, N. C. B.; Trevino, S. F.; Kline, S.; McGown, L. B.; Kiserow, D. J. *Langmuir*

2001, *17*, 3912.

(31)   Hollamby, M. J. *Phys. Chem. Chem. Phys.* **2013**, *15*, 10566.

(32)   Pauw, B. R. *J. Phys.: Condens. Matter.* **2013**, *25*, 383201.

(33)   Alexander, M.; Dalgleish, D. G. *Food Biophys.* **2006**, *1*, 2.

(34)   Filella, M.; Zhang, J. W.; Newman, M. E.; Buffle, J. *Colloid Surf., A.* **1997**, *120*, 27.

(35)   Bisceglia, M.; Acosta, E.; Kurlat, D.; Ginzberg, B. *Colloid Surf., A.* **1996**, *108*, 137.

(36)   Deen, G. R.; Pedersen, J. S. *Langmuir* **2008**, *24*, 3111.

(37)   Deen, G. R.; Oliveira, C. L. P.; Pedersen, J. S. *J. Phys. Chem. B* **2009**, *113*, 7138.

(38)   Blochowicz, T.; Gogelein, C.; Spehr, T.; Muller, M.; Stuhn, B. *Phys. Rev. E* **2007**, *76*, 9.

(39)   Nevidimov, A. V. *Russ. J. Phys. Chem. B.* **2014**, *8*, 554.

(40)   Abel, S.; Sterpone, F.; Bandyopadhyay, S.; Marchi, M. *J. Phys. Chem. B* **2004**, *108*, 19458.

(41)   Brodskaya, E. N.; Mudzhikova, G. V. *Mol. Phys.* **2006**, *104*, 3635.

(42)   Gardner, A.; Vasquez, V. R.; Clifton, A.; Graeve, O. A. *Fluid Phase Equilib.* **2007**, *262*, 264.

(43)   Martinez, A. V.; Dominguez, L.; Malolepsza, E.; Moser, A.; Ziegler, Z.; Straub, J. E. *J. Phys. Chem. B* **2013**, *117*, 7345.

(44)   Mudzhikova, G. V.; Brodskaya, E. N. *Colloid J.* **2006**, *68*, 729.

(45)   Agazzi, F. M.; Correa, N. M.; Rodriguez, J. *Langmuir* **2014**, *30*, 9643.

(46)   Klíčová, L.; Muchová, E.; Šebej, P.; Slavíček, P.; Klán, P. *Langmuir* **2015**, *31*, 8284.

(47)   Fathi, H.; Kelly, J. P.; Vasquez, V. R.; Graeve, O. A. *Langmuir* **2012**, *28*, 9267.

(48)   Law, S. J.; Britton, M. M. *Langmuir* **2012**, *28*, 11699.

(49)   Acharya, D. P.; Hartley, P. G. *Curr. Opin. Colloid Interface Sci* **2012**, *17*, 274.

(50)   Vasquez, V. R.; Williams, B. C.; Graeve, O. A. *J. Phys. Chem. B.* **2011**, *115*, 2979.

(51)   Bohidar, H. B.; Behboudnia, M. *Colloid Surf., A.* **2001**, *178*, 313.

(52)   Shrestha, L. K.; Shrestha, R. G.; Abe, M.; Ariga, K. *Soft Matter.* **2011**, *7*, 10017.

(53)   Foster, T.; Sottmann, T.; Schweins, R.; Strey, R. *J. Chem. Phys.* **2008**, *128*, 064902.

(54)   Silva, B. F. B.; Marques, E. F.; Olsson, U.; Linse, P. *J. Phys. Chem. B* **2009**, *113*, 10230.

(55)   Lang, J.; Mascolo, G.; Zana, R.; Luisi, P. L. *J. Phys. Chem.* **1990**, *94*, 3069.

(56)   Rodenas, E.; Perez-Benito, E. *J. Phys. Chem.* **1991**, *95*, 4552.

(57)   Bumajdad, A.; Eastoe, J. *J. Colloid Interface Sci.* **2004**, *274*, 268.

(58)   Fang, J.; Venable, R. L. *J. Colloid Interface Sci.* **1987**, *116*, 269.

(59)   Faucompre, B.; Lindman, B. *J. Phys. Chem.* **1987**, *91*, 383.

(60)   Cussler, E. L. *Diffusion: Mass Transfer in Fluid Systems*; Cambridge University Press, 1997.

(61)   Willis, S. A.; Dennis, G. R.; Zheng, G.; Price, W. S. *J. Mol. Liq.* **2010**, *156*, 45.

(62)   Price, W. S. *Nmr Studies of Translational Motion: Principles and Applications*; Cambridge University Press, 2009.

(63)   Hansen, S. *Journal of Chemical Physics* **2004**, *121*, 9111.

(64)   Söderman, O.; Stilbs, P.; Price, W. S. *Concepts Magn. Reson.* **2004**, *23A*, 121.

(65)   Jonstromer, M.; Jonsson, B.; Lindman, B. *J. Phys. Chem.* **1991**, *95*, 3293.

(66)   Lekkerkerker, H. N. W.; Dhont, J. K. G. *J. Chem. Phys.* **1984**, *80*, 5790.

(67)   Nazario, L. M. M.; Hatton, T. A.; Crespo, J. *Langmuir* **1996**, *12*, 6326.

(68)   Evans, G. T.; James, C. P. *J. Chem. Phys.* **1983**, *79*, 5553.

(69)   Jonsson, B.; Wennerstrom, H.; Nilsson, P. G.; Linse, P. *Colloid. Polym. Sci.* **1986**, *264*, 77.

(70)   Law, S. J. PhD, University of Birmingham, 2015.

(71)   Atik, S. S.; Thomas, J. K. *J. Am. Chem. Soc.* **1981**, *103*, 4367.

(72)   Webb, G. A. *Annual Reports on NMR Spectroscopy*; Elsevier Science, 2007.

(73)   Begum, F.; Mollah, M. Y. A.; Rahman, M. M.; Susan, M. A. H. *J. Chem.* **2015**, *2015*, 10.

(74)   Biswas, S.; Bhattacharya, S. C.; Moulik, S. P. *Indian J. Chem. Sect A-Inorg. Bio-Inorg. Phys. Theor. Anal. Chem.* **2001**, *40*, 1210.

(75)   Kaushik, P.; Vaidya, S.; Ahmad, T.; Ganguli, A. K. *Colloid Surf., A.* **2007**, *293*, 162.

(76)   Arleth, L.; Pedersen, J. S. *Phys. Rev. E* **2001**, *63*, 18.

(77)   Kotlarchyk, M.; Chen, S. H.; Huang, J. S. *J. Phys. Chem.* **1982**, *86*, 3273.

(78)   Kotlarchyk, M.; Stephens, R. B.; Huang, J. S. *J. Phys. Chem.* **1988**, *92*, 1533.

(79)   Klicova, L.; Sebej, P.; Stacko, P.; Filippov, S. K.; Bogomolova, A.; Padilla, M.; Klan, P. *Langmuir* **2012**, *28*, 15185.

(80)   Amararene, A.; Gindre, M.; Le Huerou, J. Y.; Urbach, W.; Valdez, D.; Waks, M. *Phys. Rev. E* **2000**, *61*, 682.

(81)   Jain, T. K.; Cassin, G.; Badiali, J. P.; Pileni, M. P. *Langmuir* **1996**, *12*, 2408.

(82)   Almgren, M.; Johannsson, R.; Eriksson, J. C. *J. Phys. Chem.* **1993**, *97*, 8590.

(83)   Tovstun, S. A.; Razumov, V. F. *J. Colloid Interface Sci.* **2010**, *351*, 485.

(84)   Halliday, N. A. PhD, University of Birmingham, 2011.

(85)   Capek, I. *Nanocomposite Structures and Dispersions*; Elsevier Science, 2006.

(86)   Fletcher, P. D. I.; Howe, A. M.; Robinson, B. H. *J. Chem. Soc., Faraday Trans. I.* **1987**, *83*, 985.

(87)   Barreleiro, P. C. A.; Alexandridis, P. *J. Colloid Interface Sci.* **1998**, *206*, 357.

(88)   Lang, J.; Zana, R.; Bauer, R.; Hoffmann, H.; Ulbricht, W. *J. Phys. Chem.* **1975**, *79*, 276.

(89)   Cui, X. H.; Yang, X. Y.; Chen, H.; Liu, A. H.; Mao, S. Z.; Liu, M. L.; Yuan, H. Z.; Luo, P. Y.; Du, Y. R. *J. Phys. Chem. B* **2008**, *112*, 2874.

(90)   Lemyre, J. L.; Ritcey, A. M. *Langmuir* **2010**, *26*, 6250.

(91)   Guo, W.; Brown, T. A.; Fung, B. M. *J. Phys. Chem.* **1991**, *95*, 1829.

(92)   Barreleiro, P. C. A.; Alexandridis, P. *J. Colloid Interface Sci.* **1998**, *206*, 357.

(93)   Dalvi, V. H.; Rossky, P. J. *Proceedings of the National Academy of Sciences of the United States of America* **2010**, *107*, 13603.

(94)   Bastogne, F.; Nagy, B. J.; David, C. *Colloid Surf., A.* **1999**, *148*, 245.

(95)   Lang, J.; Lalem, N.; Zana, R. *J. Phys. Chem.* **1991**, *95*, 9533.

(96)   Giustini, M.; Palazzo, G.; Colafemmina, G.; Della Monica, M.; Giomini, M.; Ceglie, A. *J. Phys. Chem.* **1996**, *100*, 3190.

(97)   Palazzo, G.; Carbone, L.; Colafemmina, G.; Angelico, R.; Ceglie, A.; Giustini, M. *Phys. Chem. Chem. Phys.* **2004**, *6*, 1423.

(98)   Mathew, D. S.; Juang, R. S. *Sep. Purif. Technol.* **2007**, *53*, 199.

(99)   Mali, K. S.; Dutt, G. B. *J. Chem. Phys.* **2009**, *131*, 8.

(100)   Plucinski, P.; Reitmeir, J. *Colloid Surf., A.* **1995**, *97*, 157.

(101)   Naoe, K.; Takeuchi, C.; Kawagoe, M.; Nagayama, K.; Imai, M. *J. Chromatogr. B* **2007**, *850*, 277.

(102)   Sarma, S.; Gohain, B.; Dutta, R. K. *J. Dispersion Sci. Technol.* **2006**, *27*, 899.

(103)   Leung, R.; Shah, D. O. *J. Colloid Interface Sci.* **1987**, *120*, 330.

(104)   PerezCasas, S.; Castillo, R.; Costas, M. *J. Phys. Chem. B* **1997**, *101*, 7043.

(105)   Zhang, X. G.; Chen, Y. J.; Liu, J. X.; Zhao, C. Z.; Zhang, H. J. *J. Phys. Chem. B* **2012**, *116*, 3723.

(106)   Bansal, V. K.; Shah, D. O.; Oconnell, J. P. *J. Colloid Interface Sci.* **1980**, *75*, 462.

(107)   Hou, M. J.; Shah, D. O. *Langmuir* **1987**, *3*, 1086.

(108)   Lin, J.; Zhou, W. L.; O'Connor, C. J. *Mater. Lett.* **2001**, *49*, 282.

(109)   Halliday, N. A.; Peet, A. C.; Britton, M. M. *J. Phys. Chem. B.* **2010**, *114*, 13745.

(110)   Fukumi, T.; Fujiwara, Y.; Arata, Y.; Fujiwara, S. *Bull. Chem. Soc. Jpn.* **1968**, *41*, 41.

(111)   Oakes, J. *J. Chem. Soc., Faraday Trans. I.* **1973**, *69*, 1311.

(112)   Rule, G. S.; Hitchens, T. K. *Fundamentals of Protein NMR Spectroscopy*; Springer, 2006.

(113)   Bellocq, A. M.; Biais, J.; Clin, B.; Lalanne, P.; Lemanceau, B. *J. Colloid Interface Sci.* **1979**, *70*, 524.

(114)   Hansen, J. R. *J. Phys. Chem.* **1974**, *78*, 256.

(115)   Kumar, C.; Balasubramanian, D. *J. Colloid Interface Sci.* **1980**, *74*, 64.

(116)   Nilsson, P. G.; Lindman, B. *J. Phys. Chem.* **1984**, *88*, 5391.

(117)   Nilsson, P. G.; Lindman, B. *J. Phys. Chem.* **1983**, *87*, 4756.

(118)   Giustini, M.; Murgia, S.; Palazzo, G. *Langmuir* **2004**, *20*, 7381.

(119)   Bera, A.; Ojha, K.; Kumar, T.; Mandal, A. *Colloid Surf., A.* **2012**, *404*, 70.

(120)   Bardhan, S.; Kundu, K.; Paul, B. K.; Saha, S. K. *Colloid Surf., A.* **2013**, *433*, 219.

(121)   Gradzielski, M. *Curr. Opin. Colloid Interface Sci* **2008**, *13*, 263.

(122)   Ceglie, A.; Das, K. P.; Lindman, B. *Colloid Surf.* **1987**, *28*, 29.

(123)   Smith, D. H.; Johnson, G. K.; Wang, Y. H. C.; Lim, K. H. *Langmuir* **1994**, *10*, 2516.

(124)   Stubenrauch, C.; Tessendorf, R.; Salvati, A.; Topgaard, D.; Sottmann, T.; Strey, R.; Lynch, I. *Langmuir* **2008**, *24*, 8473.

(125)   Liu, D. J.; Ma, J. M.; Cheng, H. M.; Zhao, Z. G. *Colloid Surf., A.* **1998**, *135*, 157.

(126)   Kuntsche, J.; Horst, J. C.; Bunjes, H. *Int. J. Pharm.* **2011**, *417*, 120.

(127)   Krauel, K.; Girvan, L.; Hook, S.; Rades, T. *Micron.* **2007**, *38*, 796.

(128)   Almgren, M.; Edwards, K.; Karlsson, G. *Colloid Surf., A.* **2000**, *174*, 3.

(129)   Egelhaaf, S. U.; Schurtenberger, P.; Muller, M. *J. Microsc. (Oxf)* **2000**, *200*, 128.

(130)   Steinbrecht, R. A.; Zierold, K. *Cryotechniques in Biological Electron Microscopy*; Springer Berlin Heidelberg, 2012.

(131)   Belkoura, L.; Stubenrauch, C.; Strey, R. *Langmuir* **2004**, *20*, 4391.

(132)   Mondain-Monval, O. *Curr. Opin. Colloid Interface Sci* **2005**, *10*, 250.

(133)   Hasegawa, M.; Sugimura, T.; Suzaki, Y.; Shindo, Y.; Kitahara, A. *J. Phys. Chem.* **1994**, *98*, 2120.

(134)   Sauer, M.; Hofkens, J.; Enderlein, J. *Handbook of Fluorescence Spectroscopy and Imaging: From Ensemble to Single Molecules*; Wiley, 2010.

(135)   Corbeil, E. M.; Levinger, N. E. *Langmuir* **2003**, *19*, 7264.

(136)   Lakowicz, J. R. In *Principles of Fluorescence Spectroscopy*; Lakowicz, J., Ed.; Springer US: 2006, p 277.

(137)   Bauduin, P.; Touraud, D.; Kunz, W.; Savelli, M. P.; Pulvin, S.; Ninham, B. W. *J. Colloid Interface Sci.* **2005**, *292*, 244.

(138)   Eicke, H. F.; Borkovec, M.; Dasgupta, B. *J. Phys. Chem.* **1989**, *93*, 314.

(139)   Kallay, N.; Chittofrati, A. *J. Phys. Chem.* **1990**, *94*, 4755.

(140)   Granqvist, C. G.; Hunderi, O. *Phys. Rev. B* **1978**, *18*, 1554.

(141)   Bruggeman, D. A. G. *Ann. Phys.-Berlin* **1935**, *24*, 636.

(142)   Bottcher, C. J. F. *Recl. Trav. Chim. Pays-Bas-J. Roy. Neth. Chem. Soc.* **1945**, *64*, 47.

(143)   Bordi, F.; Cametti, C. *Colloid. Polym. Sci.* **1998**, *276*, 1044.

(144)   Bordi, F.; Cametti, C.; Di Biasio, A. In *Trends in Colloid and Interface Science Xiii*; Tezak, D., Martinis, M., Eds. 1999; Vol. 112, p 93.

(145)   Liu, D. J.; Ma, J. M.; Cheng, H. M.; Zhao, Z. G. *Colloid Surf., A.* **1999**, *148*, 291.

(146)   Bowcott, J. E.; Schulman, J. H. *Z. Elektrochem.* **1955**, *59*, 283.

(147)   Moulik, S. P.; Digout, L. G.; Aylward, W. M.; Palepu, R. *Langmuir* **2000**, *16*, 3101.

(148)   Paul, B. K.; Nandy, D. *J. Colloid Interface Sci.* **2007**, *316*, 751.

(149)   Birdi, K. S. *Colloid. Polym. Sci.* **1982**, *260*, 628.

(150)   Gu, G. X.; Wang, W. Q.; Yan, H. K. *J. Therm. Anal.* **1998**, *51*, 115.

(151)   Case, D. A.; Darden, T. A.; Cheatham, T. E.; Simmerling, C. L.; Wang, J.; Duke, R. E.; Luo, R.;

Walker, R. C.; Zhang, W.; Merz, K. M.; Roberts, B.; Hayik, S.; Roitberg, A.; Seabra, G.; Swails, J.; Götz,

A. W.; Kolossváry, I.; Wong, K. F.; Paesani, F.; Vanicek, J.; Wolf, R. M.; Liu, J.; Wu, X.; Brozell, S. R.;

Steinbrecher, T.; Gohlke, H.; Cai, Q.; Ye, X.; Wang, J. M.; Hsieh, M.-J.; Cui, G.; Roe, D. R.; Mathews, D.

H.; Seetin, M. G.; Salomon-Ferrer, R.; Sagui, C.; Babin, V.; Luchko, T.; Gusarov, S.; Kovalenko, A.; P.A.,

K.; University of California, San Francisco: 2012.

(152)   Brooks, B. R.; Brooks, C. L.; Mackerell, A. D.; Nilsson, L.; Petrella, R. J.; Roux, B.; Won, Y.;

Archontis, G.; Bartels, C.; Boresch, S.; Caflisch, A.; Caves, L.; Cui, Q.; Dinner, A. R.; Feig, M.; Fischer, S.;

Gao, J.; Hodoscek, M.; Im, W.; Kuczera, K.; Lazaridis, T.; Ma, J.; Ovchinnikov, V.; Paci, E.; Pastor, R. W.;

Post, C. B.; Pu, J. Z.; Schaefer, M.; Tidor, B.; Venable, R. M.; Woodcock, H. L.; Wu, X.; Yang, W.; York,

D. M.; Karplus, M. *J. Comput. Chem.* **2009**, *30*, 1545.

(153)   Van der Spoel, D.; Lindahl, E.; Hess, B.; Groenhof, G.; Mark, A. E.; Berendsen, H. J. C. *J.

Comput. Chem.* **2005**, *26*, 1701.

(154)   González, M. A. *JDN* **2011**, *12*, 169.

(155)   Mills, A. J.; Wilkie, J.; Britton, M. M. *J. Phys. Chem. B* **2014**, *118*, 10767.

(156)   Binks, D. A.; Spencer, N.; Wilkie, J.; Britton, M. M. *J. Phys. Chem. B* **2010**, *114*, 12558.

(157)   Foster, T.; Sottmann, T.; Schweins, R.; Strey, R. *J. Chem. Phys.* **2008**, *128*, 054502.

(158)   Schatzel, K. *Adv. Colloid Interface Sci.* **1993**, *46*, 309.

(159)   Finsy, R. *Adv. Colloid Interface Sci.* **1994**, *52*, 79.

(160)   Song, Y. Q.; Venkataramanan, L.; Burcaw, L. *J. Chem. Phys.* **2005**, *122*, 8.

(161)   Song, Y. Q.; Venkataramanan, L.; Hurlimann, M. D.; Flaum, M.; Frulla, P.; Straley, C. *J. Magn.

Reson.* **2002**, *154*, 261.

(162)   Hergert, W.; Wriedt, T. *The Mie Theory: Basics and Applications*; Springer Berlin Heidelberg,

2012.

2. Theory of Nuclear Magnetic Resonance

2.1 Basics of Nuclear Magnetic Resonance

A nucleus is NMR active when the spin quantum number, I, is non-zero. The spin quantum number, I, is determined by the number of unpaired nucleons, with each unpaired nucleon contributing a value of ½.[1] A nucleus where $I \neq 0$, has inherent spin and possesses spin angular momentum,[2] I, and charge. The motion of this charge induces a magnetic moment, μ, according to Equation 2.1, where γ is the gyromagnetic ratio of the nucleus.[2]

$$\mu = \gamma I \qquad \text{Equation 2.1}$$

When an external magnetic field is applied, the magnetic moments, μ, align with respect to the magnetic field,[3] B_0. The magnetic field, B_0, causes the spins to precess,[3] Figure 2.1, at a frequency known as the Larmor frequency, ω_0, which is defined by Equation 2.2.

$$\omega_0 = -\gamma B_0 \qquad \text{Equation 2.2}$$
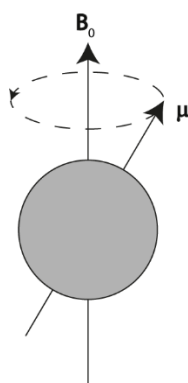
Figure 2.1: A schematic of the precession of a nucleus in a static magnetic field B_0, this precessional frequency is known as the Larmor frequency.

For each atomic nucleus with spin quantum number, I, there are $2I + 1$ possible spin states[2] which, in the absence of a magnetic field, are all degenerate. This degeneracy is lost when an external magnetic field, B_0, is applied, to give equally spaced energy levels[1,4] with $\Delta E = \frac{h\gamma B_0}{2\pi}$, where h is Planck's constant. Each energy level has energy, $E_m = -\frac{h}{2\pi}\gamma m B_0$, where m is the magnetic quantum number and has values $m = I, I-1, ..., -I$. A nucleus with $I = \frac{1}{2}$ will have two possible spin states with $m = \frac{1}{2}$ and $-\frac{1}{2}$, Figure 2.2, which are labelled α and β states, respectively. The α and β states are stable eigenstates which represent a superposition of spin states and are commonly denoted spin-up (α state) and spin-down (β state).[2,4] With multiple spins, the populations of these $2I + 1$ energy levels are in accordance with the Boltzmann distribution,[1,3,4] Equation 2.3. The α state has slightly lower energy than the β state and therefore at thermal equilibrium the Boltzman distribution predicts there is a slight population excess of spins in the α state. This population excess gives rise to the bulk magnetisation vector,[2,3] M_0, which lies in the direction of the highest populated spin state, usually the α state.

$$\frac{N_\alpha}{N_\beta} = \exp^{\frac{-\Delta E}{k_B T}}$$
<div align="right">Equation 2.3</div>
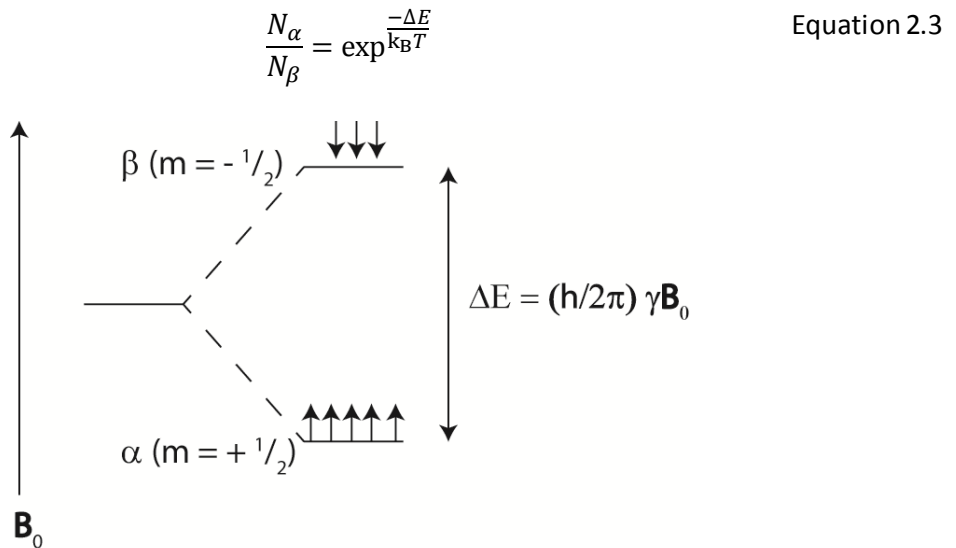
Figure 2.2: An energy diagram to show the orientation of the spins of an $I = \frac{1}{2}$ nucleus in an external magnetic field, B_0 with spin up (parallel to B_0), α, occupying the lowest energy level and spin down (anti-parallel to B_0), β, the highest energy level.

Effect of Radiofrequency (rf) Radiation

The bulk magnetisation vector, M_0, can be manipulated by the application of a radiofrequency (rf) pulse. The rf pulse is usually applied in the direction of the external magnetic field, which is usually the *z* axis. The rf pulse is given an angle, which is related to the strength and duration of the rf pulse. A 90° rf pulse transfers M_0 into the transverse plane (*x-y* plane) and in doing so makes the population of spins in the α and β states equal. Immediately after a 90° pulse the spins are said to have phase coherence, where the spin precession is synchronized.[2] A 180° pulse inverts the population of spins in the α and β states; therefore, for a system at thermal equilibrium with a population excess of spins in the α state, application of a 180° rf pulse results in a population excess of spins in the β state, placing M_0 on the *–z* axis. NMR signal is observable when M_0 is in the transverse plane,[3] therefore the NMR signal is maximum immediately after a 90° pulse.

Rotating frame

To enable the visualisation of the magnetisation, M_0, in the transverse plane and to aid the explanation of the processes occurring throughout a pulse sequence, a rotating frame of reference is introduced.[2] In the "laboratory frame" (Figure 2.3a), M_0 is precessing in the *x-y* plane at the Larmor frequency, ω_0, which makes it difficult to visualise and track the magnetisation, M_0, in the transverse plane. A real-life example of this "laboratory frame" is watching a child on a fairground carousel: you see the child move towards and away from you, but it is difficult to follow the track of the child from a stationary position.[2] To simplify this "laboratory frame" the "rotating frame" is introduced. In the "rotating frame" (Figure 2.3b) the *z* axis remains stationary, which lies in the same direction as the *z* axis in the "laboratory frame", but the *x-y* plane is rotating at Larmor frequency, ω_0. The rotation of the *x-y* plane has the effect of making the magnetisation, M_0, appear stationary,[2,4] and hence enables M_0 to be easily observed and tracked. The real-life example of the rotating frame is to watch the

child from a point on the carousel, so the observer is now rotating at the same frequency and hence the child now appears stationary.[2] This "rotating frame" will be used to aid the explanation of how M_0 is affected throughout the pulse sequences explained in this chapter.
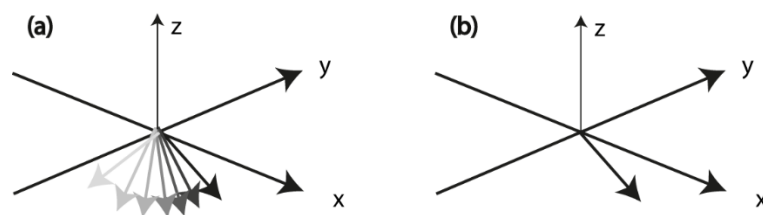
Figure 2.3: (a) The "laboratory frame" where M_0 is precessing at ω_0 but the x-y plane is stationary. (b) The "rotating frame" where the x-y plane precesses at ω_0 along with M_0 and hence M_0 appears stationary.

NMR Signal

Each nucleus in the transverse plane precesses and has an associated magnetic moment. This rotating magnetic moment produces an oscillating electric field.[3] This electric field passes through the rf coil which is around the sample, and produces an oscillating electric current in the wire.[3] This oscillating electric current is detected over a period of time and is known as the NMR signal. As spins in the transverse plane endeavour to return to thermal equilibrium, i.e. M_0 in the z axis, this detectable NMR signal will slowly decay over time. The decay of the detected signal in the transverse plane is known as the free-induction decay (FID), Figure 2.4. The detectable FID is known as the time-domain signal (signal is measured as a function of time), which is Fourier transformed to produce frequency-domain signal. This frequency-domain signal is the most common representation of the NMR signal and is denoted the NMR spectrum.
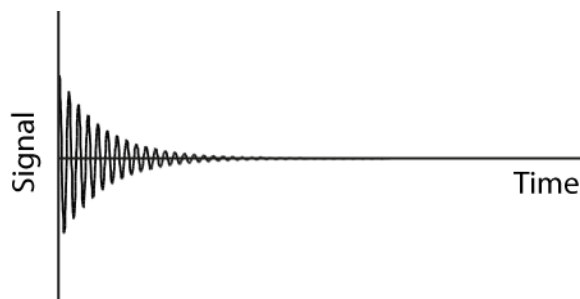
Figure 2.4: A schematic of the free-induction decay.

Chemical Shift

NMR active nuclei in a molecule will not all precess at the same rate, due to the non-homogeneous distribution of electrons within a molecule. The external magnetic field, B_0, causes the electrons to move and hence the electrons induce a local magnetic field.[3] Therefore, the protons in a molecule will experience a slightly different magnetic field, depending on their positions within the molecule and proximity to electrons.[2,3] As a result, the spins will precess at different frequencies which affects the position at which their signal appears in a NMR spectrum,[1] Equation 2.4. Therefore, each signal that appears in a NMR spectrum represents each proton environment in a molecule.

$$\delta = \frac{(v - v_{\text{ref}})}{v_{\text{ref}}} \times 10^6$$
                                                Equation 2.4

where δ is the chemical shift, v is the Larmor frequency of the nucleus of interest, and v_{ref} is the resonance frequency of a reference nucleus. The chemical shift is related to the local environment of the proton within a molecule and hence it is a vital factor in structure elucidation.

Spin Coupling

The appearance of a NMR signal in a spectrum is not solely dominated by the chemical shift, it is also affected by spin-spin coupling. These spin-spin couplings can give valuable information on the local environment of the spin and can therefore aid structure elucidation. Two possible mechanisms in which the magnetic fields of nuclei can interact are dipolar coupling and J-coupling (also known as scalar coupling).

J-coupling

J-coupling is an indirect method of magnetic field interaction of two nuclear spins through electrons in a covalent bond connecting the two nuclei.[1] A nuclear spin, H_A, has a magnetic interaction with electrons in a covalent bond which polarises the magnetic field of the electrons. If another nuclear spin, H_B, is in close proximity, it experiences the distortion of the electrons in the covalent bond and splits the H_A resonance in two,[1] which is known as a doublet. The splitting pattern is not restricted to doublets, a peak can be split by multiple neighbouring nuclei resulting in a multiplet peak. The splitting pattern depends on the number of coupling nuclei and hence aids the determination of the molecular structure.

J-coupling is exploited in the 2D correlation spectroscopy (COSY) experiment which enables the determination of J-coupling network within a molecule, and hence can determine the chemical shift of spins that interact through covalent or hydrogen bonds.[1] In this 2D COSY experiment magnetisation is transferred between spins by means of J-coupling.[1] A typical COSY spectrum can be found in Figure 2.5, where the two axes represent chemical shift at two different time points of the experiment, ω_1 and ω_2. Peaks that appear off-diagonal are a result of J-coupling between two spins which reside at different chemical shifts. On-diagonal peaks have the same chemical shift $\omega_1 = \omega_2$ and hence no J-coupling occurs.
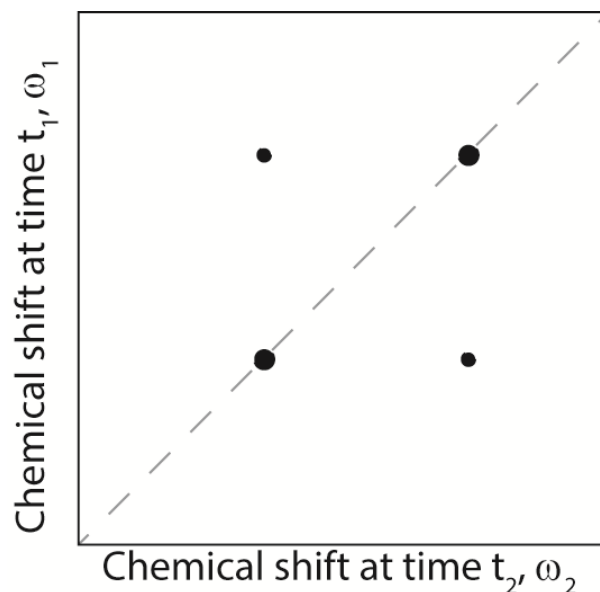
Figure 2.5: A schematic of a typical 2D COSY spectrum showing on-diagonal and off-diagonal peaks.

Dipolar Coupling

Dipolar coupling is a mechanism whereby spins couple through space[1] as a result of interaction of their magnetic fields.[3] The strength of the dipolar coupling is distance dependent; stronger dipolar coupling occurs when two spins are in close proximity.[1] In solutions, which are studied throughout this thesis, dipolar coupling interactions are averaged to zero; therefore, no peak splitting is observed.[1] This type of coupling can be either intra- or inter-molecular. Dipolar couplings can be exploited to determine molecular structure of complex molecules through the use of nuclear Overhauser spectroscopy (NOESY). NOESY is similar to COSY, but magnetisation is transferred by means of dipolar coupling.[1] A NOESY spectrum is very similar to a COSY spectrum, Figure 2.5, where the two axes represent chemical shift before, δ_1, and after, δ_2, the mixing time, τ_m, and consists of both on-diagonal and off-diagonal peaks. Off-diagonal peaks in a NOESY spectrum occur as a result of dipolar coupling between two spins at different chemical shifts, and hence are used to determine spins that are close in space.[4] It is also worth noting the NOESY sequence can also measure chemical exchange[1] that occurs between spins with separate chemical shifts. When using the NOESY sequence

to measure chemical exchange it is known as exchange spectroscopy (EXSY). As a consequence, this sequence can result in off-diagonal peaks that occur as a result of both dipolar coupling and chemical exchange. As a result, it can be difficult to differentiate between off-diagonal peaks that develop from dipolar coupling or chemical exchange.[3] However, for small molecules, peaks responsible for dipolar coupling are negative and chemical exchange peaks are positive.[3]

2.2 Relaxation

A NMR spectrum can give a wealth of information about the environment of a nuclear spin from the splitting pattern and the position of peaks in a spectrum. Another factor which is characteristic of spins and their environment is relaxation. Relaxation does not affect the NMR spectrum as dramatically, but is still an important property that can tell us more about molecular motion and the spin environment. At thermal equilibrium, the spin states are populated according to the Boltzmann distribution where there is a population excess of spins occupying the α state. This thermal equilibrium is disrupted by the application of a 90° rf pulse which results in an equal population of spins in the α and β states. The process of the spins' returning to thermal equilibrium after disruption is known as relaxation. The two different types of relaxation are spin-lattice or longitudinal relaxation, T_1, and spin-spin or transverse relaxation, T_2.

Spin-Lattice Relaxation, T_1

T_1 relaxation time is the time taken for the spins to return to the Boltzman distribution of spins in the α and β states (i.e. equilibrium population of the α and β states). To re-establish the Boltzman distribution, spins are required to transition between the α and β states which are induced by spin motion resulting in local magnetic field fluctuations.[1,2] Spins can only transition between the

α and β states if these fluctuating local magnetic fields match the Larmor frequency.[1,2] Spin transitions can also occur as a result of dipolar coupling and hence contribute to T_1 relaxation.[1] The spin flip process emits energy which causes an increase in the local spin vibrations and hence temperature.[1] The total bulk temperature does not change as the local temperature change is so small.[1]
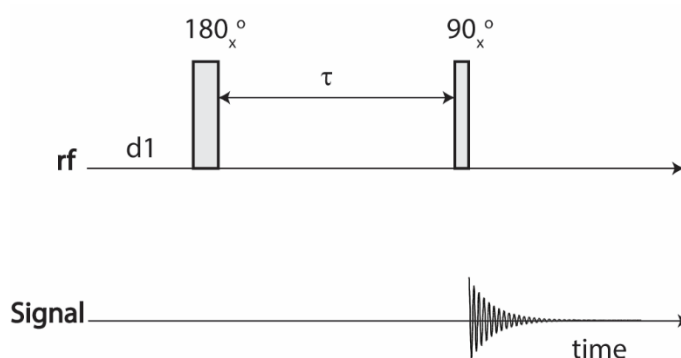
Figure 2.6: An inversion recovery pulse sequence used to measure T_1 relaxation.

Spin-lattice relaxation (T_1) is measured using an inversion recovery pulse sequence,[5] Figure 2.6. Initially, a time period equal to approximately 5T_1, labelled d1 in Figure 2.6, is required to ensure the system is at equilibrium, with the Boltzmann distribution of spins where there is an excess of spins populating the α state. A 180° pulse is applied which inverts the spin populations to give a population excess of spins in the β state to place $\boldsymbol{M}_0$ along the –z axis. During time, τ, spin-lattice relaxation takes place, where the spins start to return to their equilibrium state through spin transitions between the α and β states (or $\boldsymbol{M}_0$ returning to its original position on the +z axis). Finally, a 90° pulse enables these spins to be observable by NMR by positioning $\boldsymbol{M}_0$ in the transverse plane, where the FID is then collected. This process is repeated for a range of τ values,[4] which has an effect on the resultant signal intensity. The signal intensity of a peak of interest is monitored as a function of τ, and fitted to Equation 2.5 to obtain the T_1 relaxation time.

$$\frac{S(\tau)}{S(0)} = 1 - 2e^{-\frac{\tau}{T_1}}$$

Equation 2.5

where $S(\tau)$ is the signal at time τ and $S(0)$ is the signal at $\tau = 0$. The plot of signal intensity, $S(\tau)$, against τ, Figure 2.7, starts with negative intensity, passes through zero and becomes positive as τ increases, which is characteristic of signal acquired using the inversion recovery pulse sequence to measure T_1 relaxation. The negative signal at small τ values is a result of a small amount of relaxation occurring during τ, which results in $\boldsymbol{M_0}$ remaining on the $-z$ axis and hence a negative signal. However, as τ is increased, more relaxation takes place and $\boldsymbol{M_0}$ gradually becomes positive (on the $+z$ axis) until it returns to the equilibrium position.
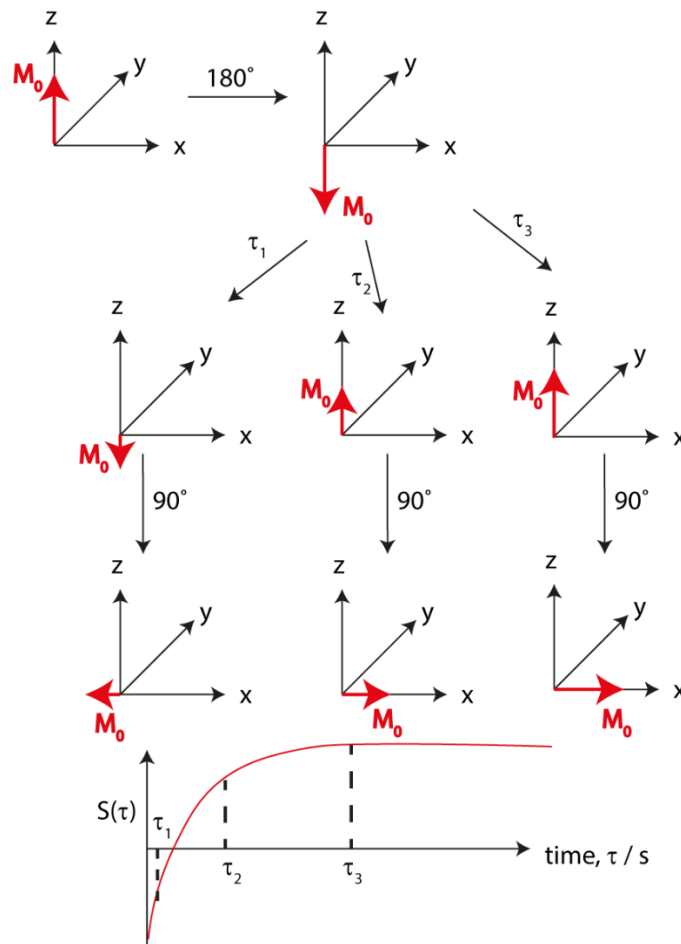
Figure 2.7: A representation of how the bulk magnetisation vector, $\boldsymbol{M_0}$ is affected throughout the course of the inversion recovery pulse sequence. The observed NMR signal, $S(\tau)$, as a function of time, τ, is plotted at the bottom of this figure.

Spin-Spin (T_2) Relaxation

T_2 relaxation is a measure of how long it takes the spins to de-phase within the transverse plane.[2] After a 90° pulse, the populations of spins in the α and β states are equal and the spins have phase coherence. This phase coherence is maintained as long as all the spins experience the same magnetic field. In reality, this is not the case; each spin experiences a slightly different magnetic field and so will precess at different frequencies.[2] If the spins precess at different frequencies, the phase coherence will be lost and the spins begin to fan out or de-phase. The differences in magnetic field can be due to their chemical environment (T_2): neighbouring nuclei induce local magnetic fields via inter- or intra-molecular interactions and random molecular motions, or the inhomogeneity in the $\boldsymbol{B}_0$ field, $T_2(\Delta\boldsymbol{B}_0)$, which is usually minimised via shimming.[1,2] The effect of $\boldsymbol{B}_0$ inhomogeneity $T_2(\Delta\boldsymbol{B}_0)$ is of no chemical interest but is an inherent feature of NMR.[1] Both T_2 and $T_2(\Delta\boldsymbol{B}_0)$ combine to give an effective T_2 parameter denoted T_2^*, Equation 2.6.

$$\frac{1}{T_2^*} = \frac{1}{T_2} + \frac{1}{T_2(\Delta\boldsymbol{B}_0)} \qquad \text{Equation 2.6}$$

The linewidth of a peak, $\nu_{1/2}$, in a NMR spectrum is determined by T_2^*, Equation 2.7. A smaller T_2^* will give a broader peak due to the inverse relationship.

$$\upsilon_{1/2} = \frac{1}{\pi T_2^*} \qquad \text{Equation 2.7}$$

T_2 can be measured using a spin echo pulse sequence,[2] Figure 2.8. The spin echo refocuses any spins that are de-phased as a result of $\boldsymbol{B}_0$ inhomogeneity, $T_2(\Delta\boldsymbol{B}_0)$, hence removing this contribution allowing the measurement of the absolute T_2 value.
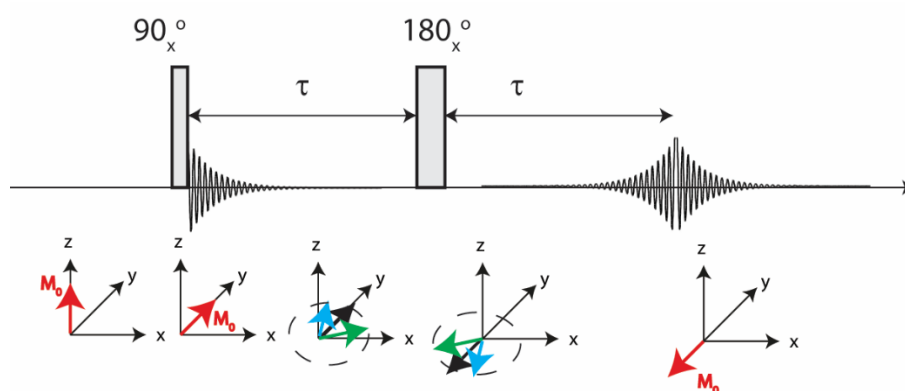
Figure 2.8: The spin echo pulse sequence with a vector model to show the evolution of the magnetisation.

Following the first 90° pulse of the spin echo pulse sequence, the spins begin to de-phase for a time period, τ, due to the range of magnetic field strengths they experience, which consequently slowly reduces $\boldsymbol{M}_0$ in the transverse plane. After τ, a 180° pulse is applied which flips the magnetisation and the spins are then allowed to precess for a further τ period. The precession of spins during this second τ period enables the spins to be totally refocused by the end of the time period. The refocusing of spins in this way is known as the spin echo.[6] The spins de-phased as a result of $\boldsymbol{B}_0$ inhomogeneity, $T_2(\Delta\boldsymbol{B}_0)$, will be completely refocused at this point;[2] however, spins de-phased as a result of random molecular motion leading to spin-spin relaxation, T_2, will not be completely refocused and hence a signal attenuation is observed. The T_2 relaxation time can be determined by repeating the spin echo experiment for a number of different τ values. As τ increases, the spins experience a greater amount of relaxation and hence the resultant signal is reduced. However, refocusing of magnetisation by the spin echo is not only affected by T_2 relaxation, it is also dependent on spins experiencing the same magnetic field throughout the sequence.[2] Therefore, if spins diffuse during τ to an environment of differing field, the spins will not be refocused. With increasing τ, the effect of diffusion becomes more severe and hence less reliable for T_2 relaxation time measurements. An alternative approach is the Carr-Purcell-Meiboom-Gill[7] (CPMG) experiment,

Figure 2.9, where the spin echo sequence [$\tau - 180° - \tau$] is repeated with a short τ to refocus any J-modulation and to form multiple echoes.[2] The decay of these echoes is dependent on T_2; therefore, by performing a series of experiments with increasing the value of n, the T_2 relaxation time can be determined by fitting the signal decay, $S(2\tau)$, to Equation 2.8, where $S(0)$ is the signal at t = 0. A typical signal decay for a CPMG experiment is shown in Figure 2.10.

$$\frac{S(2\tau)}{S(0)} = e^{-\left(\frac{2\tau}{T_2}\right)}$$

Equation 2.8
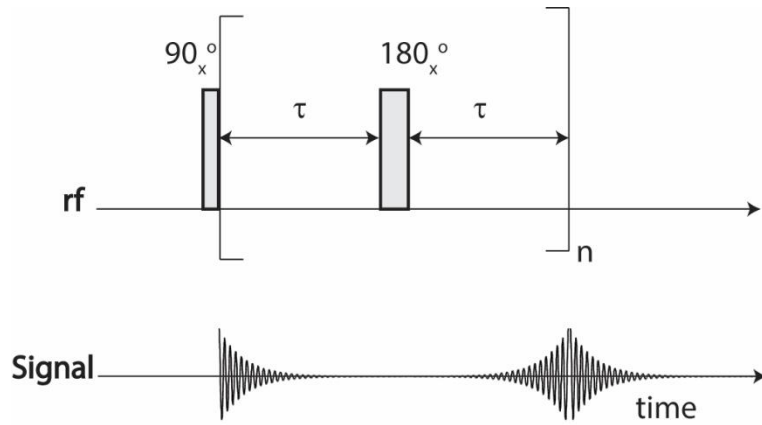
Figure 2.9: The Carr-Purcell-Meiboom-Gill (CPMG) pulse sequence used to measure T_2 relaxation.
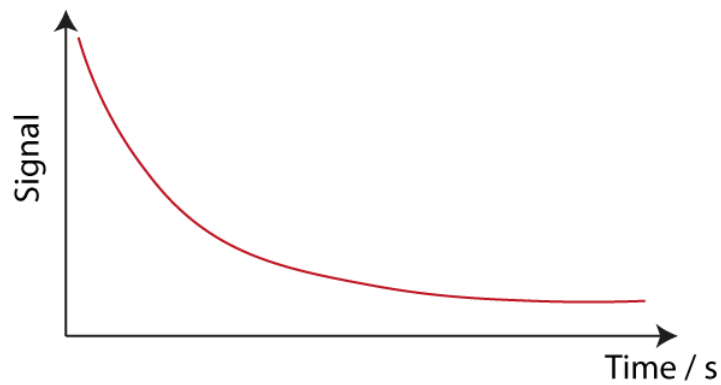
Figure 2.10: A schematic of a typical signal decay as a function of time from a CPMG experiment as a result of T_2 relaxation.

Relaxation and Rotational Correlation Time

T_1 and T_2 relaxation times are dependent on temperature and viscosity of the sample as these factors affect vibrational, rotational and translational motion of spins. The rotational correlation time, τ_c, is used as a measure of rotational diffusion of a molecule and is defined as the time a molecule takes to rotate by one radian.[1] Small molecules, higher temperature and less viscous solvents result in short τ_c values, whereas large molecules, lower temperature and viscous solvents give long τ_c values. The dependence of T_1 and T_2 relaxation with the rotational correlation time, τ_c, is plotted in Figure 2.11. As molecular tumbling increases (short τ_c), T_2 relaxation increases; therefore shorter T_2 relaxation times are obtained at higher temperatures and in less viscous solutions. The trend for T_1 relaxation is different, at short τ_c values longer T_1 relaxation times are observed, due to faster magnetic field fluctuations when compared with the Larmor frequency. Long T_1 relaxation times are also seen for long τ_c values because of slower magnetic field fluctuations compared with the Larmor frequency. The shortest T_1 relaxation time is given when the magnetic fluctuations match the Larmor frequency.[1]
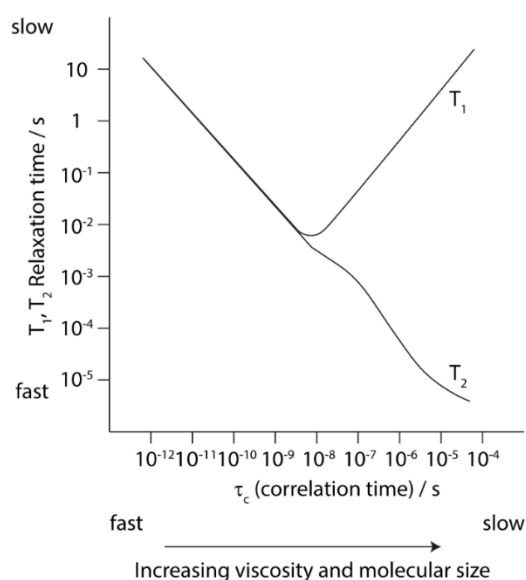
Figure 2.11: The dependence of T_1 and T_2 relaxation with the rotational correlation time, τ_c, with the regions of fast and slow relaxation and tumbling labelled.

Cross Relaxation and Nuclear Overhauser Effect (NOE)

Nuclear Overhauser effect (NOE) is a phenomenon based on cross relaxation, and involves the relaxation behaviour of two inequivalent spins that are interacting via dipolar coupling.[1,4] Two inequivalent spins I and S that are dipolar coupled have multiple spin-lattice (T_1) relaxation pathways, and four different energy levels, $\alpha_I \alpha_S$ where I and S spins populate the α state, $\alpha_I \beta_S$ where I spins populate the α state and S spins populate the β state, $\beta_I \alpha_S$ where I spins occupy the β state and S spins occupy the α state and $\beta_I \beta_S$ where I and S spins occupy the β state. The $\alpha_I \alpha_S$ and $\beta_I \beta_S$ levels have energy $-\omega_0$ and $+\omega_0$, respectively[1] and the $\alpha_I \beta_S$ and $\beta_I \alpha_S$ are midway between with zero energy, Figure 2.12. There are a total of six relaxation pathways available to I and S which involve either a single spin flip or a double spin flip. There are four different single spin flip pathways which are labelled W_1 in Figure 2.12, these are nothing more than spin-lattice relaxation, T_1, pathways.[1] Alternatively, there are double spin flip pathways, W_0 and W_2, which are known as cross relaxation pathways.[1] These cross-relaxation processes will result in transfer of magnetisation from one spin to the another dipolar coupled spin, leading to the nuclear Overhauser effect (NOE).[4,8]
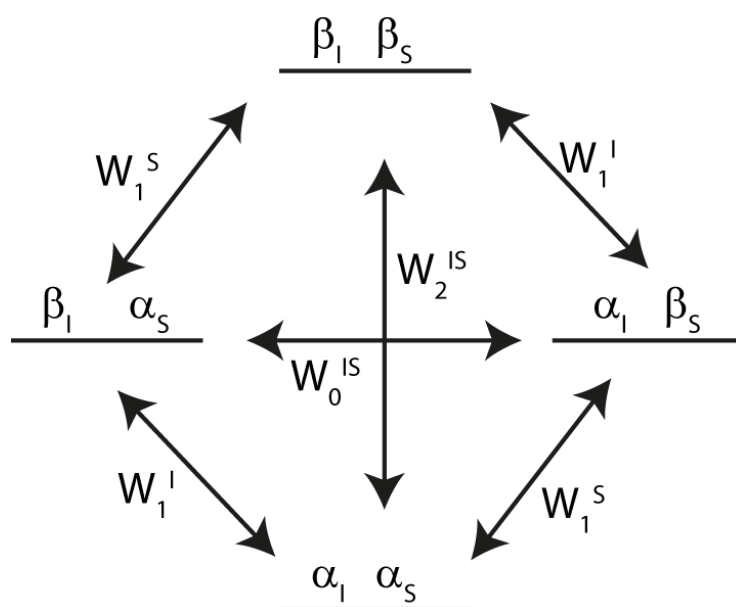
Figure 2.12: Energy levels for two inequivalent spins I and S showing the six dipolar relaxation pathways.

The nuclear Overhauser effect (NOE) arises when an rf field is applied to a spin e.g. S, to saturate it. This has the effect of making the population of α_S and β_S states equal without affecting the population difference of α_I and β_I which remain the same, Figure 2.13b. After this saturation, the S spins will endeavour to return to their equilibrium state via the six relaxation pathways. If the system takes the W_2^{IS} route where spins in the $\beta_I \beta_S$ state are converted to the $\alpha_I \alpha_S$ state, the population difference between α_I and β_I states is increased, Figure 2.13c, due to cross-relaxation transferring magnetisation from the S to I spins. This has the effect of increasing the intensity of the I resonance in the NMR spectrum. The rate of cross relaxation decreases rapidly as the distance between the two coupling spins increases, the spins are usually ≤ 5 Å apart when this phenomenon occurs.[4] This makes the nuclear Overhauser effect an extremely important tool as it can be exploited to aid structural determination of larger and complex molecules by determining spins that are close in proximity in space, through 2D NOESY.
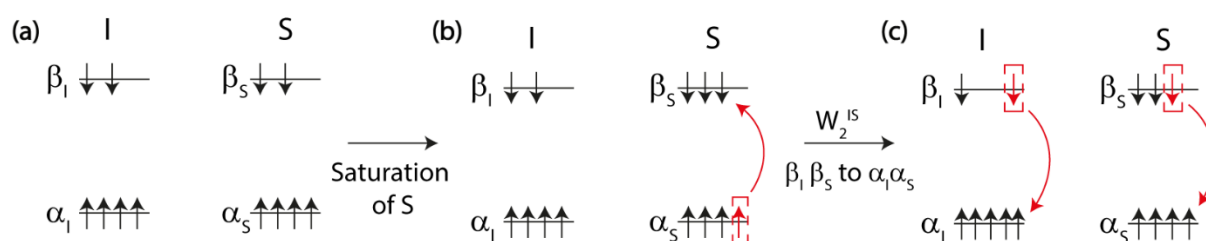
Figure 2.13: The effect of cross relaxation pathway W_2^{IS} on the nuclear Overhauser effect (NOE) when spin S is saturated.

2.3 Diffusion

The random motion of molecules in a pure liquid at thermal equilibrium is known as self-diffusion and is given a self-diffusion coefficient,[9] D, which has units of m^2 s^{-1}. Diffusion NMR techniques measure self-diffusion[9] and rely on the application of pulsed magnetic field gradients to

encode the position of a molecule,[2] tracking the diffusion path to obtain the distance travelled in the direction of the pulsed magnetic field gradients as a function of time. The root mean square displacement, d, is related to the diffusion coefficient, D, via Equation 2.9, [2,10-12] where Δ is the total time the molecule is allowed to diffuse and is known as the observation time.

$$d = \sqrt{2D\Delta}$$
Equation 2.9

Diffusion measurements are often performed to gain information on a molecule or a molecular aggregate size by means of the diffusion coefficient, D, via the Stokes-Einstein relation,[13] Equation 1.7. The Stokes-Einstein relation in Equation 1.7 can only be used for spherical particles or aggregates. Variations of the Stokes-Einstein relation can be found in the literature[9,14] for a wide range of geometries such as cylinders and ellipsoids that are oblate and prolate (Equation 1.8 – 1.10). The Stokes-Einstein relation shows that the diffusion coefficient, D, is affected by size, viscosity and temperature. An increase in viscosity increases the frictional force, making the molecules move slower and therefore decreasing the diffusion coefficient. The same trend is observed with increasing size, R_h: a larger particle cannot move as quickly as a smaller particle due to increased chance of collisions, resulting in a smaller diffusion coefficient. Temperature has an opposite effect: an increase in temperature leads to greater translational kinetic energy and hence the speed of the particle increases, resulting in a larger diffusion coefficient.

The self-diffusion coefficient is determined through the use of pulsed magnetic field gradient (PFG) NMR. In these PFG sequences two magnetic field gradients are applied in short pulses[15] that have a well-defined separation to measure molecular motion.[16] Applying these magnetic field gradient pulses enables spins to be spatially encoded. The applied magnetic field varies linearly in the direction the magnetic field gradient is applied and, therefore, the spins will experience a slightly different magnetic field gradient depending on their positions within the sample, r, resulting in

differing precessional frequencies.[17] The precessional frequency of a spin as a function of position in the sample, $\boldsymbol{r}$, is given by Equation 2.10, where $\boldsymbol{G}$ is the magnetic field gradient strength.[17] The stronger magnetic field gradient strength felt by a spin will result in a greater precessional frequency. The application of a magnetic field gradient pulse allows the spins to be spatially encoded through the formation of a helix of phase of precessing spins, Figure 2.14, which is the basis of measuring diffusion via PFG sequences. The two main PFG sequences are pulsed gradient spin echo (PGSE) and pulsed gradient stimulated echo (PGSTE), which are explained below.

$$\omega(\boldsymbol{r}) = \gamma \boldsymbol{B}_0 + \gamma \boldsymbol{G}\boldsymbol{r}$$

Equation 2.10
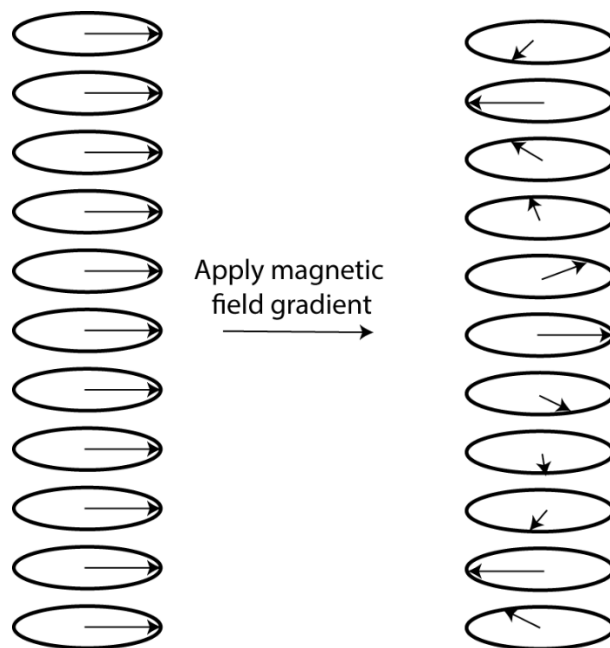
Figure 2.14: A schematic representation showing the helix of phase formed after the application of a magnetic field gradient which allows the spins to be spatially encoded for position.

Pulsed Gradient Spin Echo (PGSE)

The first PFG method was demonstrated by Stejskal and Tanner[18] and incorporates magnetic field gradient pulses into the spin echo, Figure 2.8, and is still widely used in its original form. This

sequence is known as the pulsed gradient spin echo (PGSE) and is demonstrated in Figure 2.15. As with the spin echo sequence, the 90° pulse places the magnetisation in the transverse plane. Immediately after this pulse all the spins have phase coherence and precess at the same rate. A magnetic field gradient pulse is applied between the 90° and 180° pulses of the spin echo, which produces a helix of phase, due to the spatial location of the spins resulting in the spins experiencing slightly different magnetic field gradient strengths, Equation 2.10. The 180° pulse inverts the magnetisation and has the effect of reversing the sign of the precession i.e., the sign of the phase angle, ϕ, or, the sign of the applied magnetic field gradients and static field.[19] Therefore, when the second magnetic field gradient pulse is applied, the helix of phase is unwound and refocuses the magnetisation. If there is no diffusion during the time, Δ, between the two magnetic field gradient pulses, all the spins feel the same magnetic field for both magnetic field gradient pulses and hence the magnetisation is totally refocussed (black vectors in Figure 2.15). If diffusion takes place during Δ, where molecular motion is incoherent and random,[20] the spins migrate from their original position and hence feel a different gradient strength for the second magnetic field gradient pulse. As a result, spins are not totally refocussed which leads to a distribution of phase shifts, ϕ, (red vectors in Figure 2.15). The phase shift, ϕ, is proportional to the amount of displacement due to diffusion during the observation time,[19] Δ. A loss of signal intensity is observed as a result of the phase shifts.

Diffusion coefficients can be obtained by repeating the experiment with varying observation time, Δ, magnetic field gradient pulse duration, δ, or magnetic field gradient strength, $\boldsymbol{G}$, to obtain a signal attenuation.[2] The most common method is to vary the magnetic field gradient strength $\boldsymbol{G}$ and keep the time periods, δ and Δ, constant. The experimental parameters, $\boldsymbol{G}$, Δ and δ are typically set so that the signal is attenuated to ≤ 1 % to enable accurate determination of the diffusion coefficients.[2] While this PGSE sequence is regularly utilised to measure diffusion, there are some disadvantages associated with this method. One of the main disadvantages is the sensitivity to T_2

relaxation. In this PGSE experiment, the magnetisation is stored in the transverse plane during the observation time, Δ. Spins stored in the transverse plane are subjected to T_2 relaxation processes and hence signal can be lost during Δ as a result of T_2 relaxation.[21,22] In systems where T_2 is longer than the observation time, Δ, this is not an issue. However, when $T_2 < \Delta$ too much signal is lost to relaxation during Δ, reducing the signal-to-noise ratio. Therefore, this pulse sequence is unsuitable for systems that contain components of interest with short T_2 relaxation times, which are typically larger, slower moving molecules.
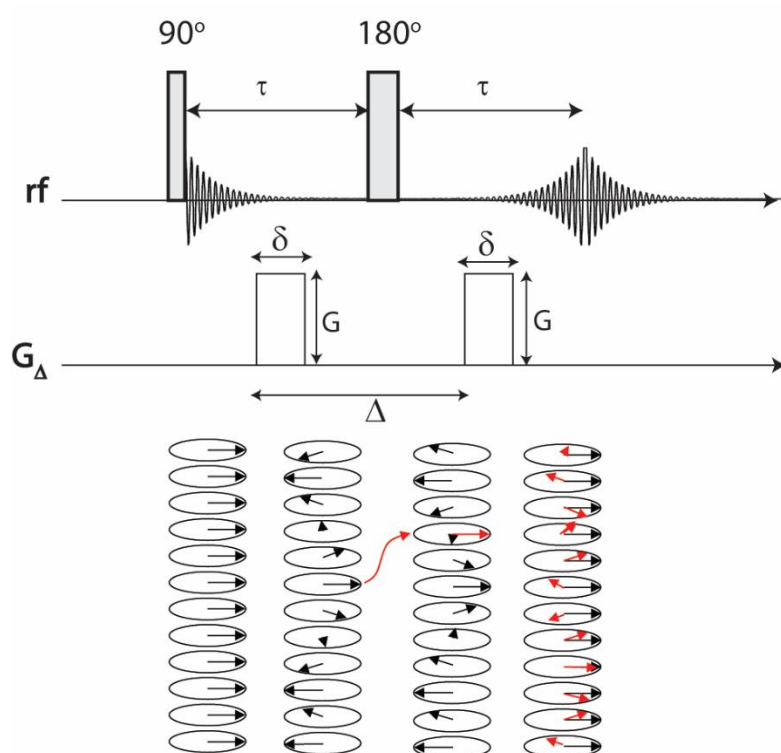
Figure 2.15: A pulsed gradient spin echo (PGSE) sequence used to measure the diffusion of molecules. The spatial encoding of the spins is shown below the sequence with the black representing the effect when diffusion is not present and the red representing the effects of diffusion.

Figure 2.16: The resultant phase shift, ϕ, of the magnetisation (red arrow) at the end of the PGSE experiment as a result of diffusion. The black arrow represents total refocusing of the magnetisation (no diffusion present).

In addition to the issue with T_2 relaxation, magnetisation in the transverse plane is also affected by J-coupling.[23] J-coupling during the PGSE or any spin echo experiment leads to peak phase distortions[23-26] because the evolution due to J-coupling is not refocussed by the 180° pulse,[4,27] leading to the presence of unwanted anti-phase magnetisation.[23] As a consequence, there are difficulties in analysing J-coupled resonances when a PGSE sequence is employed, which limits its application to probing only singlet resonances.

Pulsed Gradient Stimulated Echo (PGSTE)

An alternative PFG sequence uses a stimulated echo and is known as a pulsed gradient stimulated echo[22] (PGSTE) experiment. In this experiment, the spins are less susceptible to T_2 relaxation and J-coupling which was the case for the PGSE sequence. The stimulated echo sequence consist of three 90° pulses, where two 90° pulses replace the 180° pulse of the spin echo,[27] Figure 2.17. The first 90_x°, places $\boldsymbol{M}_0$ along the y axis where it is allowed to precess for time, τ, when a second 90_x° pulse is applied to place $\boldsymbol{M}_0$ in the longitudinal plane (z axis). After a time period, τ_2, a third 90_x° pulse places $\boldsymbol{M}_0$ back in the y axis where it precessess for a time, τ, before being acquired. After the second 90_x°, $\boldsymbol{M}_0$ lies in the longitudinal plane and hence is sensitive to T_1 relaxation during the τ_2 period.[27]

Although this sequence is sensitive to T_1 relaxation during τ_2, it is sensitive to T_2 relaxation and J-coupling during τ. This results in T_2 relaxation occurring during the time period, τ, after the first 90_x° pulse, resulting in the spins precessing at different frequencies and de-phasing in the transverse plane. As a result, a small proportion of the magnetisation along the y axis will develop on the x axis. Any magnetisation developed along the x axis during τ is unaffected by the second 90_x° pulse, so this magnetisation remains in the x axis.[27] The magnetisation along the x axis is unwanted and is removed by applying a spoiler or crusher gradient during the τ_2 period.[9] The amount of magnetisation along

the *x* axis depends on the length of τ and the T_2 relaxation time. Any magnetisation in the *x* axis is lost and hence reduces the signal-to-noise ratio.

It is important to note that the stimulated echo generates two additional spin echoes.[27] The first is the echo of the first 90° pulse generated by the second 90° pulse. The second additional echo is the echo of the second 90° pulse generated by the third 90° pulse. However, Hahn[6] has shown that as many as five spin echoes can be produced during this sequence. In addition to these spin echoes, a stimulated echo occurs at an interval after the third 90° rf pulse equal to that between the first two 90° pulses,[22] τ. This stimulated echo is the signal acquired at the end of the sequence, therefore it is imperative that the time period between the first two 90° pulse and the period between the last 90° pulse and acquisition is identical in order to acquire the whole signal. Interference between the additional spin echoes and the stimulated echo must be avoided and is achieved through phase cycling.
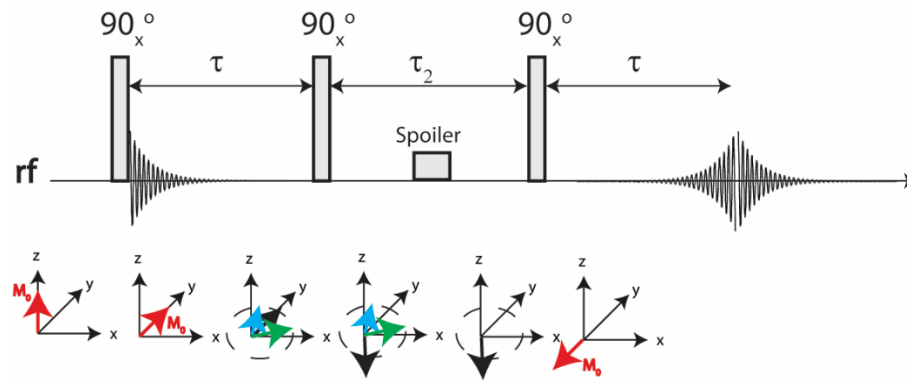
Figure 2.17: The stimulated echo pulse sequence with a vector model to show the evolution of the magnetisation.

In the PGSTE sequence the magnetic field gradient pulses are inserted between the first two 90° pulses and just before the last 90° pulse, Figure 2.18, so $\boldsymbol{M}_0$ is in the longitudinal plane during the observation time, $\varDelta$, where T_1 relaxation is prevalent. This is advantageous as T_1 relaxation times are

longer than T_2 relaxation times, and hence longer Δ can be employed, making the PGSTE sequence particularly important for systems with short T_2 relaxation times.[22] Since this sequence is usually utilised for probing systems with short T_2 relaxation times, the time period, τ, needs to be minimised[28] to avoid the effects of J-coupling[2] and signal loss due to T_2 relaxation.[21,22] The two magnetic field gradients are separated by two 90° pulses which act in the same way as the 180° pulse in the spin echo and reverse the sign of the applied magnetic field gradients and static field.[19] Therefore the two magnetic field gradients have the same effect on the magnetisation as described for the spin echo, Figure 2.15 and allow the measurement of diffusion.
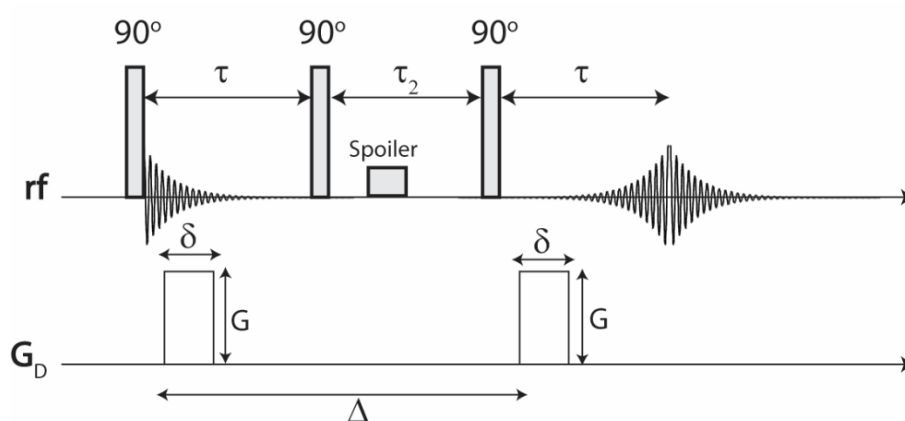
Figure 2.18: Pulsed gradient stimulated echo (PGSTE) pulse sequence used to measure diffusion of molecules.

Determination of Diffusion Coefficient

As mentioned previously, the most common method of determining the diffusion coefficient using PFG experiments is to repeat the experiments with incremented magnetic field gradient strength, **G**. If **G** is incremented, both the PGSE and PGSTE sequences produce a signal attenuation, which is related to the diffusion coefficient. Separate signal attenuations can be obtained for each resonance in an NMR spectrum by integrating the area under the peaks, to produce individual diffusion coefficients. Plotting the signal attenuation as a function of increasing magnetic field

gradient strength produces a signal attenuation curve, Figure 2.19. This signal attenuation curve is

fitted to the Stejskal-Tanner relationship,[18] Equation 2.11, to obtain the average diffusion coefficient

using the experimental parameters, δ, Δ and G, and the gyromagnetic ratio, γ, (γ = 26.75 × 10^7 rad s^{-1}

T^{-1} for ^1H protons). Alternatively, the diffusion coefficient can be determined by plotting $\ln[S(G)/S(0)]$

against G^2, where $S(G)$ is the signal at G and $S(0)$ is the signal at G = 0 T m^{-1}. This plot yields a straight

line, Figure 2.19b, where the slope is proportional to $-D$.

$$\frac{S_{(G)}}{S_{(0)}} = e^{-\left(\gamma^2\delta^2 G^2 D\left(\Delta-\frac{\delta}{3}\right)\right)}$$
Equation 2.11
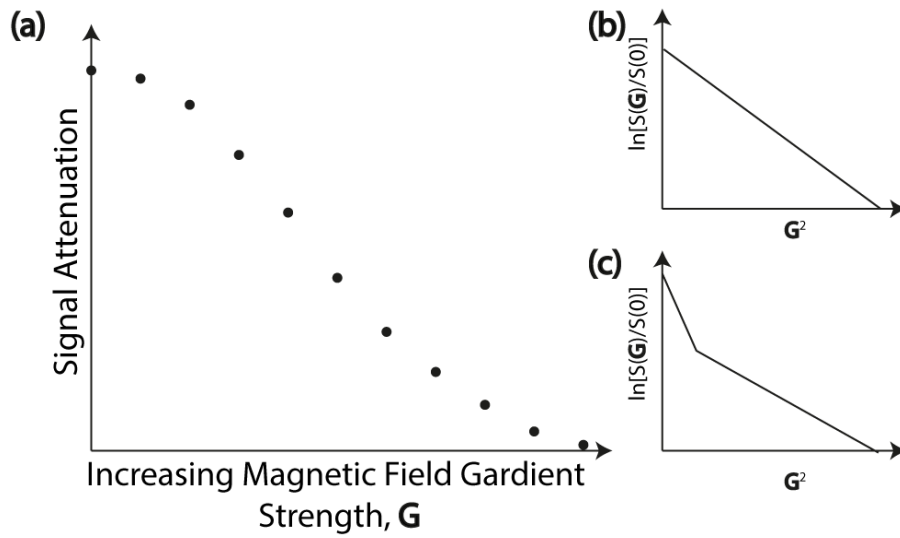
Figure 2.19: A schematic of (a) the signal attenuation due to diffusion as a function of increasing magnetic field gradient strength, G, (b) the $\ln[S(G)/S(0)]$ vs G^2 plot where a single diffusion coefficient is obtained and (c) the $\ln[S(G)/S(0)]$ vs G^2 plot where two diffusion coefficients are obtained.

When a molecule of interest is present in multiple environments, which have significantly

different diffusion coefficients, the signal attenuation will not fit perfectly to the mono-exponential

Stjeskal-Tanner relationship, Equation 2.11. In these cases, a modification of the Stejskal-Tanner

relationship is required to ensure a good fit to the signal attenuation is obtained. A bi-exponential

modification of the Stejskal-Tanner relationship is provided in Equation 2.12, where two average

diffusion coefficients can be obtained.[29] When two diffusion coefficients can be determined from the signal attenuation, the ln[$S(\boldsymbol{G})/S$(0)] vs $\boldsymbol{G}^2$ plot deviates from the single line observed in Figure 2.19b, to a superposition of two lines of different gradients representing each diffusion coefficient, Figure 2.19c.

$$\frac{S(\boldsymbol{G})}{S(0)} = x\left(e^{-\left(\gamma^2\boldsymbol{G}^2\delta^2 D\left(\Delta-\frac{\delta}{3}\right)\right)}\right) + (1-x)e^{-\left(\gamma^2\boldsymbol{G}^2\delta^2 D\left(\Delta-\frac{\delta}{3}\right)\right)} \qquad \text{Equation 2.12}$$

Factors Impacting Diffusion Measurements

There are a number of factors that can have an impact on diffusion measurements in PFG sequences. In this section we explore the effect of eddy currents, gradient mis-match, convection and cross relaxation on diffusion measurements. These are by no means all of the factors that can affect diffusion measurement; a full exhaustive list of factors affecting diffusion measurements can be found in a number of books.[9,21] The factors listed above have a negative impact on diffusion measurements as they can result in additional signal attenuation and hence overestimate the diffusion coefficient and mis-interpretation of the experimental data.[9]

Eddy Currents

The rapid rise and fall of magnetic field gradient pulses can generate currents in surrounding conducting surfaces, known as eddy currents.[9] These currents have an associated magnetic field which can distort the magnetic field gradient pulse profiles and last for a period after the magnetic field gradient pulses are switched off.[21] These eddy currents cause a number of issues for PFG measurements,[9] including phase changes in the observed spectrum and additional changes in the attenuation. The intensity of eddy currents becomes more severe with increased magnetic field gradient strength and if the rise and fall time of the magnetic field gradients are short.[9] It is essential

not to manipulate further magnetisation or acquire in the presence of eddy currents,[9] and hence a delay after the magnetic field gradient pulse is applied, t_e (or the gradient stabilisation time), to allow for dissipation of the eddy currents. PGSTE sequences have been modified to include this t_e delay, prior to acquisition and it is known as the longitudinal eddy current delay (LED) sequence, Figure 2.20a.

A common method for determining the presence of eddy currents is to perform a simple diffusion measurement on a high molecular weight polymer, usually polydimethylsiloxane (PDMS). PDMS has a very slow diffusion coefficient (10^{-15} m^2 s^{-1}) and as a result no or very little attenuation due to diffusion is expected with the magnetic field gradient strengths available[30,31] ($0 - 110$ T m^{-1}). Any observed attenuation is a consequence of eddy current effects.[9] To avoid the generation of eddy currents, a number of methods can be employed. The simplest is to alter the magnetic field gradient pulse so the rise and fall time is longer[21] or to use shaped magnetic field gradient pulses to replace the common rectangular pulses.[9,30] Alternatively, the pulse sequences can be modified to counteract the eddy current effects by using bipolar gradients, known as the bipolar pulse pair stimulated echo (BPP-STE) sequence.[9] In this pulse sequence, each magnetic field gradient pulse is replaced by two magnetic field gradient pulses of opposing sign and half the duration ($\delta/2$), separated by a 180° pulse, Figure 2.20b.[2,32] The 180° pulse inverts the magnetisation and reverses the sign of the second magnetic field gradient in the bipolar pulse pair, and consequently is equivalent to the magnetic field gradient in the conventional PGSTE experiment.[9] The opposite sign of these bipolar pulse pair magnetic field gradients is the key aspect in eliminating eddy current effects. The eddy currents arising from the first bipolar pulse pair magnetic field gradient will be cancelled out by the effects of the second magnetic field gradient of the bipolar pulse pair, due to the opposite polarity.[9] This pulse sequence is robust and effective in removing eddy current effects, and hence is employed in measurements throughout this thesis. The bipolar pulse pairs can also be incorporated into the LED sequence, which is known as the BPP-LED,[33] Figure 2.20c.
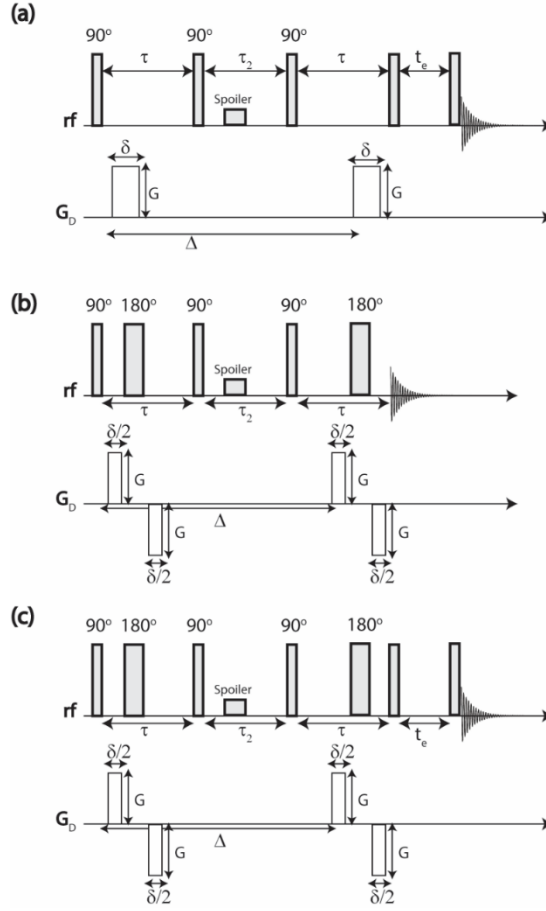
Figure 2.20: Pulse sequences that can be employed to measure diffusion and eliminate the effects of eddy currents where (a) is the longitudinal eddy current delay (LED) sequence, (b) is the bipolar pulse pair stimulated echo (BPP-STE) and (c) is the bipolar pulse pair with longitudinal eddy current delay (BPP-LED). In this figure G is the magnetic field gradient strength, δ is the duration of the magnetic field gradient, Δ is the time the spins are allowed to diffuse, τ and τ_2 are evolution time periods, t_e is a delay inserted to allow the eddy currents to decay.

Gradient Mis-match

In PFG experiments, the magnetic field gradient pulse must be stable and perfectly reproducible to obtain accurate diffusion measurements.[9,30,34,35] If the two magnetic field gradient pulses do not match, i.e. do not have equal magnetic field gradient strength, **G**, and duration, δ, the helix of phase produced by the first magnetic field gradient pulse cannot be completely refocussed by the second magnetic field gradient pulse, which will result in position dependent local phase shifts and cause significant loss of the echo signal intensity.[30,36] As a result, the signal attenuation decays

faster and hence the diffusion coefficient appears larger.[30] The cause of gradient mis-match is usually the gradient amplifier: some gradient amplifiers cannot produce reproducible noise-free magnetic field gradient pulses in quick succession.[30] Gradient mis-match issues are amplified when either stronger magnetic field gradients or longer magnetic field gradient durations are employed.[30] Price et al.[30] have reported how gradient mis-match can be reduced by using shaped magnetic field gradient pulses, e.g. half sine, so the rise and fall time is decreased enabling the amplifier to produce reproducible magnetic field gradient pulses.

Convection

Convective flow is introduced into a sample due to temperature gradients causing the upward flow of warmer, less dense fluid.[2] Increased severity of these temperature gradients produces more extreme convection within the sample, which is commonly introduced during variable temperature measurements. Convection currents provide an additional force on nuclei, resulting in larger displacements than self-diffusion. As a result, convection will lead to an enhancement in the signal attenuation, Figure 2.21b, and hence lead to larger diffusion coefficients and in extreme cases, the signal attenuation goes negative for a period before increasing to zero,[2] Figure 2.21c.

The likelihood for convection to occur is characterised by the Rayleigh number (R),[2,9] Equation 2.13, where $\mathbf{g}$ is the acceleration due to gravity, α is the thermal expansion, κ is the thermal diffusivity of the liquid, υ is the kinematic viscosity, r is the radius of the sample NMR tube and ΔT is the temperature gradient. Therefore, the likelihood of convection is governed by r and ΔT, and hence the use of narrower NMR tubes can reduce the effects of convection.[9,37]

$$R = \frac{\mathbf{g}\alpha}{\kappa\upsilon}r^4\Delta T \qquad\qquad \text{Equation 2.13}$$

Convection can also be reduced by spinning the sample, which produces an extra force in the sample which has a stabilising effect and reduces the convective flow.[2,9,38] Alternatively, the diffusion measurements can be performed using a convection compensated sequence such as the double stimulated echo[2] (DSTE).
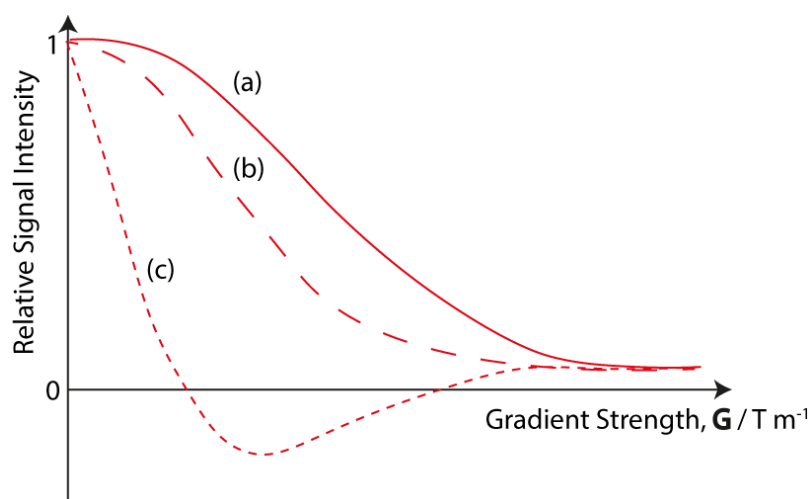
Figure 2.21: A schematic of the diffusion signal attenuation when (a) no convection is present, (b) moderate convection is present resulting in a faster decay and (c) extreme convection is present resulting in negative signal intensity.

Cross Relaxation

The nuclear Overhauser effect (NOE) results in modulation of the echo signal in a stimulated echo experiment.[39] In stimulated echo experiments, the magnetisation is stored on the longitudinal axis (z axis) to avoid J-coupling and T_2 relaxation effects during the observation time, $\varDelta$. However, magnetisation held in this axis can be subjected to chemical exchange[40] and cross-relaxation effects,[40,41] which is particularly prevalent in systems where there are large, slow moving molecule and small, fast moving molecules[39,40,42] e.g. a large macromolecule in water. Any sequence where the magnetisation is held in the longitudinal axis for a significant period is at risk of cross relaxation effects, therefore care must also be taken when using LED sequences where the eddy current delay,

t_e, is particularly long.[33] As discussed previously, cross relaxation affects the signal intensities through the NOE, and hence considerably complicates diffusion measurements.[9] Cross relaxation during diffusion experiments can lead to the presence of multi-exponential signal attenuation, or a mono-exponential signal attenuation where the decay rate increases (a larger diffusion coefficient) as Δ is increased.[40] Both these factors can lead to mis-interpretation of the diffusion experiment, particularly when the signal attenuation becomes multi-exponential where it could lead to erroneous interpretation of chemical exchange. It has been reported[40] that cross relaxation can be minimized by analysing resonances with limited or no NOE and, more importantly employ short observation times ($\Delta \leq 20$ ms).

2.4 Inverse Laplace Transform (ILT)

The inverse Laplace transform[43,44] (ILT) can be used in the analysis of NMR relaxation and diffusion data[29] to obtain distributions of relaxation times or diffusion coefficients. The inverse Laplace transform is given in Equation 2.14 where $S(t)$ is the time related data (the signal attenuation), and Rt is the probability distribution of $S(t)$. This equation can be written specifically for diffusion data[20,45] (Equation 2.15) and T_2 relaxation data[45] (Equation 2.16), where $G(D_j)$ is the distribution of diffusion coefficients, $G\left(T_{2j}\right)$ is the distribution of T_2 relaxation times and ε_j is the noise.

$$f(t) = \mathcal{L}^{-1}\{S(t)\} = \frac{1}{2\pi i}\int_{\gamma-i\infty}^{\gamma+i\infty} S(t)e^{(Rt)dt}$$

Equation 2.14

$$S(t_i) = g_i = \sum G(D_j)e^{\left(-\left(\gamma^2 G^2 \delta^2 D_i \left(\Delta - \frac{\delta}{3}\right)\right)\right)} + \varepsilon_j$$

Equation 2.15

Equation 2.16

$$S(t_i) = g_i = \sum G(T_{2j})e^{\left(-\left(\frac{2\tau}{T_{2j}}\right)\right)+\varepsilon_j}$$

The ILT is a mathematically ill-posed problem[21] in the sense that a small amount of noise in the data can cause large changes in the resultant spectrum.[43] The ill-posed nature of the ILT arises from the multiplication of $G(D_j)$ or $G\left(T_{2j}\right)$ by an increasing exponential function,[20,21] which consequently causes noise to be included as measurements.[20] This problem is avoided by the use of constraints in the form of a regularisation procedure.[21,44,46] The regularisation parameter, α, controls the product of $G(D_j)$ or $G\left(T_{2j}\right)$ and the increasing exponential function, by providing restrictions to avoid fitting the noise.[20] The regularization parameter, α, measures the smoothness of the resultant distribution function, and its value must be optimised to avoid bias.[44] If α is too large, fitting to noise becomes an issue. When α is too small, over-smoothing is an issue[20] and the inversion reduces to a conventional least-squares fitting. As a consequence, the resultant distribution function likely exhibits sharp features that are unstable[44,47] and are not reproducible. Therefore, due to the extreme restriction of the data the precision of the resultant distribution function is compromised.[20] The optimum value of α was chosen in accordance to Fordham,[46] which involves measuring χ^2 for a range of α values, where χ is the fit error as a function of α.[29,44,46] The optimum value of α corresponds to the lowest value of α before χ^2 rises rapidly. In this regularisation procedure it is assumed the data are non-negative, and the distribution function is smooth, where the noise has random fluctuations in intensity around zero, and is added to the signal of interest (relaxation or diffusion decay).[44] When the ILT procedure is applied to T_2 relaxation data, a plot of $G(T_2)T_2$ vs $\log_{10}(T_2)$, where $G(T_2)$ is the distribution function with respect to T_2. The maximum point at the top of this distribution function provides the average T_2 relaxation time, T_2^{avg}. A similar plot is produced for

diffusion data but with respect to the diffusion coefficient, so a plot of $\mathbf{G}(D)D$ vs $\log_{10}(D)$, where $\mathbf{G}(D)$ is the distribution function with respect to D.

While the discussion so far has focussed on the 1D ILT, focus is now turned to the 2D ILT which can be utilised in the analysis of 2D NMR data sets. [21,27,48] The 2D ILT is commonly used in 2D relaxation and diffusion experiments, which are used to correlate molecular dynamic interactions[48] and can also be utilised to quantify exchange. [49,50] In these 2D relaxation and diffusion experiments, the 2D ILT can be used to convert the 2D relaxation or diffusion signal attenuation matrix, into a 2D distribution of either relaxation times or diffusion coefficients. As mentioned previously, the 1D ILT is a notoriously ill-posed problem, [43] and hence the 2D ILT must be approached with caution. [48] Initially, the 2D ILT required large amounts of computer power to perform, and due to the size of the 2D matrices, a great deal of memory was required to store it, compared with storing the 1D data-sets, [21] and hence its use was impractical and was avoided. However, in 2002, a more robust algorithm was developed that enabled the 2D ILT to be performed on a basic desktop computer, [44,51-53] leading to more widespread use of the 2D ILT. This robust algorithm compresses the 2D matrix to a more manageable size, [44,48] and rearranges the matrix into a 1D format by consecutive ordering of the matrix rows or columns. [48] This in effect transforms the problem back into a 1D format, [48] and hence the same regularisation procedure was applied with the same assumptions: the data are non-negative and the distribution function is smooth, where the noise has random fluctuations in intensity around zero and is added to any intended signal (e.g. relaxation or diffusion signal attenuation). This type of noise is described as being additive and Gaussian with zero-mean. The development of this robust 2D ILT has enabled the development of a wide range of 2D NMR experiments, which previously would not have been possible.

2.5 References

(1)   Hore, P. J. *Nuclear Magnetic Resonance*; Oxford University Press, 1995; Vol. 32.

(2)   Claridge, T. D. W. *High-Resolution NMR Techniques in Organic Chemistry*; 2nd Edition ed.;
Elsevier, 2009; Vol. 27.

(3)   Levitt, M. H. *Spin Dynamics: Basics of Nuclear Magnetic Resonance*; Second Edition ed.; John
Wiley & Sons Ltd, 2008.

(4)   Keeler, J. *Understanding NMR Spectroscopy*; Second Edition ed.; John Wiley & Sons, Ltd,
2010.

(5)   Vold, R. L.; Waugh, J. S.; Klein, M. P.; Phelps, D. E. *J. Chem. Phys.* **1968**, *48*, 3831.

(6)   Hahn, E. L. *Phys. Rev.* **1950**, *80*, 580.

(7)   Meiboom, S.; Gill, D. *Rev. Sci. Instrum.* **1958**, *29*, 688.

(8)   Croasmun, W. R.; Carlson, R. M. K. *Two-Dimensional NMR Spectroscopy: Applications for
Chemists and Biochemists*; VCH Publishers, Inc., 1987; Vol. 9.

(9)   Price, W. S. *NMR Stidies of Translational Motion: Principles and Applications*; Cambridge
University Press, 2009.

(10)   Lahrech, H.; Zoula, S.; Farion, R.; Remy, C.; Decorps, M. *Magn. Reson. Med.* **2001**, *45*, 409.

(11)   Nikolic, D.; Nesic, L. In *7th International Conference of the Balkan Physical Union Vols 1 and 2*;
Angelopoulos, A., Fildisis, T., Eds.; Amer Inst Physics: Melville, 2009; Vol. 1203, p 1292.

(12)   Perez, Y.; Lahrech, H.; Cabanas, M. E.; Barnadas, R.; Sabes, M.; Remy, C.; Arus, C. *Cancer Res.*
2002, *62*, 5672.

(13)   Edward, J. T. *J. Chem. Educ.* **1970**, *47*, 261.

(14)   Willis, S. A.; Dennis, G. R.; Zheng, G.; Price, W. S. *J. Mol. Liq.* **2010**, *156*, 45.

(15)   Johnson, C. S. *Prog. Nucl. Magn. Reson. Spectrosc.* **1999**, *34*, 203.

(16)   Nicolay, K.; Braun, K. P. J.; de Graaf, R. A.; Dijkhuizen, R. M.; Kruiskamp, M. J. *NMR Biomed.*
2001, *14*, 94.

(17)   Vallatos, A. PhD, University of Birmingham, 2014.

(18)   Stejskal, E. O.; Tanner, J. E. *J. Chem. Phys.* **1965**, *42*, 288.

(19)   Price, W. S. *Concepts Magn. Reson.* **1997**, *9*, 299.

(20)   Law, S. J. PhD, University of Birmingham, 2015.

(21)   Callaghan, P. T. *Translational Dynamics & Magnetic Resonance: Principles of Pulsed Gradient Spin Echo NMR*; Oxford University Press, 2011.

(22)   Tanner, J. E. *J. Chem. Phys.* **1970**, *52*, 2523.

(23)   Torres, A. M.; Zheng, G.; Price, W. S. *Magn. Reson. Chem.* **2010**, *48*, 129.

(24)   Momot, K. I.; Kuchel, P. W. *Concepts Magn. Reson. Part A* **2006**, *28A*, 249.

(25)   Momot, K. I.; Kuchel, P. W.; Chapman, B. E. *J. Magn. Reson.* **2005**, *176*, 151.

(26)   Stilbs, P. *Prog. Nucl. Magn. Reson. Spectrosc.* **1987**, *19*, 1.

(27)   Callaghan, P. T. *Principles of Nuclear Magnetic Resonance Microscopy*; Clarendon Press, 1993.

(28)   Zick, K.; GmbH, B. B., Ed. 2009.

(29)   Law, S. J.; Britton, M. M. *Langmuir* **2012**, *28*, 11699.

(30)   Price, W. S.; Hayamizu, K.; Ide, H.; Arata, Y. *J. Magn. Reson.* **1999**, *139*, 205.

(31)   Price, W. S. *NMR Studies of Translational Motion: Principles and Applications*; Cambridge University Press, 2009.

(32)   Wider, G.; Dotsch, V.; Wuthrich, K. *J. Magn. Reson. Ser. A* **1994**, *108*, 255.

(33)   Avram, L.; Cohen, Y. *J. Am. Chem. Soc.* **2005**, *127*, 5714.

(34)   Hrovat, M. I.; Wade, C. G. *J. Magn. Reson.* **1981**, *45*, 67.

(35)   Hrovat, M. I.; Wade, C. G. *J. Magn. Reson.* **1981**, *44*, 62.

(36)   Callaghan, P. T. *J. Magn. Reson.* **1990**, *88*, 493.

(37)   Hayamizu, K.; Price, W. S. *J. Magn. Reson.* **2004**, *167*, 328.

(38)   Lounila, J.; Oikarinen, K.; Ingman, P.; Jokisaari, J. *J. Magn. Reson. Ser. A* **1996**, *118*, 50.

(39)   Dvinskikh, S. V.; Furo, I. *J. Magn. Reson.* **2000**, *146*, 283.

(40)   Chen, A.; Shapiro, M. *J. Am. Chem. Soc.* **1999**, *121*, 5338.

(41)   Yan, J. L.; Kline, A. D.; Mo, H. P.; Zartler, E. R.; Shapiro, M. J. *J. Am. Chem. Soc.* **2002**, *124*, 9984.

(42)   Peschier, L. J. C.; Bouwstra, J. A.; deBleyser, J.; Junginger, H. E.; Leyte, J. C. *J. Magn. Reson. Ser. B* **1996**, *110*, 150.

(43)   Song, Y. Q.; Venkataramanan, L.; Burcaw, L. *J. Chem. Phys.* **2005**, *122*, 8.

(44)   Song, Y. Q.; Venkataramanan, L.; Hurlimann, M. D.; Flaum, M.; Frulla, P.; Straley, C. *J. Magn. Reson.* **2002**, *154*, 261.

(45)   Borgia, G. C.; Brown, R. J. S.; Fantazzini, P. *J. Magn. Reson.* **1998**, *132*, 65.

(46)   Fordham, E. J.; Sezginer, A.; Hall, L. D. *J. Magn. Reson. Ser. A* **1995**, *113*, 139.

(47)   Casanova, F.; Perlo, J.; Blümich, B. *Single-Sided Nmr*; Springer Berlin Heidelberg, 2011.

(48)   Callaghan, P. T.; Godefroy, S.; Ryland, B. N. *Magn. Reson. Imaging* **2003**, *21*, 243.

(49)   Callaghan, P. T.; Furo, I. *J. Chem. Phys.* **2004**, *120*, 4032.

(50)   Washburn, K. E.; Callaghan, P. T. *Phys. Rev. Lett.* **2006**, *97*, 4.

(51)   Monteilhet, L.; Korb, J. P.; Mitchell, J.; McDonald, P. J. *Phys. Rev. E* **2006**, *74*, 9.

(52)   Rodts, S.; Bytchenkoff, D. *J. Magn. Reson.* **2010**, *205*, 315.

(53)   Vallurupalli, P.; Hansen, D. F.; Lundstrom, P.; Kay, L. E. *J. Biomol. NMR* **2009**, *45*, 45.

3. NMR and Molecular Dynamics Study of the Size, Shape, and Composition of Reverse Micelles in a Cetyltrimethylammonium Bromide (CTAB)/Hexane/Pentanol/Water Microemulsion

3.1 Introduction

The ability of RMs to form uniformly stable nano-sized droplets that can encapsulate hydrophilic entities in hydrophobic environments has led to their use in a wide range of applications such as templates in the synthesis of nanoparticles,[1-4] drug delivery and biomolecule carriers,[5-7] and reactors for chemical and enzymatic reactions.[8-10] Therefore, there is great interest in understanding the RM microstructure as well as their shape and size. These properties have been probed using a range of techniques such as dynamic light scattering,[11] fluorescence spectroscopy,[12,13] conductivity,[14] molecular modelling[15-18] and nuclear magnetic resonance.[19-22] `

While these techniques have been utilised to characterise a range of RM systems, the most common and widely studied RMs are those formed with sodium bis(2-ethylhexyl) sulfosuccinate (AOT). AOT RMs are relatively simple as they do not require the presence of a co-surfactant to form RMs.[23] Other surfactants, like cetyltrimethylammonium bromide (CTAB), cannot form RMs without the help of a co-surfactant,[1,4,24,25] and hence this complicates their characterisation using these techniques. As a consequence, CTAB RMs are considerably less studied than their AOT counterparts.

The difficulty in characterising CTAB RMs, and other co-surfactant containing RM systems, is due to the presence and distribution of the co-surfactant, resulting in RMs of added complexity. Understanding the role of the co-surfactant in RM formation and how the co-surfactant partitions between the reverse micelle and continuous phase, will aid characterisation of these RMs. Previous reports[21] have suggested the co-surfactant resides in both the RM interface and the continuous

phase. Knowledge of the distribution of co-surfactant molecules is vital, particularly when determining the size of RMs using the Stokes-Einstein equation, Equation 1.7, as the viscosity of the continuous phase is required. The presence of co-surfactant molecules in the continuous phase will affect its viscosity[21] and will consequently result in inaccurate droplet sizes. If the amount of co-surfactant in the continuous phase is known, a corrected viscosity can be determined to enable a more accurate droplet size determination.

While the presence of co-surfactant molecules complicates the characterisation of CTAB RMs, there are some advantages associated with the presence of a co-surfactant. The addition of a co-surfactant to reverse micelle systems has been reported to affect the fluidity of the interface,[26] the response of probe molecules in the RM interface,[12] the structure and solubilisation of enzymes in RMs[27,28] and the shape and size of nanoparticles synthesised within RM core.[2,29] Therefore, the presence of a co-surfactant in quaternary microemulsions (four different components in the RM) not only aids the stability of nanoparticles[2] but also provides a useful additional parameter, P_0, which determines the amount of co-surfactant present. This parameter, P_0, can easily be changed to regulate the amount of alcohol and as a result the size, shape, and interface rigidity of the RM can be controlled,[1] giving significant advantages in the many applications of RM systems.

There is significant interest in understanding the microstructure, size and shape of RM systems containing co-surfactants, particularly those consisting of CTAB.[4,25,27] CTAB RMs are often combined with pentanol as the co-surfactant, because of its stronger van der Waal interactions with CTAB[29] than other alcohol co-surfactants. This was demonstrated by Chen et al.[29] when synthesising Au nanoparticles in the CTAB/pentanol/hexane/water reverse microemulsion. Chen et al.[29] reported the nanocrystals to be monodisperse and spherical, whereas those synthesised by Lin et al.[30] in the CTAB/n-butanol/octane/water RM were found to grow into nanocrystals of different shapes with a broad polydispersity, suggesting the CTAB and pentanol combination is superior for nanoparticle

synthesis. The CTAB/pentanol/hexane/water RM has also been utilised by Curri et al.[2] in the synthesis of CdS nanoclusters, which was found to be more desirable than the AOT/iso-octane/water RM due to the presence of a co-surfactant. Combining pentanol with CTAB was also found to be superior in solubilising enzymes in the water core of CTAB RMs.[28] The structure of the enzyme in the CTAB/pentanol/iso-octane/water RM was closer to its native structure than when CTAB/hexanol/iso-octane/water RM was employed. The combination of hexanol and CTAB resulted in an unfavourable structural change of the lipase.

The CTAB/pentanol/hexane/water RM system was also studied by Palazzo et al.[21] using diffusion NMR measurements, to determine the RM size and pentanol distribution. Through their diffusion measurements, they obtained a single averaged diffusion coefficient for pentanol, D_{obs}, and therefore it was suggested the pentanol exchanges between the RM interface and the continuous phase. Using D_{obs} and the Lindman equation[31,32] (Equation 1.15), they showed the proportion of pentanol in the RM interface, P_{mic}, can be determined. This required *a priori* knowledge of the diffusion of pentanol in the continuous phase, D_{bulk}, and using the diffusion of CTAB which was used as a measure of the RM diffusion,[20,21] D_{mic}. With the knowledge of the pentanol distribution, the viscosity of the continuous phase was established and hence the average droplet radius of the RMs was determined. The droplet radii were explored as a function of (i) water content, ω_0, at a fixed interface composition and (ii) interface composition by increasing the pentanol concentration at fixed ω_0. It was found that with an increase in water content, the radii increased, but an increase of pentanol in the interface reduced the droplet size. They stated that the droplets remained spherical throughout all compositional changes.

Palazzo et al.[21] reported these CTAB/pentanol/hexane/water RMs to be spherical but the true shape of these CTAB RMs remains unknown. A study by Fang et al.[3] has shown that the shape of CTAB RMs deviates from spherical, particularly with higher water content. In contrast, it has been

reported that CTAB will form spherical RMs at compositions close to the critical micelle concentration[4] due to its moderate tail length. The shape of RMs has been determined using molecular modelling,[15-18,33-37] with the main focus on those containing AOT as a surfactant.[15-18,34,35] Very little molecular modelling has been performed on CTAB RMs, although Rodriguez et al.[33] have studied a benzylhexadecyldimethylammonium chloride (BHDC) RM, which has the same headgroup as CTAB, and found the shape deviated from spherical to ellipsoidal. Recently, a molecular simulation of the CTAB/chloroform/water RM system has been reported and indicates the droplet exhibits a prolate shape, particularly as the water pool size increases.[36] Although the molecular modelling of RMs seem to suggest an ellipsoidal structure,[15-18,33,36] none of these have been on studies of RMs that contain an alcohol co-surfactant. Therefore, the true shape of CTAB RMs remains ambiguous, particularly those consisting of CTAB and pentanol. Knowledge of the shape of RMs is particularly important when determining the size of droplets via the Stokes-Einstein equation, Equation 1.7, which is only valid for spherical structures.[38] To gain accurate droplet sizes of ellipsoidal structures the use of modified Stokes-Einstein equations (Equations 1.8 – 1.10) are necessary.[39,40]

In this chapter the CTAB/pentanol/hexane/water reverse microemulsion is investigated using diffusion NMR and molecular modelling to determine the shape, size and co-surfactant distribution, and how these properties change as a function of temperature. This investigation shows the first combination of molecular modelling and NMR data of CTAB reverse micelles to accurately determine their size and shape. Combining these two analytical techniques has also enabled the distribution of the co-surfactant to be probed in more detail.

3.2 Experimental

Sample Preparation

The reagents cetyltrimethylammonium bromide (CTAB, Sigma-Aldrich, 98 %), pentanol (Sigma-Aldrich, 99 %), hexane (Fisher-Scientific, reagent grade) and water (purified with a MilliQ™ system, resistivity 18 MΩ cm, TOC ≤ 5 ppb) were used to prepare the CTAB/pentanol/hexane/water microemulsion in these investigations. Microemulsions were prepared by dissolving 0.2 g CTAB in 8.394 ml hexane, 0.487 ml pentanol and 0.068 ml pure water and shaking for approximately 2 minutes. This produces a microemulsion consisting of reverse micelles with a water/CTAB molar ratio, ω_0, of 6.9, a pentanol/CTAB ratio, P_0, of 8.2, a total CTAB concentration, [CTAB], of 0.06 M and a volume fraction, ϕ_d, of 0.05 (Appendix 1). NMR measurements were taken approximately 1 hour after sample preparation.

NMR Measurements

NMR experiments were performed on a Bruker DMX300 spectrometer equipped with a 7 T superconducting magnet, operating at a proton resonance frequency of 300.13 MHz. Samples were placed in a 5 mm NMR tube, inside a 5 mm ^{1}H resonator of a Bruker Diff30 probe. The variable temperature control unit was calibrated using a methanol standard,[41] by measuring the difference in chemical shift of the OH and CH$_3$ resonances at regular temperature intervals. Magnetic field gradient strengths were calibrated by measuring the diffusivity of a n-octane sample at 289 K and compared with literature values.[42] The ^{1}H NMR spectrum of the CTAB/pentanol/n-hexane/water microemulsion is shown in Figure 3.1, with the structures, and proton numbering schemes, for CTAB and pentanol in Figure 3.2 and peak assignments listed in Table 3.1.
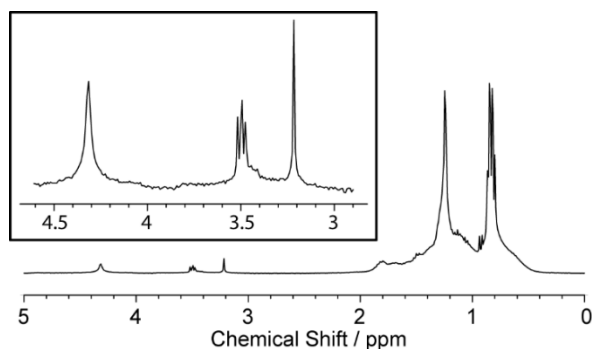
Figure 3.1: ^{1}H NMR spectra of CTAB/pentanol/hexane/water reverse microemulsion with inset showing an expanded region.

(a) $CH_3(CH_2)_{13}CH_2CH_2N(CH_3)_3Br$
      e   d   c   b   a

(b) $HOCH_2CH_2CH_2CH_2CH_3$
    f   g   h   j   k   l
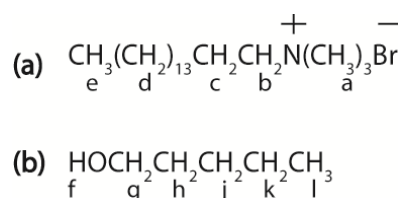
Figure 3.2: Molecular structure and numbering scheme for (a) CTAB surfactant and (b) pentanol co-surfactant.

Table 3.1: ^{1}H NMR peak assignments for CTAB/pentanol/hexane/water reverse microemulsion.

δ / ppm	Peak assignments
4.32	H_f and water
3.52	H_g
3.45	H_b
3.22	H_a
1.80	H_c
1.50	H_h
1.35-1.16	H_d, H_i, H_j, H_k
0.95-0.8	H_e, H_l

An inversion recovery experiment, $[180° - \tau - 90° - acq]_n$, was used to measure the T_1 relaxation times of CTAB (H_a) and pentanol (H_g) at 298 ± 0.3 K. A series of $n = 33$ experiments were performed with logarithmically spaced time delays, τ, ranging from 5×10^{-6} s to 15 s. Spin-spin (T_2)

relaxation times for CTAB (H_a) and pentanol (H_g) were measured using ^{1}H NMR Carr Purcell Meiboom Gill (CPMG) experiments, [90 - (τ - 180 - τ)$_m$ - acq]$_n$ at 298 ± 0.3 K. A repetition time of 15 s was used to collect four signal averages, n, with 16 echoes, m, varied from 0 to 1024 with a delay of τ = 2 ms.

Diffusion coefficients for the H_a resonance of CTAB and H_g of pentanol were measured using ^{1}H NMR pulsed gradient stimulated echo with bipolar pulse pairs (BPP–STE) experiments [41,43,44] at 289 ± 0.3 K and 298 ± 0.3 K. Measurements were performed at three observation times of 10 ms, 40 ms and 450 ms using 32 magnetic field gradient steps. Experimental parameters used for each experiment were δ = 3 ms, $\varDelta$ = 40 ms and $\boldsymbol{G}_{max}$ = 0.9 T m^{-1}; or δ = 2 ms, $\varDelta$ = 450 ms and $\boldsymbol{G}_{max}$ = 0.4 T m^{-1}; or δ = 3 ms, $\varDelta$ = 10 ms and $\boldsymbol{G}_{max}$ = 1.9 T m^{-1}. A repetition time (T_R) of 12 s is necessary to ensure $T_R \geq$ (5 x T_1) for all the spins, which required long experimental times. Therefore, to avoid these long experimental times and minimize any changes in the system over time, data were collected at a T_R of 6 s (3 to 5 x T_1). A comparison between the data collected at T_R of 6 s and 12 s was made, and no differences were observed so T_R = 6 s was used for all experimental data collected in this chapter. Previous studies have used pulsed gradient spin echo [21] (PGSE) and stimulated echo [45] (PGSTE) measurements, whereas these measurements are performed using a bipolar pulse pair stimulated echo (BPP–STE) sequence, to access stronger magnetic field gradients required for shorter observation times. To ensure there were no effects from the increased magnetic field gradient strengths used with short observation times, the gradient stabilization delay was checked using a high molecular-weight polydimethylsiloxane (PDMS) sample. [46] To eliminate the possibility of observations being a result of pulse sequence artefacts, a comparison was made between PGSE, PGSTE and BPP-STE experiments in Appendix 2. No artefacts were found and hence there is no pulse sequence artefact in this case. Average diffusion coefficients were determined using the Stejskal–Tanner equation (Equation 2.11). Where a mono-exponential fit was poor, a bi-exponential fit was performed (see Appendix 2); the data are always fitted to the minimum number of components necessary.

Viscosity and Density Measurements

Kinematic viscosity measurements of solutions of pentanol in *n*-hexane, over the concentration range of $0-1$ M, were performed at 289 K and 298 K using an Ubbelohde size 0 viscometer. Density measurements of the pentanol/*n*-hexane solutions were determined by weighing 10 ml of the sample, which had been kept at 289 ± 0.1 K or 298 ± 0.1 K. The dynamic viscosity (η) was calculated using the kinematic viscosity (υ) and density (ρ) data (Equation 3.1).

$$\upsilon = \frac{\eta}{\rho}$$
Equation 3.1

Molecular Modelling

Molecular mechanics and molecular dynamics (MD) calculations have been carried out using combined ff03[47] and gaff[48] force fields within AMBER v12.[49] Unless stated otherwise, all dynamic simulations were performed at 300 K and constant volume with periodic boundaries, and with a EWALD non-bonded cut off of 12 Å. Sampling of geometries, and velocities every 10 ps (5000 steps) during the data-gathering phase.

Droplet Construction for Calculations.

Initially, a water droplet was constructed by solvation of a single water molecule with the *solvateshell* command within AMBER LEaP, using a thickness of 50 Å. A layer of CTAB surfactant molecules was constructed around the water droplet with the CTAB headgroup close to the water and the hydrophobic chains pointing away. Once the CTAB layer was complete a second layer of pentanol was constructed around the droplet with the hydroxyl group pointing away and the tails pointing towards the centre of the droplet. Orientation and distributions of the CTAB and pentanol molecules were arranged randomly using a purpose built code.[50] CTAB and pentanol placement around the droplet was performed using the same method as previously reported.[51] Sufficient

bromide ions were added using the *addion* option in LEaP to ensure an overall neutral charge of the droplet. This process gave a ω_0 value similar to the experimental ω_0 value employed. A minimization was performed with no periodic box boundaries for a maximum of 100,000 cycles so the RMS gradients < 2 and have a $\boldsymbol{G}_{max}$ < 10^2. The minimization closes any gaps that may be present in the CTAB and pentanol layers constructed.

Solvent Box Preparation.

The required number of *n*-hexane molecules for a cubic box, 100 Å in each dimension, was determined from the density of *n*-hexane (4624 molecules for a density of 0.6617 g/mL). The *n*-hexane molecules were added to the box in an ordered periodic array with a spacing of approximately 6 Å to give the correct number of *n*-hexane molecules. The ordered box of *n*-hexane was subjected to minimization for a maximum of 100,000 cycles at constant volume. The minimized box was subjected to 1 ns of equilibration dynamics at constant volume, to randomise the positions of the *n*-hexane molecules. The result was saved as an off file using the *saveoff* command in AMBER, and the box boundaries offset at 100 Å.

Droplet Solvation.

The optimized droplet was solvated using the *n*-hexane box off file prepared using the *loadoff* and *solvatebox* commands in LEaP with at least 20 Å of *n*-hexane around the optimized droplet. The solvated droplet was minimized for a maximum of 20,000 cycles so the RMS gradients < 2 and have a $\boldsymbol{G}_{max}$ < 10^2 at constant volume. The optimized solvated droplet was then equilibrated using constant pressure of 1 atm, isotropic position scaling, compressibility of 44.6 x 10^{-6} bar^{-1} and a pressure relaxation time of 1 ps, until the box size remained constant. Once the box size was constant, the equilibration was carried out at constant volume with no pressure scaling. Molecular dynamic calculations were performed on the droplet for a total of 45 ns, which includes the time for equilibration, 200 ps.

3.3 Results

The dynamic viscosity and pentanol diffusion coefficients of various concentrations of pentanol in hexane at 289 K and 298 K are presented in Figure 3.3 and Figure 3.4, respectively. The data from these two plots are utilised in the determination of the proportion of pentanol in the interface, P_{mic}, and the hydrodynamic radius, R_h, of the droplets.
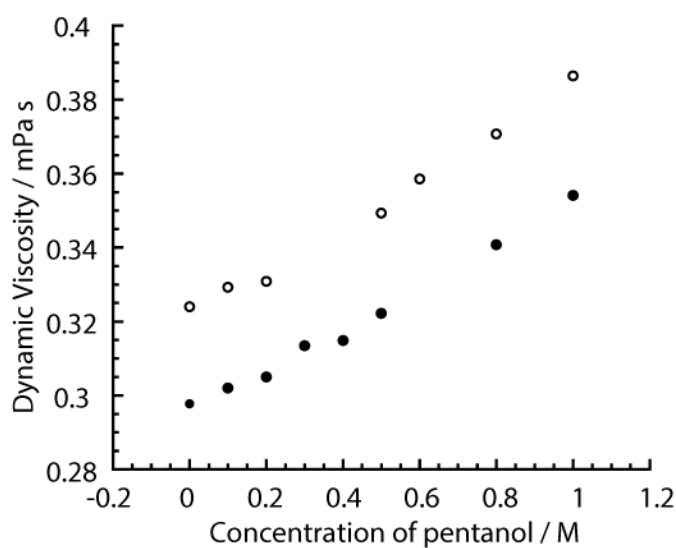
Figure 3.3: Dynamic viscosity of different concentrations of pentanol in hexane at 289 K (open circles) and 298 K (filled circles)
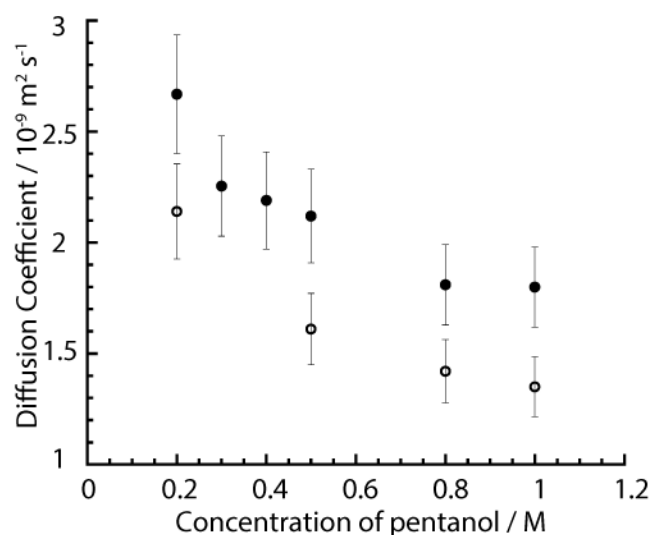
Figure 3.4: Plot of the diffusion coefficient of pentanol in *n*-hexane at various concentrations at 289 K (open circles) and 298 K (filled circles).

Diffusion measurements were performed on the CTAB/pentanol/hexane/water reverse microemulsion using a BPP-STE sequence, to determine the diffusion coefficients of CTAB and pentanol. A PGSTE sequence was employed because it has a number of advantages over PGSE sequences, which are sensitive to J-coupling[52] and T_2 relaxation.[43,53] Peaks with J-coupling cannot be measured using PGSE sequences due to significant peak distortions, and hence only singlet peaks can be selected. This is an issue in this system as the triplet alcohol peak, H_g, cannot be acquired, only the alcohol hydroxyl, H_f, is a singlet. The hydroxyl is in exchange with the water core[54] and hence can affect the resultant diffusion coefficient. There are no issues with the CTAB analysis using H_a as this is a singlet. PGSE sequences are sensitive to T_2 relaxation and hence the observation time, Δ, can only be varied up to or on the order of T_2. This is an issue in this system due to very short T_2 relaxation times of components in the RM, as a result of reduced motional freedom.[55] PGSTE sequences are sensitive to T_1 relaxation during Δ, which is significantly longer than T_2 in the systems of interest here, allowing much longer observation times to be reached. However, stimulated echo sequences can be sensitive to the effects of cross-relaxation[56] when $\Delta > 20$ ms. Cross-relaxation is not an issue in these experiments due to the very short ($\Delta = 10$ ms) observation time employed.

The diffusion coefficients, D, at $\Delta = 10$ ms, $\Delta = 40$ ms and $\Delta = 450$ ms for CTAB and pentanol at 298 K are listed in Table 3.2. At short observation times, ($\Delta \leq 40$ ms) CTAB exhibits two diffusion coefficients, representing CTAB in the RM interface and the continuous phase. The smaller diffusion coefficient is associated with CTAB in the RM interface due to the restricted motion of CTAB in this environment. When the observation time is longer, ($\Delta = 450$ ms) a single average diffusion coefficient is obtained indicating the CTAB is exchanging between the RM interface and the continuous phase.

Two diffusion coefficients are also obtained for the pentanol at short observation times ($\Delta \leq$ 40 ms), suggesting the pentanol is also distributed between the RM interface and continuous phase. The smaller diffusion coefficient for pentanol at $\Delta = 10$ ms, is similar to the corresponding smaller

diffusion coefficient of CTAB, which is associated with the RM diffusion. Since these two values are similar, it can be assumed that the slower moving pentanol component, $D_{\mathrm{CS}}^{\mathrm{mic}}$, is associated with the RM interface and the faster pentanol component, D_{bulk}, is associated with the continuous phase. Pentanol exchanges between these two environments because of the presence of a single averaged diffusion coefficient at long observation times ($\Delta = 450$ ms). The proportion of pentanol in the RM interface was determined using the Lindman equation (Equation 1.15) and the procedure outlined by Palazzo et al.[21] The average pentanol diffusion coefficient at long observation time ($\Delta = 450$ ms) was used as D_{obs}, and the smaller CTAB diffusion coefficient at $\Delta = 10$ ms was approximated as the RM diffusion coefficient, D_{mic}. The diffusion coefficient for pentanol in the continuous phase, D_{bulk}, was determined from a range of solutions containing pentanol in hexane, Figure 3.4, where initially all the pentanol was assumed to be in the continuous phase. Using this D_{bulk} value, a proportion of pentanol in the interface, P_{mic}, was determined and hence a new continuous phase composition, D_{bulk}, was obtained. Using this corrected D_{bulk}, a corrected P_{mic} value was determined, and then the process was repeated until the values for P_{mic} converged to give a P_{mic} value of 0.4. From this P_{mic} value, a continuous phase viscosity of 0.311 mPa s was determined using the dynamic viscosity data at 298 K in Figure 3.3.

Table 3.2: The diffusion coefficients at $\Delta = 10$ ms, 40 ms and 450 ms for CTAB and pentanol in the CTAB/pentanol/hexane/water reverse microemulsion at 298 K.

	CTAB	Pentanol
D at $\Delta = 10$ ms / 10^{-9} m² s⁻¹	0.22 ± 0.02 (86 %); 1.20 ± 0.1 (16 %)	0.24 ± 0.03 (4 %); 1.62 ± 0.1 (96 %)
D at $\Delta = 40$ ms / 10^{-9} m² s⁻¹	0.24 ± 0.02 (92 %); 1.54 ± 0.3 (8 %)	0.404 ± 0.02 (8 %); 1.65 ± 0.1 (92 %)
D at $\Delta = 450$ ms / 10^{-9} m² s⁻¹	0.374 ± 0.03	1.55 ± 0.1

The T_1 and T_2 relaxation times for CTAB and pentanol in the CTAB/pentanol/hexane/water reverse microemulsion at 298 K are listed in Table 3.3. A single T_1 relaxation time is obtained for both CTAB and pentanol. Two T_2 relaxation time constants were determined for pentanol, further demonstrating pentanol is distributed between the RM interface and the continuous phase. The shorter T_2 relaxation time represents pentanol in the RM interface due to the reduced motional freedom.[57] Two T_2 relaxation time constants are also obtained for CTAB, further suggesting a distribution between the RM interface and the continuous phase.

Table 3.3: The T_1 and T_2 relaxation times of CTAB and pentanol in the CTAB/pentanol/hexane/water reverse microemulsion at 298 K.

	CTAB	Pentanol
T_1 relaxation time / s	0.44 ± 0.02	2.00 ± 0.04
T_2 relaxation time / s	0.783 ± 0.03 (46 %); 0.246 ± 0.01 (54 %)	0.837 ± 0.07 (61 %) 0.027 ± 0.002 (39 %)

To probe the dynamics of the system, measurements were also performed on the CTAB/pentanol/hexane/water system at 289 K. The diffusion coefficients, D, at Δ = 10 ms, 40 ms and Δ = 450 ms for CTAB and pentanol at 289 K are listed in Table 3.4. The behaviour of CTAB and pentanol is similar to that observed in the system at 298 K. Two diffusion coefficients are obtained for both CTAB and pentanol at short observation times, ($\Delta \leq$ 40 ms) suggesting they are both distributed between the RM interface and the continuous phase. CTAB and pentanol are still exchanging between these two environments as they both possess a single average diffusion coefficient at Δ = 450 ms. Using the same procedure as outlined above, the proportion of pentanol in the RM interface, P_{mic}, at 289 K was determined to be 0.42. Therefore, the continuous phase viscosity was determined to be 0.338 mPa s using the data in Figure 3.3.

Table 3.4: The diffusion coefficients at Δ = 10 ms, 40 ms and 450 ms for CTAB and pentanol in the CTAB/pentanol/hexane/water reverse microemulsion at 289 K.

	CTAB	Pentanol
D at Δ = 10 ms / 10^{-9} m² s^{-1}	0.206 ± 0.020 (80 %) 1.11 ± 0.10 (20 %)	0.243 ± 0.020 (5 %) 1.36 ± 0.10 (95 %)
D at Δ = 40 ms / 10^{-9} m² s^{-1}	0.208 ± 0.020 (88 %) 1.20 ± 0.10 (12 %)	0.42 ± 0.03 (11 %) 1.40 ± 0.10 (89 %)
D at Δ = 450 ms / 10^{-9} m² s^{-1}	0.225 ± 0.020	1.23 ± 0.09

The hydrodynamic radii, R_h, of the RMs at 289 K and 298 K were determined using the Stokes-Einstein equation (Equation 1.7), where the droplets are assumed to be spherical. [38] The hydrodynamic radii, R_h, are listed in Table 3.5, along with the smaller CTAB diffusion coefficient at Δ = 10 ms, and viscosity data utilised in this calculation. The smaller CTAB diffusion coefficients were utilised as this is the best approximation for the diffusion of the RM droplet. [20]

Table 3.5: The hydrodynamic radius, R_h, of the droplets at 289 K and 298 K which were determined using the Stokes-Einstein equation (Equation 1.7) and the smaller CTAB diffusion coefficient at Δ = 10 ms and the dynamic viscosity listed in this table.

Temperature, T / K	D_{CTAB} / 10^{-9} m² s^{-1}	Dynamic Viscosity, η / mPa s	Hydrodynamic radius, R_h / nm
289	0.206 ± 0.02	0.338	3.04 ± 0.27
298	0.22 ± 0.02	0.311	3.13 ± 0.28

The CTAB/hexane/pentanol/water microemulsion was also investigated using molecular dynamics, which enabled the distribution of pentanol molecules within the microemulsion to be modelled. Over the period of the simulation, there is a redistribution of pentanol molecules between the RM interface and the continuous phase. The number of pentanol molecules in the interface was

tracked as a function of simulation time by calculating the pentanol:CTAB ratio in the interface. This was determined by calculating the number of pentanol molecules that were within 8 Å, the equilibrated interface thickness, of any CTAB nitrogen atoms in the RM. Figure 3.5 shows this ratio as a function of simulation time and shows the equilibrium amount of pentanol in the interface is reached after 6 ns. Analysis showed that after 45 ns of simulation time, the proportion of pentanol in the RM interface was determined to be 0.45, with the remaining residing in the continuous phase. By tracking pentanol molecules throughout the simulation, it is clear pentanol molecules exchange between the interface and continuous phase. Additionally, an individual CTAB molecule was also observed to exchange between the RM and continuous phase.
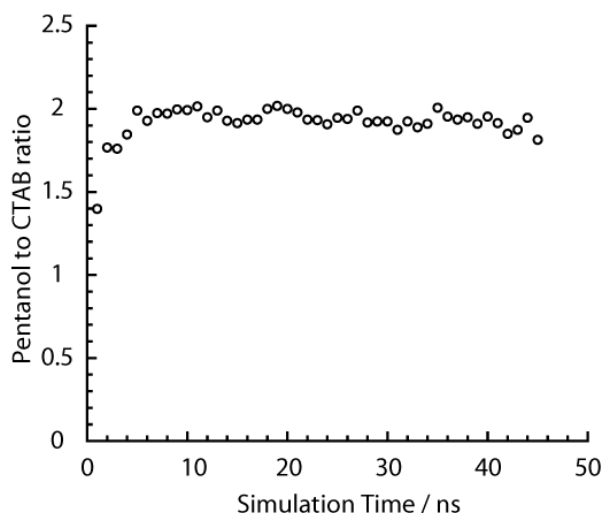
Figure 3.5: Plot of the pentanol to CTAB ratio in the interface of the simulated RM as a function of simulation time.

MD simulation snapshots at set times throughout the simulation of the RM droplet can be found in Figure 3.6 and they show the RM deviated from the initial spherical structure to oblate. Size distributions of the water core radius (R_w), Figure 3.7, and the hydrodynamic radius (R_h), Figure 3.8, were obtained by determining the distance of each CTAB nitrogen atom (for R_w) and terminal carbon (for R_h) from the centre of the RM. The non-symmetrical nature of these size distributions further indicates a deviation from perfectly spherical geometry.[58]
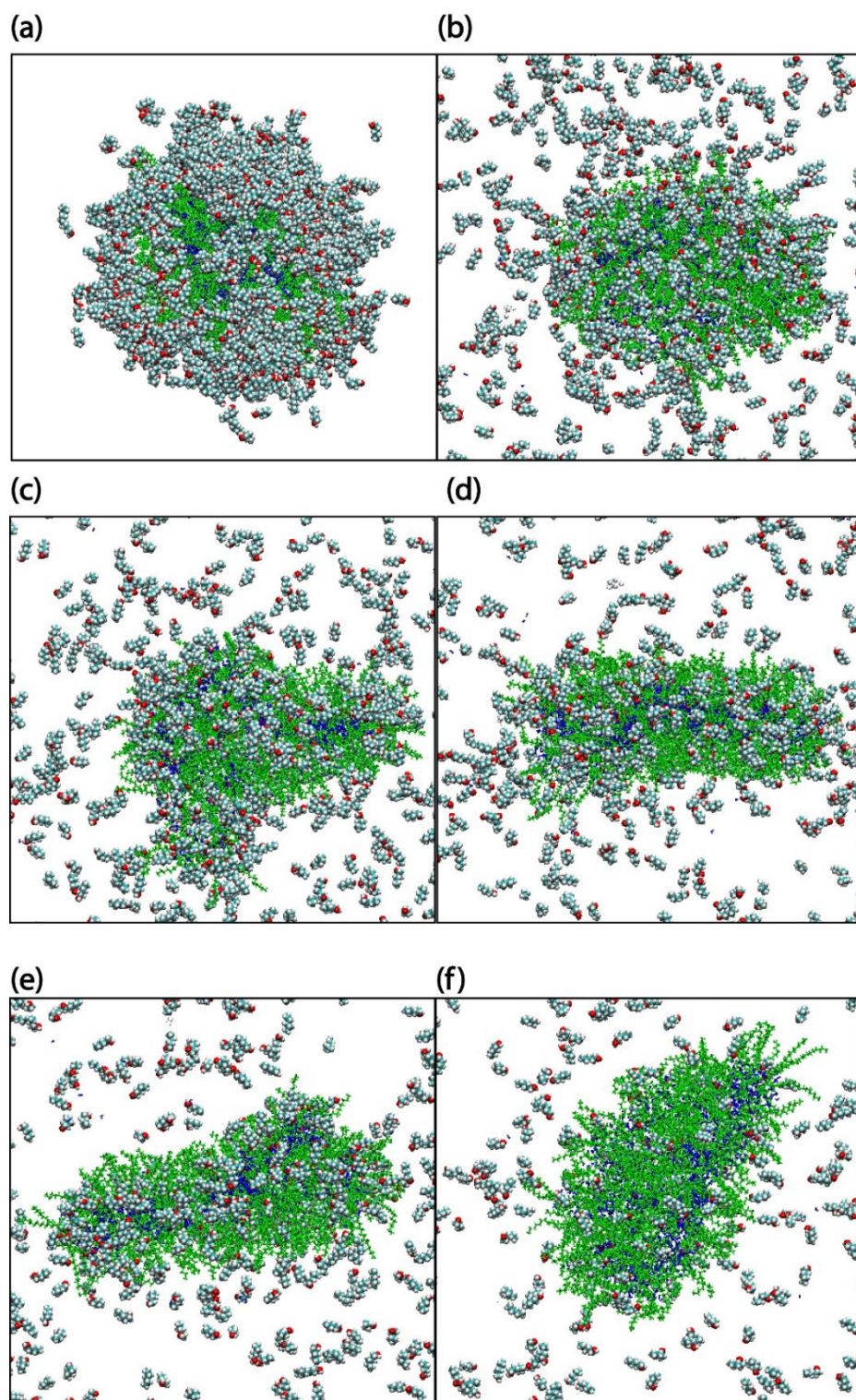
Figure 3.6: Molecular dynamic snapshots of a RM in the CTAB/pentanol/hexane/water microemulsion at simulations times of (a) 200 ps, (b) 5 ns, (c) 10 ns, (d) 15 ns, (e) 20 ns, and (f) 45 ns. The hexane molecules have been removed and only the RM is displayed with CTAB molecules shown in green and water in blue. Pentanol is coloured by atom, with white for hydrogen, blue for carbon, and red for oxygen.
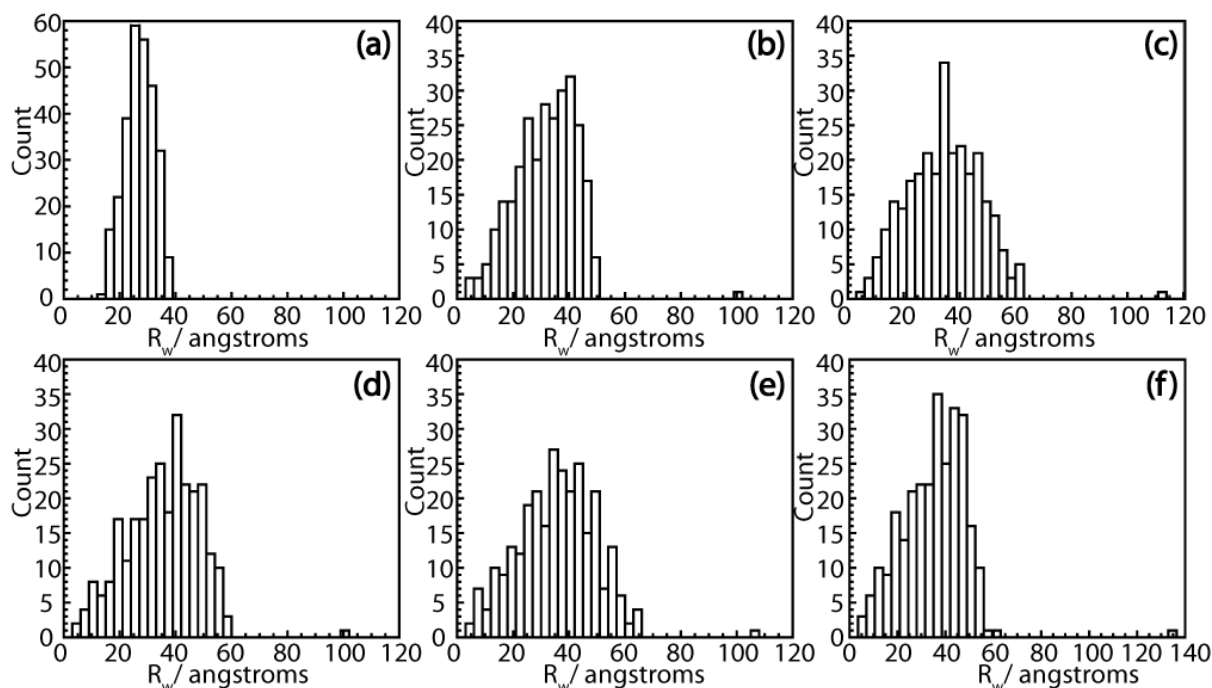
Figure 3.7: Distributions of the root-mean-square of the distance (R_w) between the centre of the droplet and each CTAB nitrogen atom at the following time points (a) 200 ps, (b) 5 ns, (c) 10 ns, (d) 15 ns, (e) 20 ns, and (f) 45 ns.
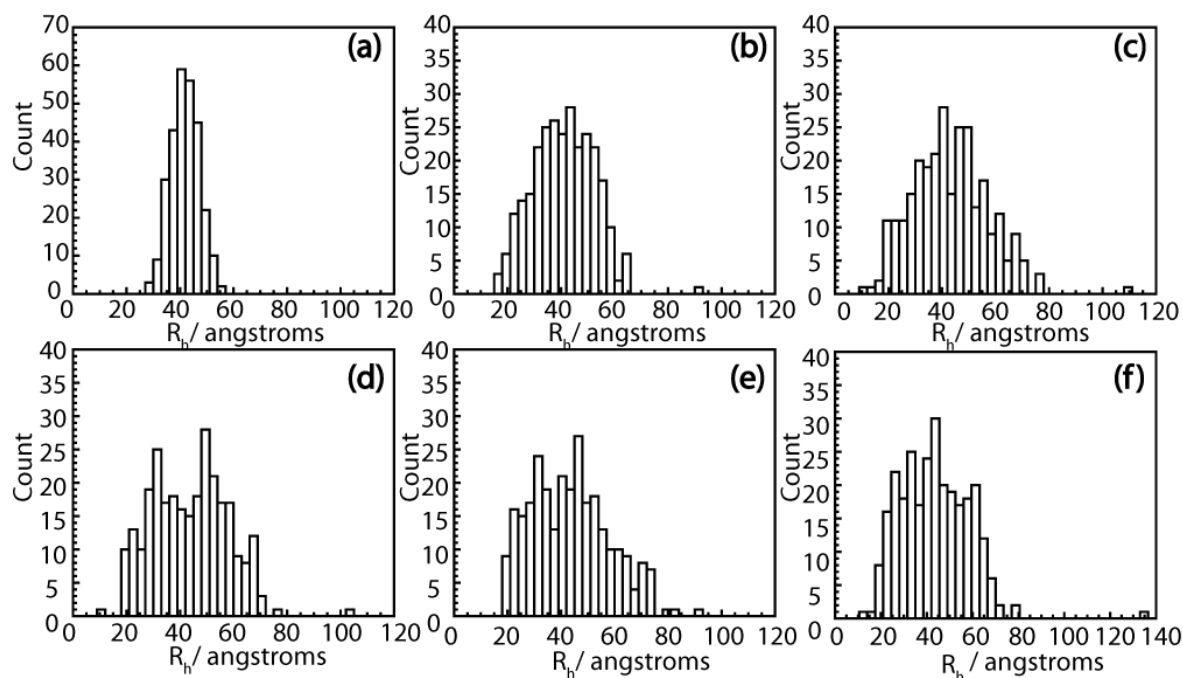
Figure 3.8: Distributions of the root-mean-square of the distance (R_h) between the centre of the droplet and each terminal CTAB carbon at the following time points (a) 200 ps, (b) 5 ns, (c) 10 ns, (d) 15 ns, (e) 20 ns, and (f) 45 ns.

The shape of the reverse micelle droplet was quantified by calculating the lengths of the three semi-axes a, b and c, using the three principle moments of inertia[15,17] I_1, I_2 and I_3 and Equations 1.3, 1.4 and 1.5. The three semi-axes are plotted in Figure 3.9a as a function of simulation time and shows $a \approx b > c$, indicating an oblate structure that stabilises after 15 ns of simulation time. The average values for these three semi-axes and their standard deviations are a = 5.82 ± 0.16 nm, b = 5.01 ± 0.16 nm and c = 2.41 ± 0.074 nm. From the values of a, b and c, the eccentricity value was calculated using Equation 1.6. The eccentricity value was tracked as a function of simulation time in Figure 3.9b, which shows the eccentricity value also equilibrates after approximately 15 ns to give an eccentricity value of 0.91, further demonstrating deviation from spherical geometry.
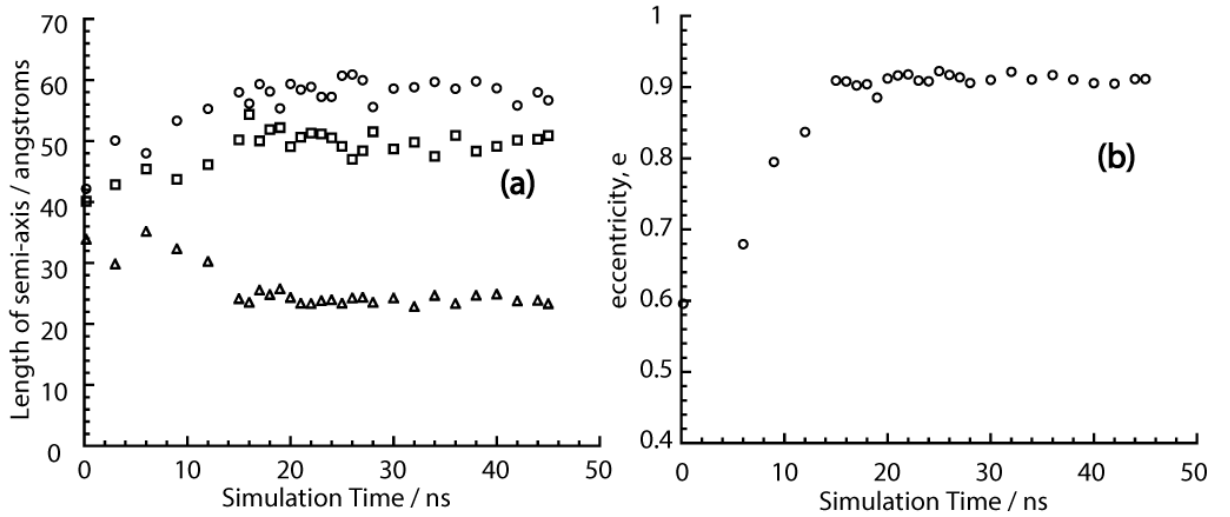
Figure 3.9: Plot (a) of the lengths of the three semi-axes a, b, and c in angstroms as a function of simulation time represented as circles (semi-axis a), squares (semi-axis b), and triangles (semi-axis c). Plot (b) gives the eccentricity value, e, as a function of simulation time.

As the RM is oblate, the previously determined droplet sizes, which were assumed to be spherical, were corrected using a modified Stokes-Einstein equation for non-spherical structures (Equation 1.8), and a shape factor, F_{oblate}, for an oblate ellipsoid (Equation 1.10), where $p = \frac{c}{a}$. Equation 1.8 corrects the hydrodynamic radius to obtain R_H (radius of a sphere with identical volume

to the oblate spheroid) by adjusting the translational and rotational frictional movement of the

oblate structure when compared to the corresponding friction for a sphere of the same volume. [39,40,59]

$$R_H = \frac{k_B T}{6\pi\eta D^0 F_{oblate}}$$

Equation 1.8

$$F_{oblate} = \frac{\sqrt{\left(\frac{1}{p}\right)^2 - 1}}{\left(\frac{1}{p}\right)^{\frac{2}{3}} \arctan\left(\sqrt{\left(\frac{1}{p}\right)^2 - 1}\right)}$$

Equation 1.10

Using the values of a and c from the MD simulation, a value of $p = 0.41$ was obtained, from

which $F_{oblate} = 1.068$ and R_H values were calculated and can be found in Table 3.6. A relationship

between the R_H, a and c was obtained by assuming the volume of the spherical droplet is equal to the

volume of the corresponding oblate structure, Equation 3.2. Using this relationship and $c = 0.41a$

(from the expression for p) the major semi-axis, a, and the minor semi-axis, c, were obtained from

the experimental diffusion data, which can be found in Table 3.6.

$$\frac{4}{3}\pi a^2 c = \frac{4}{3}\pi R_H{}^3$$

Equation 3.2

Table 3.6: The radii of the RM droplet at 289 K and 298 K where the droplet is assumed to be spherical, R_h, which was corrected for the determined oblate structure, R_H, and the semi-axes a and c determined using a combination of molecular modelling and the diffusion data.

Temperature, T / K	R_h (spherical) / nm	R_H (oblate) / nm	Lengths of semi-axes a and c / nm
289	3.04 ± 0.27	2.85 ± 0.26	$a = 3.84 \pm 0.10$ $c = 1.57 \pm 0.05$
298	3.13 ± 0.28	2.93 ± 0.26	$a = 3.95 \pm 0.10$ $c = 1.61 \pm 0.05$

3.4 Discussion

Investigation of the CTAB diffusion data showed that at short observation times ($\Delta \leq 40$ ms) two diffusion coefficients were obtained, whereas a single averaged diffusion coefficient was acquired at long observation times ($\Delta \geq 450$ ms). The presence of two diffusion coefficients, where one is much smaller than the other, indicates CTAB is distributed between the RM interface and the continuous phase, and exchange takes place between them, as evidenced by the single average diffusion coefficient. The presence of CTAB in the RM interface and continuous phase is also suggested by the T_2 relaxation data, where two time constants were obtained. CTAB is thought to be in the continuous phase as either monomers, or as has been observed in CTAB/water/i-octane/n-hexanol RMs containing [Ru(bpy)$_3$]$^{2+}$, small CTAB aggregates,[60] Figure 3.10. Application of the Lindman equation, using the data at $\Delta = 10$ ms, returns a weighted-average of $D_{av} = 3.74 \times 10^{-10}$ m^2 s^{-1}, which compares well with the value $D = 3.63 \times 10^{-10} \pm 0.1$ m^2 s^{-1} measured at $\Delta = 450$ ms.
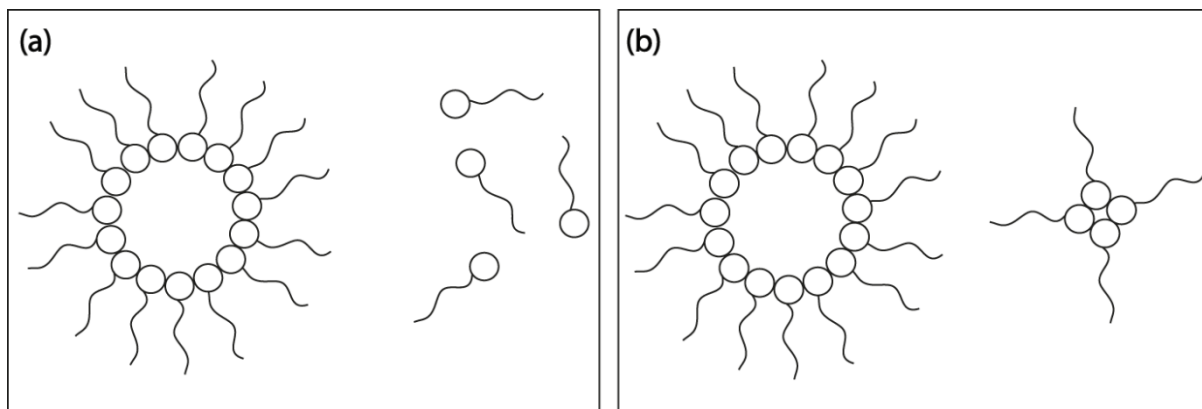
Figure 3.10: A schematic of possible CTAB distribution in the RM where (a) shows CTAB in the RM and as monomers in the continuous phase and (b) shows CTAB in the RM and as small aggregates in the continuous phase

The distribution of CTAB between the RM interface and the continuous phase was rather surprising due to the low solubility of CTAB in hexane, and the lack of this observation in previous measurements performed on this system by Palazzo et al.[21] However, the measurements by Palazzo et al.[21] were performed with a long Δ and δ values,[61] (Δ = 140 ms, G = 0.07 T m^{-1} and δ varied between 14 and 32 ms) which resulted in an averaged CTAB diffusion coefficient, and hence the CTAB in the continuous phase was not observed. While Palazzo et al.[21] only observed one CTAB environment in the CTAB/pentanol/hexane/water reverse microemulsion, two different CTAB environments have previously been observed in a CTAB reverse microemulsion (CTAB/water/i-octane/n-hexanol) by Rack et al.[60] Through the use of lifetime decay data for excited state [Ru(bpy)$_3$]$^{2+}$, they were able to determine the presence of smaller CTAB RMs with ω_0 = 0 in addition to RMs with ω_0 > 0 when [Ru(bpy)$_3$]$^{2+}$ is incorporated into CTAB/water/i-octane/n-hexanol reverse micelles. Therefore, it is possible that the CTAB in the continuous phase could be present as smaller aggregates, Figure 3.10b, in this CTAB/pentanol/hexane/water reverse microemulsion.

Distribution of CTAB between the RM interface and continuous phase was also observed in the molecular modelling of the RM droplet. A single CTAB molecule escapes the RM interface after 2.1 ns of simulation time, hovers near the interface, briefly entering 1 ns later, before diffusing further away into the continuous phase, where it remained for the rest of the simulation. Our

simulations suggest that the CTAB is stabilised by pentanol molecules in the continuous phase, with only pentanol molecules within a radius of 15 Å of the CTAB, and hexane molecules located further away at 20 Å, Figure 3.11. The presence of a single CTAB molecule in the continuous phase is significant as it demonstrates that CTAB can reside there, provided there are pentanol molecules to stabilise it. Therefore, this also provides some evidence that the CTAB could also be present in the continuous phase as a monomer, Figure 3.10a. While there is evidence for CTAB to be present in the continuous phase as monomer or as small aggregates, the exact form is unknown and further investigations are required to determine this.
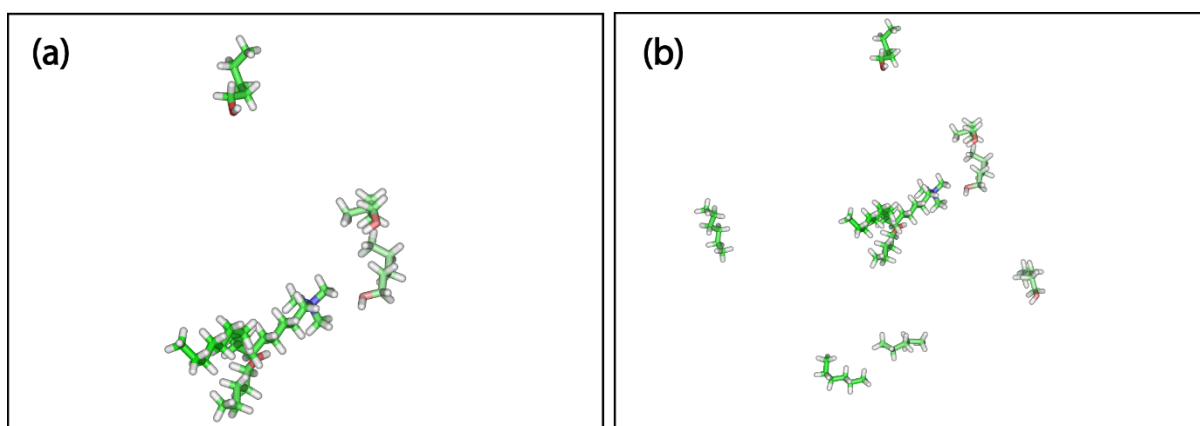
Figure 3.11: A MD snapshot at 24 ns showing the molecules surrounding the free CTAB molecule at (a) 15 Å distance and (b) 20 Å distance. All carbon atoms are green, hydrogen white, nitrogen blue and oxygen red.

The NMR data also suggest that the pentanol is distributed between the RM interface and the continuous phase,[21,62,63] as evidenced by two diffusion coefficients at $\Delta \leq 40$ ms and two T_2 relaxation time constants. At long observation times ($\Delta = 450$ ms), a single weighted-average diffusion coefficient is observed, suggesting pentanol exchanges between the RM and continuous phase. Determining the proportion of pentanol in these two environments is vital as it provides information on the microstructure of the RM and enables the determination of the continuous phase viscosity required for droplet sizing. The proportion of pentanol in the interface, P_{mic}, was determined

to be 0.42 and 0.40 at 289 K and 298 K, respectively, using the Lindman equation and a similar procedure to that of Palazzo et al.[21] However, there was a slight difference in the method used in this P_{mic} determination from the method employed by Palazzo et al.[21] In this analysis, $D_{bulk}\eta$ is not assumed to be a constant, as was done previously, instead experimental values of D_{bulk} from various concentrations of pentanol in hexane were used, Figure 3.4. Palazzo et al.[21] performed this procedure on the CTAB/pentanol/hexane/water RM at 298 K and obtained a P_{mic} of 0.3, which is slightly lower than the P_{mic} calculated in this chapter at 298 K (P_{mic} = 0.4). The value for D_{mic} employed by Palazzo et al.[21] was larger than the one utilised in the calculation of P_{mic} for this chapter, due to the single averaged diffusion coefficient for CTAB obtained by Palazzo et al.[21] Therefore, a combination of the difference in D_{mic} and the slight change in the method for P_{mic} determination, may provide a possible explanation for the slightly higher P_{mic} obtained in these investigations at 298 K, compared with those of Palazzo et al.[21] The calculated P_{mic} values of 0.42 and 0.40 at 289 K and 298 K respectively are consistent with those previously reported in the literature.[14,63] P_{mic} values have been determined by Schulman titration and conductivity measurements, where P_{mic} values of 0.46 (CTAB/pentanol/ hexane/water)[45] and 0.31 (CTAB/butanol/heptane/water at 303 K)[14] have been reported, respectively. The calculated P_{mic} values are also consistent with those determined through the molecular modelling, where at 45 ns, the proportion of pentanol in the simulated droplet was 0.45. The interfacial ratio of pentanol/CTAB (r) for the simulated droplet is 1.93 ± 0.05, while the pentanol:CTAB ratios for the microemulsion at 289 K (r = 4.3) and 298 K (r = 3.8) are expected.

Although these calculated P_{mic} values are consistent with the literature and the molecular simulation, the pentanol diffusion data at $\varDelta$ = 10 ms are not consistent and gave a much lower proportion of pentanol in the interface of 0.05 and 0.04 at 289 K and 298 K, respectively. This suggests the diffusion data significantly underestimate the amount of pentanol in the RM interface. The pentanol populations determined from the diffusion data at $\varDelta$ = 10 ms could be skewed if there is exchange occurring during the 10 ms observation time, which may explain the different proportion

of pentanol in the interface. Both literature[14,62] and molecular simulations predict a greater amount of interfacial pentanol; therefore, there must be a significant proportion of pentanol molecules residing in the interface that are assumed to be in the continuous phase by the pentanol diffusion data at Δ = 10 ms. It is possible that this proportion of pentanol molecules is exchanging at a faster rate than the proportion of pentanol in the interface, which may lead to a weighted average of D_{bulk} and an underestimation of the amount of pentanol in the interface. This interpretation suggests that there is a small proportion of pentanol molecules in the interface (0.05 and 0.04) that possess slow exchange (milliseconds) but there is a significant proportion of pentanol molecules in the interface exchanging on a timescale typically expected for co-surfactant exchange in these reverse microemulsion systems,[64,65] Figure 3.12b.

Exchange of pentanol molecules between the RM interface and the continuous phase is also observed in the molecular simulations. Each pentanol molecule that exchanges between the interface and continuous phase in this simulation was tracked over a 3.5 ns snapshot of the simulation and the average residence time in the interface was determined as a function of the average distance from the RM centre, Figure 3.13. This investigation showed that a longer residence time is obtained for pentanol molecules closest to the RM centre and hence closer to the water core. Therefore, the MD simulations suggest that the slower exchanging pentanol molecules observed in the diffusion data, are those that are closest to the water core, Figure 3.12. While exchange of these "core" pentanol molecules appears slow at Δ = 10 ms, they do exchange with the continuous phase at longer times. This is shown in the measurements at Δ = 450 ms, where only a single weighted average diffusion coefficient is observed.
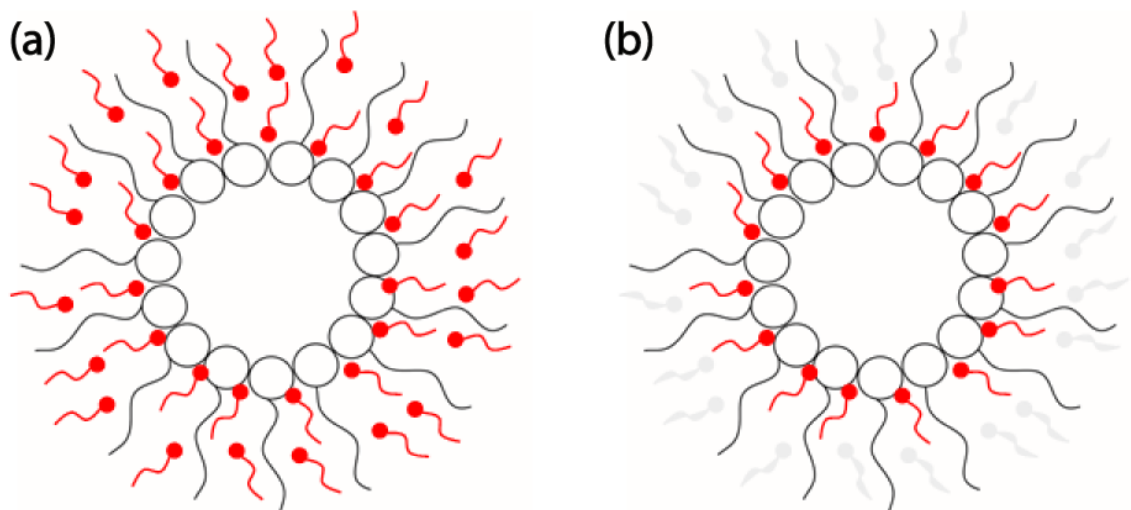
Figure 3.12: Schematic of P_{mic} determined by different methods where (a) is determined by the Lindman equation and represents all the pentanol in the interface, ⬤〰 ; (b) is the relative contribution from the diffusion measurement of pentanol at $\Delta = 10$ ms where ⬤〰 is the slowly exchanging pentanol molecules, and ◯〰 is pentanol undergoing fast exchange.
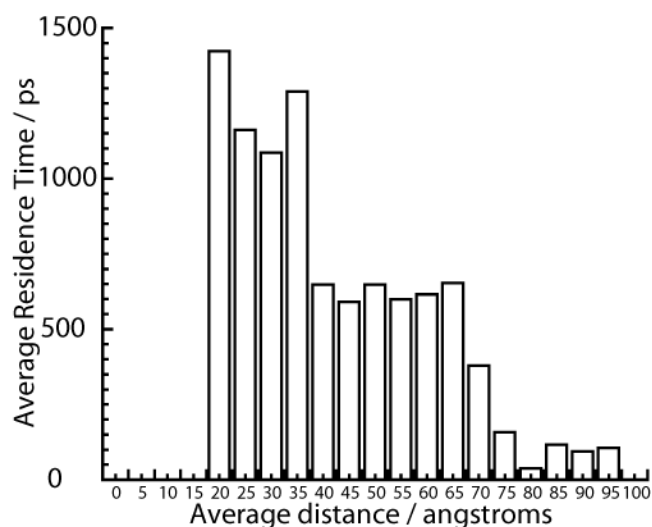
Figure 3.13: The relationship between the average distance a pentanol molecule lies from the centre of the RM and the average residence time of pentanol in the interface, which was determined by using the pentanol molecules that exchange between the interface and continuous phase during a 3.5 ns snapshot.

The slower exchange of a small portion of pentanol molecules in the interface is also supported by relaxation data. Two T_2 relaxation time constants are obtained for pentanol at both

temperatures. If exchange were fast a single average T_2 relaxation time would be observed. This also further supports the distribution of pentanol between the RM interface and the continuous phase, where pentanol in the interface has a shorter relaxation time, due to reduced motional freedom.[55]

Through the determination of the proportion of pentanol in the interface, P_{mic}, for the reverse microemulsion at 289 K and 298 K, a slight increase in interfacial pentanol at the lower temperature was observed. This is consistent with previous CTAB reverse micelle measurements by Mitra et al.[66] This change in interfacial pentanol observed by Mitra et al.[66], which was determined by Shulmans titration,[67] was attributed to the change in hydrophilicity of the surfactant with temperature,[66] and hence a change in the required amount of alcohol to maintain the hydrophile-lipophile balance (HBL).[66]

The amount of pentanol in the interface has also been reported to affect the size of the RM droplets. A greater amount of pentanol in the interface increases the interfacial curvature by increasing the effective packing parameter, favouring the formation of smaller droplets.[21,68-70] This is observed in the experimental data where smaller droplets were determined at 289 K where the P_{mic} value was higher. It is also well known that the addition of a co-surfactant, in this case pentanol, makes RMs more stable[4,71] by altering the distance between the charged headgroups of CTAB, leading to a decrease in the electrostatic repulsions.[4] This could lead to the smaller RM droplets observed at 289 K being more stable than the RM droplets at 298 K.

While the amount of interfacial pentanol affects the size of the droplets, it is also reported that the sizes are affected by temperature changes.[14,72,73] It has been reported by Bisal et al.[14] that an increase in temperature has the effect of reducing the radii of RM droplets for AOT RMs, by reducing the interfacial tension, hence favouring an increased number of droplets with a reduced radius. However, it was stated, CTAB was an exception to this trend as the radius was found to remain unchanged. Zulauf et al.[73] also reported a decrease in droplet radii with an increase in temperature,

but only above 50°C, which was attributed to evaporation of small amounts of water in the microemulsion. Husein et al.[72] investigated the effect of temperature on the uptake of AgBr in CTAB/butanol/water reverse micelles. They reported the uptake of AgBr in the RMs increased almost linearly with temperature and attributed the observation to one of two explanations. Firstly, larger RMs are formed with higher temperatures and, secondly, there is an increase in RM aggregation due to decreased interface rigidity. Both explanations are indicative of larger RMs of CTAB/butanol/water with increased temperature. As there seems to be conflicting reports on the effect of temperature on the size of RMs, it would seem that the droplet size reduction is more of a co-surfactant effect than a temperature effect. However, Mitra et al.[66] have suggested that the amount of co-surfactant in the interface is affected by changes in temperature. Therefore, more work needs to be undertaken to determine whether temperature or interfacial co-surfactant is the cause of the changes in droplet size.

The size of the droplets were initially calculated for this microemulsion using the Stokes-Einstein equation, which assumed a spherical geometry, to obtain the hydrodynamic radius, R_h. These radii, R_h = 3.04 ± 0.27 at 289 K and R_h = 3.13 ± 0.28 at 298 K, are consistent with previously reported sizes by Palazzo et al.[21] and Lang et al.,[74] which also assumed a spherical geometry. However, more accurate droplet sizes were determined by taking into account the oblate structure determined by molecular simulations, to give R_H values. These R_H values represent the radius of a sphere with identical volume to the oblate spheroid, and are slightly smaller than the R_h values. Although the R_h and R_H radii are different, they are not significant, and hence the amount the RM deviates from spherical shape is not enough to affect the diffusion of the RMs[40] or the resultant diffusion coefficient as a result of obstruction from other RM droplets, known as the obstruction effect.[75] However, a higher droplet fraction than the one employed in this study (ϕ_d = 0.05) may lead to this shape deviation, affecting the diffusion of the RM and obstruction effects more significantly[22,75] and hence this shape deviation must not be ignored. While the calculation of R_H

corrects the radius for the oblate structure, it does not give a true representation of the oblate droplet as it should possess two droplet radii. By using the MD simulated RM aspect ratio and the experimentally corrected droplet sizes, R_H, the two droplet radii a and c were able to be determined. This gives a more accurate representation of the RM droplets, particularly since the experimentally determined diffusion coefficients are utilised in determining a and c.

The presence of oblate RM droplets will result in areas of the interface having different degrees of curvature. Increased interface curvature is associated with a greater amount of pentanol in the interface;[21,68-70] therefore, as the interface curvature varies in these oblate structures it is possible there is a non-homogeneous distribution of pentanol in the interface. The pentanol distribution in the interface can be probed using the molecular simulations by determining the pentanol/CTAB ratio at different regions of the RM interface. At regions of high interface curvature (Figure 3.14a) a pentanol/CTAB ratio of 4.3 was obtained, whereas a ratio of 1.6 was determined at low curvature regions (Figure 3.14b). This analysis of the molecular simulation suggests there is a greater amount of pentanol at higher curvature regions, which can be seen visually in Figure 3.14. Therefore, it is suggested that the more the shape deviates from spherical, the greater the deviation in the distribution of pentanol in the interfacial layer.
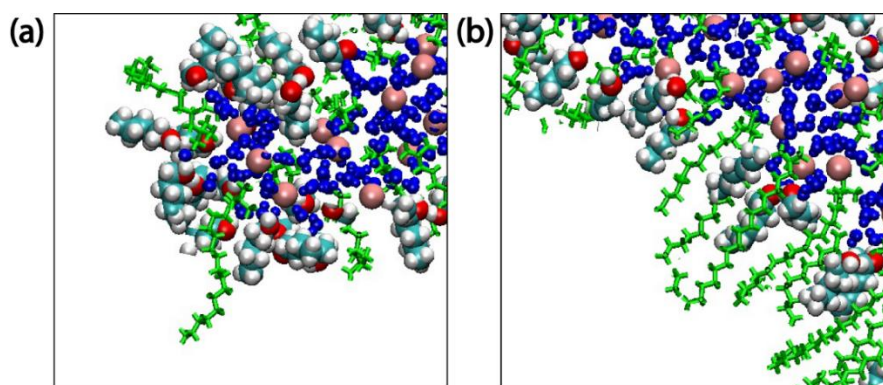
Figure 3.14: Molecular dynamic snapshots of the CTAB/pentanol/hexane/water RM interface at 45 ns showing (a) high curvature region and (b) low curvature region. CTAB molecules are shown in green, bromide in pink, water in dark blue, and pentanol is coloured by atom, with white for hydrogen, blue for carbon, and red for oxygen.

3.5 Conclusion

By measuring the diffusion coefficients for pentanol and CTAB at short and long observation times, it was possible to determine the distribution of CTAB and pentanol between the RM interface and continuous phase. An average diffusion coefficient at longer observation times indicated exchange occurs between these two environments, which was concluded to be on the millisecond timescale for both CTAB and pentanol. Mapping of the CTAB and pentanol molecules was also possible using the molecular simulation due to the use of a hexane solvent box. Both the simulations and experimental data showed that the pentanol molecules move between the interface and continuous phase, as do the CTAB molecules, which was not previously thought.

The sizes of the RM droplets were determined and were found to vary slightly with temperature. At the higher temperature of 298 K, the droplets were slightly larger with less pentanol in the RM interface. The origin of this change in droplet size is unknown and is thought to be due to temperature or an effect of the different amounts of pentanol in the interface. More work need to be performed to fully understand the origin of these droplet size discrepancies. While there were changes in the size of the droplets with temperature, there were no significant changes in the RM dynamics.

The molecular simulations were vital in determining the oblate shape of CTAB RMs, which is a deviation from the frequently assumed spherical geometry. This deviation from spherical geometry resulted in a non-homogeneous distribution of pentanol molecules in the interface. A higher pentanol/CTAB ratio was obtained at points of increased curvature on the molecular simulated RM droplet. Using the MD simulated RM aspect ratio, the experimental droplet sizes were corrected for the oblate shape to obtain two droplet radii, *a* and *c*. This is the first example of combining the results of molecular simulations with NMR diffusion data to obtain the lengths of the semi-axes *a* and *c*, and hence more accurate droplet sizes.

3.6 References

(1)   Capek, I. *Adv. Colloid Interface Sci.* **2004**, *110*, 49.

(2)   Curri, M. L.; Agostiano, A.; Manna, L.; Della Monica, M.; Catalano, M.; Chiavarone, L.; Spagnolo, V.; Lugara, M. *J. Phys. Chem. B* **2000**, *104*, 8391.

(3)   Fang, X.; Yang, C. *J. Colloid Interface Sci.* **1999**, *212*, 242.

(4)   Uskokovic, V.; Drofenik, M. *Surf. Rev. Lett.* **2005**, *12*, 239.

(5)   Kogan, A.; Garti, N. *Adv. Colloid Interface Sci.* **2006**, *123*, 369.

(6)   Luisi, P. L. *Angew. Chem., Int. Ed.* **1985**, *24*, 439.

(7)   Sharon, M.; Ilag, L. L.; Robinson, C. V. *J. Am. Chem. Soc.* **2007**, *129*, 8740.

(8)   Fendler, J. H. *Accounts Chem. Res.* **1976**, *9*, 153.

(9)   McIlwaine, R. E.; Fenton, H.; Scott, S. K.; Taylor, A. F. *J. Phys. Chem. C* **2008**, *112*, 2499.

(10)   Pileni, M. P. *J. Phys. Chem.* **1993**, *97*, 6961.

(11)   Schatzel, K. *Adv. Colloid Interface Sci.* **1993**, *46*, 309.

(12)   Corbeil, E. M.; Levinger, N. E. *Langmuir* **2003**, *19*, 7264.

(13)   Rodenas, E.; Perez-Benito, E. *J. Phys. Chem.* **1991**, *95*, 4552.

(14)   Bisal, S.; Bhattacharya, P. K.; Moulik, S. P. *J. Phys. Chem.* **1990**, *94*, 350.

(15)   Abel, S.; Sterpone, F.; Bandyopadhyay, S.; Marchi, M. *J. Phys. Chem. B* **2004**, *108*, 19458.

(16)   Gardner, A.; Vasquez, V. R.; Clifton, A.; Graeve, O. A. *Fluid Phase Equilib.* **2007**, *262*, 264.

(17)   Martinez, A. V.; Dominguez, L.; Malolepsza, E.; Moser, A.; Ziegler, Z.; Straub, J. E. *J. Phys. Chem. B* **2013**, *117*, 7345.

(18)   Mudzhikova, G. V.; Brodskaya, E. N. *Colloid J.* **2006**, *68*, 729.

(19)   Halliday, N. A.; Peet, A. C.; Britton, M. M. *J. Phys. Chem. B.* **2010**, *114*, 13745.

(20)   Law, S. J.; Britton, M. M. *Langmuir* **2012**, *28*, 11699.

(21)   Palazzo, G.; Lopez, F.; Giustini, M.; Colafemmina, G.; Ceglie, A. *J. Phys. Chem. B* **2003**, *107*, 1924.

(22)   Söderman, O.; Stilbs, P.; Price, W. S. *Concepts Magn. Reson.* **2004**, *23A*, 121.

(23)   Hauser, H.; Haering, G.; Pande, A.; Luisi, P. L. *J. Phys. Chem.* **1989**, *93*, 7869.

(24)   Crans, D. C.; Schoeberl, S.; Gaidamauskas, E.; Baruah, B.; Roess, D. A. *J. Biol. Inorg. Chem.* **2011**, *16*, 961.

(25)   Eastoe, J.; Hollamby, M. J.; Hudson, L. *Adv. Colloid Interface Sci.* **2006**, *128*, 5.

(26)   Mali, K. S.; Dutt, G. B. *J. Chem. Phys.* **2009**, *131*, 8.

(27)   López-Quintela, M. A.; Tojo, C.; Blanco, M. C.; García Rio, L.; Leis, J. R. *Curr. Opin. Colloid Interface Sci* **2004**, *9*, 264.

(28)   Naoe, K.; Takeuchi, C.; Kawagoe, M.; Nagayama, K.; Imai, M. *J. Chromatogr. B* **2007**, *850*, 277.

(29)   Chen, F. X.; Xu, G. Q.; Hor, T. S. A. *Mater. Lett.* **2003**, *57*, 3282.

(30)   Lin, J.; Zhou, W. L.; O'Connor, C. J. *Mater. Lett.* **2001**, *49*, 282.

(31)   Nilsson, P. G.; Lindman, B. *J. Phys. Chem.* **1983**, *87*, 4756.

(32)   Nilsson, P. G.; Lindman, B. *J. Phys. Chem.* **1984**, *88*, 5391.

(33)   Agazzi, F. M.; Correa, N. M.; Rodriguez, J. *Langmuir* **2014**, *30*, 9643.

(34)   Brodskaya, E. N.; Mudzhikova, G. V. *Mol. Phys.* **2006**, *104*, 3635.

(35)   Graeve, O. A.; Fathi, H.; Kelly, J. P.; Saterlie, M. S.; Sinha, K.; Rojas-George, G.; Kanakala, R.; Brown, D. R.; Lopez, E. A. *J. Colloid Interface Sci.* **2013**, *407*, 302.

(36)   Klíčová, L.; Muchová, E.; Šebej, P.; Slavíček, P.; Klán, P. *Langmuir* **2015**, *31*, 8284.

(37)   Nevidimov, A. V. *Russ. J. Phys. Chem. B.* **2014**, *8*, 554.

(38)   Cussler, E. L. *Diffusion: Mass Transfer in Fluid Systems*; Cambridge University Press, 1997.

(39)   Price, W. S. *NMR Studies of Translational Motion: Principles and Applications*; Cambridge University Press, 2009.

(40)   Willis, S. A.; Dennis, G. R.; Zheng, G.; Price, W. S. *J. Mol. Liq.* **2010**, *156*, 45.

(41)   Claridge, T. D. W. *High-Resolution NMR Techniques in Organic Chemistry*; 2nd Edition ed.; Elsevier, 2009; Vol. 27.

(42)   Tofts, P. S.; Lloyd, D.; Clark, C. A.; Barker, G. J.; Parker, G. J. M.; McConville, P.; Baldock, C.; Pope, J. M. *Magnet. Reson. Med.* **2000**, *43*, 368.

(43)   Callaghan, P. T. *Translational Dynamics & Magnetic Resonance: Principles of Pulsed Gradient Spin Echo NMR*; Oxford University Press, 2011.

(44)   Wu, D. H.; Chen, A. D.; Johnson, C. S. *J. Magn. Reson. Ser. A* **1995**, *115*, 260.

(45)   Giustini, M.; Murgia, S.; Palazzo, G. *Langmuir* **2004**, *20*, 7381.

(46)   Price, W. S.; Hayamizu, K.; Ide, H.; Arata, Y. *J. Magn. Reson.* **1999**, *139*, 205.

(47)   Duan, Y.; Wu, C.; Chowdhury, S.; Lee, M. C.; Xiong, G. M.; Zhang, W.; Yang, R.; Cieplak, P.; Luo, R.; Lee, T.; Caldwell, J.; Wang, J. M.; Kollman, P. *J. Comput. Chem.* **2003**, *24*, 1999.

(48)   Wang, J. M.; Wolf, R. M.; Caldwell, J. W.; Kollman, P. A.; Case, D. A. *J. Comput. Chem.* **2004**, *25*, 1157.

(49)   Case, D. A.; Darden, T. A.; Cheatham, T. E.; Simmerling, C. L.; Wang, J.; Duke, R. E.; Luo, R.;

Walker, R. C.; Zhang, W.; Merz, K. M.; Roberts, B.; Hayik, S.; Roitberg, A.; Seabra, G.; Swails, J.; Götz,

A. W.; Kolossváry, I.; Wong, K. F.; Paesani, F.; Vanicek, J.; Wolf, R. M.; Liu, J.; Wu, X.; Brozell, S. R.;

Steinbrecher, T.; Gohlke, H.; Cai, Q.; Ye, X.; Wang, J. M.; Hsieh, M.-J.; Cui, G.; Roe, D. R.; Mathews, D.

H.; Seetin, M. G.; Salomon-Ferrer, R.; Sagui, C.; Babin, V.; Luchko, T.; Gusarov, S.; Kovalenko, A.; P.A.,

K.; University of California, San Francisco: 2012.

(50)   Wilkie, J., Programme available from the author (J.W) on request j.wilkie@bham.ac.uk.

(51)   Binks, D. A.; Spencer, N.; Wilkie, J.; Britton, M. M. *J. Phys. Chem. B* **2010**, *114*, 12558.

(52)   Torres, A. M.; Zheng, G.; Price, W. S. *Magn. Reson. Chem.* **2010**, *48*, 129.

(53)   Tanner, J. E. *J. Chem. Phys.* **1970**, *52*, 2523.

(54)   Halliday, N. Ph.D. Thesis, University of Birmingham, 2011.

(55)   Guo, W.; Fung, B. M.; Orear, E. A. *J. Phys. Chem.* **1992**, *96*, 10068.

(56)   Chen, A.; Shapiro, M. *J. Am. Chem. Soc.* **1999**, *121*, 5338.

(57)   Callaghan, P. T. *Principles of Nuclear Magnetic Resonance Microscopy*; Clarendon Press,

1993.

(58)   Shrestha, L. K.; Sato, T.; Dulle, M.; Glatter, O.; Aramaki, K. *J. Phys. Chem. B* **2010**, *114*, 12008.

(59)   Hansen, S. *J. Chem. Phys.* **2004**, *121*, 9111.

(60)   Rack, J. J.; McCleskey, T. M.; Birnbaum, E. R. *J. Phys. Chem. B* **2002**, *106*, 632.

(61)   Palazzo, G., Personal Communication Via E-Mail for Experimental Paramaters.

(62)   Giustini, M.; Palazzo, G.; Colafemmina, G.; Della Monica, M.; Giomini, M.; Ceglie, A. *J. Phys.

Chem.* **1996**, *100*, 3190.

(63)   Palazzo, G.; Carbone, L.; Colafemmina, G.; Angelico, R.; Ceglie, A.; Giustini, M. *Phys. Chem. Chem. Phys.* **2004**, *6*, 1423.

(64)   Barreleiro, P. C. A.; Alexandridis, P. *J. Colloid Interface Sci.* **1998**, *206*, 357.

(65)   Hansen, J. R. *J. Phys. Chem.* **1974**, *78*, 256.

(66)   Mitra, R. K.; Paul, B. K.; Moulik, S. P. *J. Colloid Interface Sci.* **2006**, *300*, 755.

(67)   Bowcott, J. E.; Schulman, J. H. *Z. Elektrochem.* **1955**, *59*, 283.

(68)   Curri, M. L.; Agostiano, A.; Mavelli, F.; Della Monica, M. *Mat Sci Eng C-Bio S* **2002**, *22*, 423.

(69)   PerezCasas, S.; Castillo, R.; Costas, M. *J. Phys. Chem. B* **1997**, *101*, 7043.

(70)   Zhang, X. G.; Chen, Y. J.; Liu, J. X.; Zhao, C. Z.; Zhang, H. J. *J. Phys. Chem. B* **2012**, *116*, 3723.

(71)   Xu, S.; Zhou, H. C.; Xu, J.; Li, Y. D. *Langmuir* **2002**, *18*, 10503.

(72)   Husein, M. A.; Rodil, E.; Vera, J. H. *Langmuir* **2006**, *22*, 2264.

(73)   Zulauf, M.; Eicke, H. F. *J. Phys. Chem.* **1979**, *83*, 480.

(74)   Lang, J.; Mascolo, G.; Zana, R.; Luisi, P. L. *J. Phys. Chem.* **1990**, *94*, 3069.

(75)   Jonstromer, M.; Jonsson, B.; Lindman, B. *J. Phys. Chem.* **1991**, *95*, 3293.

4. Investigating the Effect of Alcohol Chain Length on the CTAB/alcohol/hexane/water Microemulsion using NMR and Molecular Modelling.

4.1 Introduction

In the previous chapter, nuclear magnetic resonance (NMR) and molecular modelling were employed to characterise the microstructure of the CTAB/pentanol/hexane/water reverse micelle system. These measurements show that the co-surfactant and surfactant are distributed between both the RM interphase and continuous phase, and exchange between these two environments is observed and is in the millisecond timescale. Although these studies provided information on the dynamics and distribution of the co-surfactant, the influence of the co-surfactant on the physical properties of reverse micelles was not clear. In this chapter, the influence the co-surfactant chain length has on the size, shape, composition and dynamics of quaternary CTAB reverse microemulsions was investigated.

Addition of an alcohol co-surfactant to a reverse microemulsion can affect the size, shape and polydispersity of nanoparticles synthesised in RMs. The effect of alcohol chain length on nanoparticles has been investigated by Chen et al.[1] They suggested pentanol is a better co-surfactant than butanol because more spherical monodispersed nanocrystals were formed in the CTAB/pentanol/hexane/water microemulsion than in previous studies on the CTAB/butanol/octane/water microemulsion,[2] which produced polydisperse nanoparticles with a range of shapes. They attributed the superiority of pentanol as a co-surfactant to the formation of stronger van der Waals interactions between pentanol and CTAB resulting in a more stable interface. The alcohol chain length has been reported to affect the structure of enzymes solubilised in RMs. Naoe et al.[3] investigated the structure of *Mucor miehei* lipase solubilised in CTAB/iso-

octane/alcohol/water where the alcohol was pentanol and hexanol. They reported the structure of the lipase is closer to its native structure when the co-surfactant was pentanol rather than hexanol.

It has been reported that the formation and physical properties of reverse micelles is affected by the hydrocarbon chain length of the co-surfactant and the continuous oil phase.[4-6] Bansal et al.[7] suggested that more stable microemulsions are formed when the chain length of the alcohol co-surfactant and the oil continuous phase is approximately equal to the chain length of the surfactant molecules. At this point, the water solubilisation capacity of the reverse micelles is optimum, due to the cohesive interactions between hydrocarbon chains. The findings of Bansal et al.[7] suggests the alcohol chain length will significantly impact the water solubilisation capacity of a reverse micelle system. As the alcohol chain length is increased, the water solubilisation capacity generally increases, reaches a maximum where alcohol and oil chain length are approximately equal to surfactant chain length, and then decreases, Figure 4.1. This trend has been observed in many reverse micelle systems including cationic,[8] anionic[9] and non-ionic[10-14] surfactant molecules.
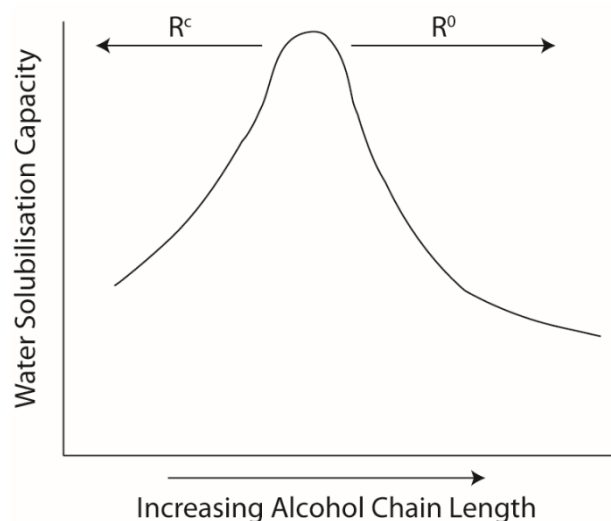
Figure 4.1: A schematic of the water solubilisation trend for reverse micelle systems as a function of alcohol chain length.

An alternative explanation for this water solubilisation trend in RMs was given by Hou and Shah,[9] who rationalised it in terms of interface curvature and the strength of the attraction between RM droplets. [8,9,15] The initial increase in water solubilisation for the short chain alcohol RM systems is limited by R^c,[8,9,12,15] which is a critical point where the microemulsion starts to become unstable and is dependent upon the attraction between the droplets. At this critical value, R^c, the microemulsion separates into two phases of spheres in the same continuous phase.[9,16,17] The two coexisting phases of spheres are thought to be droplets of identical radii present in high and low volume fraction.[16,17] These attractive interactions are determined by the overlap between micelle interfaces which is related to the ability of the oil to penetrate the interfacial layer.[18] As the alcohol chain length increases, the interface becomes more rigid and less oil can penetrate the interface, decreasing the attraction between droplets, increasing the value of R^c and the water solubilisation capacity.[9] The decrease in water solubilisation for longer chain alcohol microemulsions is limited by the radius of spontaneous curvature, R^0. This is dominated by the difference between the interactions of the head groups of the surfactant and alcohol compared with the tails.[8,9] These two interactions are not uniform for all alcohol chain lengths and hence will cause a difference in interface curvature. The interaction between the alcohol and the surfactant head group is uniform for all alcohol chain lengths.[8] However, the interaction between the alcohol and surfactant tails vary with alcohol chain length: an increase in alcohol size increases the stress between the tails. Therefore, as the alcohols increase in size, stress on the tails is much greater than the head groups and hence R^0 is reduced, decreasing the water solubilisation capacity.[8,9] In addition to the alcohol chain length, a decrease in the oil chain length and a decrease in the size of the polar head of the surfactant molecules also leads to a decrease in R^0 and hence water solubilisation.[9]

The amount of water solubilised in reverse micelles is commonly expressed as the water to surfactant ratio, ω_0.[19,20] As ω_0 increases, the radius of the droplet, R_h, also increases,[19-21] therefore one would expect the effect of alcohol chain length on R_h to show a similar trend to that of water

solubilisation capacity. Perez-Casas et al.[22] performed dynamic light scattering (DLS) measurements on the AOT/decane/alcohol/water system where the alcohol chain length was varied. From this study, they determined that the size of the reverse micelles increase for microemulsions containing short chain alcohols up to ethanol, where the size then gradually decreases on going to longer chain alcohols. This is a similar trend to the water solubilisation capacity, but the radius was not rationalised in the same way, i.e. in terms of R^c and R^0. It was suggested that the ethanol and methanol are situated in the water core, due to the increased water solubility and the lack of change in the continuous phase viscosity. The increased radius for ethanol can be rationalised through the larger molar volume compared with methanol. The other alcohols are distributed between the interface and the continuous phase, as the continuous phase viscosity increased rapidly upon addition of the alcohols. The shrinkage of these droplets can be attributed to the spontaneous curvature of the droplet, R^0, as with the water solubilisation capacity. A similar trend was observed by both Lin et al.[23] using dynamic light scattering (DLS) and Howe et al.[24] through small angle neutron scattering (SANS).

A different trend was observed by Zana et al.[8] when studying three different reverse microemulsions composed of surfactants, DTAB, TTAB and CTAB, with alcohols from propanol through to undecanol in chlorobenzene. The size of the CTAB/chlorobenzene/alcohol/water RM system was 3.17 nm, 2.2 nm and 1.95 nm when the alcohol was propanol, butanol and pentanol, respectively. The TTAB/chlorobenzene/alcohol/water RM system decreased in size from 3.64 nm when the alcohol employed was propanol to 2.15 nm for pentanol. The size of the DTAB/cholorobenzene/alcohol/water RMs were larger with sizes of 3.56 nm, 2.47 nm and 2.09 nm when the co-surfactant was butanol, pentanol and hexanol, respectively. In general, they observed a decrease in the size of the water core, R_w, with increasing alcohol chain length for all surfactants. This is in contrast to the water solubilisation capacity where a peak at pentanol was observed. They stated that the droplet size is determined by just the interface curvature, R^0, irrespective of the

factors influencing the water solubilisation capacity, i.e. R^c. The size of reverse micelles is governed by the interface flexibility and surfactant packing parameter, P (Equation 4.1).[8,15,25]

$$P = v/la$$ Equation 4.1

where v is the volume of the hydrophobic moieties, l is the length of the surfactant chain and a is the optimum cross-sectional area of the head group at the water pool. An increase in the surfactant packing, P, leads to a decrease in the interface curvature, R^0 and hence R_w.[8] Increasing the alcohol chain length, will increase the molar volume of the hydrophobic moieties, v, and hence P, therefore decreasing R_w.[8,15,25]

In addition to the water solubilisation capacity and droplet size, the alcohol chain length also has an effect on the percolation threshold of a reverse micelle system.[26] The percolation threshold corresponds to a point where the microemulsion droplets merge to form infinite channels,[27] and is commonly characterised by a large increase in conductivity.[8,15,28] The main factor that dominates the percolation threshold is the attractive interactions between droplets.[27-30] In Zana and co-workers[8] interpretation of the water solubilisation trend, RMs with short chain alcohols are dominated by the attractive droplet interactions. RMs with shorter alcohols have greater attractive interactions and a more fluid interface, therefore the interface opens more readily when droplets collide to form larger aggregates associated with percolation.[15] Therefore, microemulsions containing a short chain alcohol will have a lower percolation threshold[8,15] than those with longer chain alcohol co-surfactants. The onset of percolation is also affected by the continuous phase viscosity.[15,30] A more viscous continuous phase decreases the chance of droplets colliding and aggregating, making percolation more difficult.[15,30] As the alcohol co-surfactant is distributed between the RM and the continuous phase,[31,32] alcohol in the continuous phase leads to an increase in continuous phase viscosity and hence can also affect the onset of percolation.

In this chapter, NMR relaxation and diffusion measurements are used to investigate the CTAB/alcohol/hexane/water reverse micelle microemulsions, where the alcohol is varied from butanol to heptanol, and the CTAB/alcohol/pentane/water microemulsion where the alcohol is pentanol and hexanol. Molecular simulations are also presented for CTAB RMs with each of the four alcohol co-surfactants in n-hexane. Using a combination of these experimental and modelling data, we investigate the influence of the co-surfactant chain length on the size, shape, composition and dynamics of quaternary CTAB reverse microemulsions.

4.2 Experimental

Sample Preparation.

Cetyltrimethylammonium bromide (CTAB, Sigma-Aldrich, 98%), n-hexane (Fisher-Scientific, reagent grade), n-pentane (Fisher-Scientific, > 99 %) and water (purified with a MilliQ^{TM} system, resistivity 18 MΩ cm, TOC ≤ 5 ppb) were used, along with various linear alcohols, to produce CTAB/alcohol/n-hexane/water and CTAB/alcohol/n-pentane/water quaternary microemulsions. The alcohols used were butanol (Sigma-Aldrich, ≥ 99.4 %), pentanol (Sigma Aldrich, 99%), hexanol (Acros Organics, 98 %) and heptanol (Sigma-Aldrich, 98 %). Microemulsions were prepared by dissolving 0.2 g CTAB in 8.394 ml n-hexane or n-pentane and 0.068 ml water, along with the required amount of alcohol, and shaking for approximately 2 minutes. The alcohol/CTAB molar ratio, P_0, was kept constant at 8.2, therefore the required additions of alcohol was 0.412 ml, 0.487 ml, 0.565 ml and 0.636 ml for butanol, pentanol, hexanol and heptanol, respectively, see Appendix 1. The water/CTAB molar ratio, ω_0, is 6.9 and the volume droplet fraction, ϕ, is 0.05 for all microemulsions studied. The composition of each reverse micelle is summarised in Table 4.1. NMR measurements were taken approximately 1 hour after sample preparation for all samples, with additional measurements for the CTAB/pentanol/hexane/water system taken after approximately 6 hours.

Table 4.1: Composition of each CTAB/alcohol/hexane/water and CTAB/alcohol/pentane reverse microemulsion.

Alcohol	Volume of alcohol / mL	Volume of water / mL	Mass of CTAB / g	Volume of oil / mL
CTAB/alcohol/hexane/water reverse microemulsion				
Butanol	0.412	0.068	0.2	8.394
Pentanol	0.487	0.068	0.2	8.394
Hexanol	0.565	0.068	0.2	8.394
Heptanol	0.636	0.068	0.2	8.394
CTAB/alcohol/pentane/water reverse microemulsion				
Pentanol	0.487	0.068	0.2	8.394
Hexanol	0.565	0.068	0.2	8.394

NMR Measurements.

NMR experiments were performed on the same spectrometer and experimental setup as described in chapter 3. The proton numbering schemes for CTAB and the alcohols are shown in Figure 4.2. The ^{1}H NMR spectrum for each alcohol system can be found in Appendix 3. NMR measurements of the CTAB surfactant were performed using the same proton resonance utilised in chapter 3 (H_a). The proton environment used for the alcohol measurements are those on the carbon in the α position to the hydroxyl group, H_g, at $\delta \approx 3.5$ ppm. Measurements were performed on the hydroxyl proton peak at $\delta \approx 4.3$ ppm, which represents a combination of the water hydroxyl and alcohol hydroxyl (H_f) protons.
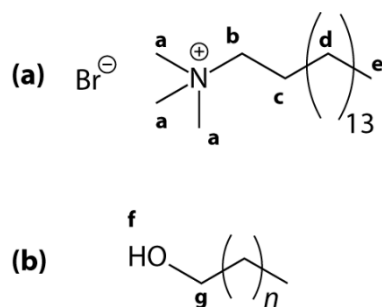
Figure 4.2: Schematic and proton numbering of (a) the surfactant, CTAB, and (b) the alcohol co-surfactant where n = 2 for butanol, n = 3 for pentanol, n = 4 for hexanol and n = 5 for heptanol.

Spin-spin (T_2) relaxation times for CTAB (H_a) and alcohol (H_g) were measured using ^{1}H NMR

Carr Purcell Meiboom Gill (CPMG) experiments, $[90 - (\tau - 180 - \tau)_m - acq]_n$ at 298 $\pm$ 0.3 K. A

repetition time of 10 s was used to collect eight signal averages, n, with 16 echoes, m, varied from 0

to 1024 with a delay of τ = 2 ms. An inversion recovery experiment, $[180° - \tau - 90° - acq]_n$, was used

to measure the T_1 relaxation times of CTAB (H_a) and alcohol (H_g) at 298 $\pm$ 0.3 K. A series of n = 33

experiments were performed with logarithmically spaced time delays, τ, ranging from 5×10^{-6} s to

15 s. A total of eight signal averages, n, were collected with a repetition time of 10 s.

Diffusion coefficients for the H_a resonance of CTAB and H_g of alcohol were measured using ^{1}H

NMR pulsed gradient stimulated echo with bipolar pulse pairs (BPP–STE) experiments[33-35] at 298 $\pm$ 0.3

K. Data were collected at observation times of $\varDelta$ = 10 or 20 and 400 ms, using 32 magnetic field

gradient steps, and δ = 2 ms, $\varDelta$ = 400 ms and $\boldsymbol{G}_{max}$ = 0.45 T m^{-1}; δ = 2 ms, $\varDelta$ = 100 ms and $\boldsymbol{G}_{max}$ = 0.9 T

m^{-1}; δ = 2 ms, $\varDelta$ = 20 ms and $\boldsymbol{G}_{max}$ = 1.9 T m^{-1}; or δ = 2 ms, $\varDelta$ = 10 ms and $\boldsymbol{G}_{max}$ = 2.7 T m^{-1}. Diffusion

coefficients were determined using the same procedure in chapter 3 through the use of the Stejskal-

Tanner relationship (Equation 2.11).

The amount of alcohol in the interface, P_{mic}, was determined using the same procedure

outlined in chapter 3 which utilises the Lindman equation (Equation 1.15). The average co-surfactant

diffusion coefficient at long observation time was used as D_{obs} and the CTAB diffusion coefficient was

approximated as the RM diffusion coefficient, D_{mic}. In the case of CTAB/n-hexane/n-pentanol/water

system, the smaller of the two CTAB diffusion coefficients values were used. The diffusion coefficient

for the co-surfactant in the continuous phase, D_{bulk}, was determined from a range of solutions

containing each co-surfactant in hexane. D_{bulk} for pentanol in pentane and hexanol in pentane were

determined assuming a constant relationship[32] between D and viscosity of $D\eta$ = 6.4×10^{-13} N.

Viscosity Measurements.

Kinematic viscosity measurements of solutions of alcohol in *n*-hexane, over the

concentration range of $0 - 1$ M, were performed at 298 K using an Ubbelohde size 0 viscometer.

Density measurements of the alcohol/*n*-hexane solutions were determined by weighing 10 ml of the

sample, which had been kept at 298 ± 0.1 K. The dynamic viscosity (η) was calculated using the

kinematic viscosity (υ) and density (ρ) data via Equation 3.1. The dynamic viscosity of

pentanol/pentane and hexanol/pentane at 298 K were taken directly from previous measurements

performed by Sastry et al.[36]

Molecular Mechanics and Molecular Dynamics (MD) Calculations.

The CTAB/alcohol/hexane/water RM droplets where the alcohol is butanol, hexanol and

heptanol were investigated by molecular dynamics using the same theoretical setup as described in

chapter 3. Molecular dynamics (MD) calculations for the CTAB/pentanol/n-hexane/water droplet was

reported previously,[31] as in chapter 3.

Droplet Construction.

The droplets were constructed using the same method outlined in chapter 3 for the

CTAB/pentanol/hexane/water RM droplet. The procedure was repeated three times to produce

three different droplets where the co-surfactant layer was constructed from butanol, hexanol or

heptanol. All the alcohol co-surfactant molecules were oriented so that the hydroxyl group points

away from the droplet core.

Droplet Solvation.

A *n*-hexane solvent was prepared for our publication[31] (detailed in chapter 3), and was

utilized in the solvation of these droplets. Each optimized droplet was solvated with at least 20 Å of

n-hexane, with the *solvatebox* command within AMBER LEaP. The solvated droplets were minimized

for a maximum of 40,000 cycles so the RMS gradients < 2 and have a G_{max} <10^2 at constant volume.

The droplets were equilibrated using constant pressure of 1 atm, isotropic position scaling, compressibility of 44.6 x 10^{-6} bar^{-1} and a pressure relaxation time of 1 ps, until the box size remained constant. This equilibration period ranged from 200 – 500 ps depending on the system. Once the box size was constant, the equilibration was carried out at constant volume with no pressure scaling. Molecular dynamics calculations were performed for each droplet for a minimum of 18 ns, which includes the time for equilibration.

4.3 Results

Viscosity

Figure 4.3 and Figure 4.4 show plots of dynamic viscosity against co-surfactant concentration for a range of alcohols in hexane and pentane, respectively. Figure 4.5 shows a plot of the diffusion of various concentrations of alcohol in hexane.
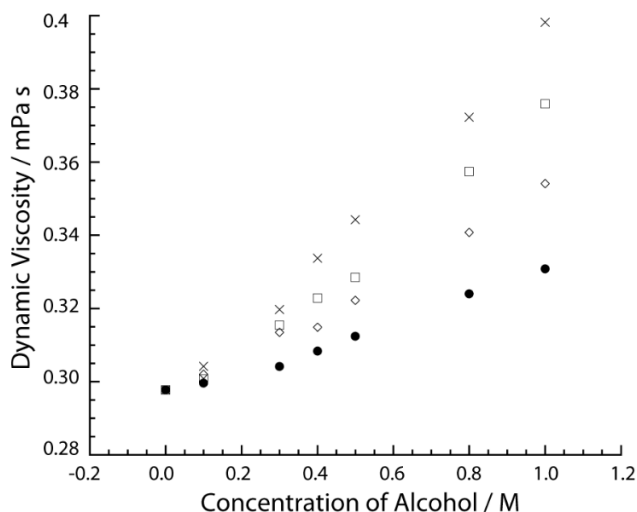
Figure 4.3: Dynamic viscosity of different concentrations of the four alcohols, butanol (●), pentanol (◇), hexanol (□) and heptanol (✕), in hexane.
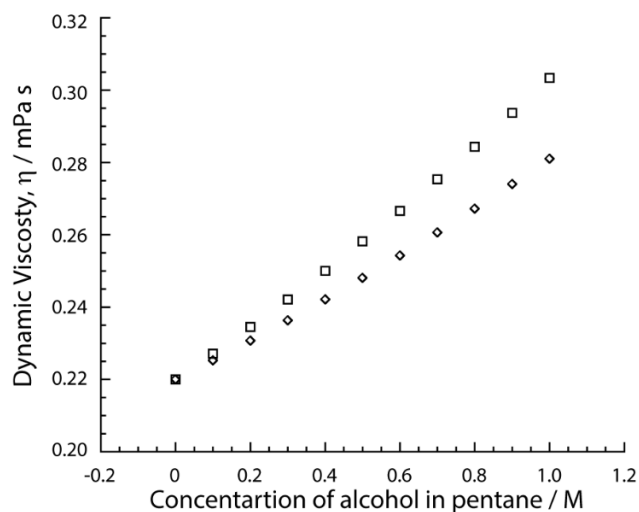
Figure 4.4: Dynamic viscosity of various concentrations of pentanol ($\diamond$) and hexanol ($\square$) in pentane at 298 K, reproduced from data published by Saatry et al.[36]
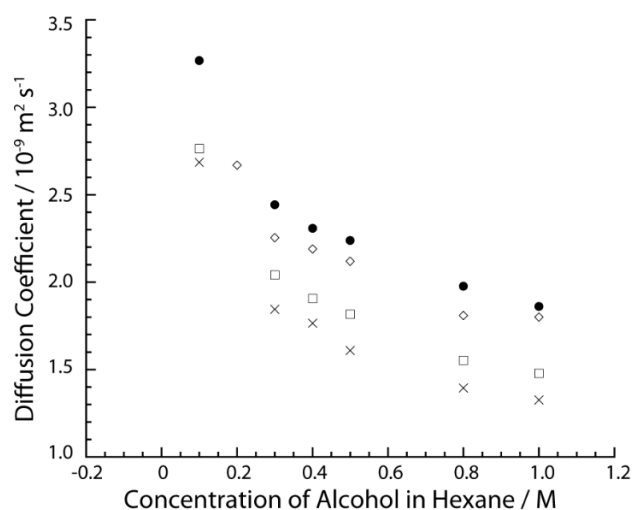
Figure 4.5: A plot of the alcohol diffusion coefficient as a function of alcohol concentration in hexane a 298 K where butanol ($\bullet$), pentanol ($\diamond$), hexanol ($\square$) and heptanol ($\times$), in hexane.

NMR Measurements

Diffusion coefficients, D, at $\Delta = 10$ ms or 20 ms and $\Delta = 400$ ms, T_1 and T_2 relaxation times along with the calculated P_{mic} for the alcohol co-surfactant in the CTAB/alcohol/hexane/water and CTAB/alcohol/pentane/water reverse microemulsions are shown in Table 4.2.

A single T_1 relaxation time constant can be fitted to the alcohol T_1 data for all microemulsions, which decreases as a function of increasing alcohol chain length (Figure 4.6a). The alcohol exhibits two T_2 relaxation time constants, indicating the alcohol is distributed between the RM and the continuous phase. It is expected that alcohol in the continuous phase will exhibit longer T_2 relaxation times (T_2^{bulk}) than those in the RM interface (T_2^{mic}), because of their greater rotational mobility, which average the dipole-dipole interactions they experience from other spins in the system.[37] The more restricted mobility experienced by co-surfactant molecules in the RM interface increases dipolar interactions, increasing the relaxation rate, hence leading to a shorter T_2. The T_2^{bulk} of alcohol in the CTAB/alcohol/hexane/water systems, Figure 4.6a, generally decreases as the alcohol chain length increases. However, T_2^{mic}, Figure 4.6b, is unchanged for all alcohols when hexane is the continuous phase except when the alcohol co-surfactant is pentanol.
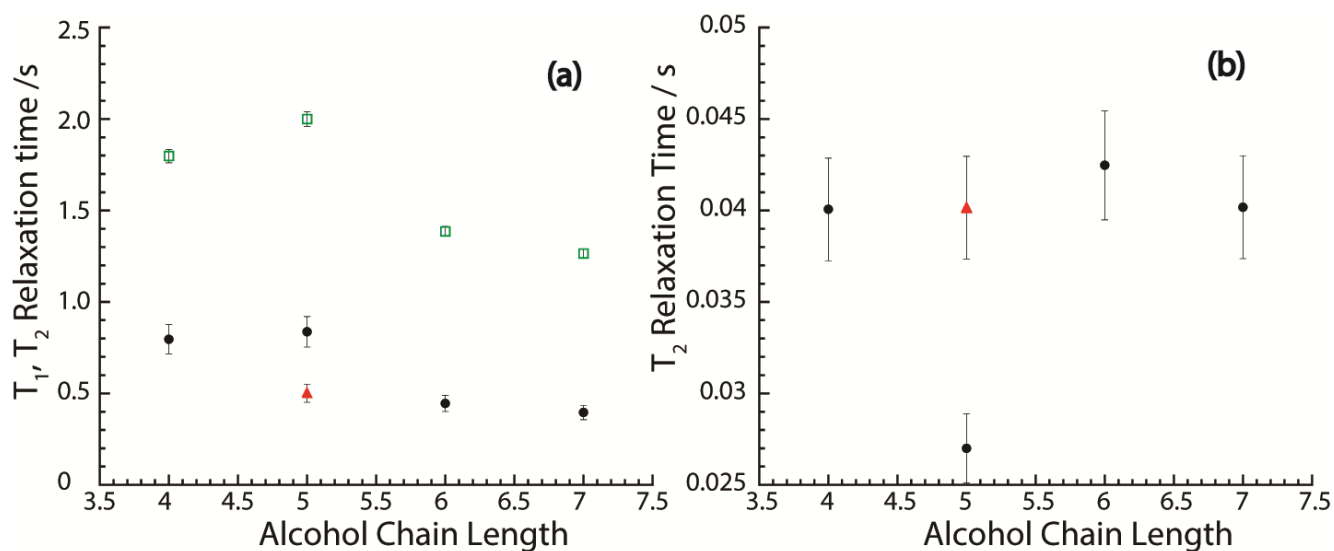
Figure 4.6: A plot of the relaxation behaviour of alcohol as a function of alcohol chain length. (a) Plots the T_1 relaxation, ☐, the long T_2 relaxation component (T_2^{bulk}), ● and T_2^{bulk} after 6 hours, ▲. (b) Plots the short T_2 relaxation component (T_2^{mic}), ●, and T_2^{mic} after 6 hours, ▲.

Table 4.2: The T_1, T_2 relaxation times and diffusion coefficients, D, at $\Delta < 20$ ms and 400 ms for the alcohol, H_g, proton environment in the CTAB reverse micelles studied, where * represents measurements after 6 hours.

System	T_1 / s	T_2 / s	D at $\Delta < 20$ ms /10^{-9} m² s⁻¹	D at $\Delta = 400$ ms /10^{-9} m² s⁻¹	P_{mic}
CTAB/alcohol/hexane/water reverse microemulsion					
Butanol	1.798 ± 0.04	0.04 ± 0.002 (72 %) 0.796 ± 0.07 (28 %)	1.57 ± 0.02	1.58 ± 0.1	0.39
Pentanol	2.00 ± 0.04	0.027 ± 0.002 (39 %) 0.837 ± 0.07 (61 %)	0.24 ± 0.03 (4 %) 1.62 ± 0.02 (96 %)	1.55 ± 0.1	0.40
Pentanol*		0.04 ± 0.002 (62 %) 0.501 ± 0.04 (37 %)	0.305 ± 0.04 (4 %) 1.50 ± 0.02 (96 %)	1.53 ± 0.09 ($\Delta = 40$ ms)	0.39
Hexanol	1.386 ± 0.03	0.042 ± 0.003 (70 %) 0.445 ± 0.04 (29 %)	0.20 ± 0.03 (4 %) 1.32 ± 0.02 (96 %)	1.36 ± 0.09	0.37
Heptanol	1.265 ± 0.02	0.04 ± 0.002 (68 %) 0.396 ± 0.03 (32 %)	0.26 ± 0.03 (4 %) 1.28 ± 0.02 (96 %)	1.30 ± 0.09	0.33
CTAB/alcohol/pentane/water reverse microemulsion					
Pentanol	1.951 ± 0.04	0.053 ± 0.003 (31 %) 0.972 ± 0.08 (69 %)	0.30 ± 0.04 (7 %) 1.96 ± 0.03 (93 %)	2.29 ± 0.15	0.31
Hexanol	1.682 ± 0.03	0.019 ± 0.001 (40 %) 0.458 ± 0.04 (60 %)	0.3 ± 0.04 (3 %) 1.55 ± 0.02 (97 %)	1.57 ± 0.1	0.46

Two diffusion coefficients are required to fit the alcohol diffusion data at short observation times for pentanol, hexanol and heptanol. A large and small diffusion coefficient were obtained where the large diffusion coefficient (D_{CS}^{bulk}) represents alcohol molecules in the continuous phase. The small diffusion coefficient (D_{CS}^{mic}) is associated with alcohol in the interface due to the restricted mobility within the interfacial layer. At longer observation times, a single averaged diffusion

coefficient is obtained indicating the alcohol exchanges between the interface and continuous phase on a millisecond timescale. However, the CTAB/butanol/hexane/water microemulsion exhibits a single diffusion coefficient for butanol at both short and long observation times, which could be due to faster exchange of butanol between the RM and continuous phase. The large alcohol diffusion coefficients in the CTAB/alcohol/hexane/water microemulsion (D_{CS}^{bulk}) are plotted in Figure 4.7, which shows a reduction in the diffusion coefficient as the alcohol size increases. The CTAB/pentanol/hexane/water system behaves anomalously with a smaller alcohol diffusion coefficient than expected, however, after 6 hours, the diffusion coefficient follows the general trend set by the other alcohol systems. The reduced larger pentanol diffusion coefficient in the initial CTAB/pentanol/hexane/water system is possibly a result of the distribution of the surfactant CTAB; in chapter 3 it was concluded that the CTAB in this system is distributed between both the RM interface and the continuous phase. The presence of CTAB in the continuous phase could hinder pentanol diffusion in this phase, and hence result in a smaller diffusion coefficient than expected, when compared with the corresponding diffusion coefficients of the alcohols in the other CTAB/alcohol/hexane/water systems, where CTAB is present in only the RM interface.
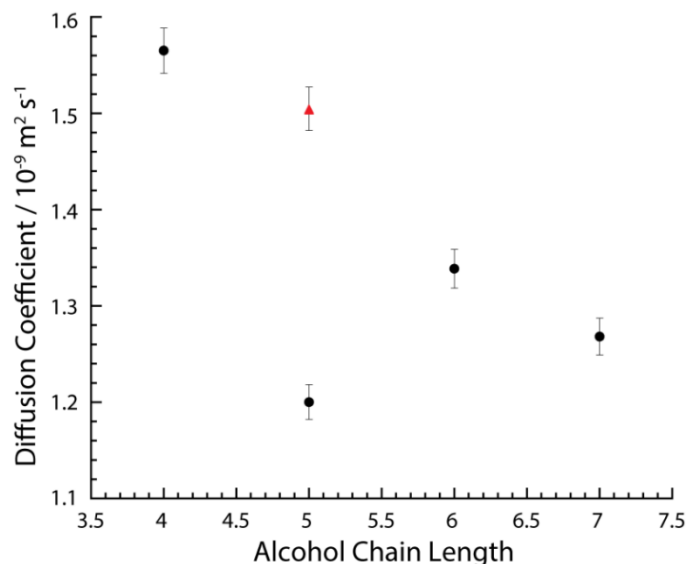
Figure 4.7: A plot of the larger diffusion coefficients, D_{CS}^{bulk}, at short Δ for alcohol proton environment, H_g, as a function of alcohol chain length with ● representing the initial diffusion coefficient and ▲ the diffusion coefficient after 6 hours.

The diffusion and relaxation measurements of the CTAB in the CTAB/alcohol/hexane/water and CTAB/alcohol/pentane/water reverse microemulsions, along with the calculated hydrodynamic radius, R_h, are shown in Table 4.3. A single T_1 relaxation time is obtained for the CTAB for all the systems. A single T_2 relaxation time and diffusion coefficient are obtained for all microemulsions studied, except the CTAB/pentanol/hexane/water reverse microemulsion. The CTAB/pentanol/hexane/water RM has two T_2 relaxation times and diffusion coefficients, as observed in chapter 3 where it was suggested CTAB is distributed between the RM interface and the continuous phase, as either monomer or small aggregates. However, after approximately 6 hours, only one CTAB environment is observed in the CTAB/pentanol/hexane/water RM, as evidenced by a single T_2 relaxation time and diffusion coefficient. The diffusion coefficients and relaxation times for the CTAB in the CTAB/alcohol/hexane/water microemulsions are represented in Figure 4.8, as a function of alcohol chain length. The sizes of the RMs were determined using the Stokes-Einstein equation, with the CTAB diffusion coefficients and viscosity data in Table 4.3.

Table 4.3: The T_1, T_2 relaxation times and diffusion coefficients, D, at $\Delta < 20$ ms and 400 ms for CTAB H_a proton environment in the CTAB reverse micelles studied, where * represents measurements after 6 hours.

System	T_1 / s	T_2 / s	D at $\Delta < 20$ ms /10^{-9} m^2 s^{-1}	D at $\Delta =400$ ms /10^{-9} m^2 s^{-1}	η / mPa s	R_h / nm
CTAB/alcohol/hexane/water reverse microemulsion						
Butanol	0.401 ± 0.02	0.344 ± 0.01	0.21 ± 0.02	0.328 ± 0.03	0.307	3.44
Pentanol	0.440 ± 0.02	0.783 ± 0.03 (46 %) 0.246 ± 0.01 (54 %)	0.22 ± 0.02 (86%) 1.2 ± 0.1 (14 %)	0.374 ± 0.03	0.308	3.13
Pentanol*	–	0.332 ± 0.01	0.204 ± 0.02	0.215 ± 0.02 (Δ = 40 ms)	0.309	3.47
Hexanol	0.366 ± 0.02	0.320 ± 0.01	0.22 ± 0.02	0.34 ± 0.03	0.312	3.11
Heptanol	0.362 ± 0.01	0.315 ± 0.01	0.22 ± 0.02	0.36 ± 0.03	0.322	3.03
CTAB/alcohol/hexane/water reverse microemulsion						
Pentanol	0.399 ± 0.02	0.327 ± 0.01	0.28 ± 0.02		0.24	3.30
Hexanol	0.387 ± 0.02	0.315 ± 0.01	0.29 ± 0.03		0.24	3.13
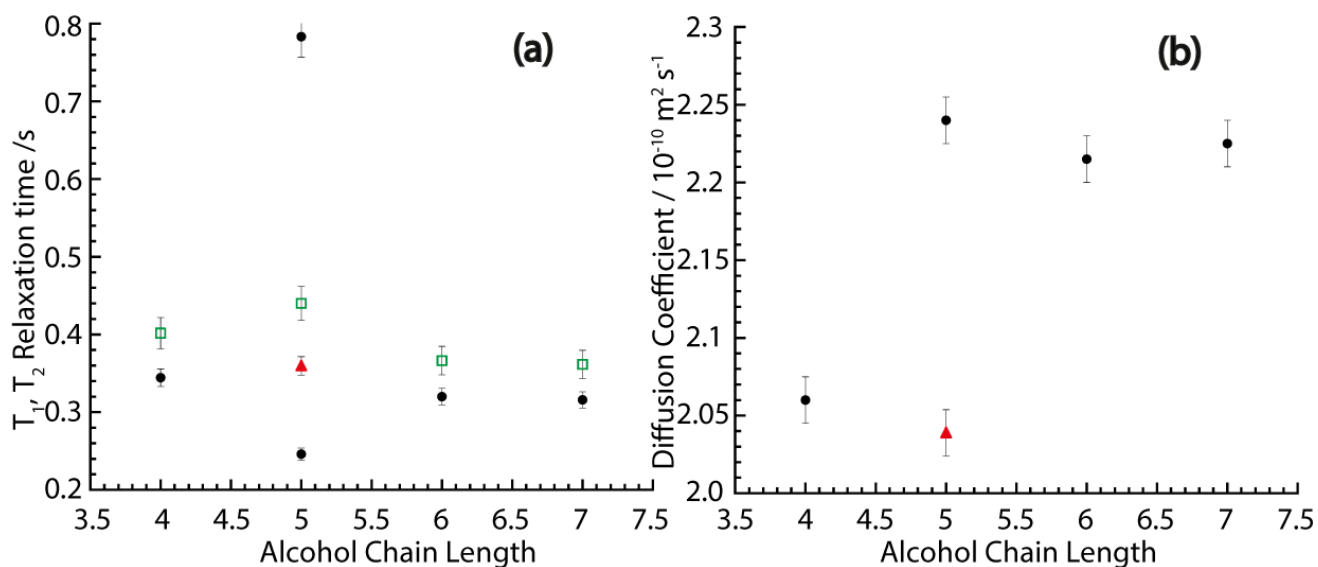
Figure 4.8: The T_1 and T_2 relaxation times (a) and diffusion coefficients (b) for CTAB H_a proton environment in the CTAB/alcohol/hexane/water RMs as a function of increasing alcohol chain length represented as □ (T_1 relaxation), ● (initial T_2 relaxation/ diffusion coefficient) and ▲ (T_2 relaxation/diffusion coefficient after 6 hours).

Table 4.4 shows the relaxation times and diffusion coefficients for the hydroxyl resonance, which consists of water hydroxyl and alcohol hydroxyl, H_f.

Table 4.4: The T_1, T_2 relaxation times and diffusion coefficients, D, at $\Delta < 20$ ms and 400 ms for hydroxyl proton environment in the CTAB reverse micelles studied, where * represents measurements after 6 hours.

System	T_1 / s	T_2 / s	D at $\Delta < 20$ ms /10^{-9} m² s⁻¹	D at $\Delta = 400$ ms /10^{-9} m² s⁻¹
CTAB/alcohol/hexane/water reverse microemulsion				
Butanol	0.973 ± 0.04	0.111 ± 0.01	0.821 ± 0.009	0.9 ± 0.03
Pentanol	1.107 ± 0.04	0.019 ± 0.002 (39 %) 0.160 ± 0.01 (61 %)	0.877 ± 0.07	0.981 ± 0.08
Pentanol*		0.061 ± 0.005	0.744 ± 0.01	
Hexanol	0.878 ± 0.02	0.096 ± 0.001	0.722 ± 0.01	0.926 ± 0.05
Heptanol	0.850 ± 0.03	0.083 ± 0.01	0.682 ± 0.008	1.02 ± 0.09
CTAB/alcohol/pentane/water reverse microemulsion				
Pentanol	0.834 ± 0.03	0.0603 ± 0.005	0.970 ± 0.01	1.29 ± 0.08
Hexanol	0.944 ± 0.03	0.0697 ± 0.006	0.85 ± 0.01	1.02 ± 0.07

The hydroxyl proton resonance requires a fit to one T_1 relaxation time constant and diffusion coefficient for all reverse microemulsions studied. A single T_2 relaxation time constant is also required to fit the hydroxyl T_2 data for all microemulsions except the CTAB/pentanol/hexane/water reverse microemulsion. This microemulsion has two T_2 relaxation times for the hydroxyl proton resonance but, after 6 hours one time constant is obtained. This suggests the hydroxyl proton is distributed between two environments which merge to form one over a period of time, rather like the behaviour of CTAB in this microemulsion. Therefore, it is possible that water is associated with the CTAB in the RM interface and in the continuous phase. The diffusion coefficients and relaxation times for the hydroxyl proton environment in the CTAB/alcohol/hexane/water microemulsions are represented in Figure 4.9 as a function of alcohol chain length. The diffusion coefficient of the hydroxyl proton environment decreases as alcohol chain length increases but, the

CTAB/pentanol/hexane/water system initially has as larger diffusion coefficient that is much smaller

after 6 hours.
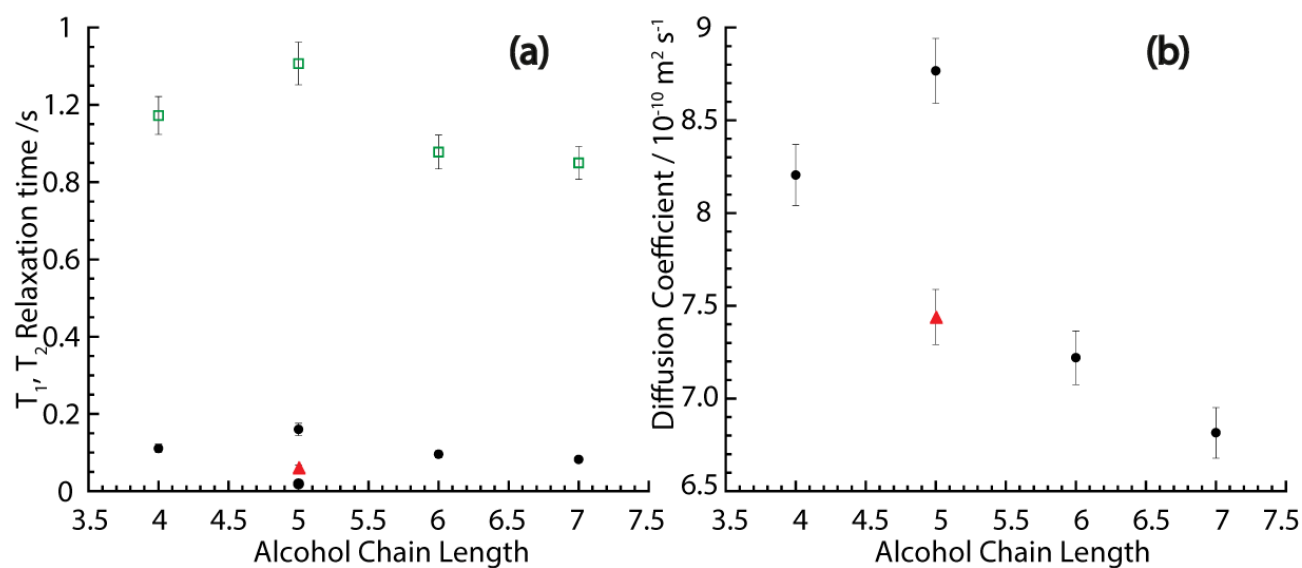
Figure 4.9: The T_1 and T_2 relaxation times (a) and diffusion coefficients (b) for hydroxyl proton environment in the CTAB/alcohol/hexane/water RMs as a function of increasing alcohol chain length represented as □ (T_1 relaxation), ● (initial T_2 relaxation/ diffusion coefficient) and ▲ (T_2 relaxation/diffusion coefficient after 6 hours).
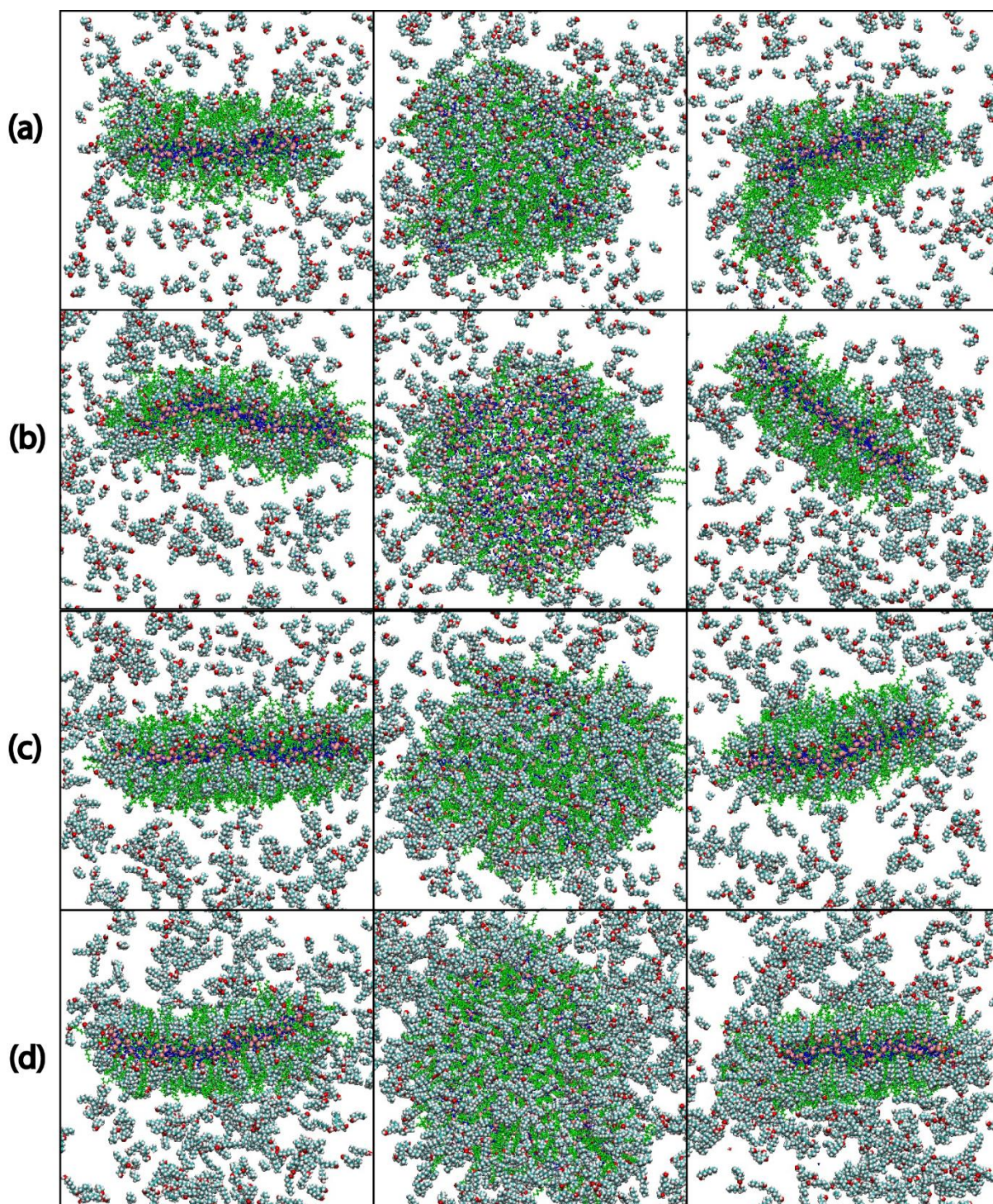
Figure 4.10: Molecular simulation snapshots of CTAB/*n*-hexane/n-alkanol/water reverse micelles for (a) butanol (18 ns), (b) pentanol (45 ns), (c) hexanol (18 ns) and (d) heptanol (18 ns), taken at the simulation times given in brackets. The hexane molecules have been removed and only the RM is displayed with CTAB molecules shown in green and water in blue. Each co-surfactant is coloured by atom, with white for hydrogen, blue for carbon and red for oxygen.

Snapshots of the molecular simulated CTAB/alcohol/hexane/water droplets, taken from three different angles can be found in Figure 4.10. The shapes of the RM simulated droplets were tracked over the simulation time by calculating the lengths of the three semi-axes (*a*, *b* and *c*) and the eccentricity, *e*, which can be found in Figure 4.11 and Figure 4.12. These show a clear deviation from the initial spherical geometry to an oblate structure. The proportion of alcohol co-surfactant in the RM interface was also determined over the course of the simulation, which was calculated by devising the number of alcohol molecules that were within 8 Å, the equilibrated interphase thickness, of any CTAB nitrogen atoms in the RM. A plot of the alcohol to CTAB ratio for all droplets during the simulation is given in Figure 4.13.
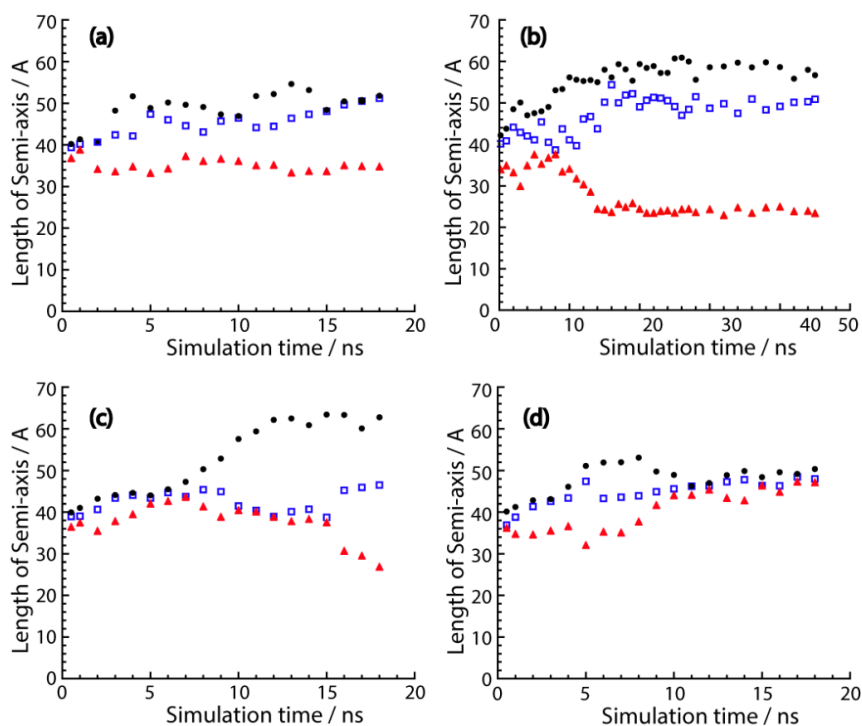
Figure 4.11: A plot of the lengths of the three semi-axes *a* (black circles), *b* (blue squares) and *c* (red triangles) in angstroms as a function of simulation time for the CTAB/*n*-hexane/n-alkanol/water reverse micelles (a) butanol, (b) pentanol, (c) hexanol, (d) heptanol
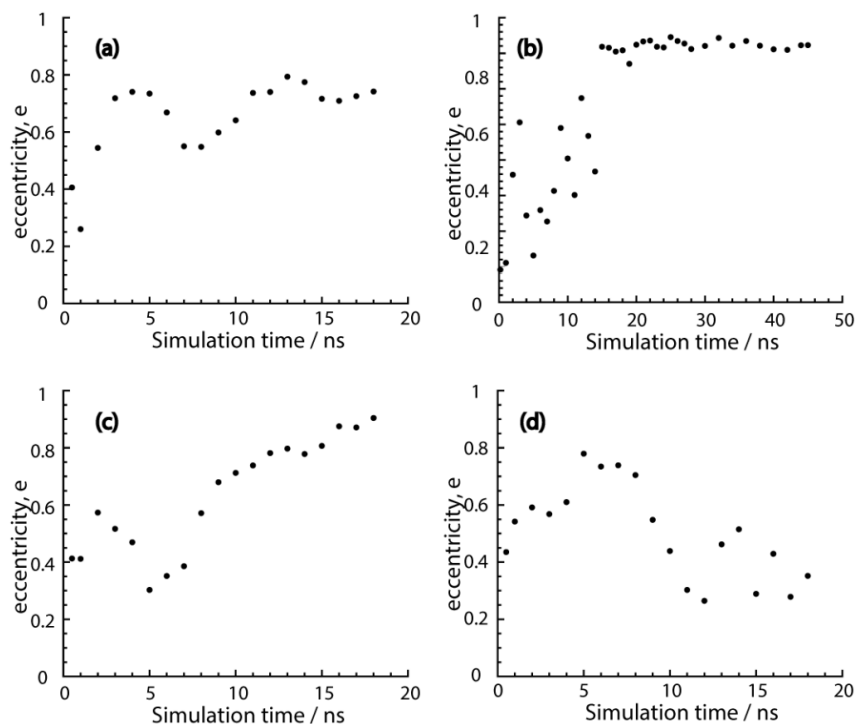
Figure 4.12: A plot of the eccentricity value, e, as a function of simulation time for each co-surfactant, (a) butanol, (b) pentanol, (c) hexanol, (d) heptanol.
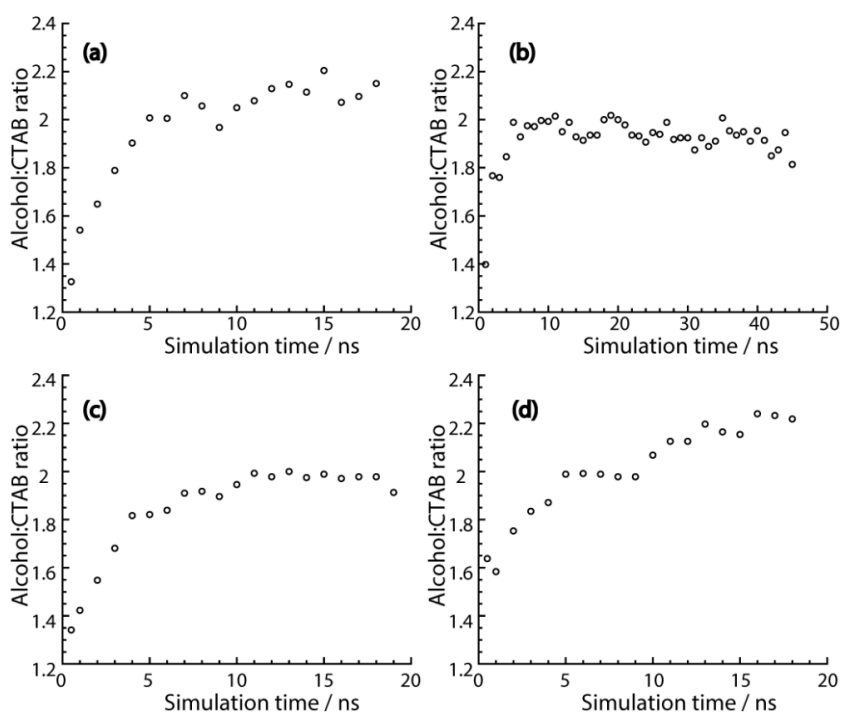
Figure 4.13: A plot of the alcohol to CTAB ratio in the interface of the simulated RM as a function of simulation time for the CTAB/*n*-hexane/n-alkanol/water reverse micelles (a) butanol, (b) pentanol, (c) hexanol, (d) heptanol

4.4 Discussion

The alcohol co-surfactant is distributed between the RM and the continuous phase, as evidenced by two T_2 relaxation times and diffusion coefficients. Alcohol residing in the RM will have a shorter T_2 relaxation time (T_2^{mic}) and small diffusion coefficient ($D_{\mathrm{CS}}^{\mathrm{mic}}$), and alcohol in the continuous phase will have a longer T_2 relaxation time (T_2^{bulk}) and larger diffusion coefficient ($D_{\mathrm{CS}}^{\mathrm{bulk}}$). At long observation times, a single value of diffusion coefficient for the co-surfactant, D_{obs}, is observed, which is a weighted average of the two environments and indicates exchange of the co-surfactant between the continuous phase and RM interface. These observations suggest molecular exchange of the co-surfactant between the two environments is on the millisecond timescale. However, the CTAB/butanol/hexane/water system has two T_2 relaxation times and only one diffusion coefficient at both short and long Δ for butanol. The T_2 relaxation times suggest butanol is distributed between the RM and the continuous phase but the presence of a single, averaged, diffusion coefficient suggests the exchange between these two environments is faster for butanol than for the other alcohols. Butanol is the smallest alcohol utilised in this study and hence the interface will be the least rigid,[9] due to the weaker van der Waals forces between the surfactant and alcohol.[1,38] These weaker van der Waals forces may lead to the alcohol's residing in the interphase for a shorter period, and hence increasing the exchange rate.

The exchange of co-surfactant between the RM interphase and the continuous phase increases the complexity of the systems and, as was discussed in chapter 3, determining the proportion of interfacial alcohol directly from diffusion data is difficult. The amount of interfacial alcohol can also be determined from the relative contributions from the two T_2 relaxation time constants or by calculating the P_{mic} value using the Lindman equation (chapter 3). The relative proportion of alcohol in the two environments from the T_2 relaxation and diffusion data can be found in Table 4.2. In all the microemulsions, except the initial CTAB/pentanol/hexane/water system, the

major T_2 component is associated with alcohol in the RM interphase, $T_2{}^{\text{mic}}$, with the proportion being

0.6 – 0.7. However, in the initial CTAB/pentanol/hexane/water system, alcohol in the continuous

phase, $T_2{}^{\text{bulk}}$, is the major component, with the proportion of alcohol in the RM being 0.4. However,

after 6 hours, the contribution from the short T_2 component increases to 0.6, a value comparable

with those observed for the other CTAB/alcohol/hexane/water systems. This difference in the

relative contributions of the T_2 components is believed to be associated with the distribution of the

surfactant. In the initial CTAB/pentanol/hexane/water microemulsion, CTAB is present in the

interphase and the continuous phase, with the major T_2 component associated with CTAB in the RM,

T_2^{mic}. The presence of CTAB in the continuous phase leads to the increased contribution of pentanol

in the continuous phase, T_2^{bulk}. After 6 hours, the CTAB environments combine so that all the

surfactant resides in the RM. This redistribution of surfactant molecules leads to a re-organisation of

co-surfactant molecules, increasing the contribution of alcohol in the RM, T_2^{mic}. This re-organisation

is less obvious in the diffusion data for the co-surfactant. The short observation time diffusion data

gives a proportion of alcohol in the RM as 0.03 – 0.07, for all microemulsions, including both the

initial and aged CTAB/pentanol/hexane/water microemulsion. This fraction is small compared with

the literature[32,39,40] and was suggested in chapter 3 to represent a small proportion of the co-

surfactants, except butanol, exchanging on the order of milliseconds.

The proportions of interfacial alcohol from the T_2 relaxation and diffusion data are

significantly different. This is due to the exchange of co-surfactant occurring on a similar timescale to

the T_2 relaxation and diffusion measurements, thus affecting the relative contributions of each time

constant. In addition to the different relative contributions, neither the amount of interfacial alcohol

from the T_2 relaxation time data nor the diffusion data match that of the calculated P_{mic} value in

Table 4.2. In calculating P_{mic}, the viscosity, η, and diffusion, $D_{\text{CS}}^{\text{bulk}}$, of alcohol in hexane, Figure 4.3

and Figure 4.5, respectively, was utilised to determine D_{bulk} used in the Lindman equation. However,

the pentane systems employed the relationship $D_{\text{bulk}}\eta = 6.4 \times 10^{-13}$ N and the viscosity data in Figure

4.4 (reproduced from Sastry et al.[36]) to obtain D_{bulk} and hence P_{mic}. The calculated P_{mic} for the

microemulsions are on the order of 0.3 – 0.4, which is consistent with the literature[32,39,40] and hence

is the best representation for the distribution of co-surfactant molecules in reverse microemulsions.

The P_{mic} values for all CTAB/alcohol/hexane/water microemulsions are represented in Figure 4.14

and show a general decrease in P_{mic} as alcohol chain length increases, with the exception of the

CTAB/pentanol/hexane/water system which has the largest P_{mic}. The amount of alcohol in the

interface was also determined from the molecular simulations by tracking the ratio of co-

surfactant:surfactant over time, Figure 4.13. The ratios, and hence the amounts of interfacial alcohol,

for all the droplets were comparable, ranging between 2 – 2.2.
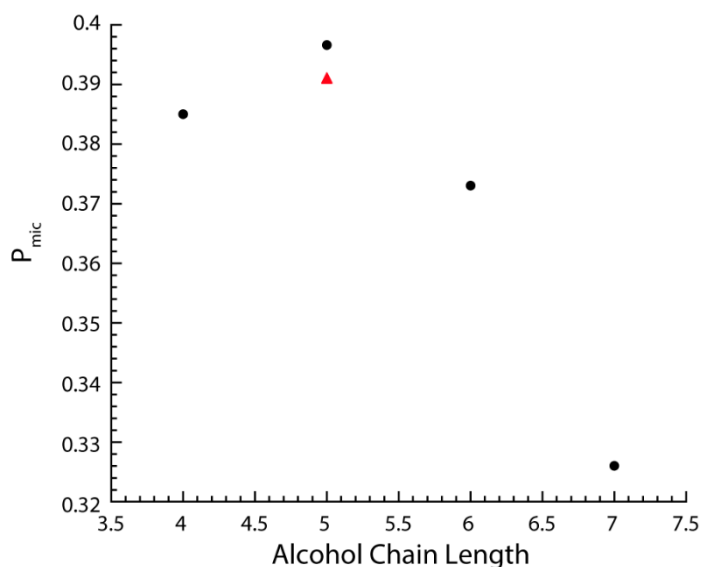
Figure 4.14: A plot to show the variation of P_{mic} with alcohol chain length in the hexane systems with ● representing the short mixing time and ▲ the long mixing time.

With the knowledge of P_{mic}, the corrected continuous phase viscosity, η, can be determined,

Table 4.3, which increases with increasing alcohol size. This increase in viscosity, along with the

increase in alcohol size, reduces the tumbling motion and explains the decrease in alcohol T_1, T_2^{bulk}

and D_{CS}^{bulk} in CTAB/alcohol/hexane/water microemulsions, as the alcohol chain length increases.[41]

The knowledge of the correct composition of the continuous phase, and hence the viscosity, allows accurate droplet sizes to be determined using the CTAB diffusion coefficient at short Δ, or smaller CTAB diffusion coefficient if two components are present, and the Stokes-Einstein equation (Equation 1.7). These hydrodynamic radii are listed in Table 4.3 and show a decreasing radius as the alcohol chain length increases. This trend was also observed in reverse microemulsions of CTAB/alcohol/chlorobenzene/water measurements performed by Zana et al.[8] The size of the RM droplet for the CTAB/pentanol/hexane/water system changes over a 6 hour period, the two CTAB environments described in chapter 3 combine to give a single CTAB environment which, as a consequence, produces larger droplets. This makes the RM droplets for the CTAB/pentanol/hexane/water microemulsion after 6 hours the largest of all the microemulsions studied.

The aged CTAB/pentanol/hexane/water system does not follow the trend of decreasing droplet radius as the alcohol chain length increases. The reasons for this were initially thought to be due to the formation of a more stable microemulsion, as a consequence of an ideal combination of the alcohol and oil chain lengths compared with the chain length of the surfactant molecules as suggested by Bansal et al.[7] They suggested that when this ideal combination was reached, the water solubilisation capacity is maximum. With this in mind, NMR measurements were performed on the CTAB/hexanol/pentane/water system, where the sum of the alcohol and oil chain lengths was identical to the CTAB/pentanol/hexane/water system. These measurements showed only RM droplets are formed, as evidenced by a single T_2 and D for CTAB, showing similar behaviour to the CTAB/alcohol/hexane/water microemulsions when the alcohol is not pentanol. This confirmed that the length of the alcohol and oil compared to the surfactant is not a factor leading to this unique behaviour of the CTAB/pentanol/hexane/water system. Relaxation and diffusion measurements were also performed on the CTAB/pentanol/pentane/water microemulsion, to investigate whether the behaviour observed in the CTAB/pentanol/hexane/water system was due to a unique property of

pentanol. The CTAB in the CTAB/pentanol/pentane/water RM has a single T_2 relaxation time and

diffusion coefficient, therefore all the CTAB is assumed to be associated in the RM interface. Thus,

these investigations of CTAB/pentanol/pentane/water RM did not provide any insight as to why the

CTAB/pentanol/hexane/water system behaves differently and hence the origin of this behaviour still

remains unclear.

While the size of the alcohol co-surfactant has a slight effect on the hydrodynamic radius of

the droplets, it is expected to affect the interface fluidity,[8,9,38] which consequently may affect the

shape of the RM droplets. The previous molecular simulations in chapter 3 showed the

CTAB/pentanol/hexane/water droplet deviates from spherical to an oblate structure. The same

analysis was carried out on the CTAB/alcohol/hexane/water molecular simulated RM droplets, where

the alcohol is butanol, hexanol and heptanol, to probe the shape of the droplets. The three semi-axes

(a, b and c) were calculated, using Equations 1.3, 1.4 and 1.5, and are plotted in Figure 4.11 as a

function of simulation time. From the quantities of the semi-axes, the eccentricity, e, can be

calculated using Equation 1.6, which gives a measure of the shape of the RM; when $e = 0$, a spherical

structure is present but when $e = 1$, an oblate or prolate structure is expected. A plot of the

eccentricity values as a function of simulation time can be found in Figure 4.12, and the values of

eccentricity at 18 ns are 0.72 (butanol), 0.91 (pentanol), 0.90 (hexanol), 0.35 (heptanol). These

values, combined with the snapshots in Figure 4.10, and the semi-axes values, Figure 4.11, show the

RM droplets have an oblate structure. The eccentricity value for the heptanol RM droplet suggests a

shape closer to spherical ($e = 0$) than disc- or rod-like ($e = 1$), however, inspection of the MD

snapshots in Figure 4.10, shows a clear disc-like structure. The heptanol RM droplet is bent which

affects the calculation of the semi-axes a, b and c by making one axis appear longer and hence the

droplet more spherical. The CTAB/pentanol/hexane/water molecular simulated droplet gives the

highest eccentricity value, showing the greatest deviation from spherical when compared with the

other droplets.

The eccentricity values, and hence the RM shape, appears to follow the same trend in RM size, where a maximum is observed for the CTAB/pentanol/hexane/water reverse microemulsion after 6 hours. It is possible that these variations in the shape could have an impact on the diffusion of these reverse micelles[42] or obstruction effects between them,[43] resulting in the diffusion and size variations observed. However, as the aspect ratio ($\lesssim 2$) and the droplet fraction ($\phi_d = 0.05$) of the RMs is low, this possibility may be a little surprising.

The peak in R_h and P_{mic} for the CTAB/pentanol/hexane/water RM provides a separation between the behaviour of short chain alcohols vs long chain alcohols. This separation of long and short chain alcohols is also demonstrated in the water solubilisation capacity as a function of alcohol chain length, Figure 4.1. Hou and Shah[9] reported the water solubilisation capacity changes as a function of alcohol chain length due to competing effects of the interface curvature, and the strength of the RM interactions. The water solubilisation capacity increases with decrease in attraction between droplets, and an increase in the interface curvature. As the chain length increases, there is a decrease in the RM attraction, and a decrease in the interface curvature. The larger droplet size of the CTAB/pentanol/hexane/water microemulsion after 6 hours, could be due to the maximum water solubilisation capacity residing at pentanol for the CTAB/alcohol/hexane/water systems, as pentanol is able to balance better the two competing interactions. A water solubilisation capacity peak at pentanol was observed by Zana et al.[8] for the CTAB/alcohol/chlorobenzene/water system.

This peak in water solubilisation capacity corresponds to the point at which a phase separation into two coexisting phases of spheres in the same continuous phase occurs.[9,16,17] These coexisting phases of spheres are thought to be the same size but present in high and low volume fraction.[16,17] The CTAB/pentanol/hexane/water microemulsion has a bimodal distribution of droplet sizes which, after 6 hours, becomes unimodal. Although the reason for the presence of two droplet sizes in the CTAB/pentanol/hexane/water microemulsion is unknown, it is possible it could be a

precursor to this phase separation since an actual phase separation was not observed. However, this is not clear and more work needs to be undertaken.

These investigations of the CTAB/alcohol/hexane/water, and CTAB/alcohol/pentane/water reverse microemulsions by NMR relaxation and diffusion measurements, indicate that the CTAB/pentanol/hexane/water system behaves differently, with an initial bimodal distribution of droplet sizes. The CTAB/pentanol/hexane/water reverse microemulsion is a commonly used system, and the different behaviour observed in this study may have important implications for those using it as a medium for nanoparticle synthesis or enzyme reactions. It could also go some way to explain the reason behind some of the anomalous behaviour previously observed[1,3] in the CTAB/pentanol/hexane/water reverse microemulsions.

4.5 Conclusion

NMR measurements of diffusion and relaxation have demonstrated the alcohol in CTAB/alcohol/hexane/water and CTAB/alcohol/pentane/water is distributed between the RM and the continuous phase, and exchanges between the two environments. This exchange is on the order of 10^{-3} s with the exception of CTAB/butanol/hexane/water microemulsion where the exchange is thought to be faster. All microemulsions, except the initial CTAB/pentanol/hexane/water microemulsion, exhibit unimodal droplet sizes, where the droplet size, R_h, decreases with increasing alcohol chain length. The initial CTAB/pentanol/hexane/water microemulsion has bimodal droplet sizes, for reasons that still remain unclear, which become unimodal after approximately 6 hours to produce the largest droplets of all the microemulsions studied. This larger droplet is believed to be due to the pentanol co-surfactant solubilising the most water, by balancing the opposing factors of interface rigidity and attraction between droplets which govern the water solubilisation capacity of RMs. Molecular modelling of the CTAB/n-hexane/alcohol/water microemulsions has shown the

shape of the droplet deviates from spherical to an oblate structure and the co-surfactant:surfactant

ratio in the RM is approximately equal for all simulated microemulsions.

The CTAB/pentanol/hexane/water RM exhibits different behaviour to the other RMs

investigated. This microemulsion is a commonly used reverse micelle[1,3,32,38,40] and therefore, its

unique behavior must be considered when employing this RM for these purposes such as reactors for

nanoparticle synthesis, enzymatic reactions and encapsulation of biomolecules. It may also give an

explanation as for the why this system gives more spherical monodispersed nanoparticles[1] and does

not affect the structure of enzymes solubilised within its core.[3] However, more work does needs to

be undertaken to understand fully why this microemulsion exhibits two droplet sizes and if it does

indeed possess a greater water solubilisation capacity as proposed in this chapter.

4.6 References

(1)   Chen, F. X.; Xu, G. Q.; Hor, T. S. A. *Mater. Lett.* **2003**, *57*, 3282.

(2)   Lin, J.; Zhou, W. L.; O'Connor, C. J. *Mater. Lett.* **2001**, *49*, 282.

(3)   Naoe, K.; Takeuchi, C.; Kawagoe, M.; Nagayama, K.; Imai, M. *J. Chromatogr. B* **2007**, *850*, 277.

(4)   Bansal, V. K.; Chinnaswamy, K.; Ramachandran, C.; Shah, D. O. *J. Colloid Interface Sci.* **1979**, *72*, 524.

(5)   Higuchi, W. I.; Misra, J. *J. Pharm. Sci.* **1962**, *51*, 455.

(6)   Sjoblom, E.; Friberg, S. *J. Colloid Interface Sci.* **1978**, *67*, 16.

(7)   Bansal, V. K.; Shah, D. O.; Oconnell, J. P. *J. Colloid Interface Sci.* **1980**, *75*, 462.

(8)   Lang, J.; Lalem, N.; Zana, R. *J. Phys. Chem.* **1991**, *95*, 9533.

(9)   Hou, M. J.; Shah, D. O. *Langmuir* **1987**, *3*, 1086.

(10)   Ezrahi, S.; Tuval, E.; Aserin, A.; Garti, N. *J. Colloid Interface Sci.* **2005**, *291*, 263.

(11)   Ezrahi, S.; Tuval, E.; Aserin, A.; Garti, N. *J. Colloid Interface Sci.* **2005**, *291*, 273.

(12)   Garti, N.; Aserin, A.; Ezrahi, S.; Wachtel, E. *J. Colloid Interface Sci.* **1995**, *169*, 428.

(13)   Mehta, S. K.; Kaur, G.; Mutneja, R.; Bhasin, K. K. *J. Colloid Interface Sci.* **2009**, *338*, 542.

(14)   Yaghmur, A.; Aserin, A.; Garti, N. *Colloid Surf. A-Physicochem. Eng. Asp.* **2002**, *209*, 71.

(15)   Zhang, X. G.; Chen, Y. J.; Liu, J. X.; Zhao, C. Z.; Zhang, H. J. *J. Phys. Chem. B* **2012**, *116*, 3723.

(16)   Huh, C. *J. Colloid Interface Sci.* **1984**, *97*, 201.

(17)   Safran, S. A.; Turkevich, L. A. *Phys. Rev. Lett.* **1983**, *50*, 1930.

(18)   Lemaire, B.; Bothorel, P.; Roux, D. *J. Phys. Chem.* **1983**, *87*, 1023.

(19)   De, T. K.; Maitra, A. *Adv. Colloid Interface Sci.* **1995**, *59*, 95.

(20)   Malik, M. A.; Wani, M. Y.; Hashim, M. A. *Arab. J. Chem.* **2012**, *5*, 397.

(21)   López-Quintela, M. A.; Tojo, C.; Blanco, M. C.; García Rio, L.; Leis, J. R. *Curr. Opin. Colloid Interface Sci.* **2004**, *9*, 264.

(22)   PerezCasas, S.; Castillo, R.; Costas, M. *J. Phys. Chem. B* **1997**, *101*, 7043.

(23)   Lin, T. L.; Hu, Y.; Lee, T. T. In *Trends in Colloid and Interface Science Xi*; Rosenholm, J. B., Lindman, B., Stenius, P., Eds.; Dr Dietrich Steinkopff Verlag: Berlin 33, 1997; Vol. 105, p 268.

(24)   Howe, A. M.; Toprakcioglu, C.; Dore, J. C.; Robinson, B. H. *J. Chem. Soc. Faraday Trans. I* **1986**, *82*, 2411.

(25)   Bardhan, S.; Kundu, K.; Saha, S. K.; Paul, B. K. *J. Colloid Interface Sci.* **2013**, *411*, 152.

(26)   Hong, D. P.; Kuboi, R. *Biochem. Eng. J.* **1999**, *4*, 23.

(27)   Jada, A.; Lang, J.; Zana, R. *J. Phys. Chem.* **1989**, *93*, 10.

(28)   Cazabat, A. M.; Langevin, D.; Meunier, J.; Pouchelon, A. *Adv. Colloid Interface Sci.* **1982**, *16*, 175.

(29)   Hamilton, R. T.; Billman, J. F.; Kaler, E. W. *Langmuir* **1990**, *6*, 1696.

(30)   Liu, D. J.; Ma, J. M.; Cheng, H. M.; Zhao, Z. G. *J. Dispersion Sci. Technol.* **1999**, *20*, 513.

(31)   Mills, A. J.; Wilkie, J.; Britton, M. M. *J. Phys. Chem. B* **2014**, *118*, 10767.

(32)   Palazzo, G.; Lopez, F.; Giustini, M.; Colafemmina, G.; Ceglie, A. *J. Phys. Chem. B* **2003**, *107*, 1924.

(33)   Callaghan, P. T. *Translational Dynamics & Magnetic Resonance: Principles of Pulsed Gradient Spin Echo NMR*; Oxford University Press: Oxford, 2011.

(34)   Claridge, T. D. W. *High-Resolution NMR Techniques in Organic Chemistry*; 2nd Edition ed.; Elsevier, 2009; Vol. 27.

(35)   Wu, D. H.; Chen, A. D.; Johnson, C. S. *J. Magn. Reson. Ser. A* **1995**, *115*, 260.

(36)   Sastry, N. V.; Valand, M. K. *J. Chem. Eng. Data* **1998**, *43*, 152.

(37)   Callaghan, P. T. *Principles of Nuclear Magnetic Resonance Microscopy*; Clarendon Press, 1993.

(38)   Uskokovic, V.; Drofenik, M. *Surf. Rev. Lett.* **2005**, *12*, 239.

(39)   Bisal, S.; Bhattacharya, P. K.; Moulik, S. P. *J. Phys. Chem.* **1990**, *94*, 350.

(40)   Giustini, M.; Murgia, S.; Palazzo, G. *Langmuir* **2004**, *20*, 7381.

(41)   Hore, P. J. *Nuclear Magnetic Resonance*; Oxford University Press, 1995.

(42)   Willis, S. A.; Dennis, G. R.; Zheng, G.; Price, W. S. *J. Mol. Liq.* **2010**, *156*, 45.

(43)   Jonstromer, M.; Jonsson, B.; Lindman, B. *J. Phys. Chem.* **1991**, *95*, 3293.

5. 2D T_2–T_2 Relaxation Exchange Spectroscopy (REXSY) of CTAB/pentanol/hexane/water Reverse Micelle System

5.1 Introduction

The previous chapters in this thesis have shown co-surfactant molecules exchange between the RM interface and continuous phase, through the use of NMR relaxation and diffusion measurements. Although exchange of co-surfactant has been identified, the exchange time has not yet been determined. NMR relaxation dispersion experiments and 2D relaxation exchange spectroscopy (REXSY) can be used to quantify exchange processes by probing the T_2 relaxation time. Relaxation dispersion experiments typically measure exchange processes on the order of micro- to milli- second and are typically employed to investigate dynamic processes in supramolecular systems and have been used in protein folding,[1,2] ligand binding,[2,3] and enzyme catalysis.[4-6] Alternatively, REXSY measurements have been applied to less dynamic systems (exchange on the order of millisecond to seconds[7]), which generally consist of porous solid materials, to investigate behaviour in rocks,[8,9] cement pastes[10,11] and packed beds made of borosilicate and soda lime glass spheres.[8,12] Although REXSY measurements are generally employed in solid porous materials, some measurements have been performed on supramolecular systems such as urea in water,[13,14] multilamellar vesicles[15] and liquid crystals.[16] However, these supramolecular systems investigated by REXSY measurements are less dynamic than the supramolecular systems studied using relaxation dispersion experiments.
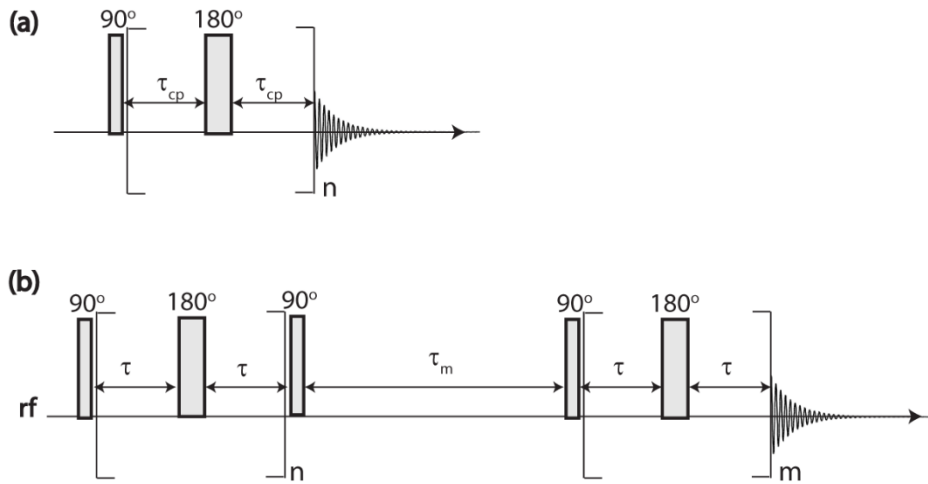
Figure 5.1: The two pulse sequences that can be used to measure exchange where (a) is the CPMG Relaxation dispersion experiment where τ_{cp} is varied and (b) the REXSY sequence where τ_m is varied.

Relaxation dispersion (Figure 5.1a) and REXSY (Figure 5.1b) experiments both utilize the Carr-Purcell-Meiboom-Gill[17,18] (CPMG) sequence typically used to measure the T_2 relaxation time. Relaxation dispersion experiments involve performing numerous CPMG experiments, where the 180° refocusing pulse separation, τ_{cp}, is varied. During this τ_{cp} time delay, exchange can occur and hence the resultant T_2 relaxation time is affected.[19,20] At longer τ_{cp} values, more exchange can occur which leads to increased averaging of the T_2 environments involved in the exchange process. Therefore, T_2 relaxation time is measured as a function of the 180° refocusing pulse separation, τ_{cp}, and is fitted to appropriate models[21-24] to obtain the exchange rate. The most widely used model for fast exchange,[20,24,25] involves plotting $1/T_2$ as a function of τ_{cp} and fitting the decay to Equation 5.1.

$$\frac{1}{T_2} = R_2\left(\frac{1}{\tau_{cp}}\right) = R_2^0 + \frac{\phi_{ex}}{k_{ex}}\left(1 - \frac{2\mathrm{tanh}\left[k_{ex}\tau_{cp}/2\right]}{k_{ex}\tau_{cp}}\right) \qquad \text{Equation 5.1}$$

where R_2^0 is the relaxation in the absence of exchange, k_{ex} is the chemical exchange rate constant and $\phi_{ex} = p_A p_B \Delta\omega^2$ with p_A and p_B representing the populations of the two sites A and B,

respectively, and $\Delta\omega$ is the difference between the chemical shift of sites A and B. Other models have been suggested for the slower exchange limit.[19,21]

Relaxation dispersion has been used to measure the exchange of the complexed inhibitor-enzyme complex tubercidin-*Escherchia coli* purine nucleoside phosphorylase to their respective uncomplexed monomers by Davies et al.[26] They determined the dissociation rate constant from complexed to uncomplexed to be 2400 s^{-1} and 900 s^{-1} at 20°C and 10°C, respectively. This confirmed their previous assumption that the dissociation rate was fast, giving exchange times of 0.4 ms and 1 ms, respectively. Determination of the dissociation rate has facilitated the determination of more accurate cross-relaxation rates in the complex. Relaxation dispersion experiments have also found a use in characterising millisecond conformational exchange processes in biomolecules.[27] The conformational fluctuations of biological molecules influence the kinetics and thermodynamics of the processes these biomolecules[28] are involved in and hence characterisation of these fluctuations is vital. Vallurupalli et al.[27] have presented a glycine specific relaxation dispersion experiment to measure the conformational exchange process of a mutant of T4 lysozyme, which facilitates the binding of ligands to an internal cavity in the protein. They determine the conformational exchange process in this protein to be in the millisecond timescale. Relaxation dispersion experiments have widespread use in protein dynamics[1,2] and are typically utilised in dynamic solution state systems.

In less dynamic systems, REXSY measurements are utilised to quantify exchange. REXSY measurements incorporate the 1D CPMG pulse sequence into a 2D NMR experiment to enable the measurement of exchange. 2D NMR methods are able to extract more information on a system of interest than the corresponding 1D NMR counterparts.[12] A 1D NMR spectrum plots intensity against frequency (usually chemical shift), whereas in 2D NMR, intensity is plotted against two frequency axes. The most common 2D NMR techniques include correlation spectroscopy (COSY) and nuclear Overhauser effect spectroscopy (NOESY) which identify the chemical shift of the spins that are

coupled via scalar or dipolar coupling.[29,30] Incorporating NMR relaxation and diffusion measurements into these 2D NMR experiments enable correlation of T_1, T_2 relaxation times or diffusion coefficient rather than chemical shift.[7,9-12]

The 2D REXSY experiment has the general format of the basic 2D NMR sequence[30] but with two additional weighting blocks to encode for T_2 relaxation,[31] Figure 5.2. The REXSY sequence involves combining two CPMG experiments separated by a mixing time (τ_m), where exchange takes place[9,11] (Figure 5.1b). This enables the T_2 relaxation time to be measured at two different times,[32] before, (the vertical axis), and after (the horizontal axis) the mixing time, rather than the single time point measured using a 1D CPMG experiment. If exchange occurs during τ_m, the spins exchange to a different environment and hence possess different T_2 relaxation times before and after τ_m. During τ_m the magnetisation is held in the longitudinal plane and hence is subjected to T_1 relaxation, therefore τ_m must be smaller than T_1 to avoid significant signal loss due to relaxation,[9,11] but long enough to observe the exchange process.[8] REXSY measurements are able to probe exchange between two or more regions of different T_2 relaxation times,[8,9] provided that the ratio $T_1/T_2 > 1$ and an appropriate mixing time, τ_m, is utilized.[8,11,33,34] REXSY measurements produce a 2D spectrum where the intensity probability distribution is plotted against T_2 relaxation time before and after the mixing time, Figure 5.3. It is this 2D spectrum, known as $\log_{10}(T_2)-\log_{10}(T_2)$ distribution matrix, that enables the determination of exchange.
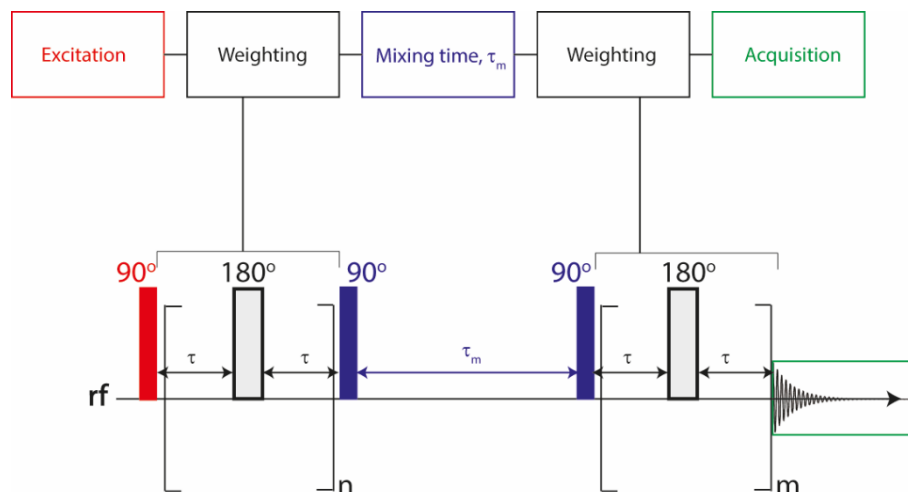
Figure 5.2: The general format of a 2D relaxation/diffusion NMR experiment, with a T_2–T_2 relaxation exchange spectroscopy (REXSY) used as an example below.
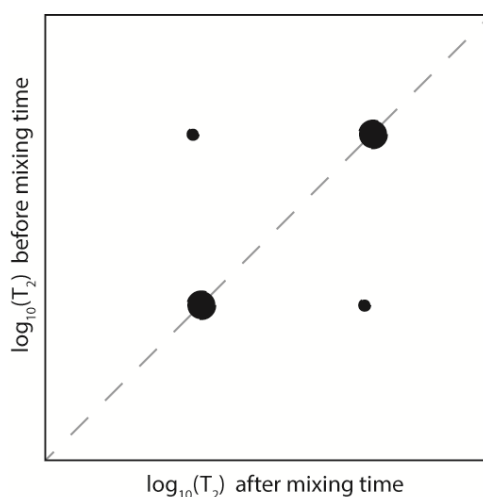
Figure 5.3: A schematic of the 2D spectrum known as the $\log_{10}(T_2)$–$\log_{10}(T_2)$ distribution matrix produced from the REXSY measurements that enable the determination of exchange.

To obtain this 2D spectrum, the T_2 relaxation decays need to be converted into an intensity distribution of T_2 relaxation times.[7,9,35] Exchange occurs as a consequence of spins moving between at least two different environments and hence at least two T_2 relaxation times are obtained for a particular exchanging spin in a REXSY experiment. Therefore, the relaxation decays from REXSY measurements will be multi-exponential, which can be converted into well-defined T_2 relaxation probability distributions[7,9,35] using the inverse Laplace transform (ILT).[9,36] The general procedure of

the 1D ILT involves applying a non-negative least squared algorithm,[7,36-38] which makes the problem ill-posed in the sense that a small amount of noise in the data can cause large changes in the resultant spectrum.[39] This ill-posed nature is a result of noise treated as part of the relaxation decay, and therefore the noise needs to be limited. To minimise this ill-posed nature, a regularisation procedure[7,35,40] is applied which provides a cut-off point to avoid fitting to the noise.[41] The regularization parameter, α, measures the smoothness in the resultant distribution function and its optimum value must be chosen to avoid bias.[35] If α is too large, fitting to noise becomes an issue and when α is too small the inversion reduces to a conventional least-squares fitting, therefore the resultant distribution function likely exhibits sharp features that are unstable,[35,42] and not reproducible. In addition to the optimal choice of α, conditions concerning the relaxation decay data and the noise have to be met or assumed. The relaxation decay data have to be non-negative and the resultant distribution of relaxation times has to be smooth. The noise has to be additive, zero mean and Gaussian,[35] i.e. the noise has random fluctuations in intensity around zero and is added to the relaxation decay signal.

Due to the ill-posed nature of the 1D ILT, application of a 2D ILT must be approached with caution.[7] The difficulty with performing a 2D ILT has had significant effects on the development of these 2D exchange experiments.[35] In 2002, a 2D ILT algorithm that can easily be carried out on an ordinary desktop computer[11,35,36,43] was developed, which led to an increased use of 2D relaxation/diffusion experiments. This 2D ILT algorithm uses single value decomposition (SVD) to compress the 2D data matrix to a more manageable size.[7,15,35] The 2D matrix is rearranged into a 1D format by consecutive ordering of the matrix rows or columns, so in effect the problem is converted back into a 1D ILT format.[7]

After applying the 2D ILT to REXSY data, the 2D $\log_{10}(T_2)-\log_{10}(T_2)$ distribution matrix is produced, a typical distribution matrix for a two site exchange process $A \leftrightharpoons B$ is shown in Figure 5.4.

In the absence of exchange, all the signal will be on the diagonal as the T_2 relaxation time is identical before and after τ_m, Figure 5.4a. However, if τ_m is sufficiently long, spins can exchange to an environment of different T_2 relaxation leading to the appearance of off-diagonal, or exchange peaks, Figure 5.4b.[9,12]
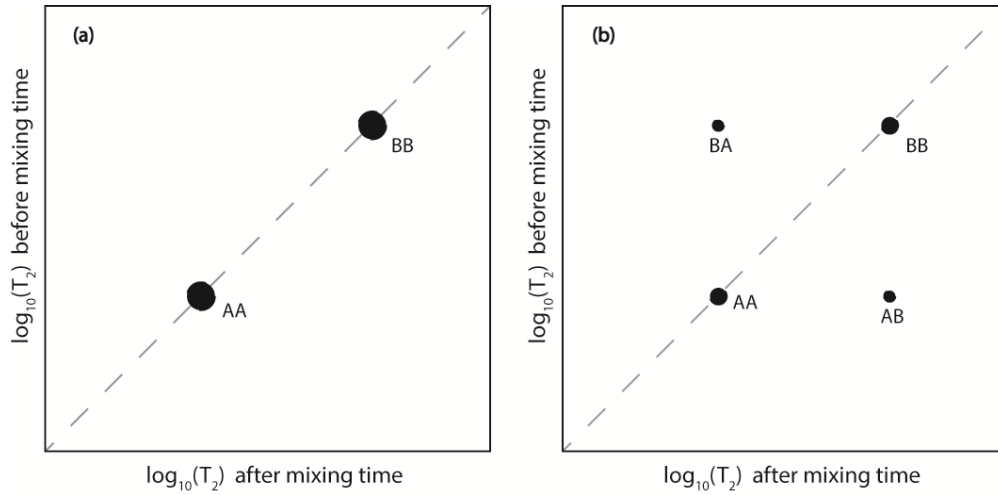
Figure 5.4: A schematic representing a typical $\log_{10}(T_2)$–$\log_{10}(T_2)$ distribution matrix for two-site exchange process $A \leftrightarrows B$, with (a) at short mixing time and (b) at long mixing time.

These exchange peaks for a two-site exchange process are often symmetric;[11] however, they will not necessarily have equal intensity,[9] due to T_1 relaxation during τ_m. For exchange peaks to be symmetrical, all the exchange processes have to be identical.[44] This is often achieved in two-site exchange processes when the equilibrium populations of the two sites are equal. If the exchange process involves three or more sites, the exchange peak will no longer be symmetrical due to the wide range of exchange rates often observed in these systems.[44]

Washburn and Callaghan[9] utilised REXSY to explore the exchange processes in a sample of porous sandstone and water. In this publication, they repeated the REXSY experiment for multiple mixing times, τ_m, and monitored the signal intensity of each exchange peak,[9] $S_{(ex)}$, which grew exponentially[9] with τ_m. They developed two equations to determine the exchange rates of a two site

exchange process ($A \rightleftharpoons B$) from the two exchange peak intensities (*AB* and *BA*). Fitting the *AB* exchange peak to Equation 5.2 will yield the exchange rate, $\tau_{\text{ex}}^{\text{AB}}$.

$$N_{\text{AB}}(t) = \frac{N_{\text{B}}\tau_{\text{AB}}}{\tau_{\text{AB}} + \tau_{\text{BA}}}\left[1 - \exp^{(-\lambda^{AB}\tau_m)}\right]$$
<div align="right">Equation 5.2</div>

where N_{AB} is the number of molecules starting in *A* and residing in *B* after τ_{m}, N_{B} is the equilibrium occupancy of *B*, τ_{AB} and τ_{BA}, respectively, are the rates at which molecules in *A* migrate to *B* and vice versa, $\lambda^{AB} = \tau_{AB}^{-1} + \tau_{BA}^{-1}$ and $\lambda^{AB^{-1}} = \tau_{\text{ex}}^{\text{AB}}$. The corresponding *BA* exchange peak grows in accordance to Equation 5.3

$$N_{\text{BA}}(t) = \frac{N_{\text{A}}\tau_{\text{BA}}}{\tau_{\text{AB}} + \tau_{\text{BA}}}\left[1 - \exp^{(-\lambda^{BA}\tau_m)}\right]$$
<div align="right">Equation 5.3</div>

Where N_{BA} is the number of molecules starting in *B* and residing in *A* after τ_{m}, N_A is the equilibrium occupancy of *A*, $\lambda^{BA^{-1}} = \tau_{\text{ex}}^{\text{BA}}$ and $\lambda^{BA} = \tau_{AB}^{-1} + \tau_{BA}^{-1}$. Using these equations they devised, Washburn and Callaghan were able to determine exchange rates of water ranging between 27 and 93 ms in the water/sandstone sample.

The intensity of the exchange peaks will eventually reach an equilibrium value, which corresponds to all the spins experiencing all environments,[12] due to averaging of the T_2 relaxation times at longer mixing times, τ_{m}. When $\tau_{\text{m}} \geq T_1$, the exchange peak intensity begins to decrease with increasing τ_{m} due to signal loss in the form of T_1 relaxation.[32] In reality, each $\log_{10}(T_2)$–$\log_{10}(T_2)$ distribution matrix will vary in intensity as a result of experimental variations; therefore it is better to utilise the ratio of exchange peak intensity to total peak intensity,[15] $S_{(ex)}/S_{(T)}$, rather than just $S_{(ex)}$ in determining the exchange rate.

At the same time as the work by Washburn and Callaghan on developing the REXSY sequence, Monteilhet et al.[11] were also working on its development. They utilised the REXSY sequence to monitor the exchange processes in water and cement mixtures, and developed the diffusive exchange model proposed by Hills et al.[45] from a 1D model to a 2D model. They used this model to estimate the exchange of water between pores of different sizes, by measuring the intensity of the well-defined exchange peaks as a function of τ_m. These measurements provided vital information on the water dynamics within the cement nanopore, and enabled the first estimation of the water exchange rate between these pores. Water exchange has also been monitored by Mitchell et al.[12] by performing 2D REXSY measurements of water in a packed bed of alternate layers of borosilicate and soda lime glass spheres. Water in contact with these two different surfaces possesses different T_2 relaxation times and hence provides an ideal separation of the two water environments to quantify exchange using REXSY. Clear exchange peaks were observed at mixing times greater than 1 s which provided an exchange time of 26 s. This exchange time is rather long due to the distance the water molecules have to travel to experience spheres of different material.

While REXSY has been utilised in solid porous materials, some measurements have been performed using supramolecular liquid samples. Griffith et al.[15] were able to measure the exchange of water in multi-lamellar vesicles consisting of linear alkylbenzene sulfonate surfactant molecules in an aqueous solution saturated with sodium sulfate with a small quantity of polymer. In multi-lamellar vesicles the surfactant molecules aggregate in aqueous solution, like micelles, to form a droplet that consists of multiple surfactant layers instead of a monolayer. In this study, they were able to identify two separate water environments, water between the surfactant layers and bulk 'free' water. Using REXSY they were able to determine two distinct exchange times of 40 ms and 830 ms. These vesicle systems are similar to reverse micelles studied in this thesis; however, vesicle systems are generally less dynamic and more stable than reverse micelles.[46-48]

In this work, the pentanol co-surfactant exchange rate in the CTAB/pentanol/hexane/water reverse micellar system is quantified, which in chapter 3, was estimated to be in the millisecond timescale. These reverse micelle systems have been reported to be extremely dynamic systems which consist of large surfactant aggregates in solution, making them similar to the supramolecular systems studied by relaxation dispersion experiments. For this reason, along with the expected millisecond exchange rate, the natural choice of experiment for quantifying pentanol exchange rate is relaxation dispersion. Relaxation dispersion experiments are able to measure easily the exchange rate and equilibrium populations of the exchanging sites.[49] The major advantage of relaxation dispersion experiments compared with REXSY experiments is the ability to reach dynamics on a micro-second timescale.[49] Relaxation dispersion experiments are also advantageous due to the 1D nature of the experiment, which allows data to be acquired relatively quickly and hence limit any time-dependent changes in the system. The 2D nature of the REXSY experiment, requires lengthy data acquisition and hence increases the experimental time.[13]

Although there are numerous advantages to the use of relaxation dispersion experiments to investigate the CTAB/pentanol/hexane/water reverse microemulsion, there are some difficulties. These CPMG relaxation dispersion experiments are sensitive to modulation of the echo trains of J-coupled spins during τ_{cp} resulting in phase artefacts.[26,49,50] Multiplet peaks with J-coupling cannot be measured using CPMG relaxation dispersion experiments, due to significant peak distortions, and hence only singlet peaks can be selected. This makes determining the exchange rates of J-coupled spins challenging due to difficulties in supressing these J modulations.[49] The J modulation artefacts become more severe in the slow pulsing limit, as τ_{cp} increases;[26] therefore τ_{cp} must be as short as possible when investigating J-coupled spins. This is a major issue for measuring exchange of pentanol in the CTAB/pentanol/hexane/water system as the only singlet resonance of the alcohol is from the hydroxyl protons. The alcohol hydroxyl proton is in exchange with water in the core of the RM,[51] and hence this resonance is a combination of alcohol hydroxyl and water. The presence of this additional

proton exchange process associated with the hydroxyl resonance, severely impedes the determination of the alcohol molecular exchange between the RM and the continuous phase from this singlet resonance. Therefore, CPMG relaxation dispersion experiments are not suitable for quantification of co-surfactant exchange in this particular system.

REXSY measurements do not have any issues associated with J-coupled spins, which makes it an advantageous method over relaxation dispersion for this particular CTAB/pentanol/hexane/water reverse microemulsion. The lack of J-modulation issues enables exchange to be determined using the pentanol CH_2 proton in the α position from the hydroxyl (H_g proton), and hence eliminating the extra hydroxyl exchange process. To enable exchange measurements to be performed using REXSY, there are some specific requirements of the system that need to be fulfilled. It is imperative that there is exchange between two regions of distinctly different T_2 relaxation times.[8] This requirement is satisfied in this system as the pentanol exchanges between the RM interface and continuous phase, where two separate T_2 relaxation times have been determined, chapter 3. If the exchange is too quick, only one averaged T_2 relaxation environment is obtained and hence the appearance of exchange peaks is not possible.[8] An additional criterion for the appearance of exchange peaks is that the T_1 relaxation time is greater than the T_2 relaxation time,[8,33] $T_1/T_2 > 1$. Again, this is not an issue for the CTAB/pentanol/hexane/water system as the T_1 values are relatively long, chapter 3.

While the CTAB/pentanol/hexane/water system seems to fulfil the requirements for the appearance of exchange peaks, REXSY measurements are typically utilised in less dynamic solid porous materials. It is widely thought that the exchange of co-surfactant in RMs is fast[52] ($<10^{-4}$ s) but the investigations in chapter 3 and 4 suggest otherwise, where the exchange was estimated to be on the millisecond timescale. REXSY can measure dynamics on the timescale of milliseconds to seconds[32] and therefore it seems that performing REXSY measurements on this system may prove

fruitful. In this chapter, we provide the first quantification of co-surfactant exchange in a dynamic reverse micelle system using REXSY.

5.2 Experimental

Sample Preparation.

The CTAB/pentanol/hexane/water reverse microemulsion was prepared using the same method, materials and quantities described in chapter 3. This produced a water/CTAB molar ratio, ω_0, of 6.9, a pentanol/CTAB molar ratio, P_0, of 8.2 and a volume fraction, ϕ, of 0.05.

NMR Measurements

NMR experiments were performed on the same spectrometer and experimental setup as described in chapter 3.

One-dimensional spin-spin (T_2) relaxation measurements were acquired using ^{1}H NMR Carr Purcell Meiboom Gill (CPMG) experiments, $[90 - (\tau - 180 - \tau)_m - acq]_a$ at 298 $\pm$ 0.3 K. Individual relaxation times were obtained for CTAB and pentanol by integrating the CTAB H_a proton resonance or the pentanol H_g proton resonance, (proton labelling can be found in chapter 3) by fitting the relaxation decay to Equation 2.8. A relaxation decay was also obtained by combining the signal of all the proton resonances to give the relaxation times for all the components of the system, CTAB, water, pentanol and hexane. A repetition time of 15 s was used to collect four signal averages, a, with 16 echoes, m, varied from 0 to 1024 with a delay of $\tau = 2$ ms. Each 1D T_2 relaxation experiment took 16 minutes to complete.

Two-dimensional T_2–T_2 relaxation exchange spectroscopy (REXSY) experiments consists of two CPMG trains separated by a mixing time, τ_m, Figure 5.1b.[9] Each CPMG train consisted of 16

echoes, *n* and *m*, both varied from 0 to 1024 logarithmically, with a delay of τ = 2 ms. A repetition

time of 15 s and 16 signal averages was used to acquire data at 11 mixing times ranging from 1 ms to

50 ms. These REXSY measurements (for each τ_m) took a total of 18 hours to complete. Individual data

were collected for CTAB and pentanol by integrating the CTAB H_a and pentanol H_g proton resonances

to produce two 2D 16 x 16 matrices of relaxation decay before and after τ_m, Figure 5.5, for CTAB and

pentanol. In addition, data were collected from all the proton resonances at once producing a 2D 16

x 16 relaxation decay before and after τ_m for all the RM components, CTAB, water, pentanol and

hexane. These 2D relaxation decay matrices are converted into 2D $\log_{10}(T_2)$–$\log_{10}(T_2)$ distribution

matrices by using a 2D inverse Laplace transform.[7,35,36] The 2D ILT uses a regularisation parameter, α,

which was chosen in accordance with Fordham.[40] This involves repeating the fitting procedure for

different values of α and measuring χ^2, where χ is the fit error, as a function of α.[35,40,53] The optimum

value of α corresponds to the lowest value of α before χ^2 rises rapidly, Figure 5.6.
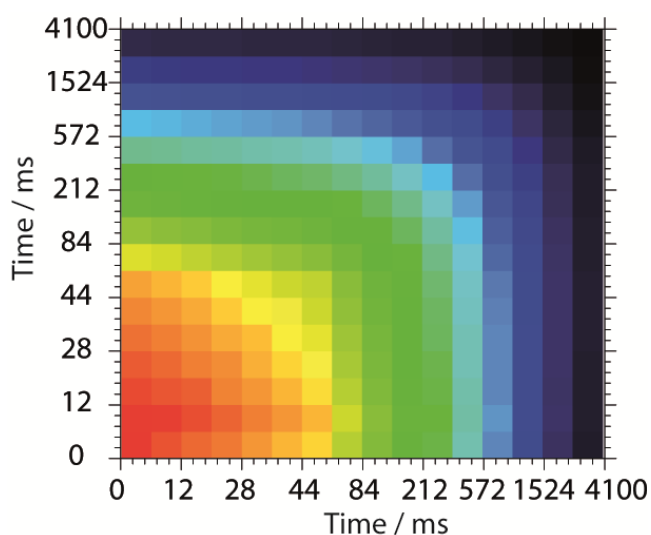
Figure 5.5: A 2D T_2 relaxation decay matrix that is converted into 2D $\log_{10}(T_2)$–$\log_{10}(T_2)$ distribution matrix by the 2D inverse Laplace transform.
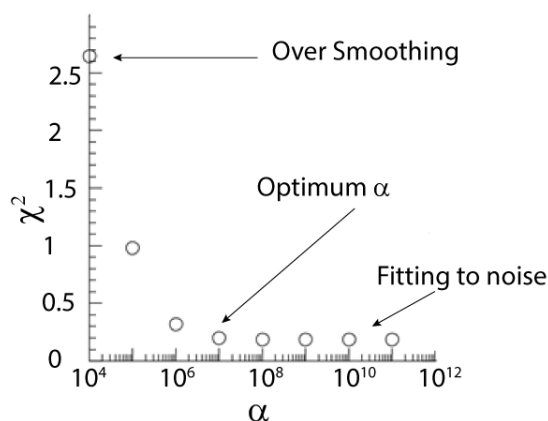
Figure 5.6: A schematic to show the optimum choice in α as a function of χ^2. This plot is produced by repeating the fitting procedure for different α and measuring χ^2, the error fit. The optimum value of α is chosen just before χ^2 begins to rise rapidly.

5.3 Theory

In this section the basic theory provided by Washburn and Callaghan[9] for determining the exchange rate will be developed with respect to the two-site exchange process in the CTAB/pentanol/hexane/water reverse micelle system. The same basic principles are applied to develop two equations for the rate of appearance of each exchange peak. The overall reaction for the exchange of molecules between the RM interface (A) and the bulk continuous phase (B) is expressed in Figure 5.7. The two environments have two distinct T_2 relaxation times, T_2^{RM} and T_2^{bulk}, which enables the appearance of exchange peaks to facilitate the exchange rate determination.
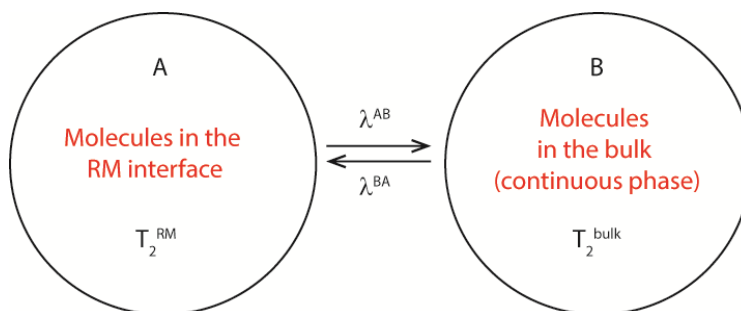
Figure 5.7: A schematic for the exchange of pentanol and/or CTAB between the RM interphase (A) and the continuous phase (B). The relaxation times in each pool, T_2^{RM} and T_2^{bulk}, are defined. The exchange is each direction is defined by λ^{AB} and λ^{BA}.

The exchange rates, λ^{AB} and λ^{BA}, are calculated by measuring the intensity of the exchange peaks as a function of time. In order to do this the reaction, $A \leftrightarrows B$, is treated as a set of two independent two-site exchanges for simplicity,[9] shown in Figure 5.8, where A is the RM interface and B is the bulk.
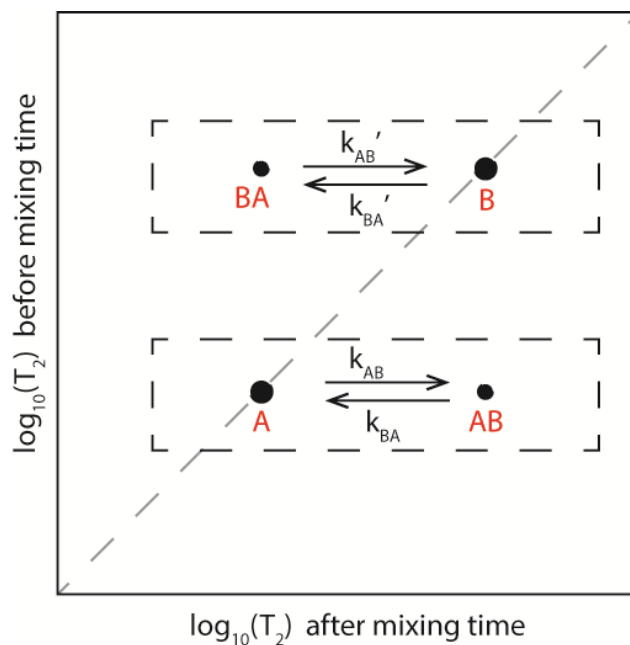
Figure 5.8: A schematic representation of the $\log_{10}(T_2)$–$\log_{10}(T_2)$ distribution matrix for the reaction $A \rightleftharpoons B$, showing the two independent two-site exchange processes for the appearance of exchange peaks.

The exchange of molecules from the RM to the bulk, Equation 5.4, is represented by the AB exchange peak. The rate of appearance of the AB exchange peak as a function of time is written by the rate equation in Equation 5.5, where N_{AA} is the number of molecules that start in the RM (A) and remain there after time, t, and N_{AB} is the number of molecules that have exchanged from the RM interface (A) to the bulk (B) during time, t.

$$A \underset{k_{BA}}{\overset{k_{AB}}{\rightleftharpoons}} AB \qquad \text{Equation 5.4}$$

$$\frac{\mathrm{d}N_{AB}}{\mathrm{dt}} = k_{\mathrm{AB}}N_{AA} - k_{\mathrm{BA}}N_{AB} \qquad\qquad \text{Equation 5.5}$$

At $t = 0$, there are no molecules that have exchanged hence $N_{AB} = 0$. Therefore, at time t, the number of molecules that started in the RM (A) and remain there, N_{AA}, can be expressed by Equation 5.3, where N_A is the number of molecules in the RM (A) at time $t = 0$.

$$N_{AA} = N_A - N_{AB} \qquad\qquad \text{Equation 5.6}$$

Substituting Equation 5.6 into Equation 5.5 produces:

$$\frac{\mathrm{d}N_{AB}}{\mathrm{dt}} = k_{\mathrm{AB}}N_A - N_{AB}(k_{\mathrm{AB}} + k_{\mathrm{BA}}) \qquad\qquad \text{Equation 5.7}$$

Integrating this equation results in the first order rate equation in Equation 5.8, where $\lambda^{\mathrm{AB}} = k_{\mathrm{BA}} + k_{\mathrm{AB}}$ and $\frac{1}{\lambda^{\mathrm{AB}}} = \tau_{\mathrm{ex}}^{\mathrm{AB}}$. The steps of this integration process can be found in Appendix 4.

$$N_{AB} = \frac{k_{\mathrm{AB}}N_A}{\lambda^{\mathrm{AB}}}\left(1 - \mathrm{e}^{-\lambda^{\mathrm{AB}}\mathrm{t}}\right) \qquad\qquad \text{Equation 5.8}$$

This relation is equivalent to the relation given by Washburn et al.[9] in Equation 5.2. Washburn et al.[9] have expressed this equation in terms of lifetimes, τ, rather than rate constants, k. They have also expressed N_{AB} in terms of the initial number of molecules in the bulk, N_B, rather than the RM interface, N_A. This was performed by using an additional relationship between N_A and N_B which was not reported.

The same procedure can be applied to the second exchange peak BA by applying the reaction stated in Equation 5.9, to obtain λ^{BA}, see Appendix 5 for full integration steps. The rate of appearance of BA exchange peak as a function of time is defined by the rate equation in Equation

5.10, where N_{BA} is the number of molecules that start in the bulk (B) and exchange to the RM (A) during time, t, and N_{BB} is the number of molecule that start and remain in the bulk (B) after time, t.

$$B \underset{k_{\mathrm{AB}}'}{\overset{k_{\mathrm{BA}}'}{\rightleftharpoons}} BA \qquad \text{Equation 5.9}$$

$$\frac{\mathrm{d}N_{BA}}{\mathrm{dt}} = k_{\mathrm{BA}}'N_{BB} - k_{\mathrm{AB}}'N_{BA} \qquad \text{Equation 5.10}$$

By following the same procedure outlined for the *AB* exchange peak, Equation 5.10 can be re-witten as Equation 5.11, where N_B is the number of molecules in the bulk (B) at time $t = 0$.

$$\frac{\mathrm{d}N_{BA}}{\mathrm{dt}} = k_{\mathrm{BA}}'N_B - N_{BA}(k_{\mathrm{AB}}' + k_{\mathrm{BA}}') \qquad \text{Equation 5.11}$$

Integrating Equation 5.11 gives the first order rate equation for the *BA* exchange peak, Equation 5.12, where $\lambda^{\mathrm{BA}} = k_{\mathrm{AB}}' + k_{\mathrm{BA}}'$ and $\frac{1}{\lambda^{\mathrm{BA}}} = \tau_{\mathrm{ex}}^{\mathrm{BA}}$.

$$N_{BA} = \frac{k_{\mathrm{BA}}'N_B}{\lambda^{\mathrm{BA}}}\left(1 - \mathrm{e}^{-\lambda^{\mathrm{BA}}\mathrm{t}}\right) \qquad \text{Equation 5.12}$$

5.4 Results and Disscussion

A series of 2D REXSY contour $\log_{10}(T_2)$–$\log_{10}(T_2)$ distribution matrices are presented in Figure 5.9 for the pentanol co-surfactant in the CTAB/pentanol/hexane/water reverse microemulsion, produced by integrating the pentanol H_g proton environment. These show clear on-diagonal features with T_2 relaxation times of 0.001 – 0.03 s and 0.4 – 0.8 s representing pentanol in the RM interface and continuous phase, respectively. These values are consistent with the T_2 relaxation times obtained for pentanol in this system after 6 hours, 0.04 s and 0.5 s, obtained using the 1D T_2
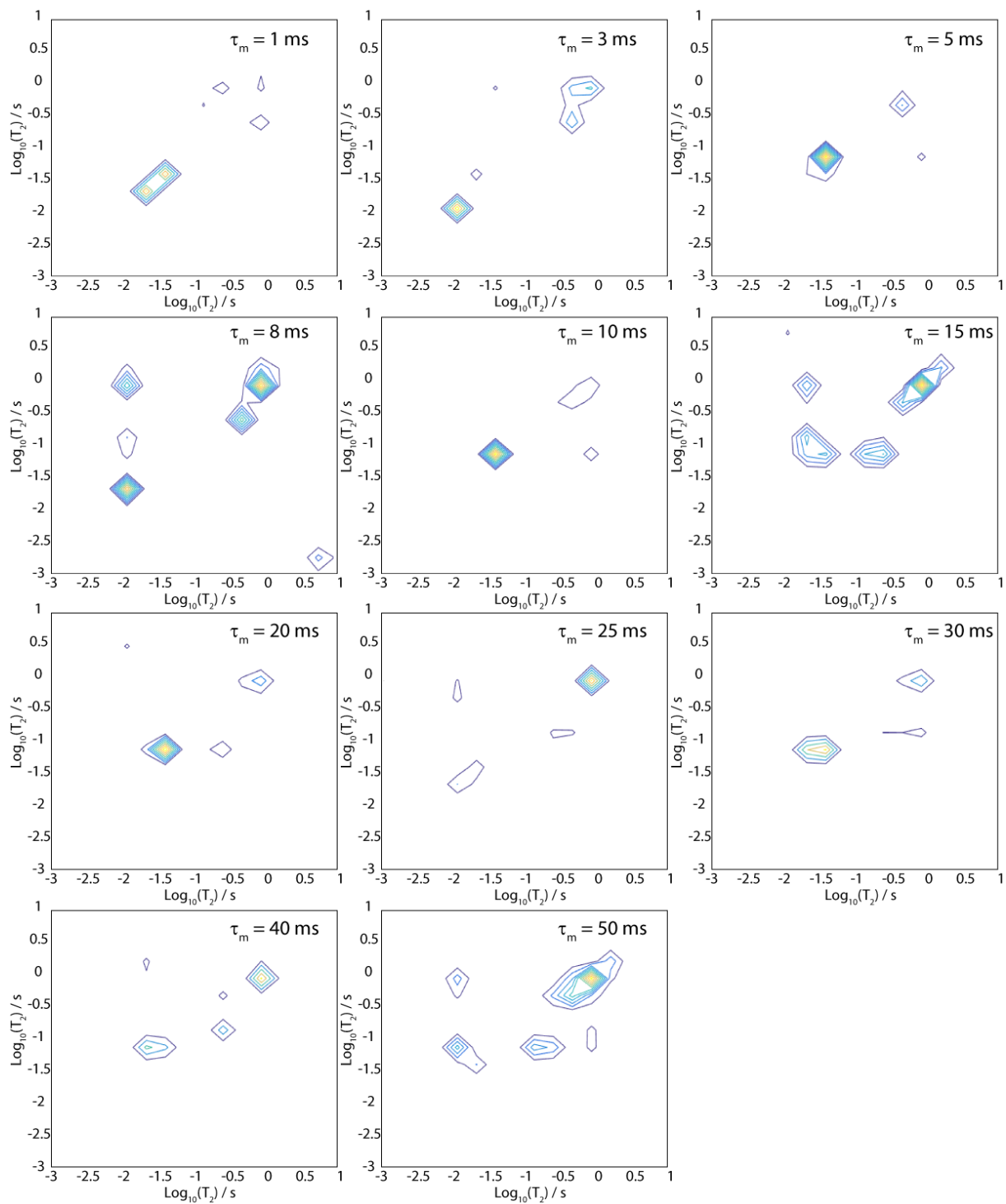
Figure 5.9: Contour $\log_{10}(T_2)$–$\log_{10}(T_2)$ distribution matrix for pentanol, H_g, at all mixing times, τ_m.
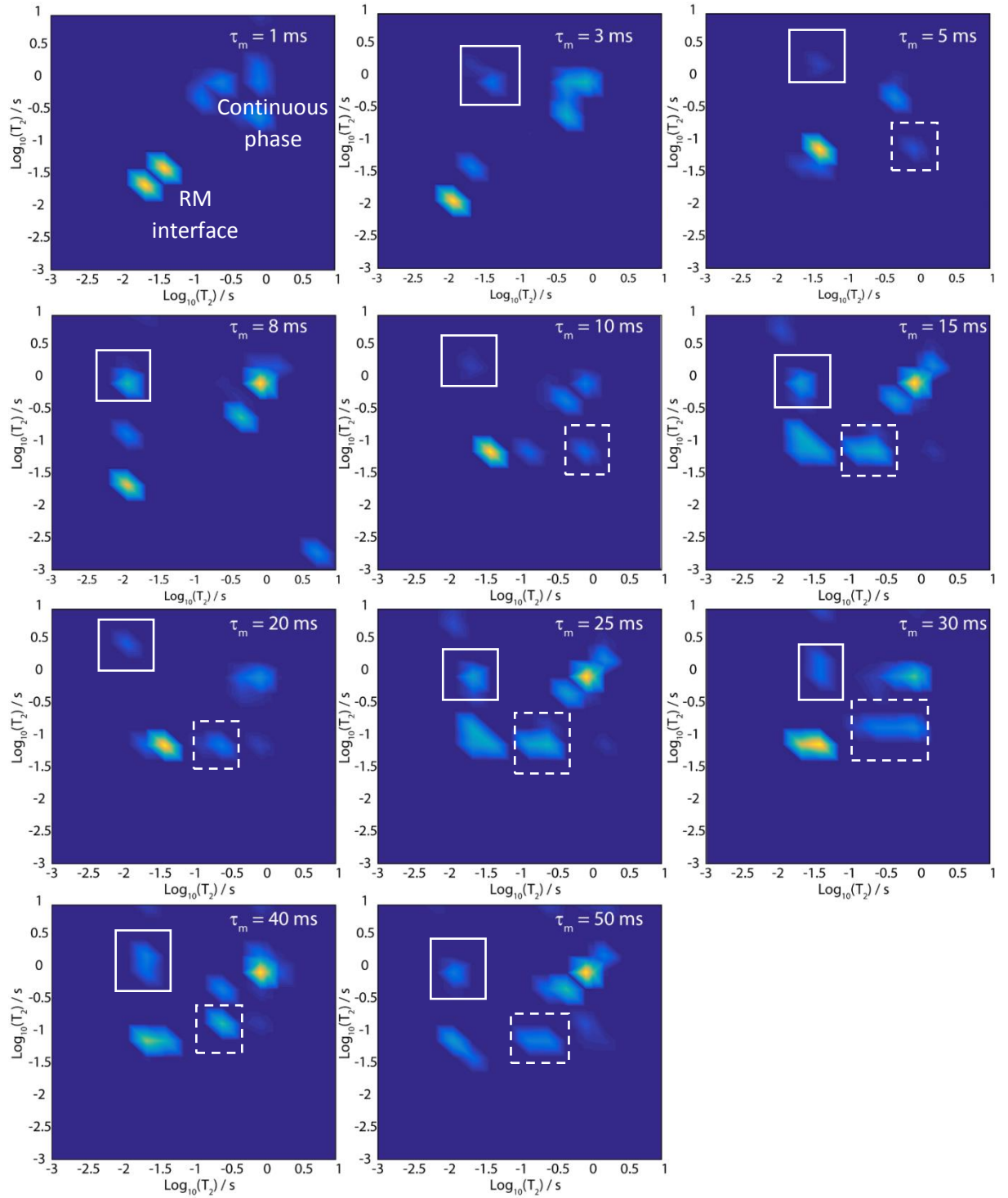
Figure 5.10: Intensity $\log_{10}(T_2)$–$\log_{10}(T_2)$ distribution matrix for pentanol, H_g, at all mixing times, τ_m. The exchange peaks are highlighted with rectangles. Solid rectangles represents pentanol exchanging from RM interphase to the continuous phase and the dashed rectangles indicates exchange from the continuous phase to the RM interphase.

relaxation time experiments in chapter 4. This indicates that these REXSY measurements are probing the system in its state after 6 hours, which not surprising considering the lengthy experimental times of 18 hours required to aquire REXSY data at each mixing time, τ_m.

The contour plots in Figure 5.9 show off-diagonal exchange peaks, which can be seen more clearly in the intensity $\log_{10}(T_2)–\log_{10}(T_2)$ plots shown in Figure 5.10 and are emphasised by rectangles, both solid and dashed. Some of these exchange peaks in the $\log_{10}(T_2)–\log_{10}(T_2)$ distribution matrices for pentanol, particularly those at mixing times of 3 ms and 8 ms, lack symmetry. Asymmetry of the exchange peaks has been reported to arise from experimental noise[11] or inequivalent exchange rates of the forward and backward reaction,[44] which is often observed in systems where exchange occurs between three or more sites.[44] In this particular case, the exchange of pentanol is a two-site exchange process so exchange peak symmetry is expected and hence the lack of symmetry is likely due to experimental noise. Additionally, there are some extra peaks that are neither on the diagonal nor designated as exchange peaks. These peaks are most likely a result of experimental noise, which is amplified during the 2D ILT procedure.[12,44] Performing the 2D ILT in the presence of noise can result in artefacts which often take the form of extra peaks in the resultant 2D spectrum.[32]

Despite these noise artefacts, there are clear off-diagonal features resulting from pentanol exchange. Integrating the intensity of these exchange peaks as a function of mixing time allows the determination of exchange time of pentanol from the RM to the continuous phase and vice versa. The exchange peak intensity for pentanol molecules exchanging from the RM interface to the continuous phase, *AB*, is shown in Figure 5.11a. As expected, the exchange peak intensity increases with mixing time and can be fitted to Equation 5.8 to obtain an exchange rate constant for pentanol molecules exchanging from the RM interface to the continuous phase, λ^{AB}, of 0.071 ± 0.03 ms^{-1} to yield an exchange time, τ_{ex}^{AB}, of 14 ± 5.6 ms. The exchange peak intensity for pentanol molecules

exchanging from the continuous phase to the RM interface, *BA*, is shown in Figure 5.11b. This exchange peak displays a large amount of scatter and could not be fitted to Equation 5.12 to determine the exchange time. The scatter in the exchange peak intensities could be due to a reduction in the signal-to-noise ratio over the period of the REXSY experiment. The first T_2 experiment of the REXSY sequence has the highest signal-to-noise ratio, as minimal signal is lost due to relaxation. Over the course of the mixing period, τ_m, signal is lost in the form of T_1 relaxation; therefore there is a reduction in the signal-to-noise ratio for the second T_2 experiment. The exchange peaks appear as a result of a different T_2 relaxation time measurements in the second T_2 experiment, compared with the first T_2 experiment. Since the second T_2 experiment has a lower signal-to-noise ratio, this may affect the resultant exchange peaks and hence explain the scatter observed.
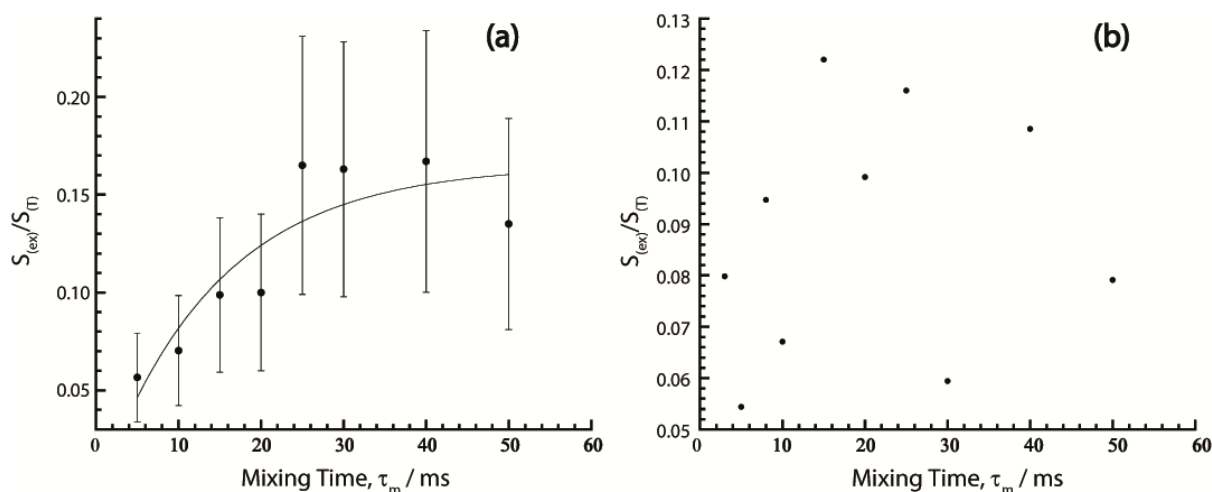
Figure 5.11: A plot of the normalised exchange peak intensity, $S_{(ex)}/S_{(T)}$, by integrating the pentanol peak, as a function of mixing time, τ_m. (a) represents exchange from the RM interphase to the continuous phase, the dashed rectangle in Figure 5.10. (b) represents exchange from the continuous phase to the RM interphase, the solid rectangle in Figure 5.10.

Although the exchange time could not be measured for pentanol exchanging from the continuous phase to the RM interface, pentanol exchanging from the RM interface to the continuous phase has been quantified. This observation is of particular importance as it provides one of the first examples of exchange quantification by integrating proton resonances, in this case the pentanol H_g

proton, to probe exchange of a specific component in a system. Previous REXSY measurements have taken the signal from all the proton resonances and therefore probe all the components of a system. When collecting the data in this way care must be taken when determing which molecular components are responsible for the exchange peaks. Even though both exchange times have not been quantified, it may be possible if the signal-to-noise ratio is improved by increasing the number of signal averages collected for each REXSY experiment. Although this may improve the signal-to-noise ratio, it will increase the experimental time which may not be desired, particularly with this time-dependent reverse micelle system.

The behaviour of CTAB was also investigated by integrating the H_a proton resonance, which yielded the 2D REXSY $\log_{10}(T_2)$–$\log_{10}(T_2)$ distribution matrices in Figure 5.12. These plots show a single peak, which sits on the diagonal at approximately $T_2 = 0.3$ s. This T_2 relaxation time is consistent with the 1D T_2 relaxation time measurements for the CTAB, $T_2 = 0.33$ s, in CTAB/pentanol/hexane/water reverse micelle after 6 hours, and represents CTAB in the RM interface. This provides further confirmation these REXSY measurements probe the aged RM system.

Previous investigations of the CTAB behaviour in CTAB/pentanol/hexane/water RM in chapter 3, provided two diffusion and T_2 relaxation time constants and suggested CTAB resides in the RM interface and the continuous phase, and exchanges between these environments on the millisecond timescale. However, these two separate environments are only obtained in the fresh samples (less than 6 hours), and hence it is not surprising that this exchange is not observed in these lengthy REXSY experiments (18 hours), as the aged system is probed. The presence of a single on-diagonal peak suggests CTAB resides in one T_2 environment without exchange; alternatively, it could suggest that exchange does occur but on a much faster timescale. If the exchange between the RM interface and continuous phase is fast, a single averaged T_2 relaxation time would prevail on-diagonal

(T_2 = 0.3 s), as observed in Figure 5.12. This fast exchange process is undetectable by REXSY

measurements as two separate T_2 environments are required to observe exchange peaks.[8]
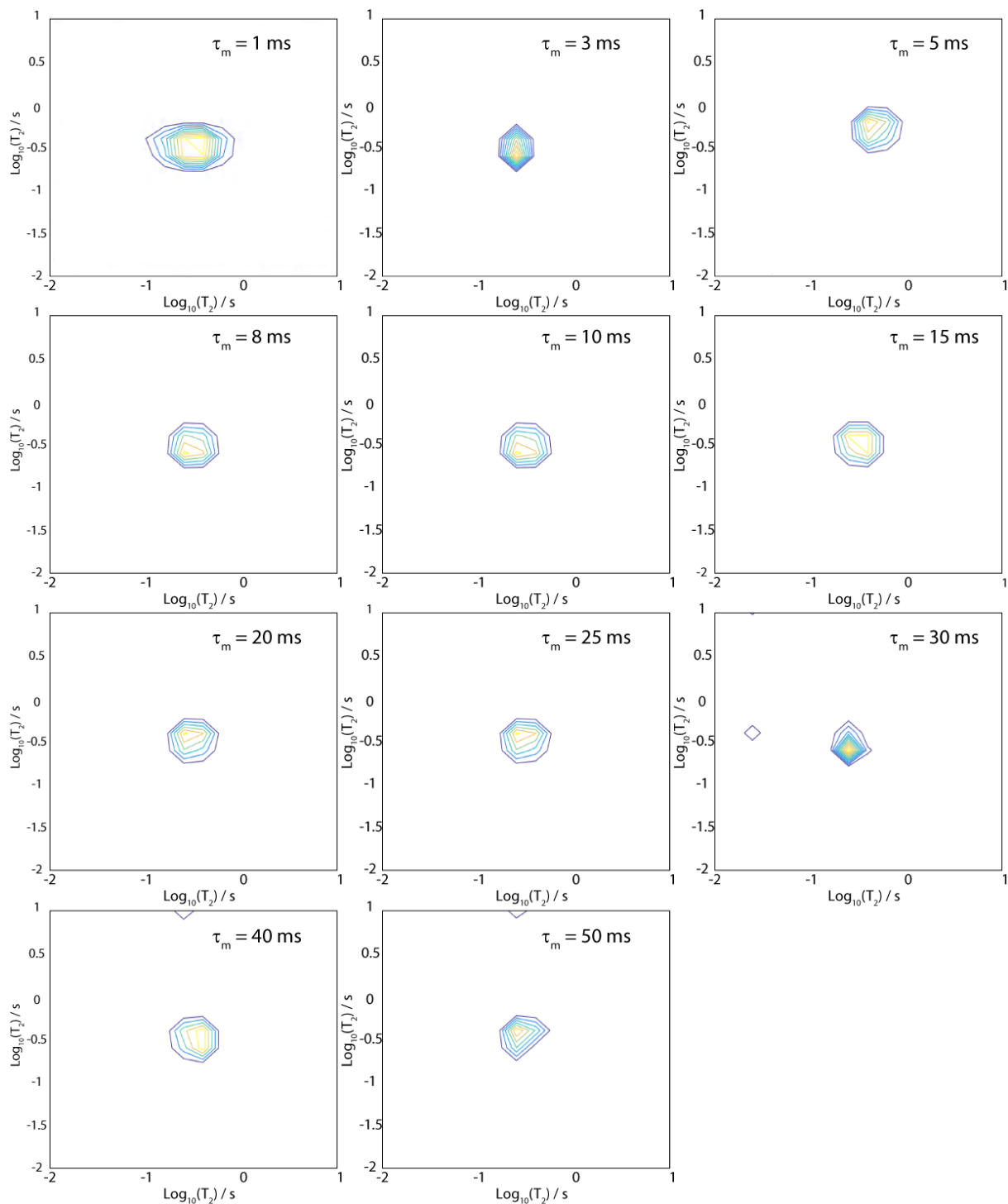
Figure 5.12: $\log_{10}(T_2)$–$\log_{10}(T_2)$ distribution plots for CTAB, H_a, for all mixing times.

While exchange processes can be determined by extracting the signal of individual components of a system by peak integration, an alternative process which involves using the signal from all the molecular components of a system is often performed. To enable exchange to be quantified using this alternative process, there must be a clear separation of T_2 relaxation times for each molecular component, so that exchange can be easily assigned to a particular molecule. If two components have the same T_2 relaxation time, it will be difficult to determine which molecule is responsible for any exchange peaks associated with this T_2 relaxation time.

All the molecules in this CTAB/pentanol/hexane/water reverse micelle system have well defined T_2 relaxation times, as can be seen in Figure 5.13, where there are three clear on-diagonal peaks. The peak with a $\log_{10}(T_2)$ value of approximately -1.1 corresponds to a T_2 of 0.1 s, representing a combination of pentanol in the RM interface ($T_2 = 0.04$ s) and water in the RM core ($T_2 = 0.06$ s). The middle peak has a T_2 relaxation time of approximately 0.6 s and represents pentanol in the continuous phase, which was previously determined to have a T_2 relaxation time of 0.5 s. The final peak on diagonal represents hexane with a T_2 of 2.5 s. A peak corresponding to CTAB should appear at $\log_{10}(T_2) = -0.5$ but, due to the low concentration of CTAB, 0.06 M, compared with water, 0.4 M, pentanol, 0.49 M, and hexane, 7 M, the CTAB peak is too weak to be observed. Since each component has a well defined T_2 relaxation time, it is possible to determine pentanol exchange using this method. The 2D REXSY $\log_{10}(T_2)$–$\log_{10}(T_2)$ distribution matrices produced by analysisng all the compents (CTAB, pentanol, water and hexane) at once are displayed in Figure 5.14, with the exchange peaks higlighted with solid and dashed rectangles.
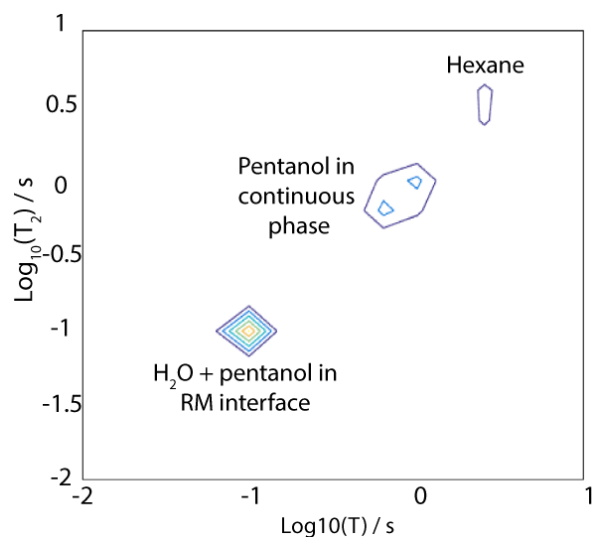
Figure 5.13: A contour plot at τ_m = 1 ms produced by using the signal from all the molecular components of the CTAB/pentanol/hexane/water reverse micelle system. The on-diagonal peaks show each molecular component has different T_2 relaxation times which are assigned in the figure.

The observed exchange peaks corresposond to the two diagonal peaks at T_2 = 0.1 s and T_2 = 0.6 s which represent water and pentanol in RM interface, and pentanol in the continuous phase, respectively. It is worth noting that exchange between the water and alcohol hydroxyl protons is expected[51] but it is fast on the NMR timescale[51] (sub milliseconds) and hence no exchange peaks will arise from this process. With this in mind, it can be concluded that the exchange peaks are due to pentanol exchanging between the RM interphase and continuous phase.
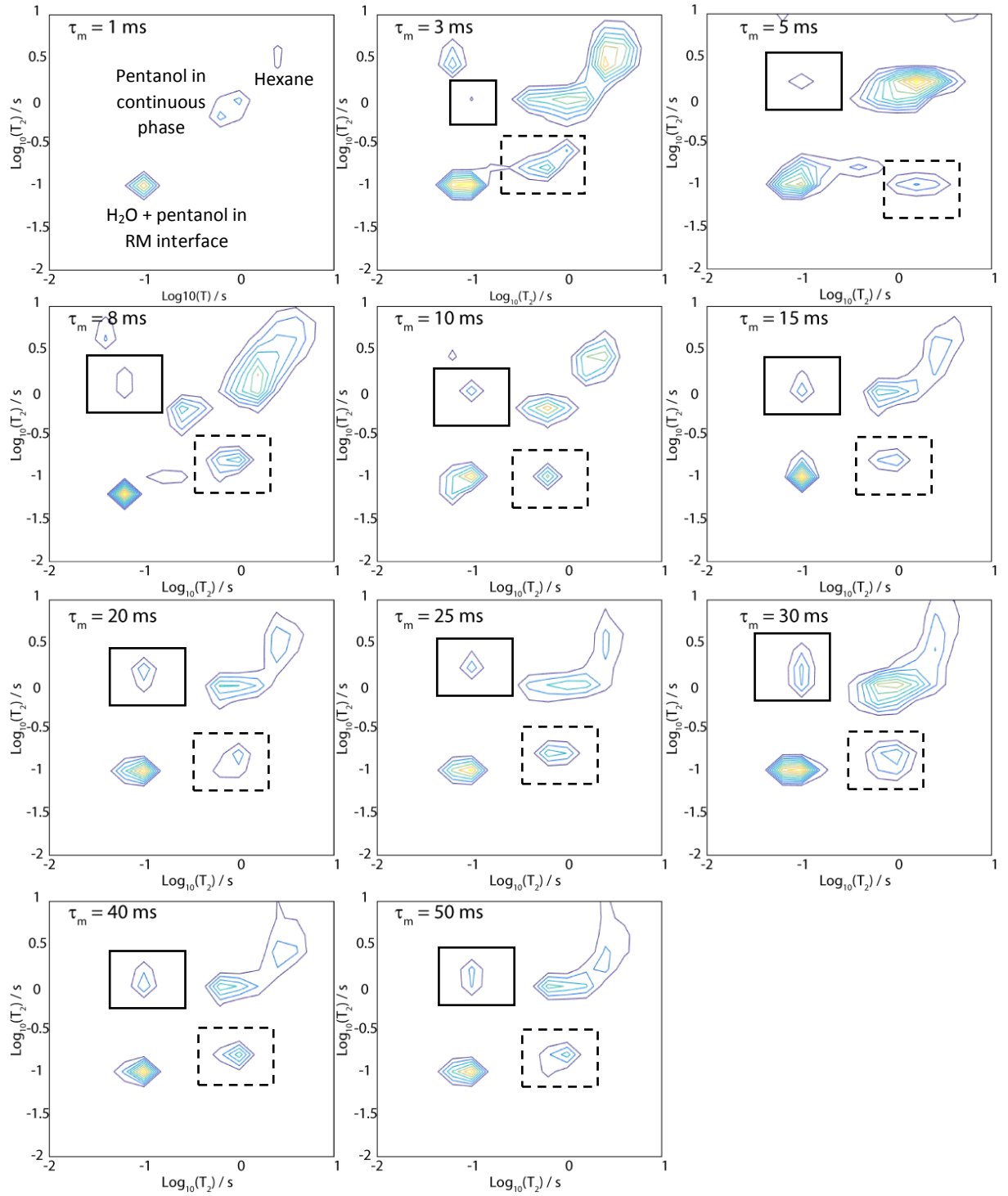
Figure 5.14: Contour plots of the $\log_{10}(T_2)$–$\log_{10}(T_2)$ distribution by taking a single point at the top of the echoes, for all mixing times, τ_m.
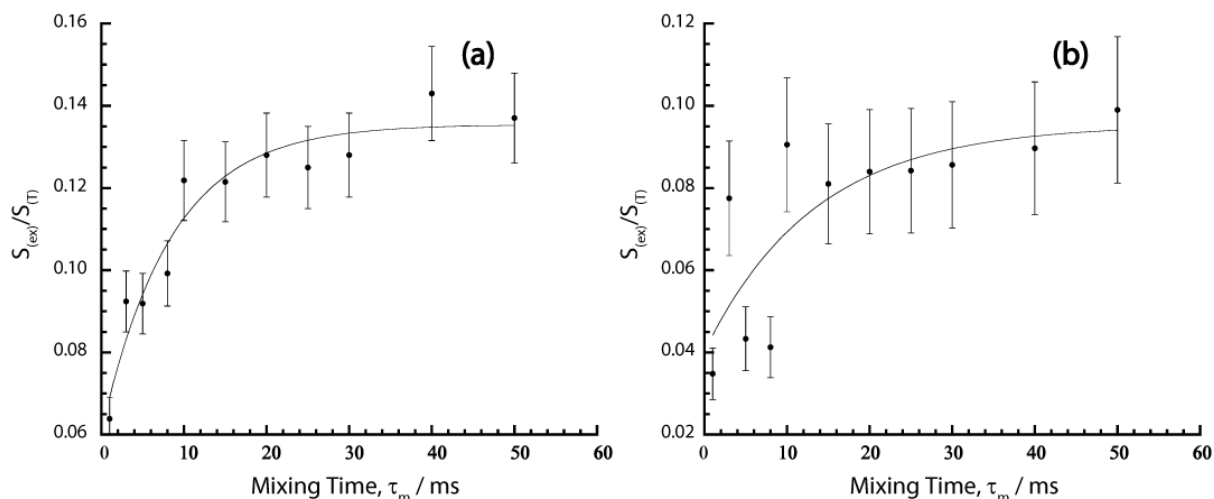
Figure 5.15: A plot of the normalised exchange peak intensity, $S_{(ex)}/S_{(T)}$, by taking a point at the top of the echoes, as a function of mixing time, τ_m. (a) represents exchange from the RM interphase to the continuous phase, the dashed rectangle in Figure 5.14. (b) represents exchange from the continuous phase to the RM interphase, the solid rectangle in Figure 5.14.

By plotting the intensity of these exchange peaks as a function of τ_m, Figure 5.15, and fitting to Equation 5.8 or Equation 5.12, the exchange time of pentanol can be determined. The exchange of pentanol from the RM interface to the continuous phase, Figure 5.15a, was able to be fitted to Equation 5.8 to obtain an exchange rate constant, λ^{AB}, of 0.12 ± 0.01 ms^{-1} and an exchange time, τ_{ex}^{AB}, of 8.4 ± 0.7 ms. The exchange peak intenisty of pentanol exchanging from the continuous phase to the RM interface is shown in Figure 5.15b and provides an exchange rate constant, λ^{BA}, of 0.075 ± 0.01 ms^{-1} and an exchange time, τ_{ex}^{BA}, of 13.3 ± 2.4 ms by fitting to Equation 5.12. The different exchange rate constants is not surprising considering the different equilibrium concentrations of pentanol in the RM interface and continuous phase; the proportion of pentanol in the interface is expected to be 0.4. At equilibrium, the rate of the two exchange processes must be equal,[54] where the rate of exchange is defined by Equation 5.13 and 5.14. Since these two equations are equal at equilibrium, and the equilbrium concentartions of A and B are not the same, neither will the rate constants, λ^{AB} and λ^{BA}, as observed in this analysis.

$$\text{Rate of exchange A to B} = \lambda_{AB}[A]_{eq} \qquad \text{Equation 5.13}$$

$$\text{Rate of exchange B to A} = \lambda_{BA}[B]_{eq} \qquad \text{Equation 5.14}$$

Analysing the data using the signal from all the molecular components has enabled both exchange times of pentanol to be determined, which was not possible when probing only the pentanol signal. The exchange peak arising as a result of pentanol exchanging from the continuous phase to the RM interface, has less scatter which enabled measurements to be made. The reduced scatter in this peak is most likely due to the higher signal-to-noise ratio, as the signal from all components in the system is much more intense than the signal from just pentanol, and the noise intensity for both methods is comparable. The higher signal-to-noise ratio of this analysis method has also provided greater symmetry in the exchange peaks, which is expected for the two site exchange process occuring in this system, and reduced the amount of extra peaks resulting from fitting to noise in the 2D ILT procedure. Therefore, this has provided one of the first full quantification of co-surfactant exchange in these dynamic and complex reverse micelle systems using REXSY measurements.

While REXSY has enabled the exchange dynamics of pentanol to be quantified, it is possible to use the exchange rate constants, λ^{AB} and λ^{BA}, to determine the proportion of pentanol in the RM interface, P_{mic}. To the best of my knowledge, this process has not been applied to REXSY measurements in the past. The determinaton of P_{mic} requires the use of the equilibrium constant, K, which can be determined using Equation 5.15.

$$K = \frac{[B]_{eq}}{[A]_{eq}} = \frac{\lambda^{AB}}{\lambda^{BA}} \qquad \text{Equation 5.15}$$

Where $[A]_{eq}$ and $[B]_{eq}$ are the equilibrium concentations of pentanol in the RM interface (*A*) and the continuous phase (*B*), respectively. Using the previously determined rate constants, $\lambda^{AB} = 0.12 \pm 0.01$ ms^{-1} and $\lambda^{BA} = 0.075 \pm 0.01$ ms^{-1} an equilibrium constant, *K* = 1.58 is determined. An expression for the equilibrium concentration of pentanol in the interface (*A*) is provided in Equation 5.16 where $[\text{Pentanol}]_T$ is the total concentration of pentanol in the system, which yielded an expression for P_{mic} (Equation 5.17) by combining with Equation 5.15.

$$[A]_{eq} = [\text{Pentanol}]_T - [B]_{eq} \qquad \text{Equation 5.16}$$

$$P_{mic} = \frac{[A]_{eq}}{[\text{Pentanol}]_T} = \frac{1}{(K+1)} \qquad \text{Equation 5.17}$$

A P_{mic} value of 0.39 was obtained using the equilibrium constant, *K* = 1.58, calculated through the analysis of the REXSY exchange peaks. The P_{mic} of this particular system has previously been calculated by the use of diffusion NMR and molecular dynamics in chapter 4, where P_{mic} = 0.39 for the aged microemulsion. This P_{mic} is in strong agreement with the one calculated using these REXSY measurements. The calculated P_{mic} using REXSY is also consistent with the literature[55,56] for this CTAB/pentanol/hexane/water system. Diffusion NMR measurements[56] gave a P_{mic} of 0.3, and P_{mic} = 0.46 was obtained using combination of Schulmans' titration and conductivity measurements.[55] The consistency of the P_{mic} calculated by REXSY measurements with that of other proven methods, not only shows that REXSY measurements can effectively be used to determine distribution of exchanging molecules but it also validates that the exchange times obtained for pentanol in this CTAB/pentanol/hexane/water RM are correct, since the exchange rate constants are utilised in the calculation of P_{mic}. This provides one of the first applications of REXSY to accurately determine the exchange time and distribution of pentanol co-surfactant in a reverse micelle system. The ability to determine the exchange and distribution of co-surfactant molecules provides further insight into the

physiochemical properties of this reverse micelle system which may help advance the uses of reverse micelles in their many wide ranging applications, including nanoparticle synthesis.

5.5 Conclusion

This chapter has provided one of the first applications of REXSY measurements on a complex and dynamic CTAB/pentanol/hexane/water reverse micelle system, which are commonly only performed on solid porous materials such as rocks. This is significant as it shows the ability of REXSY to investigate these complex and dynamic supramolecular systems commonly probed by relaxation dispersion experiments. This work has also provided one of the first examples of exchange quantification by integrating proton resonances, in this case the pentanol H_g proton, to obtain signal arising from just pentanol, allowing the exchange behaviour of solely pentanol to be probed. The exchange of pentanol from the RM interface to the continuous phase was determined to be 14 ± 5.6 ms. Unfortunately, the low signal-to-noise ratio made the quantification of pentanol exchanging from the continuous phase to the RM interface difficult. However, I believe this would be possible if a sufficient signal-to-noise ratio is obtained. This alternative method of analysing REXSY data may enable exchange to be determined in complex systems where there is not a clear separation of T_2 relaxation times for each component. Both exchange times of pentanol were able to be determined by using the combined signal from all the molecular components, CTAB, pentanol, hexane and water, instead of just solely pentanol. The exchange time of pentanol from the RM interphase to the continuous phase and vice versa were determined to be 8.4 ± 0.7 ms and 13 ± 2.4 ms, respectively.

The exchange rate constants, λ^{AB} and λ^{BA}, determined from the exchange peak analysis enabled the determination of the proportion of pentanol in the interface, P_{mic}, through the equilibrium constant, K. This is the first determination of molecular distribution in an exchanging system using REXSY measurements. The proportion of pentanol in the interphase, P_{mic}, determined

using REXSY measurements is in agreement with previous diffusion NMR measurements and the literature,[55,56] providing proof that REXSY measurements can effectively be used to determine distribution of exchanging molecules. In addition it also provides confirmation the exchange times are correct, as these are utilised in the determination of P_{mic}.

This study has demonstrated the power of these 2D REXSY experiments to obtain vital exchange behaviour and distribution of molecules within a complex and dynamic system in the solution state. These RESXY measurements have provided further insight into the physiochemical processes of these reverse micelle systems and enable advancement in their wide range of applications, where the dynamics are an important factor such as reactors for nanoparticle synthesis.

5.6 References

(1)   Hill, R. B.; Bracken, C.; DeGrado, W. F.; Palmer, A. G. *J. Am. Chem. Soc.* **2000**, *122*, 11610.

(2)   Sugase, K.; Dyson, H. J.; Wright, P. E. *Nature* **2007**, *447*, 1021.

(3)   Mulder, F. A. A.; Mittermaier, A.; Hon, B.; Dahlquist, F. W.; Kay, L. E. *Nat. Struct. Biol.* **2001**, *8*, 932.

(4)   Eisenmesser, E. Z.; Bosco, D. A.; Akke, M.; Kern, D. *Science* **2002**, *295*, 1520.

(5)   Eisenmesser, E. Z.; Millet, O.; Labeikovsky, W.; Korzhnev, D. M.; Wolf-Watz, M.; Bosco, D. A.; Skalicky, J. J.; Kay, L. E.; Kern, D. *Nature* **2005**, *438*, 117.

(6)   Vallurupalli, P.; Kay, L. E. *Proc. Natl. Acad. Sci. U. S. A.* **2006**, *103*, 11910.

(7)   Callaghan, P. T.; Godefroy, S.; Ryland, B. N. *Magn. Reson. Imaging* **2003**, *21*, 243.

(8)   Codd, S. L.; Vogt, S. J.; Hornemann, J. A.; Phillips, A. J.; Maneval, J. E.; Romanenko, K. R.; Hansen, L.; Cunningham, A. B.; Seymour, J. D. *Org. Geochem.* **2011**, *42*, 965.

(9)   Washburn, K. E.; Callaghan, P. T. *Phys. Rev. Lett.* **2006**, *97*, 4.

(10)   McDonald, P. J.; Korb, J. P.; Mitchell, J.; Monteilhet, L. *Phys. Rev. E* **2005**, *72*, 9.

(11)   Monteilhet, L.; Korb, J. P.; Mitchell, J.; McDonald, P. J. *Phys. Rev. E* **2006**, *74*, 9.

(12)   Mitchell, J.; Griffith, J. D.; Collins, J. H. P.; Sederman, A. J.; Gladden, L. F.; Johns, M. L. *J. Chem. Phys.* **2007**, *127*, 9.

(13)   Dortch, R. D.; Horch, R. A.; Does, M. D. *J. Chem. Phys.* **2009**, *131*, 11.

(14)   Lee, J. H.; Labadie, C.; Springer, C. S.; Harbison, G. S. *J. Am. Chem. Soc.* **1993**, *115*, 7761.

(15)   Griffith, J. D.; Mitchell, J.; Bayly, A. E.; Johns, M. L. *J. Phys. Chem. B* **2009**, *113*, 7156.

(16)   Callaghan, P. T.; Furo, I. *J. Chem. Phys.* **2004**, *120*, 4032.

(17)   Carr, H. Y.; Purcell, E. M. *Phys. Rev.* **1954**, *94*, 630.

(18)   Meiboom, S.; Gill, D. *Rev. Sci. Instrum.* **1958**, *29*, 688.

(19)   Dubois, B. W.; Evers, A. S. *Biochemistry* **1992**, *31*, 7069.

(20)   Wang, C. Y.; Grey, M. J.; Palmer, A. G. *J. Biomol. NMR* **2001**, *21*, 361.

(21)   Carver, J. P.; Richards, R. E. *J. Magn. Reson.* **1972**, *6*, 89.

(22)   Ishima, R.; Torchia, D. A. *J. Biomol. NMR* **1999**, *14*, 369.

(23)   Jen, J. *J. Magn. Reson.* **1978**, *30*, 111.

(24)   Luz, Z.; Meiboom, S. *J. Chem. Phys.* **1963**, *39*, 366.

(25)   Palmer, A. G. *Chem. Rev.* **2004**, *104*, 3623.

(26)   Davis, D. G.; Perlman, M. E.; London, R. E. *J. Magn. Reson. Ser. B* **1994**, *104*, 266.

(27)   Vallurupalli, P.; Hansen, D. F.; Lundstrom, P.; Kay, L. E. *J. Biomol. NMR* **2009**, *45*, 45.

(28)   Karplus, M.; Kuriyan, J. *Proc. Natl. Acad. Sci. U. S. A.* **2005**, *102*, 6679.

(29)   Hore, P. J. *Nuclear Magnetic Resonance*; Oxford University Press, 1995; Vol. 32.

(30)   Ernst, R. R.; Bodenhausen, G.; Wokaun, A. *Principles of Nuclear Magnetic Resonance in One and Two Dimensions*; Clarendon Press, 1987.

(31)   Bernin, D.; Topgaard, D. *Curr. Opin. Colloid Interface Sci.* **2013**, *18*, 166.

(32)   Callaghan, P. T. *Translational Dynamics & Magnetic Resonance: Principles of Pulsed Gradient Spin Echo NMR*; Oxford University Press, 2011.

(33)   Fleury, M.; Soualem, J. *J. Colloid Interface Sci.* **2009**, *336*, 250.

(34)   Song, Y. Q.; Zielinski, L.; Ryu, S. *Phys. Rev. Lett.* **2008**, *100*, 4.

(35)   Song, Y. Q.; Venkataramanan, L.; Hurlimann, M. D.; Flaum, M.; Frulla, P.; Straley, C. *J. Magn. Reson.* **2002**, *154*, 261.

(36)   Venkataramanan, L.; Song, Y. Q.; Hurlimann, M. D. *IEEE Trans. Signal Process.* **2002**, *50*, 1017.

(37)   Borgia, G. C.; Brown, R. J. S.; Fantazzini, P. *J. Magn. Reson.* **1998**, *132*, 65.

(38)   Lawson, C. L.; Hanson, R. J. *Solving Least Squares Problems*; Englewood Cliffs, NJ: Prentice-Hall, 1974.

(39)   Song, Y. Q.; Venkataramanan, L.; Burcaw, L. *J. Chem. Phys.* **2005**, *122*, 8.

(40)   Fordham, E. J.; Sezginer, A.; Hall, L. D. *J. Magn. Reson. Ser. A* **1995**, *113*, 139.

(41)   Law, S. J. PhD, University of Birmingham, 2015.

(42)   Casanova, F.; Perlo, J.; Blümich, B. *Single-Sided NMR*; Springer Berlin Heidelberg, 2011.

(43)   Rodts, S.; Bytchenkoff, D. *J. Magn. Reson.* **2010**, *205*, 315.

(44)   Van Landeghem, M.; Haber, A.; de Lacaillerie, J. B. D.; Blumich, B. *Concepts Magn. Reson. Part A* **2010**, *36A*, 153.

(45)   Hills, B.; Benamira, S.; Marigheto, N.; Wright, K. *Appl. Magn. Reson.* **2004**, *26*, 543.

(46)   Dryhurst, G.; Niki, K. *Redox Chemistry and Interfacial Behavior of Biological Molecules*; Springer US, 2012.

(47)   Fendler, J. H. *J. Phys. Chem.* **1980**, *84*, 1485.

(48)   Fendler, J. H. *Annu. Rev. Phys. Chem.* **1984**, *35*, 137.

(49)   Otten, R.; Villali, J.; Kern, D.; Mulder, F. A. A. *J. Am. Chem. Soc.* **2010**, *132*, 17004.

(50)   Ishima, R.; Torchia, D. A. *J. Biomol. NMR* **2003**, *25*, 243.

(51)   Halliday, N. A.; Peet, A. C.; Britton, M. M. *J. Phys. Chem. B.* **2010**, *114*, 13745.

(52)   Moulik, S. P.; Paul, B. K. *Adv. Colloid Interface Sci.* **1998**, *78*, 99.

(53)   Law, S. J.; Britton, M. M. *Langmuir* **2012**, *28*, 11699.

(54)   Atkins, P.; de Paula, J. *Atkins' Physical Chemistry*; OUP Oxford, 2010.

(55)   Giustini, M.; Murgia, S.; Palazzo, G. *Langmuir* **2004**, *20*, 7381.

(56)   Palazzo, G.; Lopez, F.; Giustini, M.; Colafemmina, G.; Ceglie, A. *J. Phys. Chem. B* **2003**, *107*,

1924.

6. 2D Diffusion Exchange Spectroscopy (DEXSY) on the CTAB/pentanol/hexane/water Reverse Microemulsion.

6.1 Introduction

The previous chapter provided details of a new method for studying exchange and distribution of pentanol in the CTAB/pentanol/hexane/water reverse microemulsion, through probing the T_2 relaxation times. This 2D REXSY method presented further proof that exchange of pentanol is on a millisecond timescale and provided exchange times of 8.4 ms and 13.3 ms. The quantification of pentanol exchange was possible due to the well-defined T_2 relaxation times for pentanol in the continuous phase and the RM interface. REXSY is not the only 2D NMR technique that has the ability to probe exchange; exchange can also be probed using diffusion exchange spectroscopy (DEXSY) where the diffusion coefficients are probed instead of T_2 relaxation times. These experiments have the ability not only to probe exchange processes[1] but also to give knowledge on domain size and polydispersity of porous media,[1] which is of particular importance to the reverse micelle systems studied in this thesis. Therefore, in this chapter, the CTAB/pentanol/hexane/water reverse microemulsion will be investigated using diffusion exchange spectroscopy (DEXSY) experiments, by integrating pulsed field gradient experiments into the 2D exchange experiments.[2] These investigations will hopefully provide further information on exchange processes and provide additional knowledge on the RM size and polydispersity.

The DEXSY sequence follows a similar format to that of the REXSY sequence, where instead of probing the T_2 relaxation, the diffusion behaviour is probed. A DEXSY sequence consists of two pulsed field gradient experiments separated by a mixing time,[1,2] τ_m, to enable the diffusion coefficients to be measured at two separate time points. The pulsed field gradient experiments used to measure diffusion in these DEXSY sequences can take the form of either pulsed gradient spin

echo[1-5] (PGSE), Figure 6.1a, or pulsed gradient stimulated echo (PGSTE) experiments,[6-8] Figure 6.1b. If

exchange occurs during τ_m, the spins exchange to a different environment and hence possess

different diffusion coefficients before and after τ_m. As with the REXSY sequence, a clear separation of

the two exchanging environments is required to determine exchange, i.e. REXSY requires the

exchanging environments to have two different T_2 relaxation times, therefore, when using this DEXSY

sequence, the exchanging environments must display separate diffusion coefficients.[1,9] The 1D

diffusion measurements of this system have showed that pentanol possesses two diffusion

coefficients at short observation times, which represent pentanol in the RM interface and the

continuous phase. As pentanol possesses this clear separation of its two environments, DEXSY should

be able to probe the exchange of pentanol in this CTAB/pentanol/hexane/water RM system,

provided short observation times are used.
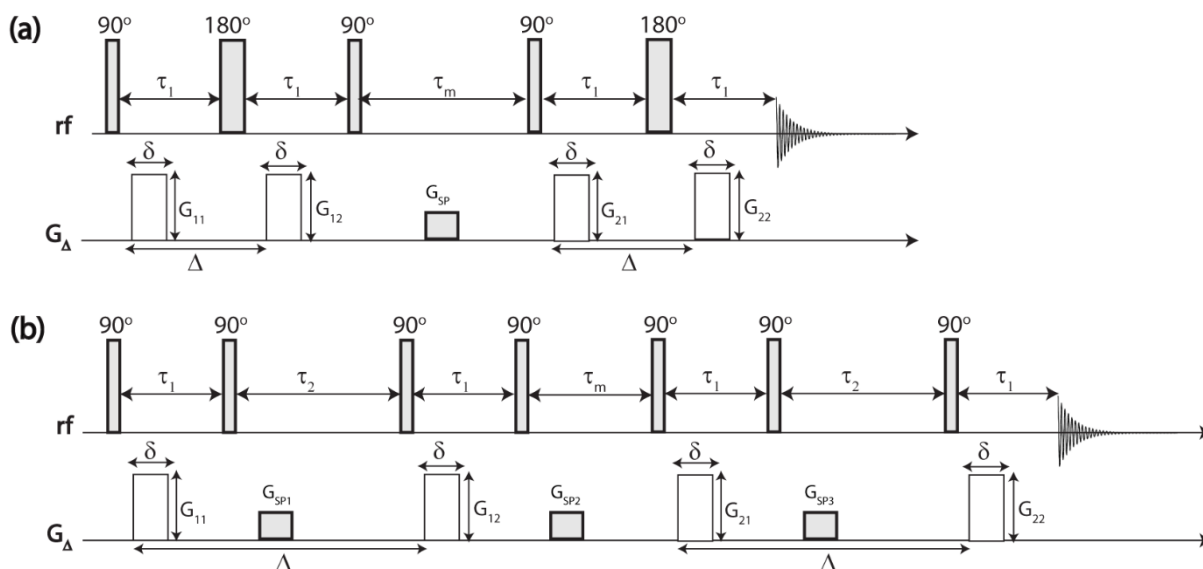
Figure 6.1: The two diffusion exchange spectroscopy (DEXSY) sequences where (a) consists of two PGSE experiments separated by a mixing time, τ_m, and known as the PGSE DEXSY sequence and (b) is the PGSTE DEXSY sequence which consists of two PGSTE experiments separated by τ_m.

DEXSY measurements produce a 2D spectrum similar to that obtained through REXSY

measurements, where the intensity probability distribution is plotted against diffusion coefficient

before and after the mixing time, Figure 6.2. As with REXSY, it is this 2D spectrum, known as the $\log_{10}(D)$–$\log_{10}(D)$ distribution matrix, that enables the determination of exchange. The $\log_{10}(D)$–$\log_{10}(D)$ distribution matrix is obtained using the same 2D inverse Laplace procedure (ILT) utilised in the REXSY measurements,[10-12] by converting the time-dependent diffusion decays into a diffusion coefficient distribution. As the same 2D ILT procedure is applied, the 2D DEXSY $\log_{10}(D)$–$\log_{10}(D)$ distribution matrices suffer from the same noise artefacts observed in the 2D REXSY $\log_{10}(T_2)$–$\log_{10}(T_2)$ distribution matrices, such as the appearance of extra off-diagonal peaks that cannot be attributed to exchange. The $\log_{10}(T_2)$–$\log_{10}(T_2)$ distribution matrices consist of on-diagonal and off-diagonal peaks. The on-diagonal peaks represent molecules that remain in the same diffusion environment during τ_m and hence do not exchange.[1-3,6] Any molecules that exchange to an environment of differing diffusion coefficients during τ_m contribute to the appearance of off-diagonal or exchange peaks.[1-3,6] By monitoring the intensity of these exchange peaks as a function of the mixing time, τ_m, the exchange rate, τ_{ex}, can be determined using the same process utilized in the REXSY measurements,[3,13] as discussed in chapter 5.
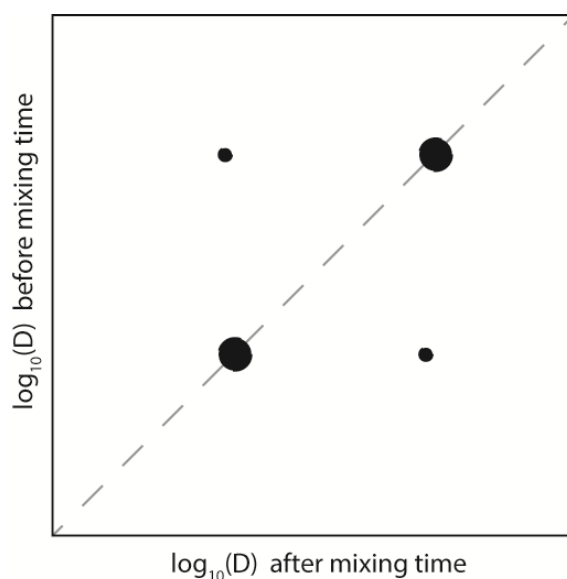
Figure 6.2: A schematic of the 2D spectrum known as the $\log_{10}(D)$–$\log_{10}(D)$ distribution matrix produced from the DEXSY measurements.

DEXSY was first introduced by Callaghan and Godefroy[2] in 2003, by exploring the use of a second dimension in PGSE NMR. They proposed the DEXSY sequence, which consists of two PGSE diffusion experiments that measure diffusion in the same direction, and are separated by a mixing time, τ_m. The sequence was applied to a 25 % AOT/water liquid crystal sample where significant water exchange was expected for $\tau_m > 100$ ms. DEXSY measurements were performed at $\tau_m = 4$ ms and $\tau_m = 500$ ms, exchange peaks were only observed for the longer mixing time and hence provided confirmation DEXSY sequence is indeed suitable for determining the presence of exchange.

While Callaghan and Godefroy introduced the DEXSY sequence to determine the presence of exchange, the procedure was developed further by Callaghan and Furo[1] in 2004. Callaghan and Furo[1] utilized a PGSE DEXSY sequence to investigate the lamellar phase liquid crystal consisting of $C_{10}E_3$ [$C_{10}H_{21}O(CH_2CH_2O)_6H$] and water, to determine the presence of water exchange and provide knowledge of the domain size and polydispersity, through the characteristic features of the off-diagonal exchange peaks. In this publication they show the off-diagonal exchange peaks do not necessarily always produce a 90° angle as one may expect,[1] Figure 6.3a. The exchange peaks can subtend a characteristic angle, α, (Figure 6.3b) which can vary between 0° and 90°, and depends on the mixing time,[1] τ_m. This angle, α, has no connection with the regularisation parameter[2,14,15] utilized in the ILT procedure.[1] The angle, α, is related to the ratio of the root mean square (RMS) displacement to the mean domain size,[1] $\frac{2D\tau_m}{d^2}$, where d is the mean domain size, D is the diffusion coefficient, τ_m is the mixing time. The quantity $2D\tau_m$ can be related to the RMS displacement over time for 1D migration,[1] $(2D\tau_m)^{1/2}$. By monitoring the variation of α as a function of the effective mixing time, $\tau_m' = \tau_m + \Delta$, they showed the mean domain size,[1] d, can be calculated using their proposed domain size distribution model.[1] This model can also provide information on the polydispersity[1] by assuming either mono- or polydisperse nature, the assumption that provides the superior fit to the data is the best estimation of the polydispersity. Using these methods, Callaghan

and Furo[1] were able to determine a mean domain size of 43 µm of the $C_{10}E_3$ [$C_{10}H_{21}O(CH_2CH_2O)_6H$] and water liquid crystals which are polydisperse in nature.
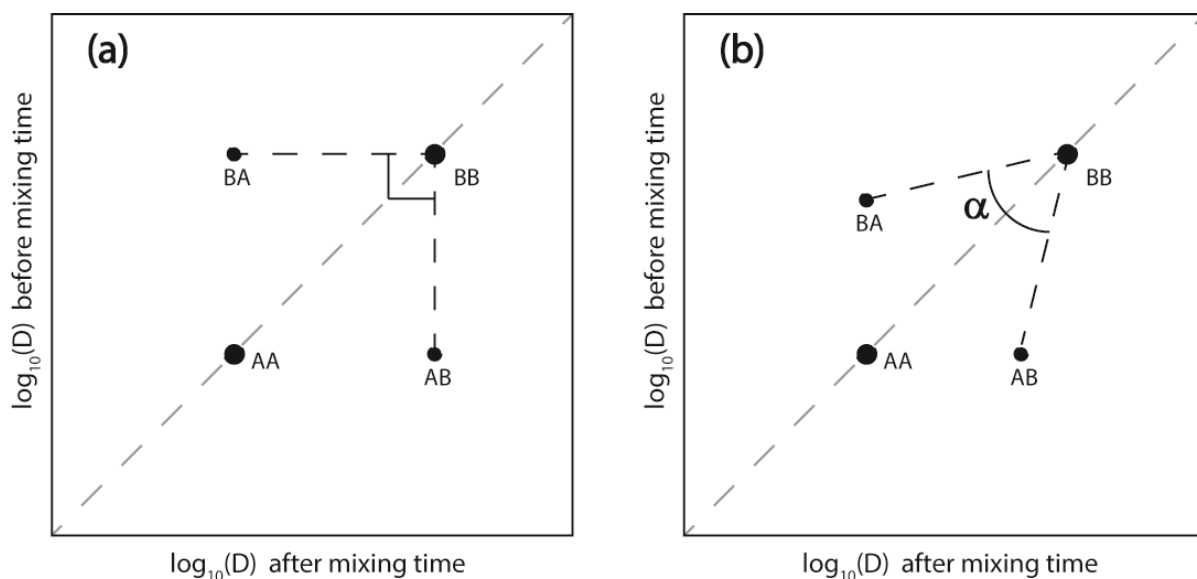
Figure 6.3: A schematic of the $\log_{10}(D)$–$\log_{10}(D)$ distribution matrix with (a) the expected 90° angle and (b) the angle, α, between the exchange peaks and the main diagonal peak.

In addition to the size and polydispersity, DEXSY can also obtain knowledge of the confining geometry structure.[4,5] Hubbard et al.[4] used PGSE DEXSY measurements to probe liquid crystals of dodecylpentaglycol ($C_{12}E_5$)/sodium dodecyl sulfate (SDS)/decane/water. DEXSY measurements were performed in both the *x*- and *z*-direction but water exchange peaks were only observed in the *x*-direction. They attributed this to one of two possible explanations. Firstly, to a shorter distance of the confining geometry in the *x*-axis compared to the *z*-axis, i.e. an ellipsoidal structure rather than spherical, hence leading to exchange occurring on a quicker timescale in the *x*-direction. Secondly, there exist some extra restrictions in the *x*-axis which are more closely spaced than the confining geometry. When combining the DEXSY results with DDCOSY measurements, which are similar to DEXSY but with the absence of a mixing time, they suggested that the presence of exchange in the *x*-axis was a result of defects in the *xy* plane of the geometries. In this study, Hubbard et al.[4] have

demonstrated the ability to probe the defect structure of lyotropic liquid crystals, which is generally difficult to characterize, through the use of DEXSY measurements.

While DEXSY has been employed to investigate the behaviour of liquid crystal samples, they have also been employed to probe the behaviour of dextran in a dispersion of polyelectrolyte multilayer (PEM) hollow capsules.[6,8] PEM capsules are tough, uniform in size, and with selective and tunable permeability,[8] and have been found to be permeable to dextran, therefore dextran exchanges between the interior and the exterior of these capsules. Galvosas et al.[6,8] utilised a PGSTE DEXSY sequence to confirm the presence of this exchange process. DEXSY measurements were performed at τ_m = 20 ms and τ_m = 200 ms, where the presence of exchange peaks at τ_m = 200 ms confirmed the occurrence of dextran exchange. No exchange is evident at a mixing time of 20 ms, but around 1.5 % exchange occurs at 200 ms; therefore, they were able to estimate the exchange time, τ_{ex}, of dextran between the PEM membrane to be 1 s.

DEXSY has also been employed to investigate the exchange behaviour in microporous zeolites.[3] Galvosas et al.[3] probed the exchange of pentane between the interior and exterior of a large pore NaX zeolite. The presence of an internal magnetic field gradient in the NaX zeolite complicated DEXSY measurements due to the introduction of gradient mis-match. In this publication, they have provided a modified PGSE DEXSY sequence which allows the detection and correction of gradient mis-match to enable DEXSY measurements to be performed. They observed exchange peaks at mixing times greater than 5 ms. The exchange peaks were analysed as a function of mixing time using the exchange model proposed by Washburn and Callaghan,[13] to provide an exchange time of 460 ms for pentane. This was the first application of the REXSY exchange model proposed by Washburn and Callaghan[13] to analyse DEXSY data.

The most commonly utilised DEXSY sequence consists of PGSE experiments,[1-5] Figure 6.1a, rather than the PGSTE DEXSY sequence,[6,8] Figure 6.1b. The PGSTE DEXSY sequence can cause a

complex superposition of wanted and unwanted magnetisation which results in significant peak phase and baseline distortions.[16-18] A 1D PGSTE experiment suffers from the presence of unwanted magnetisation by the nature of the stimulated echo sequence, where multiple spin echoes are formed,[19] resulting from each 90° pulse. To avoid interference between these echoes with the wanted stimulated echo, lengthy phase cycles and crusher gradients are used.[20] A phase cycle, varies the phase of the rf pulses and receiver coil to cancel out unwanted magnetisation, minimise artefacts and maximise the wanted magnetisation.[9,16,17] Crusher gradients also eliminate unwanted magnetisation in the transverse plane by applying a gradient to shift the phase of the unwanted magnetisation.[9,19] However, crusher gradients remove all magnetisation in the transverse plane and hence any wanted magnetisation must be transferred onto the longitudinal plane prior to application. Since the 1D PGSTE sequence has issues with unwanted magnetisation and requires the use of crusher gradients, care must be taken when implementing these PGSTE sequences in two dimensions. The amount of unwanted magnetisation is amplified in the 2D PGSTE DEXSY sequence as more spin echoes can occur due to the presence of seven 90° pulses. Therefore, particular attention must be paid to the phase cycle[18] and the use of spoiler gradients to obtain the desired magnetisation.[7,18] These phase cycles can be complicated and lead to lengthy experiments.[21]

While the PGSE DEXSY experiment is less complex than the PGSTE DEXSY, it is not suitable for use in probing the behaviour of the CTAB/pentanol/hexane/water reverse microemulsion. The PGSE DEXSY sequence cannot be used due to the issues inherent to the PGSE sequence, such as T_2 relaxation and J-coupling sensitivity. PGSE sequences, and hence the PGSE DEXSY, are sensitive to T_2 relaxation during the observation time, Δ.[9,22] Therefore, the observation time can only be varied up to or on the order of T_2, before signal is lost as a result of relaxation. This is an issue for this particular system as components in the RM have short T_2 relaxation times due to reduced motional freedom,[19] hence limiting the observation time. PGSE DEXSY experiments are also sensitive to J-coupling which leads to peak phase distortions.[23-26] As a consequence, J-coupled resonances cannot be analysed,

which therefore limits the application of PGSE DEXSY to probing only singlet resonances. Again, this is an issue for the CTAB/pentanol/hexane/water reverse microemulsion as the H_g proton resonance used to probe the behaviour of pentanol cannot be acquired, (see chapter 3 for proton assignments) only the alcohol hydroxyl is a singlet. The alcohol hydroxyl is in exchange with the water in the core of the RM,[27] and hence can affect the diffusion measurements and the probing of molecular exchange.

Due to the issues associated with the PGSE DEXSY sequence, the PGSTE DEXSY sequence will be employed in this chapter to probe the behaviour of the CTAB/pentanol/hexane/water reverse microemulsion. As a result of the complex nature of the PGSTE DEXSY sequences, significant improvements to the PGSTE DEXSY sequence available to our group were required to probe this RM system. These modifications have been outlined in detail in this chapter. PGSTE DEXSY sequences have been utilised in solid porous materials such as zeolites[7] and polyelectrolyte membrane capsules[6,8]. Therefore, this chapter provides the feasibility to use DEXSY measurements to probe dynamic systems such as the CTAB/pentanol/hexane/water reverse microemulsion.

6.2 Experimental

Sample Preparation

The CTAB/pentanol/hexane/water reverse microemulsion was prepared using the same method and materials and quantities described in chapter 3 to produce a water/CTAB molar ratio, ω_0, of 6.9, a pentanol/CTAB molar ratio, P_0, of 8.2 and a volume fraction, ϕ_d, of 0.05. Additional microemulsions were investigated by independently varying ω_0, P_0 or ϕ_d to give CTAB/pentanol/hexane/water microemulsions of different compositions, Table 6.1.

Table 6.1: Composition of each CTAB/pentanol/hexane/water microemulsion studied.

Microemulsion	CTAB / g	Pentanol / mL	Water / mL	Hexane / mL
ω_0 = 6.9, P_0 = 8.2 and [CTAB] = 0.06 M	0.2	0.487	0.068	8.394
ω_0 = 6.9, P_0 = 8.2 and [CTAB] = 0.11 M	0.4	0.974	0.136	8.394
ω_0 = 6.9, P_0 = 20 and [CTAB] =0.06 M	0.2	1.188	0.068	7.625
ω_0 = 10, P_0 = 8.2 and [CTAB] = 0.06 M	0.2	0.487	0.1	8.362
ω_0 = 30, P_0 = 8.2 and [CTAB] = 0.06 M	0.2	0.487	0.296	8.166

A bis(2-ethylhexyl) sulfosuccinate sodium salt (AOT)/octane/water reverse microemulsion was utilised to test the pulsed gradient stimulated echo (PGSTE) DEXSY pulse sequence. Bis(2-ethylhexyl) sulfosuccinate sodium salt, AOT(Fluka ≥ 96 %), n-octane (Acros, 97%) and water (purified with a MilliQ™ system, resistivity 18 MΩ cm, TOC ≤ 5 ppb) were used to produce the AOT/n-octane/water tertiary microemulsion. A 1.5 M stock AOT/n-octane solution was prepared by dissolving 6.946 g AOT in 4.375 ml n-octane. Water (1.27 ml) and n-octane (2.426 ml) were added to a 3 ml aliquot of the 1.5 M AOT/n-octane stock solution to obtain a stock microemulsion of water to surfactant ratio, ω_0 = 15 and volume droplet fraction, ϕ_d = 0.45. After equilibration overnight, 4 ml n-octane was added to 2 ml of the stock microemulsion to obtain the desired AOT/n-octane/water microemulsion with ω_0 = 15 and ϕ_d = 0.15.

A high molecular weight polymer, polydimethylsiloxane (PDMS) was used as received.

NMR Measurements

NMR experiments were performed on the same spectrometer and experimental setup as described in chapter 3. A polydimethylsiloxane (PDMS) sample was used to ensure there were no

artefacts resulting from the magnetic field gradients, such as artificial attenuation or distortion of the NMR spectrum.[28]

Diffusion NMR Measurements

1D PGSTE measurements were performed on a PDMS sample using Δ = 50 , δ = 1.5 ms, $\textbf{\textit{G}}_{max}$ = 3.5 T m^{-1} and a repetition time of 2 s with 32 magnetic field gradient steps to test the gradient stabilisation delay. A gradient stabilisation time of 1 ms and gradient ramp time of 0.1 ms were employed, which lead to no signal attenuation, and hence were utilised in all 1D and DEXSY PGSTE experiments in this chapter. Diffusion coefficients for the H$_a$ resonance of CTAB and H$_g$ resonance of pentanol were measured using ^{1}H NMR pulsed gradient stimulated echo (PGSTE) and pulsed gradient stimulated echo with bipolar pulse pair (BPP-STE) experiments[9,29,30] at 298 ± 0.3 K. Data were collected using the experimental parameters Δ = 10, δ = 1 ms, $\textbf{\textit{G}}_{max}$ = 1.9 T m^{-1} or Δ = 20 , δ = 2 ms, $\textbf{\textit{G}}_{max}$ = 1.8 T m^{-1} with 32 magnetic field gradient steps and a repetition time of 6.5 s or 2 s. Data were collected for AOT/n−octane/water reverse microemulsions using ^{1}H PGSTE experiments with experimental parameters of Δ = 20 ms, δ = 1 ms and $\textbf{\textit{G}}_{max}$ = 2 T m^{-1}, a repetition time of 2 s with 32 magnetic field gradient steps. Diffusion coefficients were determined using the same procedure in chapter 3 through the use of the Stejskal-Tanner relationship (Equation 2.11).

Diffusion Exchange Spectroscopy Measurements (DEXSY)

Two-dimensional D−D relaxation exchange spectroscopy (DEXSY) experiments consist of two PGSTE measurements separated by a mixing time, τ_m. Data for the AOT/n-octane/water reverse microemulsion were collected with δ = 1 ms, Δ = 20 ms and $\textbf{\textit{G}}_{max}$ = 2 T m^{-1} or δ = 2 ms Δ = 100 ms and $\textbf{\textit{G}}_{max}$ = 1 T m^{-1} with τ_m = 10 ms, with a repetition time of 2 s and 8 q-steps in each direction. The water peak was integrated to give a 2D matrix of signal attenuation as a function of magnetic field gradient

185

strength. PGSTE DEXSY data were collected for a PDMS sample with δ = 2 ms, Δ = 40 ms and $\textbf{\textit{G}}_{max}$ = 0.9 T m^{-1} or δ = 2 ms Δ = 100 ms and $\textbf{\textit{G}}_{max}$ = 1 T m^{-1} or δ = 3 ms, Δ = 40 ms and $\textbf{\textit{G}}_{max}$ = 1.8 T m^{-1} with τ_m = 10 ms, with a repetition time of 1.7 s and 4 q-steps in each direction. Data for the CTAB/pentanol/hexane/water reverse microemulsion were collected with δ = 3 ms, Δ = 40 ms and $\textbf{\textit{G}}_{max}$ = 0.9 T m^{-1}, τ_m = 10 ms, with a repetition time of 2 s and 32 q-steps in each direction using the original PGSTE DEXSY pulse sequence with no modifications. Data were also collected with δ = 2 ms, Δ = 20 or 40 ms, $\textbf{\textit{G}}_{max}$ = 1 or 1.8 T m^{-1} and τ_m = 10, 50, 100 or 300 ms using the final modified PGSTE DEXSY pulse sequence. Data were collected individually for CTAB and pentanol by integrating the CTAB H$_a$ and pentanol H$_g$ proton resonances, or by collecting the signal from all the RM components (CTAB, pentanol, hexane and water), to produce 2D signal attenuation matrices as a function of magnetic field gradient strength, Figure 6.4a.

In these 2D matrices the vertical axis represents the signal attenuation from magnetic field gradient steps before the mixing time, τ_m, and the horizontal gives the signal attenuation after τ_m. The first vertical column gives the signal decay over all the magnetic field gradient steps before the mixing time when the magnetic field gradient strength after the mixing time is zero, Figure 6.4b. The first horizontal row gives the signal attenuation over all the magnetic field gradient steps after the mixing time when $\textbf{\textit{G}}$ = 0 G cm^{-1} before τ_m, Figure 6.4c. By fitting both of these signal attenuations to the Stejeskal-Tanner relationship, Equation 2.11, diffusion coefficients before and after the mixing time can be obtained. Determining the diffusion coefficients before and after the mixing time is analogous to a 1D diffusion experiment.
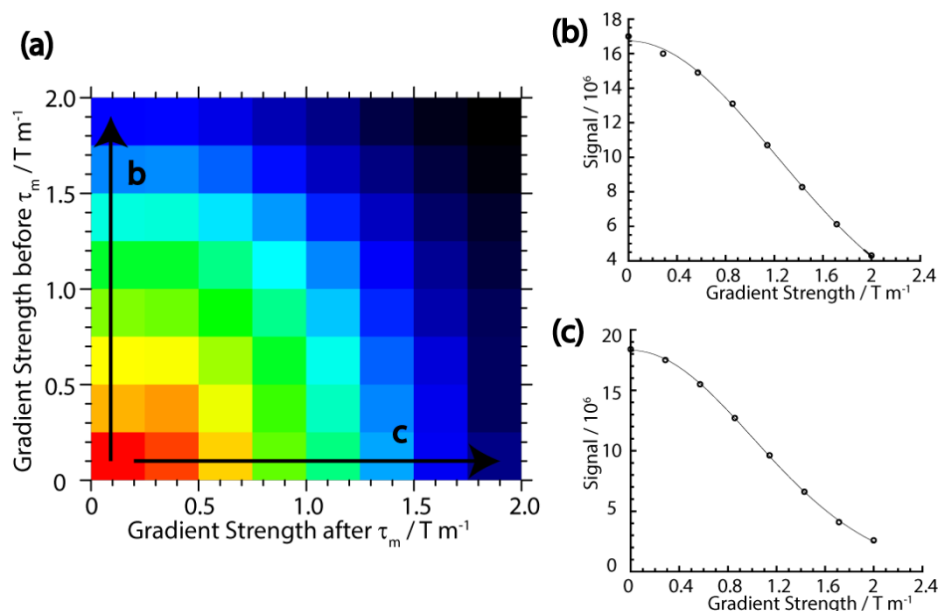
Figure 6.4: (a) An example of a 2D diffusion signal attenuation matrix, where the signal before τ_m, the first column highlighted, is plotted in (b) and the signal after τ_m, the first row highlighted, is plotted in (c).

The 2D inverse Laplace transform[2,10-12,15] is applied to the 2D signal attenuation matrix to generate a $\log_{10}(D)-\log_{10}(D)$ distribution matrix. The same 2D ILT procedure as described in chapter 5 for the REXSY data was performed in the DEXSY analysis.

6.3 Pulse Sequence Development

Measurements were performed on the CTAB/pentanol/hexane/water reverse microemulsion using the PGSTE DEXSY sequence currently accessible to our group. These DEXSY experiments produce a 2D data set which allows the NMR signal to be probed as a function of the magnetic field gradient strength before and after the mixing time, τ_m. Inspection of this 2D data set for the CTAB/pentanol/hexane/water reverse microemulsion revealed significant distortions to the NMR signal, which became more severe as the magnetic field gradient strength was incremented. As a result of these signal distortions, the peaks in the NMR spectrum either could not be phased or the phasing of the peaks became more difficult as the magnetic field gradient strength was incremented.

The peaks in a 1D PGSTE experiment on the same sample, using identical experimental parameters, maintained phase throughout all magnetic field gradient strengths. By inspecting the signal attenuation arising from the 1D PGSTE and PGSTE DEXSY experiments, it was observed that the signal attenuation was much quicker in the PGSTE DEXSY experiment.
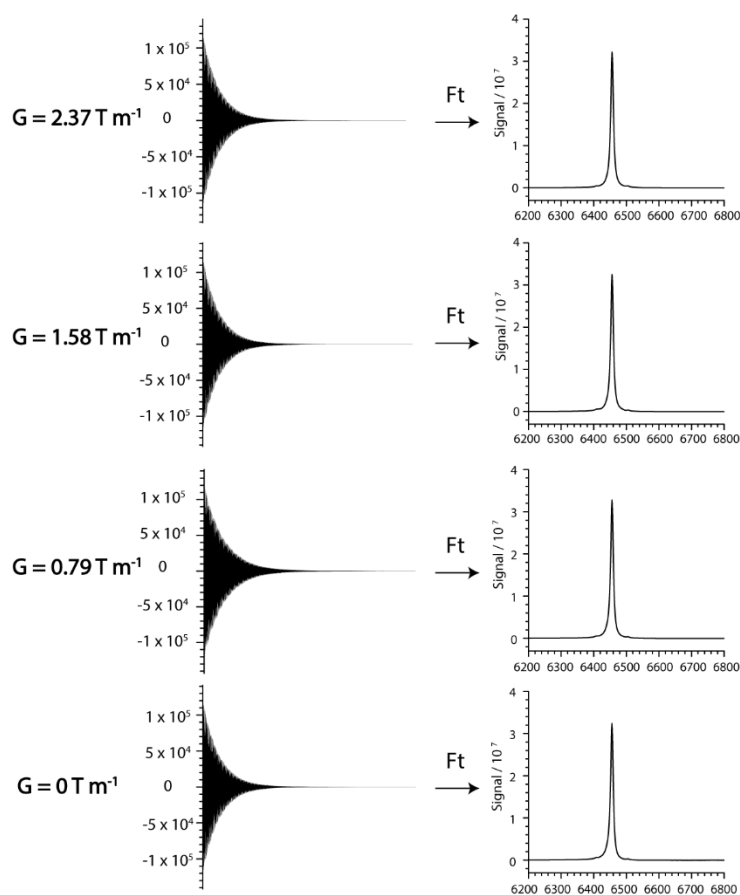
Figure 6.5: The FID decay and Fourier transformed (Ft) spectrum for PDMS using the 1D PGSTE sequence.

To determine whether these signal distortions are inherent to the CTAB/pentanol/hexane/water reverse microemulsion, 1D PGSTE and PGSTE DEXSY measurements were performed on a PDMS sample. PDMS is a high molecular weight polymer and hence diffuses very slowly (10^{-15} m^2 s^{-1}); as a result no, or very little attenuation due to diffusion is expected with the magnetic field gradient strengths available[20,28] (0 – 110 T m^{-1}). Any significant attenuation from

PDMS is a result of magnetic field gradient or phase artefacts.[20,28] No signal attenuation was observed when the 1D PGSTE sequence was performed on the PDMS sample, Figure 6.5, indicating there are no factors interfering with the PDMS signal. Conversely, when the PGSTE DEXSY sequence was performed (Figure 6.6), there was significant signal attenuation and FID distortions which, when Fourier transformed, caused peak shape phase distortions. These effects are significantly amplified for the magnetic field gradient q-steps after the mixing time, τ_m, Figure 6.6b. Since the same peak phase distortions are observed in both the CTAB/pentanol/hexane/water and PDMS samples, it is clear that the issue resides with the PGSTE DEXSY pulse sequence and not the sample.
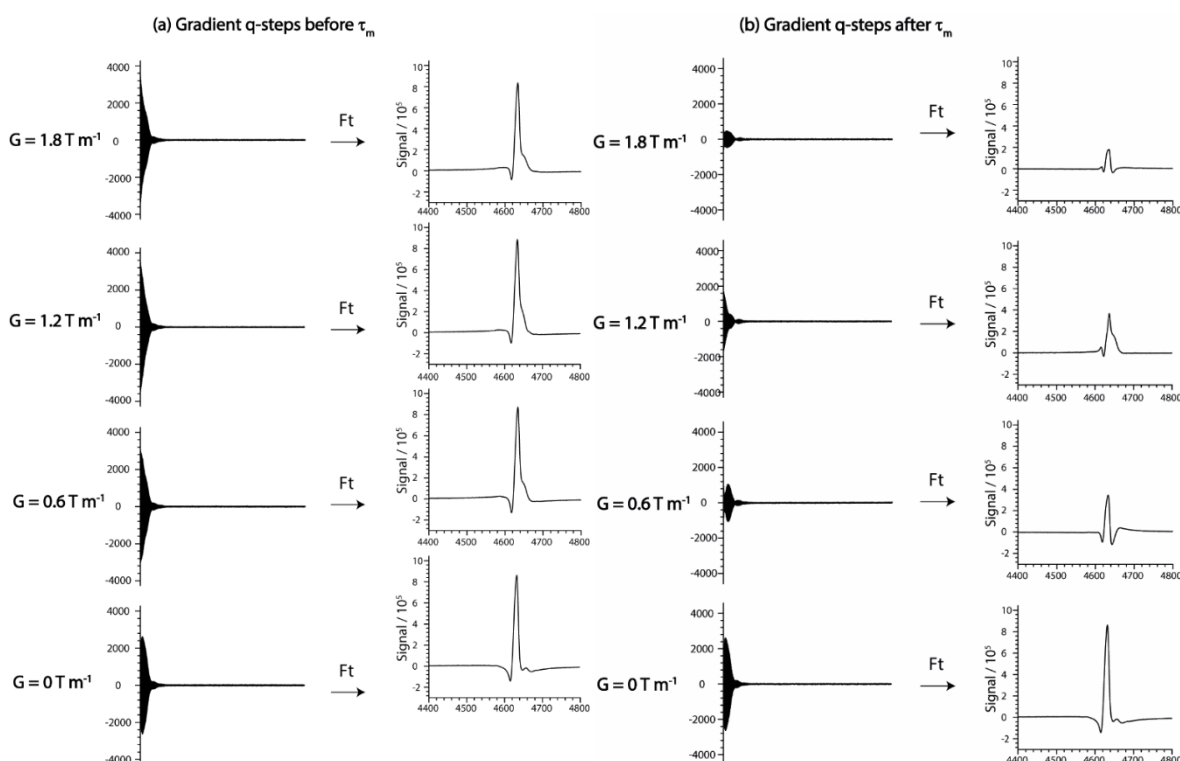
Figure 6.6: The FID decay which is Fourier transformed (Ft) for PDMS using the PGSTE DEXSY sequence for the gradient q-steps (a) before and (b) after the mixing time, τ_m. Data were collected with δ = 3 ms, Δ = 40 ms, $\boldsymbol{G}_{max}$ = 1.8 T m^{-1} and τ_m = 10 ms.

Throughout this section, a number of causes for these issues associated with the PGSTE DEXSY sequence are explored. These include eddy currents, gradient mis-match, phase cycle, pulse

sequence timings, blanking unit commands, the crusher gradients and the positions of the magnetic field gradient pulses. Each one of these potential issues is outlined in the following subsections, along with any improvements to the pulse sequence.

1. *Eddy Currents*

   Eddy currents are currents produced in the surrounding conducting material as a result of the rapid rise of the magnetic field gradient pulses.[20,31] As the magnetic field gradient strength increases, or as the rise and fall time of the magnetic field gradient pulses decreases, the effects of the eddy currents are more severe.[20] These currents have an associated magnetic field which can distort the magnetic field gradient profiles and last for a period after the magnetic field gradient pulses are switched off.[9] Eddy currents cause a number of issues for PFG measurements,[20] including phase changes in the observed spectrum and additional changes in the attenuation, which are the same issues associated with the PGSTE DEXSY sequence. Therefore, it is possible that these eddy currents are responsible for the observed signal distortions when the PGSTE DEXSY sequence is performed, hence this was explored.

   Eddy currents are minimised by inserting a delay after the magnetic field gradient pulse, known as the gradient stabilisation time, which allows the eddy currents to dissipate before further manipulation or signal acquisition.[20] The minimum gradient stabilisation time for our spectrometer was determined to be 1 ms by acquiring multiple 1D PGSTE experiments, at various gradient stabilisation times, using the PDMS sample. No signal attenuation was observed for PDMS when the gradient stabilisation time was 1 ms or greater, and hence 1 ms is sufficient to enable the eddy currents to dissipate. PGSTE DEXSY experiments were undertaken with a PDMS sample where the gradient stabilisation time was 1 ms or greater. This did not improve the artefacts observed and hence the issue cannot be a result of eddy currents.

2. Gradient Mis-Match

Diffusion measurements require the use of stable and perfectly reproducible magnetic field gradient pulses.[20] Without perfectly reproducible gradients, a situation known as gradient mis-match, the helix of phase produced by the first magnetic field gradient pulse will not be completely refocussed by the second magnetic field gradient pulse. This results in a phase-twist and causes significant loss of the signal intensity,[28,32] which affects the resultant signal attenuation due to diffusion and hence the resultant diffusion measurement. The gradient amplifier is responsible for the presence of gradient mis-match, due to the inability of some gradient amplifiers to generate reproducible magnetic field gradient pulses in quick succession.[28] Since gradient mis-match can result in significant signal loss which is not due to diffusion, and this is one of the problems associated with the PGSTE DEXSY sequence, it is possible that gradient mis-match could be an issue in the PGSTE DEXSY sequence. However, since the gradient amplifier is responsible for gradient mis-match, the artefacts associated with gradient mis-match would be present in all pulsed field gradient experiments performed, i.e. in both the 1D PGSTE and PGSTE DEXSY sequences. As the artefact is only observed in the PGSTE DEXSY sequence and not in the 1D PGSTE experiment, gradient mis-match is not an issue in this instance.

3. Phase Cycling

As previously mentioned, the phase cycle is particularly important in the PGSTE DEXSY sequence to enable efficient removal of unwanted magnetisation. An incorrect phase cycle can lead to detection of unwanted magnetisation and hence the appearance of significant peak phase distortions.[16,17] Therefore, it is possible an incorrect phase cycle could be responsible for the issues seen in the PGSTE DEXSY sequence available to us. This was explored by performing PGSTE DEXSY

measurements with different phase cycles using a PDMS sample, with the aim to obtain perfectly

phased peaks with no signal attenuation. A total of six different phase cycles were tested, including

the 8-step phase cycle reported by Callaghan et al.[18], ones based on the 1D PGSTE phase cycle and

others suggested by Klaus Zick at Bruker.[33] These phase cycles can be found in Appendix 6 along with

the 1D PGSTE phase cycle in Appendix 7. The product operators of the associated phase cycles are

shown in Appendices 6 and 7. Product operators enable one to predict how the magnetisation

evolves through the application of rf and magnetic field gradient pulses and under free precession in

the transverse plane. Magnetisation in the transverse plane evolves with a phase angle ($\omega\tau$) which is

proportional to the chemical shift of the spin. Through these product operators, it is possible to

determine where the magnetisation will end up when acquired, enabling phase cycles to be

determined so that only the wanted magnetisation is acquired. A more in-depth explanation of

product operators can be found in various text books.[9,19,21] An example of how this is performed is

shown in Figure 6.7 for the simple spin echo sequence.
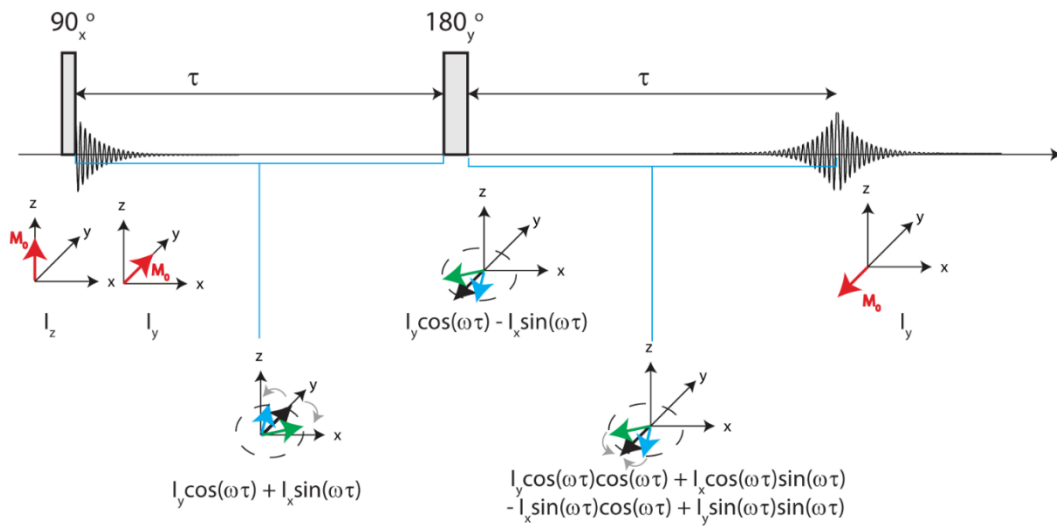
Figure 6.7: Spin echo pulse sequence showing the evolution of magnetisation and the product
operators.

Unfortunately, none of these phase cycles was able to produce perfectly phased peaks throughout all magnetic field gradient steps. The original phase cycle gave the best result, all the other phase cycles produced peaks with more severe phase distortions. Although the original phase cycle was determined to be superior, it did not produce perfectly phased peaks, which is most likely because factors other than the phase cycle are contributing to this artefact. Therefore, it was concluded that the phase cycle is not the underlying issue associated with the PGSTE DEXSY sequence signal distortions.

4. *Pulse Sequence Timings*

In a stimulated echo sequence, like PGSTE experiments, it is imperative that the time period between the first two 90° pulse and the period between the last 90° pulse and acquisition are identical,[34,35] demonstrated by τ_1 in Figure 6.8a. This ensures the start of the stimulated echo coincides with the start of acquisition. With this in mind, the same principles must be applied to the PGSTE DEXSY sequence and hence should be written as demonstrated in Figure 6.8b. However, closer inspection of the current PGSTE DEXSY sequence revealed that these two time periods were not equal. The time period between the last 90° pulse and acquisition was longer than the period between the first two 90° pulses, Figure 6.8c and hence only a portion of the stimulated echo was acquired. The pulse sequence was modified, to ensure these two time periods are equal, with the modifications displayed in Appendix 8. Although this was a necessary improvement to the pulse sequence and improved the sampling of the FID, the phase and attenuation issues still persisted.
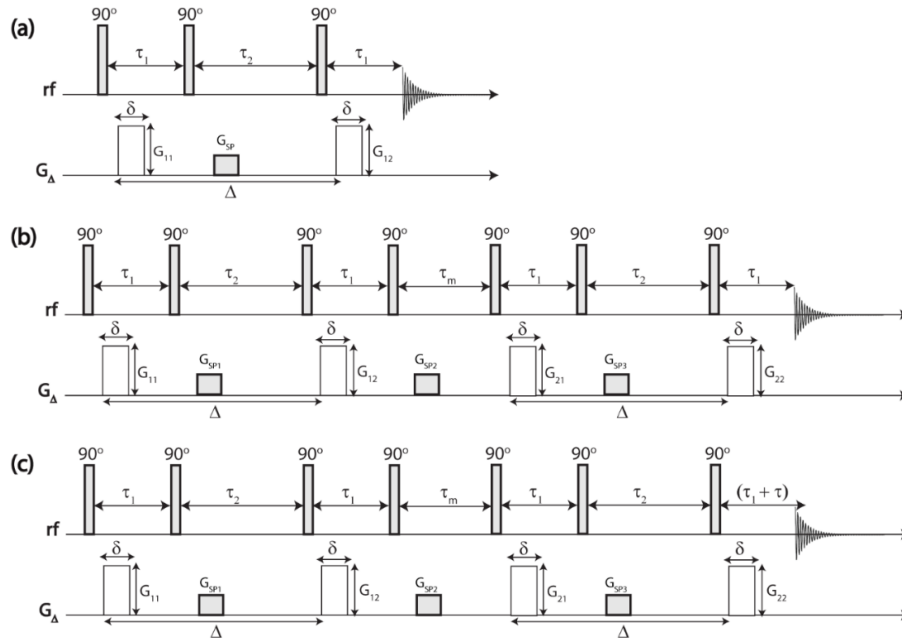
Figure 6.8: (a) 1D PGSTE pulse sequence, (b) PGSTE DEXSY pulse sequence showing the correct timings and (c) PGSTE DEXSY pulse sequence showing the current incorrect timings.

5. *Blanking Unit Commands*

When the pulsed magnetic field gradients are switched off, background noise (current) from the amplifier results in small non-random gradients.[20] These background gradients make diffusion measurements complicated as they are present during acquisition and result in signal attenuation[20] and therefore ideally should not be present. To eliminate these background gradients, the gradient coil should be blanked (disconnected from the current circuit) when the magnetic field gradient pulses are switched off.[20] In the PGSTE DEXSY sequence available to our group, the blanking commands were incorrect: the magnetic field gradients were unblanked at the start of the experiment and were not blanked again until just before acquisition. Although the magnetic field gradients were blanked during acquisition and therefore these background gradients were not presents, they are present throughout the whole of the pulse sequence. This is an issue because there should not be any form of gradients present when the magnetic field gradients are switched off, otherwise problems arise such as peak broadening and attenuation of the signal.[20] Therefore, modifications were made so that the magnetic field gradients were unblanked prior to, and blanked

immediately after, each magnetic field gradient pulse, see Appendix 9 for modifications, to eliminate

the presence of background gradients when the magnetic field gradients are switched off. PGSTE

DEXSY measurements were performed on the PDMS sample using the updated blanking unit

commands, Figure 6.9, which showed significant improvements in the shape of the FID and peak

phasing. Investigations of the PDMS signal before the mixing time, Figure 6.9a, revealed perfectly

phased peaks, with no loss in signal attenuation as the magnetic field gradient strength was

increased. However, the PDMS signal after the mixing time, Figure 6.9b, still showed signal

attenuation and peak phase distortion when the stronger magnetic field gradient was applied.

Although the PDMS signal after the mixing time is not perfect, it is an improvement of the signal

demonstrated in Figure 6.6, where the blanking commands were incorrect. Therefore, it can be

concluded these incorrect blanking unit commands were one of the major contributing factors to the

issues observed in the PGSTE DEXSY sequence that was available to our group.
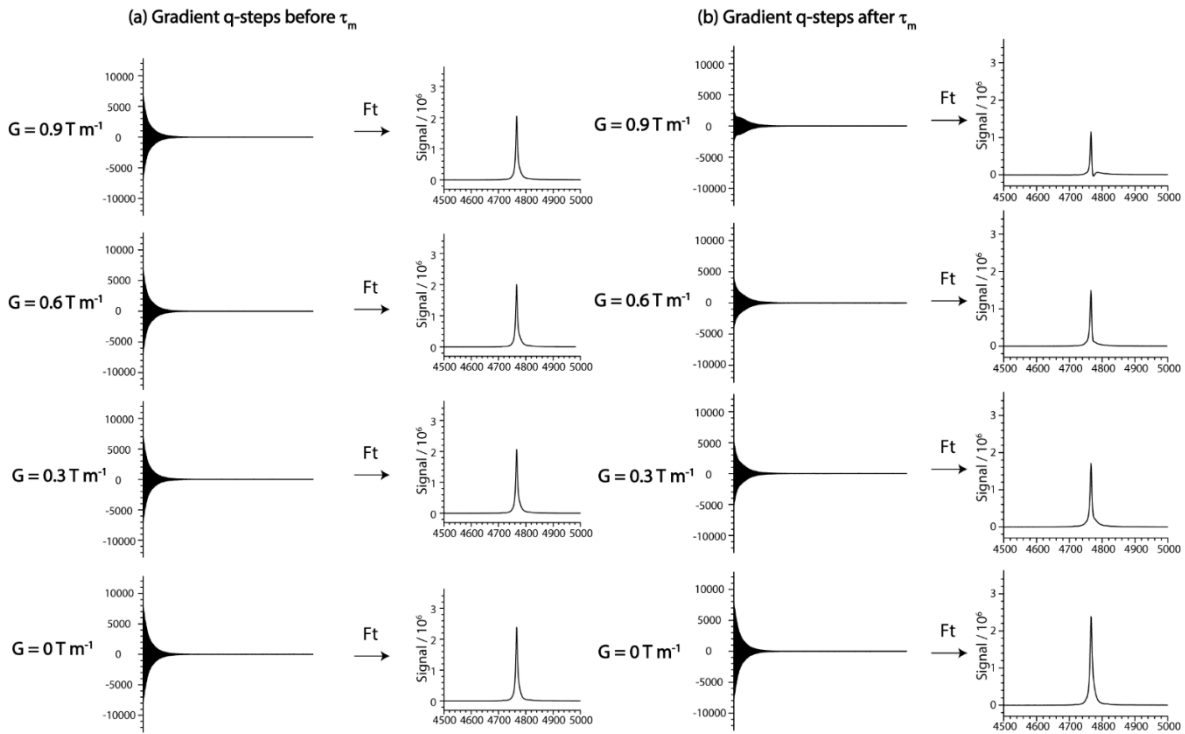
Figure 6.9: The FID decay which is Fourier transformed (Ft) for PDMS using the PGSTE DEXSY sequence, with modified blanking unit commands, for the gradient q-steps (a) before and (b) after the mixing time, τ_m. Data were acquired using $\delta = 2$ ms, $\Delta = 40$ ms, $G_{max} = 0.9$ T m^{-1} and $\tau_m = 10$ ms.

With these significant improvements to the blanking unit commands, the modified pulse

programme was tested using a more complex sample than PDMS. 1D PGSTE and PGSTE DEXSY

measurements were performed on the AOT/n-octane/water reverse microemulsion, due to the

simplicity and increased stability compared to the CTAB/pentanol/hexane/water microemulsion, and

the presence of well-defined small (AOT and water) and large (n-octane) diffusion coefficients.

Integration of the water peak in the 1D PGSTE experiment gave a diffusion coefficient D_{water}^{1D} = 5.7 ×

10^{-11} m^2 s^{-1}. The 2D water signal attenuation matrix from the PGSTE DEXSY measurements, with

modified blanking unit commands, is shown in Figure 6.10. This signal attenuation matrix has a

higher signal on the diagonal, which is shown more clearly in the signal decays in Figure 6.10b and

Figure 6.10c where the first point at zero gradient has increased intensity.

Figure 6.10: (a) 2D signal attenuation matrix for water in the AOT/n-octane/water reverse microemulsion, obtained using the PGSTE DEXSY sequence with modified blanking unit commands. Data were acquired using δ = 1 ms, Δ = 20 ms, G_{max} = 2 T m^{-1} and τ_m = 10 ms. The signal before τ_m, the first column highlighted, is plotted in (b) and the signal after τ_m, the first row highlighted, is plotted in (c).

The signal attenuation matrix was further analysed to obtain diffusion coefficients of the water before and after the mixing time, $D_{\text{water}}^{\text{before}}$ and $D_{\text{water}}^{\text{after}}$, respectively. This was done by taking the signal attenuation from the first vertical column, Figure 6.10b, and first horizontal row, Figure 6.10c, of the 2D signal attenuation matrix for water in Figure 6.10a. To enable diffusion coefficients to be obtained using the Stejskal-Tanner relationship, the first data point at higher signal intensity was removed. This analysis gave $D_{\text{water}}^{\text{before}}$ = 5.3 × 10^{-11} m^2 s^{-1} and $D_{\text{water}}^{\text{after}}$ = 2.64 × 10^{-10} m^2 s^{-1}. If the sequence is correctly functioning, the $D_{\text{water}}^{\text{before}}$ and $D_{\text{water}}^{\text{after}}$ diffusion coefficients should be approximately equal and have a similar value to $D_{\text{water}}^{\text{1D}}$. The $D_{\text{water}}^{\text{before}}$ and $D_{\text{water}}^{\text{1D}}$ are approximately the same, however $D_{\text{water}}^{\text{after}}$ is an order of magnitude bigger. A larger diffusion coefficient than expected indicates there is still an artefact affecting the signal attenuation after τ_{m}. Therefore, it can be concluded that while altering the blanking unit commands significantly improved the diffusion measurements before the mixing time, there are still issues with the pulse sequence. These issues result in the presence of the higher signal on the diagonal of the 2D signal attenuation matrix, and additional signal attenuation in the diffusion experiments after the mixing time. Since there are still issues, further modifications are needed to rectify the pulse sequence fully.

6. *Position of Magnetic Field Gradient Pulses and Spoiler Gradients*

In PGSTE experiments the magnetic field gradient pulses need to be immediately after the RF pulses to allow for the shortest possible τ_1, the time between the first two RF pulses.[36] Signal during the τ_1 period decays according to T_2 relaxation,[36] and hence in systems with short T_2 relaxation like the CTAB/pentanol/hexane/water microemulsion, the τ_1 period needs to be short, $\tau_1 < T_2$, to minimise signal loss. To avoid this issue, the time period between the 90° pulse and magnetic field gradient pulse must be as short as possible. However, there needs to be sufficient period between

the rf and magnetic field gradient pulses to enable the rf pulse to dissipate. The rf pulse is felt for a period after being switched off,[37] known as the pulse ringdown effect; therefore, if the magnetic field gradient pulse is applied too soon, the start of the signal will be corrupt. In modifying this pulse sequence to shorten τ_1, the time between the rf and magnetic field gradient pulses was decreased from 1 ms to 0.1 ms, which allows sufficient time for the rf pulse ringdown and shortens the τ_1 period by 0.9 ms. As a result, the τ_2 period, Figure 6.1b, was lengthened by 0.9 ms to ensure the total experiment time was the same.

Moreover, PGSTE experiments also require the spoiler gradients to be applied immediately after the rf pulse to ensure the spoiler de-phases the maximum amount of unwanted signal in the transverse plane. In the PGSTE DEXSY sequence available to our group, the spoiler gradient is not immediately after the 90° rf pulse, the separation is half the time of Δ and therefore varies depending upon the experimental parameters. Therefore, to ensure efficient use of the spoiler gradients, the time between the rf pulse and the spoiler gradient was reduced to 0.1 ms (the pulse ringdown delay), and the period between the spoiler and the next rf pulse was lengthened appropriately to ensure the total experimental time is unchanged. Both these modifications to the pulse sequence can be found in Appendix 10. These modifications did not remove the artefact, resulting in higher signal on the diagonal of the 2D signal attenuation matrix, Figure 6.10a, but it did improve the signal-to-noise ratio.

7. Crusher/Spoiler Gradients

Spoiler gradients are utilised in pulse sequences to eliminate any unwanted transverse magnetisation by applying a gradient to shift the phase of the unwanted spins without affecting the wanted z-magnetisation.[9] The PGSTE DEXSY sequence has three spoiler gradients, $\boldsymbol{G}_{SP1}$, $\boldsymbol{G}_{SP2}$ and $\boldsymbol{G}_{SP3}$, Figure 6.11a. In the PGSTE DEXSY sequence available to our group, these spoiler gradients all have

equal intensity and duration, Figure 6.11a, just like the magnetic field gradient pulse pairs G_{11}, G_{12} and G_{21}, G_{22}. Therefore, this could lead to the spoiler gradients' acting in a similar way to magnetic field gradient pulse pairs. The first magnetic field gradient of the pulse pair (G_{11} or G_{21}) causes the magnetisation to be twisted into a helix of phase, the second magnetic field gradient pulse (G_{12} or G_{22}) untwists this helix and refocuses the signal. This refocusing of the signal can only occur if the G and δ are identical for both magnetic field gradients of the pulse pair. Since the G and δ of the three spoiler gradients are identical, this could lead to one spoiler gradient shifting the phase of the unwanted magnetisation, only for a successive spoiler gradient to refocus it. If this occurs, the unwanted magnetisation from the first spoiler gradient is not eliminated, it is refocused later in the pulse sequence by another spoiler gradient. Therefore, not all of the unwanted magnetisation is eliminated by the spoiler gradients, resulting in signal distortions, such as peaks that cannot be phased. The refocusing of unwanted magnetisation by the spoiler gradients could be responsible for the higher signal on the diagonal of the 2D signal attenuation matrix. This was explored by modifying the spoiler gradients in the pulse sequence so that the G and δ are different for each gradient pulse. The modified spoiler gradients can be found in Figure 6.11b, and the pulse sequence modifications in Appendix 11. After these spoiler gradient, blanking unit and magnetic field gradient position modifications, PGSTE DEXSY measurements were performed on the PDMS sample, Figure 6.12, which showed very little signal attenuation both before and after the mixing time. This seems to suggest the PGSTE DEXSY sequence is now artefact-free and functioning correctly.
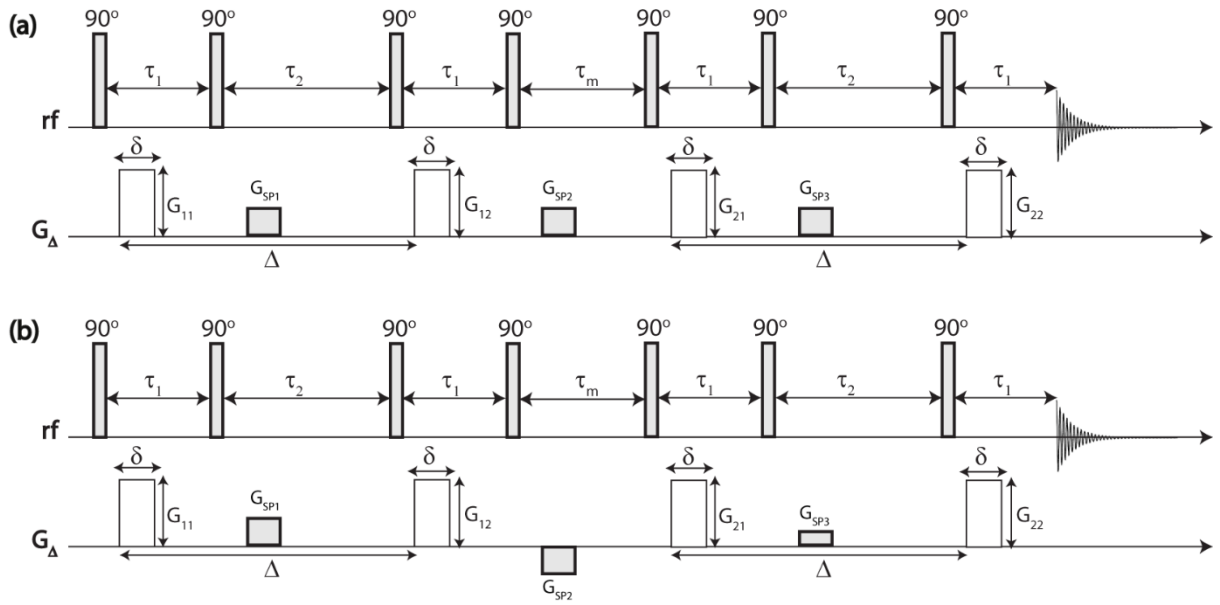
Figure 6.11: Pulse sequences to show how the spoiler gradients were modified with (a) showing the original spoiler gradients and (b) showing the modified spoiler gradients.

To further confirm the pulse sequence is now working correctly, measurements were performed on the AOT/n-octane/water reverse microemulsion by integration of the water peak to give the 2D water signal attenuation matrix shown in Figure 6.13. A clear improvement of this 2D water signal attenuation matrix is the elimination of the zipper artefact, indicating there was refocusing of unwanted magnetisation by the spoiler gradients. Further investigations obtained $D_{water}^{before} = 5.1 \times 10^{-11}$ m^2 s^{-1} and $D_{water}^{after} = 7 \times 10^{-11}$ m^2 s^{-1} which are similar to $D_{water}^{1D} = 5.7 \times 10^{-11}$ m^2 s^{-1}. As the D_{water}^{before} and D_{water}^{after} are in the region of D_{water}^{1D}, it can be concluded that the pulse sequence has been sufficiently modified for use in investigating the CTAB/pentanol/hexane/water reverse microemulsion.
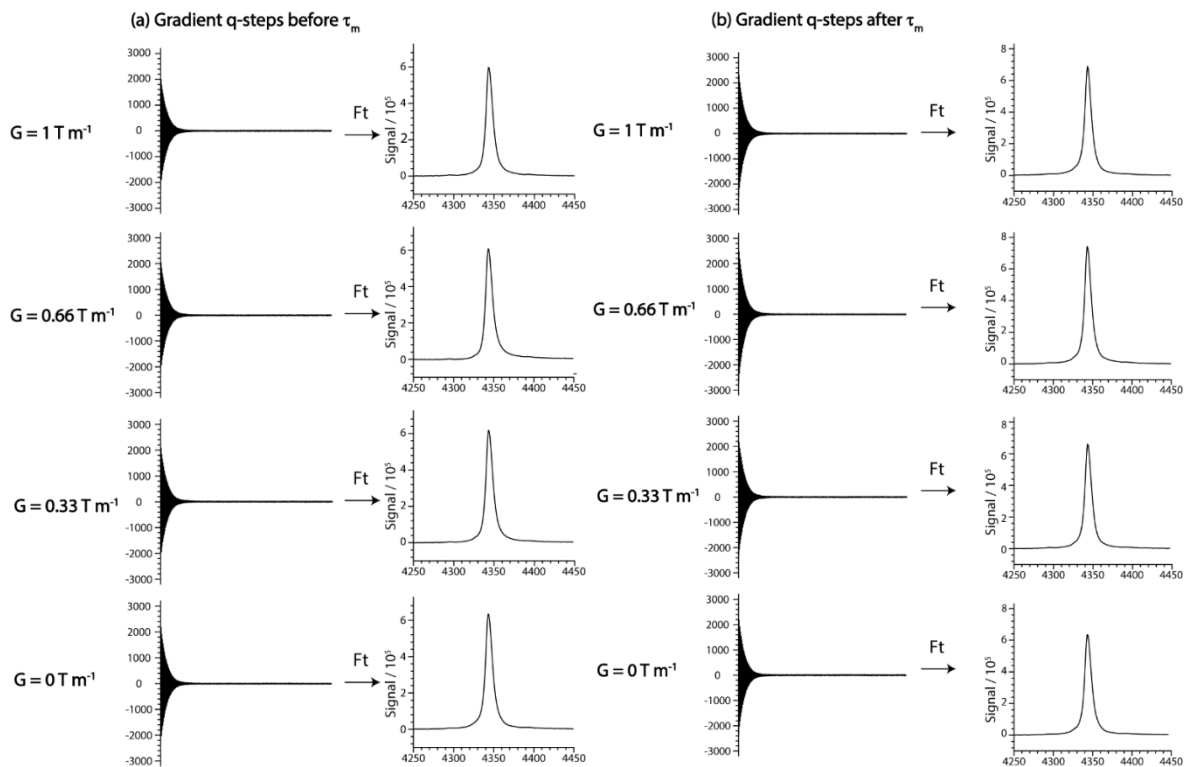
Figure 6.12: The FID decay which is Fourier transformed (Ft) for PDMS using the PGSTE DEXSY sequence, with modified spoiler gradients, for the gradient q-steps (a) before and (b) after the mixing time, τ_m. Data were acquired using δ = 2 ms, Δ = 100 ms, $\boldsymbol{G}_{max}$ = 1 T m^{-1} and τ_m = 10 ms.
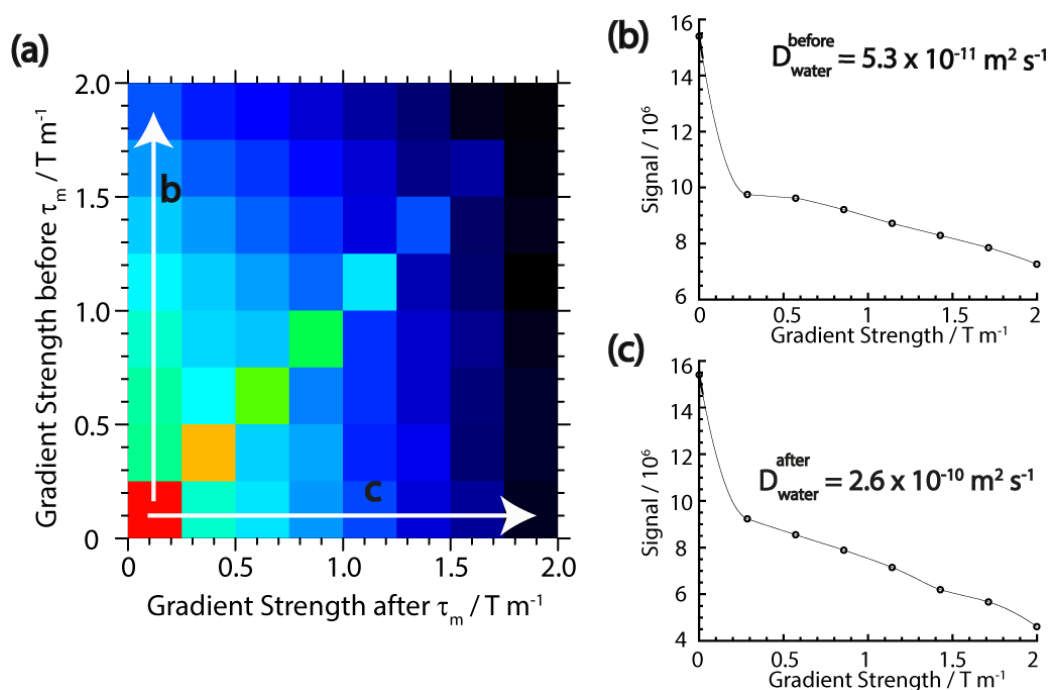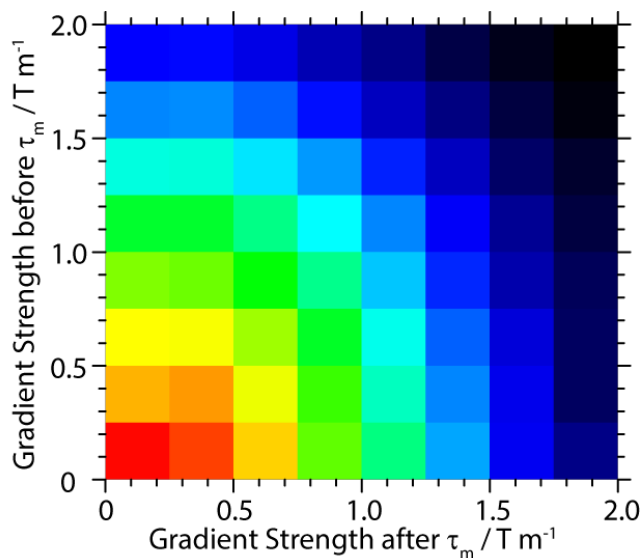

Figure 6.13: 2D signal attenuation matrix for water in the AOT/n-octane/water reverse microemulsion, obtained using the PGSTE DEXSY sequence with modified blanking unit commands. Data were acquired using δ = 2 ms, Δ = 100 ms, $\boldsymbol{G}_{max}$ = 1 T m^{-1} and τ_m = 10 ms.

6.4 Results and Discussion

A series of 2D $\log_{10}(D)$–$\log_{10}(D)$ distribution matrices for CTAB are presented in Figure 6.14. These plots show a single peak on diagonal for all mixing times at both Δ = 40 ms (Figure 6.14a–d) and Δ = 20 ms (Figure 6.14e). The diffusion coefficient of this CTAB environment is $D_{CTAB} \approx 2 \times 10^{-10}$ $m^2\,s^{-1}$ which represents CTAB in the RM interface. 1D diffusion measurements performed on this sample in preceding chapters of this thesis have demonstrated that the behaviour of CTAB changes over a period of time. Initially, two diffusion coefficients are obtained for CTAB at short observation times ($\Delta \leq$ 40 ms) representing CTAB in the RM interface and in the bulk continuous phase. However, after 6 hours, only one CTAB diffusion coefficient was obtained for both short and long observation times representing CTAB in the RM interface. Each 2D DEXSY measurement performed took a total of 37 hours to complete, which surpasses the timescale over which the system changes and hence the presence of a single CTAB environment was not surprising. The diffusion coefficient of this single CTAB peak in these 2D $\log_{10}(D)$–$\log_{10}(D)$ distribution matrices, $D_{CTAB} \approx 2 \times 10^{-10}$ $m^2\,s^{-1}$, compares well with the corresponding 1D measurement of CTAB for the aged microemulsion of $D_{CTAB}^{1D} = 2.04 \times 10^{-10}$ $m^2\,s^{-1}$. Therefore, due to the extremely long experimental time and the presence of a single CTAB environment, it was concluded that these DEXSY measurements are probing the CTAB/pentanol/hexane/water reverse microemulsion in its aged state.
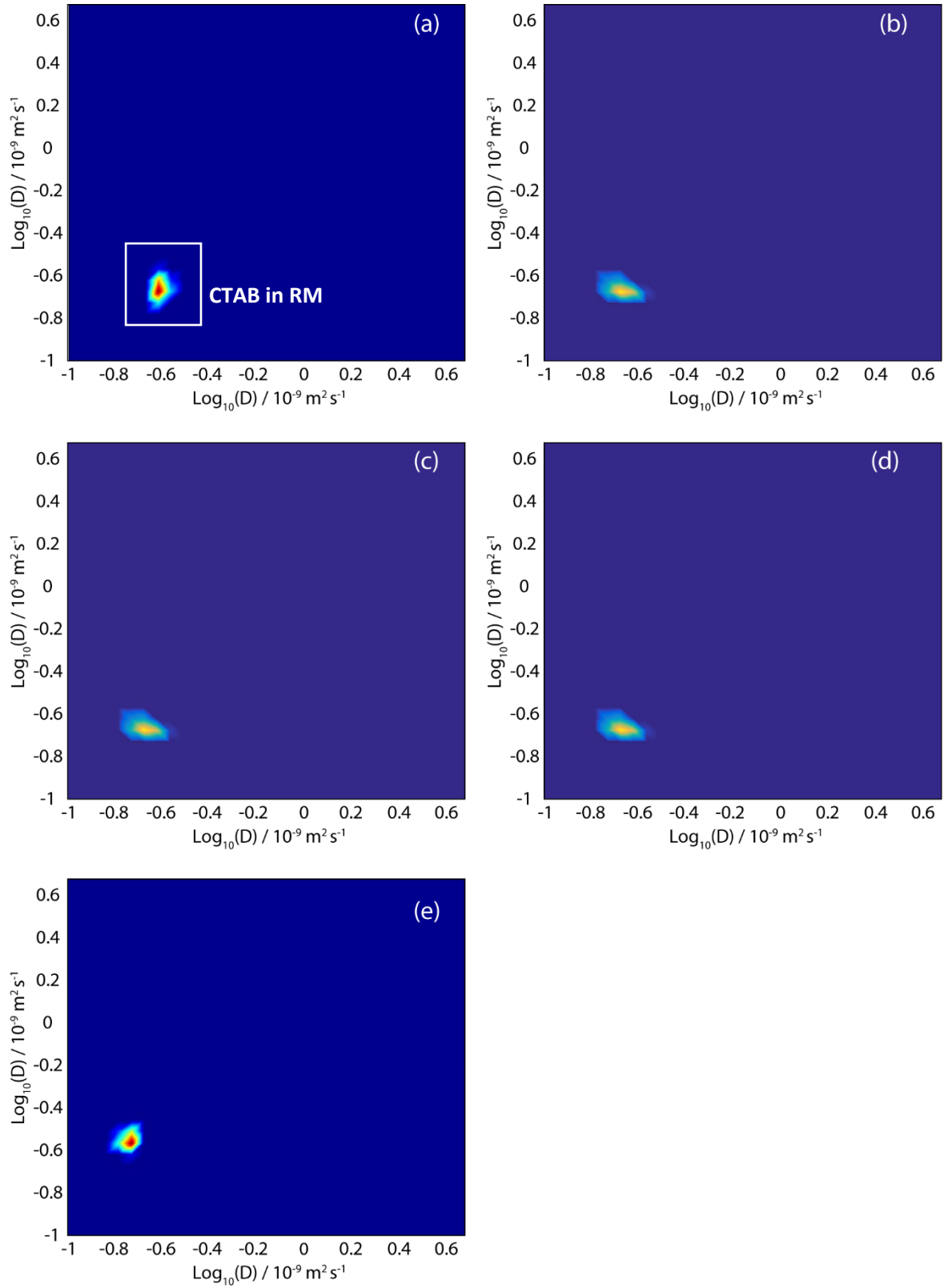
Figure 6.14: Intensity $\log_{10}(D)$–$\log_{10}(D)$ distribution matrix for CTAB, H_a, when Δ = 40 ms (a–d) and Δ = 20 ms (e) where the mixing time, τ_m, was (a) 10 ms, (b) 50 ms, (c) 100 ms, (d) 300 ms and (e) 10 ms.

The behaviour of the pentanol co-surfactant was also probed in these PGSTE DEXSY experiments to produce 2D $\log_{10}(D)$–$\log_{10}(D)$ distribution matrices, shown in Figure 6.15, for various mixing times at $\Delta = 40$ ms and $\Delta = 20$ ms. When an observation time of 40 ms is employed, a single peak on diagonal with a diffusion coefficient of approximately 1.5×10^{-9} m^2 s^{-1} is obtained in the 2D $\log_{10}(D)$–$\log_{10}(D)$ distribution matrix regardless of the mixing time, Figure 6.15a–d. This single peak represents a weighted average diffusion coefficient because pentanol is exchanging between the RM interface and the continuous phase. Previous 1D diffusion measurements of the fresh CTAB/pentanol/hexane/water reverse microemulsion, chapters 3 and 4, have obtained two pentanol diffusion coefficients, representing pentanol in the RM interface and the continuous phase, at $\Delta \leq 40$ ms and a single averaged diffusion coefficient at long Δ due to exchange between the two environments. However, these PGSTE DEXSY measurements probe the microemulsion in its aged state, because of the lengthy experimental time, and the single averaged pentanol environment due to exchange is observed at a shorter observation time of 40 ms. This suggests the pentanol exchange is faster in the aged microemulsion. However, these DEXSY measurements cannot quantify this exchange process due to the presence of a single diffusion environment: DEXSY requires the exchange to occur between two environments of different diffusion coefficients to enable the presence of exchange peaks.[1,2]

While a single on-diagonal peak is observed in the pentanol $\log_{10}(D)$–$\log_{10}(D)$ distribution matrices at $\Delta = 40$ ms, two on-diagonal peaks are obtained for pentanol when DEXSY measurements are performed using $\Delta = 20$ ms, Figure 6.15e. These two on-diagonal peaks have diffusion coefficients of $D = 2 \times 10^{-10}$ m^2 s^{-1} and $D = 1.4 \times 10^{-9}$ m^2 s^{-1}, representing pentanol in the RM interface and the continuous phase, respectively. These diffusion coefficients compare well with previous 1D diffusion measurements performed on the aged reverse microemulsion at $\Delta = 20$ ms, chapter 4, where the diffusion coefficients were $D_{CS}^{mic} = 3.05 \times 10^{-10}$ m^2 s^{-1} (0.04) and $D_{CS}^{bulk} = 1.50 \times 10^{-9}$ m^2 s^{-1} (0.96).
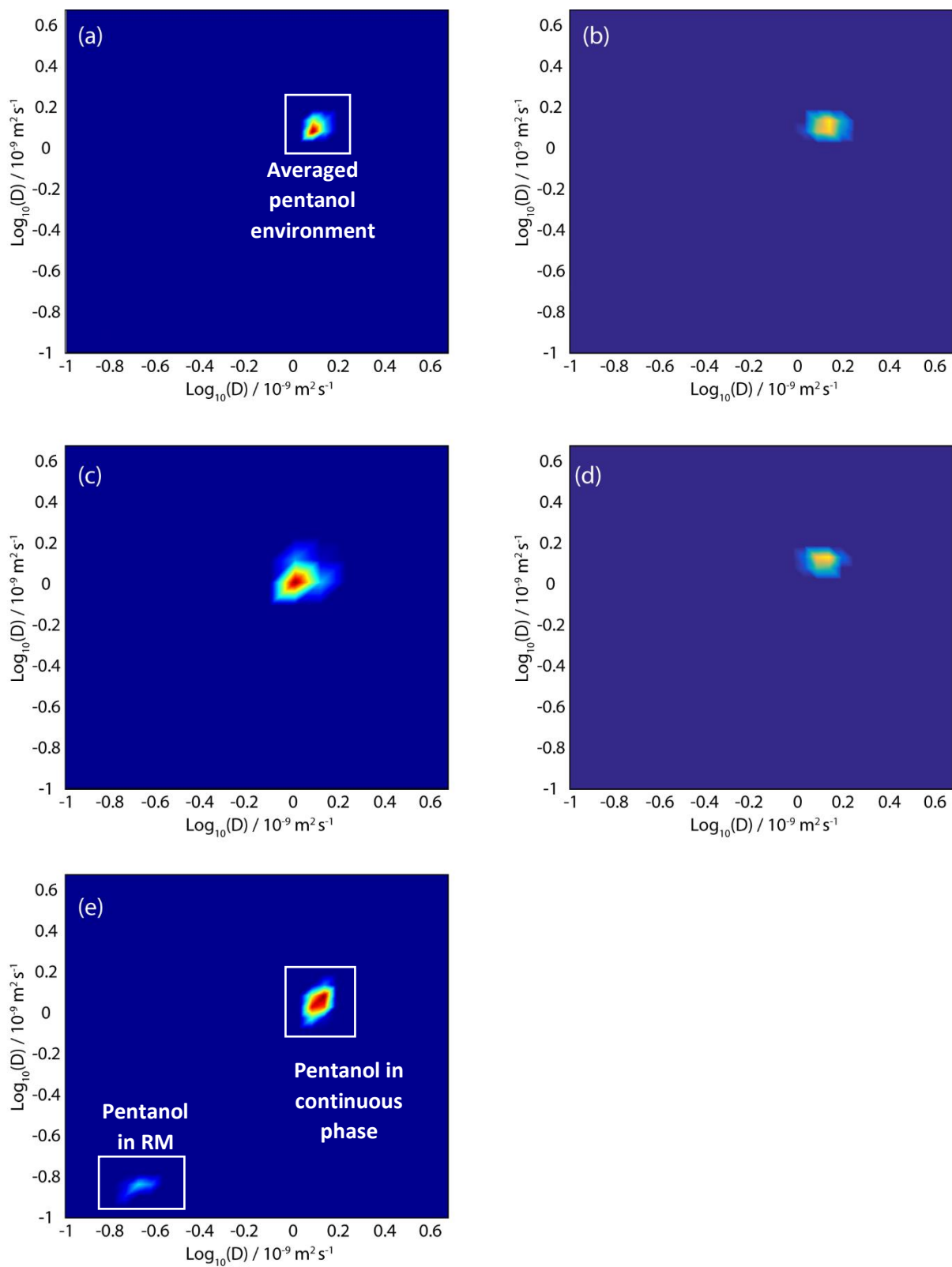
Figure 6.15: Intensity $\log_{10}(D)$–$\log_{10}(D)$ distribution matrix for pentanol, H_g, when $\Delta = 40$ ms (a–d) and $\Delta = 20$ ms (e) where the mixing time, τ_m, was (a) 10 ms, (b) 50 ms, (c) 100 ms, (d) 300 ms and (e) 10 ms.

As two separate diffusion coefficient environments are obtained in these DEXSY measurements at Δ = 20 ms for pentanol, which is known to be exchanging between these two environments, exchange peaks are expected to be present. Surprisingly, these exchange peaks are not observed, particularly since exchange peaks were observed when analysing pentanol exchange via REXSY measurements, chapter 5.

The absence of pentanol exchange peaks in this DEXSY experiment at Δ = 20 ms, but the presence of pentanol exchange peaks in REXSY measurements may be due to the different relative contributions of pentanol in the RM interface measured by the two different techniques. The previous 1D diffusion measurements performed in chapter 4 on the aged RM gave a proportion of pentanol in the interface of 0.04, which is very small. A larger amount of interfacial pentanol of 0.6 was determined by 1D T_2 relaxation measurements in the same chapter. The small amount of interfacial pentanol measured by diffusion, and hence DEXSY, is demonstrated by a very weak peak in the pentanol $\log_{10}(D)$–$\log_{10}(D)$ distribution matrix in Figure 6.15e. Since diffusion and DEXSY measurements determine a small amount of pentanol molecules in the RM interface, the amount of exchanging pentanol molecules in DEXSY measurements will be even smaller. This will result in exchange peaks of lower intensity than the peak responsible for pentanol in the RM interface at $\log_{10}(D)$ = −0.7 (D = 2 × 10^{-10} m^2 s^{-1}). The intensity of these exchange peaks are weak relative to the intensity of the peak responsible for pentanol in the continuous phase at $\log_{10}(D)$ = 0.15 (D = 1.4 × 10^{-9} m^2 s^{-1}); therefore, these exchange peaks were not visible in the $\log_{10}(D)$–$\log_{10}(D)$ distribution matrix. REXSY measurements have a higher proportion of pentanol in the RM and hence peaks due to exchanging pentanol were strong enough to be observed in the $\log_{10}(T_2)$–$\log_{10}(T_2)$ distribution plots.

As the exchange peaks were not visible in the pentanol $\log_{10}(D)$–$\log_{10}(D)$ distribution matrix due to their weak intensity, exchange was probed by taking the signal of all the RM components,

(CTAB, pentanol, hexane and water). In the REXSY chapter, this analysis was found to be advantageous due to the increased signal-to-noise ratio, and therefore it was thought it may produce exchange peaks that are strong enough to be visible using DEXSY measurements. The 2D $\log_{10}(D)-\log_{10}(D)$ distribution matrices produced using this analysis method are shown in Figure 6.16. All these plots have two peaks on-diagonal, the peak at $\log_{10}(D) = -0.8$ to -0.6 ($D = 1.6 - 2.5 \times 10^{-10}$ $m^2\ s^{-1}$) represents CTAB, pentanol and water in the RM interface and the peak at $\log_{10}(D) = 0.6$ ($D = 2.5 \times 10^{-9}\ m^2\ s^{-1}$) represents pentanol and hexane in the continuous phase. Once more, there were no observed exchange peaks as the intensity of the peak responsible for CTAB, pentanol and water in the RM is very weak and barely visible. The signal from any exchange peaks was so weak relative to the high intensity of the peak responsible for pentanol and hexane in the continuous phase, they cannot be observed.

Although the literature suggests that these DEXSY measurements should be possible as two separate diffusion coefficients are obtained,[1,9] and the diffusion fluctuations are smaller than τ_m,[2] it appears that there needs to be a significant population of each exchanging species in order to observe the vital exchange peaks. An effort was made to enhance the proportion of pentanol molecules observable in the RM interface by individually increasing ω_0, P_0 and ϕ_d, whilst keeping all the other components constant. These microemulsions were studied by 1D PGSTE measurements and showed no significant increase in the contribution of pentanol molecules in the RM interface. Therefore, it was concluded that these PGSTE DEXSY measurements are not suitable for measuring exchange in this CTAB/pentanol/hexane/water reverse microemulsion.
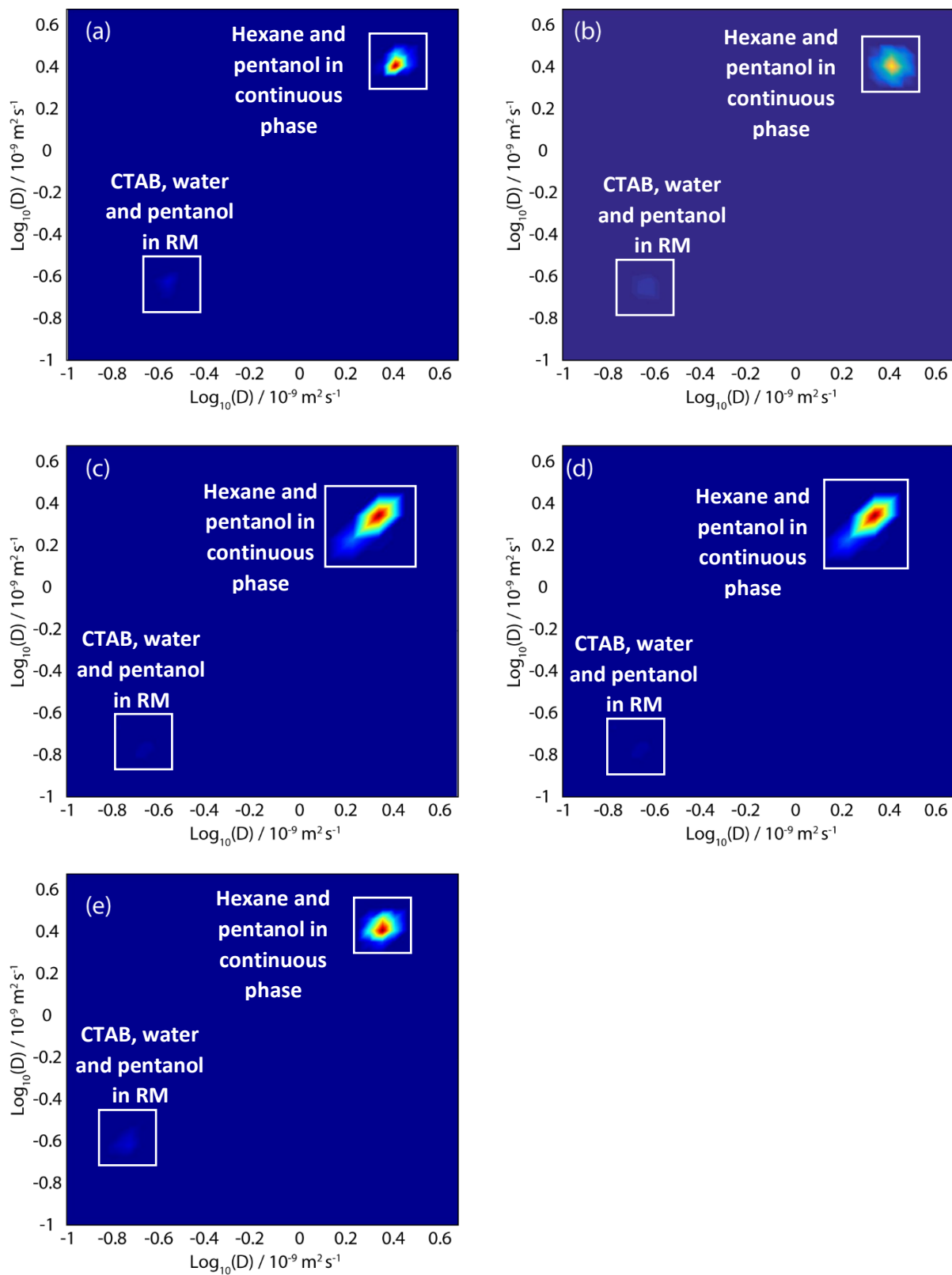
Figure 6.16: Intensity $\log_{10}(D)$–$\log_{10}(D)$ distribution matrix by taking a single point at the top of the echo when $\Delta = 40$ ms (a–d) and $\Delta = 20$ ms (e) where the mixing time, τ_m, was (a) 10 ms, (b) 50 ms, (c) 100 ms, (d) 300 ms and (e) 10 ms.

6.5 Conclusion

Initial PGSTE DEXSY measurements of the CTAB/pentanol/hexane/water reverse microemulsion revealed significant distortions to the NMR signal, which led to peaks that could not be phased and a faster rate of signal attenuation than expected. This had a substantial impact on the accuracy of DEXSY measurements of this system, and hence significant developments to the pulse sequence were required. The major modifications required included updating the blanking unit commands, modifying the amplitude of the spoiler gradients so they are no longer equal and moving the position of the spoiler gradient and magnetic field gradient pulses. These modifications were verified using PDMS and a more stable AOT/n-octane/water reverse microemulsion and enabled PGSTE DEXSY measurements to be performed on the CTAB/pentanol/hexane/water reverse microemulsion.

Due to the lengthy experimental time of these PGSTE DEXSY experiments, measurements were performed on the aged CTAB/pentanol/hexane/water reverse microemulsion and therefore only a single CTAB environment was obtained. The $\log_{10}(D)-\log_{10}(D)$ distribution plot for pentanol at $\Delta = 40$ ms showed only one averaged environment, where previously two are obtained in the initial microemulsion, therefore, it is suggested pentanol exchange is faster in the aged microemulsion. Unfortunately, no exchange peaks were observed due to the small proportion of molecules appearing in the RM interface (0.04) and hence any exchanging molecules are not visible due to their weak intensity. This led to the conclusion that PGSTE DEXSY measurements are not suitable for this system, as a significant population of molecules must reside in both the RM interface and the continuous phase to obtain observable exchange peaks. Although PGSTE DEXSY is not suitable for this particular system, it is believed these PGSTE DEXSY measurements can be applied to dynamic solution state systems, provided there is a significant population of each exchanging species in order to observe the vital exchange peaks.

6.6 References

(1)   Callaghan, P. T.; Furo, I. *J. Chem. Phys.* **2004**, *120*, 4032.

(2)   Callaghan, P. T.; Godefroy, S.; Ryland, B. N. *Magn. Reson. Imaging* **2003**, *21*, 243.

(3)   Gratz, M.; Wehring, M.; Galvosas, P.; Stallmach, F. *Micropor. Mesopor. Mat.* **2009**, *125*, 30.

(4)   Hubbard, P. L.; McGrath, K. M.; Callaghan, P. T. *Langmuir* **2005**, *21*, 4340.

(5)   Hubbard, P. L.; McGrath, K. M.; Callaghan, P. T. *J. Phys. Chem. B* **2006**, *110*, 20781.

(6)   Galvosas, P.; Qiao, Y.; Schonhoff, M.; Callaghan, P. T. *Magn. Reson. Imaging* **2007**, *25*, 497.

(7)   Neudert, O.; Stapf, S.; Mattea, C. *J. Magn. Reson.* **2011**, *208*, 256.

(8)   Qiao, Y.; Galvosas, P.; Adalsteinsson, T.; Schonhoff, M.; Callaghan, P. T. *J. Chem. Phys.* **2005**, *122*, 9.

(9)   Callaghan, P. T. *Translational Dynamics & Magnetic Resonance: Principles of Pulsed Gradient Spin Echo NMR*; Oxford University Press: Oxford, 2011.

(10)   Song, Y. Q.; Venkataramanan, L.; Burcaw, L. *J. Chem. Phys.* **2005**, *122*, 8.

(11)   Song, Y. Q.; Zielinski, L.; Ryu, S. *Phys. Rev. Lett.* **2008**, *100*, 4.

(12)   Venkataramanan, L.; Song, Y. Q.; Hurlimann, M. D. *IEEE Trans. Signal Process.* **2002**, *50*, 1017.

(13)   Washburn, K. E.; Callaghan, P. T. *Phys. Rev. Lett.* **2006**, *97*, 4.

(14)   Fordham, E. J.; Sezginer, A.; Hall, L. D. *J. Magn. Reson. Ser. A* **1995**, *113*, 139.

(15)   Song, Y. Q.; Venkataramanan, L.; Hurlimann, M. D.; Flaum, M.; Frulla, P.et al. *J. Magn. Reson.* **2002**, *154*, 261.

(16)   Bain, A. D. *J. Magn. Reson.* **1984**, *56*, 418.

(17)   Stejskal, E. O.; Schaefer, J. *J. Magn. Reson.* **1974**, *14*, 160.

(18)   Khrapitchev, A. A.; Callaghan, P. T. *J. Magn. Reson.* **2001**, *152*, 259.

(19)   Callaghan, P. T. *Principles of Nuclear Magnetic Resonance Microscopy*; Clarendon Press, 1993.

(20)   Price, W. S. *NMR Studies of Translational Motion: Principles and Applications*; Cambridge University Press, 2009.

(21)   Keeler, J. *Understanding NMR Spectroscopy*; Second Edition ed.; John Wiley & Sons, Ltd, 2010.

(22)   Tanner, J. E. *J. Chem. Phys.* **1970**, *52*, 2523.

(23)   Momot, K. I.; Kuchel, P. W. *Concepts Magn. Reson. Part A* **2006**, *28A*, 249.

(24)   Momot, K. I.; Kuchel, P. W.; Chapman, B. E. *J. Magn. Reson.* **2005**, *176*, 151.

(25)   Stilbs, P. *Prog. Nucl. Magn. Reson. Spectrosc.* **1987**, *19*, 1.

(26)   Torres, A. M.; Zheng, G.; Price, W. S. *Magn. Reson. Chem.* **2010**, *48*, 129.

(27)   Halliday, N. A.; Peet, A. C.; Britton, M. M. *J. Phys. Chem. B.* **2010**, *114*, 13745.

(28)   Price, W. S.; Hayamizu, K.; Ide, H.; Arata, Y. *J. Magn. Reson.* **1999**, *139*, 205.

(29)   Claridge, T. D. W. *High-Resolution NMR Techniques in Organic Chemistry*; 2nd Edition ed.; Elsevier, 2009; Vol. 27.

(30)   Wu, D. H.; Chen, A. D.; Johnson, C. S. *J. Magn. Reson. Ser. A* **1995**, *115*, 260.

(31)   Robertson, S.; Hughes, D. G.; Liu, Q.; Allen, P. S. *Magn. Reson. Med.* **1992**, *25*, 158.

(32)   Callaghan, P. T. *J. Magn. Reson.* **1990**, *88*, 493.

(33)   Zick, K., Personal Communication Regarding PGSTE DEXSY Phase Cycle.

(34)   Burstein, D. *Concepts Magn. Resonance* **1996**, *8*, 269.

(35)   Hahn, E. L. *Phys. Rev.* **1950**, *80*, 580.

(36)   Zick, K.; GmbH, B. B., Ed. 2009.

(37)   Simpson, J. H. *Organic Structure Determination Using 2-D NMR Spectroscopy: A Problem-Based Approach*; Elsevier/AP, 2012.

7. Concluding Remarks and Further Work

The research carried out in this thesis has focused on investigating CTAB reverse microemulsions through the use of NMR and molecular modelling. These methods have provided a more detailed picture of the reverse micelle microstructure, size, shape and the exchange processes occurring.

NMR relaxation and diffusion measurements were performed on the CTAB/alcohol/hexane/water reverse microemulsions where the alcohol was butanol, pentanol, hexanol and heptanol. Through these investigations it was determined that the co-surfactant is distributed between the RM interface and the continuous phase and it exchanges between these two environments on a millisecond timescale. This research has provided the first quantification of co-surfactant exchange in the CTAB/pentanol/hexane/water reverse microemulsion by means of relaxation exchange spectroscopy (REXSY). These measurements demonstrated the first application of REXSY, which are commonly only performed on solid porous materials such as rocks, to complex and dynamic reverse micelle systems. The exchange times of pentanol from the RM interface to the continuous phase and vice versa were determined to be 8 ms and 13 ms, respectively, through monitoring the intensity of the exchange peaks as a function of mixing time, τ_m.

Diffusion exchange spectrosopy (DEXSY) measurements were also performed on the CTAB/pentanol/hexane/water RM but proved unsuccessful. The small propotion of pentanol molecules appearing in the RM interface lead to a small proportion of exchanging molecules and hence an exchange peak of weak intensity, so weak they were not visible. Therefore, it was concluded that for successful DEXSY measurements there must be a significant population of molecules in both the RM interface and the continuous phase to obtain observable exchange peaks.

In addition to determining the exchange of co-surfactant, the proportion of alcohol in the RM interface was able to be determined using two different methods: the diffusion measurements combined with the Lindman equation and REXSY measurements. This was the first determination of interfacial co-surfactant via REXSY measurements, which was performed using a combination of the calculated exchange rates and the equilibrium constant. The proportion of co-surfactant in the RM interface calculated via REXSY is consistent with those determined using the 1D NMR diffusion data of the system, which validates this method. Therefore, this study has provided the first determination of molecular distribution in an exchanging system using REXSY measurments and hence demonstrates an alternative method of molecular distribution. The proportion of co-surfactant in the interface was dertemined for all the RM systems and was found to decrease with increasing alcohol chain length, with the exception of the CTAB/pentanol/hexane/water system which had the highest proportion of pentanol in the interface.

The CTAB/pentanol/hexane/water reverse microemulsion was found to behave differently to the other CTAB/alcohol/hexane/water RMs studied in this research. The CTAB/pentanol/hexane/water RM was found to have initially two CTAB environments; however, after time, the system changed to produce one CTAB environment which was determined to be in the RM interface. CTAB was determined to be solely in the RM interface for all the other CTAB/alcohol/hexane/water RM systems. The nature of these two CTAB environments for the CTAB/pentanol/hexane/water RM were attributed to be CTAB in the reverse micelle interface and in the continuous phase as either monomer or a small aggregate. The exact form of this CTAB in the continuous phase is unknown and further work needs to be done to determine this.

All the microemulsions were determined to have a unimodal distribution of droplet sizes where the sizes decreased with increasing alcohol chain length. However, the CTAB/pentanol/hexane/water reverse microemulsion behaves differently and initially has bimodal

droplet sizes which become unimodal over time to produce the largest droplets of all the microemulsions studied. This larger droplet was thought to be due to the pentanol co-surfactant solubilising the most water.

The shapes of the all the reverse micelle droplets were investigated using molecular dynamics and were determined to be oblate, where previously they were assumed to be spherical. The knowledge of the droplet shape has enabled the determination of two droplet radii, *a* and *c*, using a combination of the molecular modelling aspect ratio and the diffusion data. Probing the interfacial composition of the CTAB/pentanol/hexane/water molecular simulated droplet showed the change in shape is associated with a non-homogeneous distribution of pentanol in the interface, where a higher concentration of pentanol molecules is observed at high curvature regions.

While this research has provided a detailed insight into the microstructure and dynamics of these CTAB/alcohol/hexane/water reverse microemulsions, there are further investigations that need to be carried out to fully understand these systems, particularly the CTAB/pentanol/hexane/water reverse microemulsion. The CTAB/pentanol/hexane/water RM has CTAB present in the continuous phase as either monomer or as aggregates, but the exact form is unknown. This could be tested by performing electron microscopy measurements,[1] which should be able to distinguish between the two surfactant environments. Alternatively, emission spectroscopy could be employed but this technique could cause changes in the RM microstructure due to the requirement of a probe molecule.[2] It may also be possible to perform small angle neutron scattering (SANS) measurements[3,4] on the CTAB/pentanol/hexane/water system, where the hexane is deuterated. The deuteration will provide contrast between the surfactant and the hexane and may show the presence of two droplet sizes, which will confirm the presence of small CTAB aggregates in the continuous phase.

It was hypothesised that when pentanol is employed as the co-surfactant, it is able to solubilise the most water inside the RM droplets. To confirm this, measurements will need to be performed on the microemulsions with various water-to-surfactant ratios, ω_0, to explore how the size of the droplets are affected. If the CTAB/pentanol/hexane/water RM produces larger droplet sizes prior to the breakdown of the microemulsion, compared with the other CTAB/alcohol/hexane/water systems, it will provide evidence that the pentanol co-surfactant is able to solubilize a greater amount of water. In addition, performing molecular simulations on the droplets at varying ω_0 will also help determine the water solubilisation capacity and explore how ω_0 and the droplet size affect their resultant shape.

While the exchange processes in the CTAB/pentanol/hexane/water reverse microemulsion has been extensively studied with the aid of REXSY measurements, the exchange in the other systems has not been studied quite as extensively. It is possible that changing the co-surfactant chain length could affect the dynamics of the RM systems. Therefore, it would be advantageous to perform REXSY measurements on the other CTAB/alcohol/hexane/water reverse microemulsions.

7.1 References

(1)   Acharya, D. P.; Hartley, P. G. *Curr. Opin. Colloid Interface Sci* **2012**, *17*, 274.

(2)   Rack, J. J.; McCleskey, T. M.; Birnbaum, E. R. *J. Phys. Chem. B* **2002**, *106*, 632.

(3)   Foster, T.; Sottmann, T.; Schweins, R.; Strey, R. *J. Chem. Phys.* **2008**, *128*.

(4)   Hollamby, M. J. *Phys. Chem. Chem. Phys.* **2013**, *15*, 10566.

8. Appendices

Appendix 1

Quaternary microemulsions are defined using the water to surfactant ratio, ω_0, the co-surfactant to surfactant ratio, P_0, the volume droplet fraction, ϕ_d and the total surfactant concentration, [surfactant]. The CTAB/pentanol/hexane/water system used in chapter 3 and 4 has ω_0 = 6.9, P_0 = 8.2 and [CTAB] = 0.06 M, the molar volumes used for calculating these parameters are CTAB = 0.3609 L mol^{-1} and pentanol = 0.10824 L mol^{-1} and are calculated in the following way:

$$\text{CTAB} = 0.2 \text{ g}$$

$$\text{Moles CTAB} = \frac{\text{Mass CTAB}}{\text{M}_\text{R} \text{ CTAB}} = \frac{0.2 \text{ g}}{364.45 \text{ g mol}^{-1}} = 5.4877 \times 10^{-4} \text{ mol}$$

$$\text{Volume CTAB} = 5.4877 \times 10^{-4} \text{ mol} \times 0.3609 \text{ L mol}^{-1} = 1.98 \times 10^{-4} \text{ L} = 0.198 \text{ mL}$$

$$\omega_0 = \frac{\text{Moles water}}{\text{Moles CTAB}} = 6.9$$

$$\text{Moles water} = \omega_0 \times \text{moles CTAB} = 6.9 \times 5.4877 \times 10^{-4} \text{ mol} = 3.787 \times 10^{-3} \text{ mol}$$

$$\text{Volume water} = \frac{3.787 \times 10^{-3} \text{ mol} \times 18 \text{ g mol}^{-1}}{0.998 \text{ g mL}^{-1}} = 0.068 \text{ mL}$$

$$P_0 = \frac{\text{Moles pentanol}}{\text{Moles CTAB}}$$

$$\text{Moles pentanol} = P_0 \times \text{moles CTAB} = 8.2 \times 5.4877 \times 10^{-4} \text{ mol} = 4.4999 \times 10^{-3} \text{ mol}$$

$$\text{Volume pentanol} = 4.4999 \times 10^{-3} \text{ mol} \times 0.10824 \text{ L mol}^{-1} = 4.87 \times 10^{-4} \text{ L} = 0.487 \text{ mL}$$

$$[\text{CTAB}] = 0.06 \text{ M}$$

$$\text{Total Volume} = \frac{\text{Moles CTAB}}{[\text{CTAB}]} = \frac{5.4877 \times 10^{-4} \text{ mol}}{0.06 \text{ mol dm}^{-3}} = 9.14 \times 10^{-3} \text{ L} = 9.14 \text{ mL}$$

Volume hexane $= 9.14 - 0.487 - 0.068 - 0.198 = 8.387$ mL

The CTAB/alcohol/hexane/water systems used in chapter 4, have the same ω_0, P_0 and [CTAB] as the CTAB/pentanol/hexane/water system in chapter 3. Therefore, the amount of CTAB, hexane and water remains constant at 0.2 g, 8.394 mL and 0.068 mL, respectively. As the densities of the different alcohols are different, the volume of each alcohol added varied. The volume of each alcohol needed is calculated as follows:

1. **Butanol**

$\text{CTAB} = 0.2$ g

$$\text{Moles CTAB} = \frac{\text{Mass CTAB}}{\text{M}_\text{R} \text{ CTAB}} = \frac{0.2 \text{ g}}{364.45 \text{ g mol}^{-1}} = 5.4877 \times 10^{-4} \text{ mol}$$

Volume CTAB $= 5.4877 \times 10^{-4}$ mol $\times 0.3609$ L mol$^{-1} = 1.98 \times 10^{-4}$ L $= 0.198$ mL

$$\omega_0 = \frac{\text{Moles water}}{\text{Moles CTAB}} = 6.9$$

Moles water $= \omega_0 \times$ moles CTAB $= 6.9 \times 5.4877 \times 10^{-4}$ mol $= 3.787 \times 10^{-3}$ mol

$$\text{Volume water} = \frac{3.787 \times 10^{-3} \text{ mol} \times 18 \text{ g mol}^{-1}}{0.998 \text{ g mL}^{-1}} = 0.068 \text{ mL}$$

$$P_0 = \frac{\text{Moles pentanol}}{\text{Moles CTAB}}$$

Moles pentanol $= P_0 \times$ moles CTAB $= 8.2 \times 5.4877 \times 10^{-4}$ mol $= 4.4999 \times 10^{-3}$ mol

$$\text{Volume pentanol} = \frac{4.4999 \times 10^{-3} \text{ mol} \times 74.121 \text{ g mol}^{-1}}{0.8095 \text{ g mL}^{-1}} = 0.412 \text{ mL}$$

Total volume of microemulsion = 0.412 mL + 0.068 mL + 0.198 mL + 8.394 mL = 9.072 mL

$$[\text{CTAB}] = \frac{\text{Moles of CTAB}}{\text{Total Volume}} = \frac{5.4877 \times 10^{-4} \text{ mol}}{9.072 \times 10^{-3} \text{ mL}} = 0.06 \text{ M}$$

2. Hexanol

$$\text{CTAB} = 0.2 \text{ g}$$

$$\text{Moles CTAB} = \frac{\text{Mass CTAB}}{\text{M}_\text{R} \text{ CTAB}} = \frac{0.2 \text{ g}}{364.45 \text{ g mol}^{-1}} = 5.4877 \times 10^{-4} \text{ mol}$$

$$\text{Volume CTAB} = 5.4877 \times 10^{-4} \text{ mol} \times 0.3609 \text{ L mol}^{-1} = 1.98 \times 10^{-4} \text{ L} = 0.198 \text{ mL}$$

$$\omega_0 = \frac{\text{Moles water}}{\text{Moles CTAB}} = 6.9$$

$$\text{Moles water} = \omega_0 \times \text{moles CTAB} = 6.9 \times 5.4877 \times 10^{-4} \text{ mol} = 3.787 \times 10^{-3} \text{ mol}$$

$$\text{Volume water} = \frac{3.787 \times 10^{-3} \text{ mol} \times 18 \text{ g mol}^{-1}}{0.998 \text{ g mL}^{-1}} = 0.068 \text{ mL}$$

$$P_0 = \frac{\text{Moles pentanol}}{\text{Moles CTAB}}$$

$$\text{Moles pentanol} = P_0 \times \text{moles CTAB} = 8.2 \times 5.4877 \times 10^{-4} \text{ mol} = 4.4999 \times 10^{-3} \text{ mol}$$

$$\text{Volume pentanol} = \frac{4.4999 \times 10^{-3} \text{ mol} \times 102.174 \text{ g mol}^{-1}}{0.8136 \text{ g mL}^{-1}} = 0.565 \text{ mL}$$

Total volume of microemulsion = 0.565 mL + 0.068 mL + 0.198 mL + 8.394 mL = 9.225 mL

$$[CTAB] = \frac{\text{Moles of CTAB}}{\text{Total Volume}} = \frac{5.4877 \times 10^{-4} \text{ mol}}{9.225 \times 10^{-3} \text{ mL}} = 0.059 \text{ M}$$

3. Heptanol

$$CTAB = 0.2 \text{ g}$$

$$\text{Moles CTAB} = \frac{\text{Mass CTAB}}{\text{M}_R \text{ CTAB}} = \frac{0.2 \text{ g}}{364.45 \text{ g mol}^{-1}} = 5.4877 \times 10^{-4} \text{ mol}$$

$$\text{Volume CTAB} = 5.4877 \times 10^{-4} \text{ mol} \times 0.3609 \text{ L mol}^{-1} = 1.98 \times 10^{-4} \text{ L} = 0.198 \text{ mL}$$

$$\omega_0 = \frac{\text{Moles water}}{\text{Moles CTAB}} = 6.9$$

$$\text{Moles water} = \omega_0 \times \text{moles CTAB} = 6.9 \times 5.4877 \times 10^{-4} \text{ mol} = 3.787 \times 10^{-3} \text{ mol}$$

$$\text{Volume water} = \frac{3.787 \times 10^{-3} \text{ mol} \times 18 \text{ g mol}^{-1}}{0.998 \text{ g mL}^{-1}} = 0.068 \text{ mL}$$

$$P_0 = \frac{\text{Moles pentanol}}{\text{Moles CTAB}}$$

$$\text{Moles pentanol} = P_0 \times \text{moles CTAB} = 8.2 \times 5.4877 \times 10^{-4} \text{ mol} = 4.4999 \times 10^{-3} \text{ mol}$$

$$\text{Volume pentanol} = \frac{4.4999 \times 10^{-3} \text{ mol} \times 116.201 \text{ g mol}^{-1}}{0.8219 \text{ g mL}^{-1}} = 0.636 \text{ mL}$$

$$\text{Total volume of microemulsion} = 0.636 \text{ mL} + 0.068 \text{ mL} + 0.198 \text{ mL} + 8.394 \text{ mL} = 9.296 \text{ mL}$$

$$[CTAB] = \frac{\text{Moles of CTAB}}{\text{Total Volume}} = \frac{5.4877 \times 10^{-4} \text{ mol}}{9.296 \times 10^{-3} \text{ mL}} = 0.059 \text{ M}$$

Appendix 2

Diffusion data in this thesis were always fitted to the minimum number of diffusion coefficients necessary. Mono-exponential and bi-exponential fits for PGSTE and BPP-STE acquired data, at Δ = 40 ms and 298 K, for CTAB (Figure A.1 and Figure A.2) and pentanol (Figure A.3 and Figure A.4) show that a fit to two diffusion coefficients is necessary at short observation times ($\Delta \leq 40$ ms). The diffusion data acquired using these two different pulse sequences both require bi-exponential fitting and hence the behaviour observed is not a result of pulse sequence artefacts. However, the BPP-STE pulse sequence was employed throughout the chapter to eliminate the effects of eddy currents.
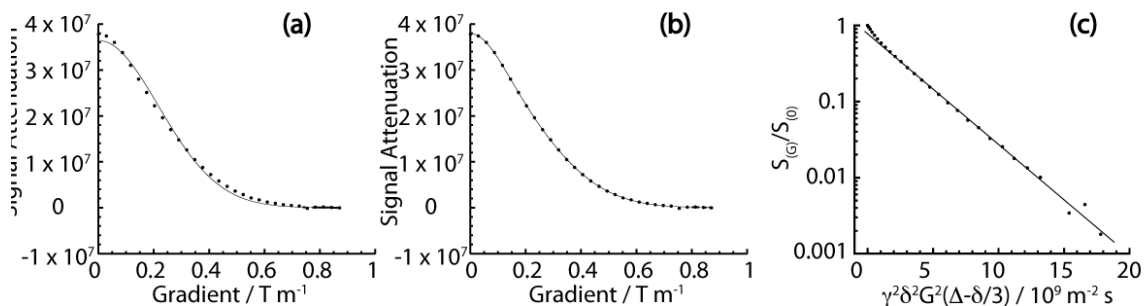
Figure A.1: Signal attenuation of CTAB, H_a, acquired using the PGSTE pulse sequence with (a) a mono-exponential fit, D = 4.42 x 10^{-10} m^2 s^{-1}, (b) a bi-exponential fit, D_{slow} = 3.41 x 10^{-10} m^2 s^{-1} (78.7 %) and D_{fast} = 1.71 x 10^{-9} m^2 s^{-1} (21.3 %), to the diffusion data and (c) log plot of signal intensity against G^2.
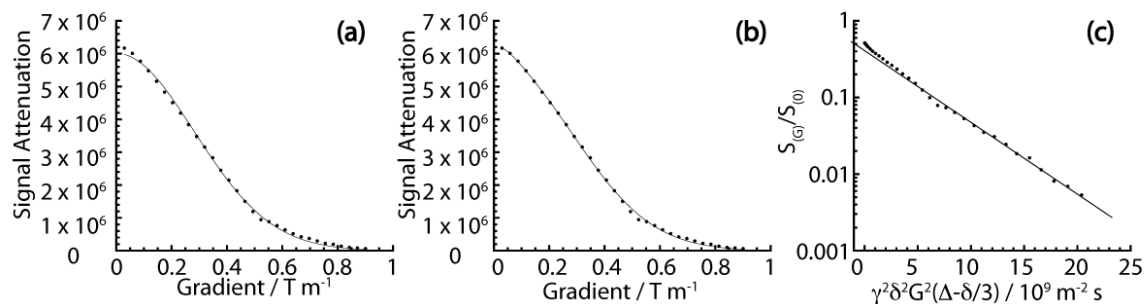
Figure A.2: Signal attenuation of CTAB, Ha, acquired using the BPP-STE pulse sequence with (a) a mono-exponential fit, D = 2.58 x 10^{-10} m^2 s^{-1}, (b) a bi-exponential fit, D_{slow} = 2.43 x 10^{-10} m^2 s^{-1} (92.3 %) and D_{fast} = 1.54 x 10^{-9} m^2 s^{-1} (7.7 %), to the diffusion data and (c) log of signal intensity against $\boldsymbol{G}^2$.
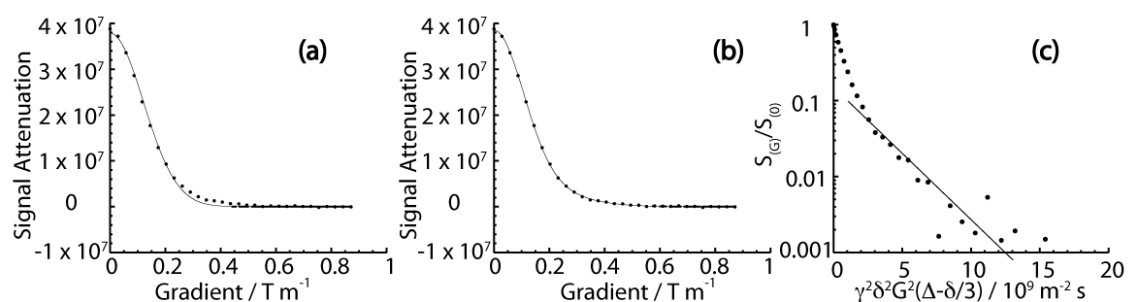
Figure A.3: Signal attenuation of pentanol, H_g, acquired using the PGSTE pulse sequence with (a) a mono-exponential fit, D = 1.42 x 10^{-9} m^2 s^{-1}, (b) a bi-exponential fit, D_{slow} = 6.87 x 10^{-10} m^2 s^{-1} and D_{fast} = 1.8 x 10^{-9} m^2 s^{-1}, to the diffusion data and (c) log of signal intensity against G^2.
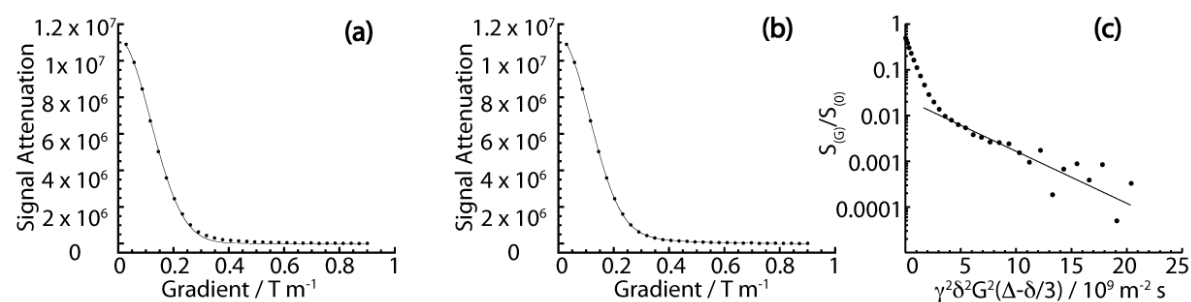
Figure A.4: Signal attenuation of pentanol, H_g, acquired using the BPP-STE pulse sequence with (a) a mono-exponential fit, D = 1.43 x 10^{-9} m^2 s^{-1}, (b) a bi-exponential fit, D_{slow} = 4.04 x 10^{-10} m^2 s^{-1} (7.7 %) and D_{fast} = 1.65 x 10^{-9} m^2 s^{-1} (92.3 %), to the diffusion data and (c) log of signal intensity against $\boldsymbol{G}^2$.

To provide a comparison between PGSE, PGSTE and BPP-STE sequences, a PGSE experiment

was performed at Δ = 140 ms (an equivalent Δ employed previously for this system). Data could not

be acquired for the pentanol, H_g, due to J-coupling issues, however the CTAB, H_a, can be found in

Figure A.5. Only one diffusion coefficient is obtained for CTAB using PGSE with Δ =140 ms where D =

2.53×10^{-10} m^2 s^{-1}. The observation of a single CTAB diffusion coefficient using these parameters and

pulse sequence is consistent with measurements made in the literature and hence it can be

concluded that no experimental artefacts play a role in the bi-exponential behaviour observed in

chapter 3 for CTAB and pentanol.
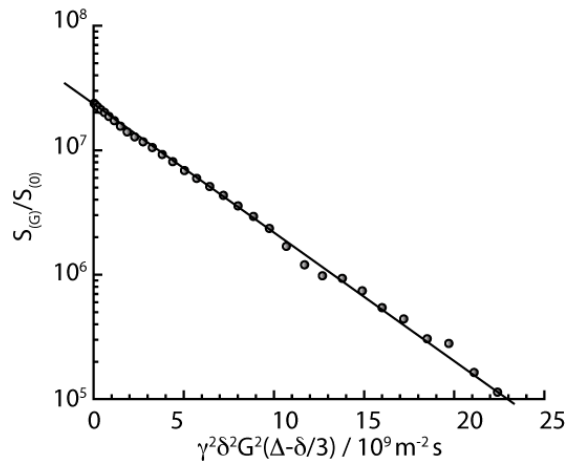
Figure A.5: Signal attenuation of CTAB, H_a, acquired using a PGSE pulse sequence at Δ = 140 ms to obtain D = 2.53 x 10^{-10} m^2 s^{-1}.

Appendix 3
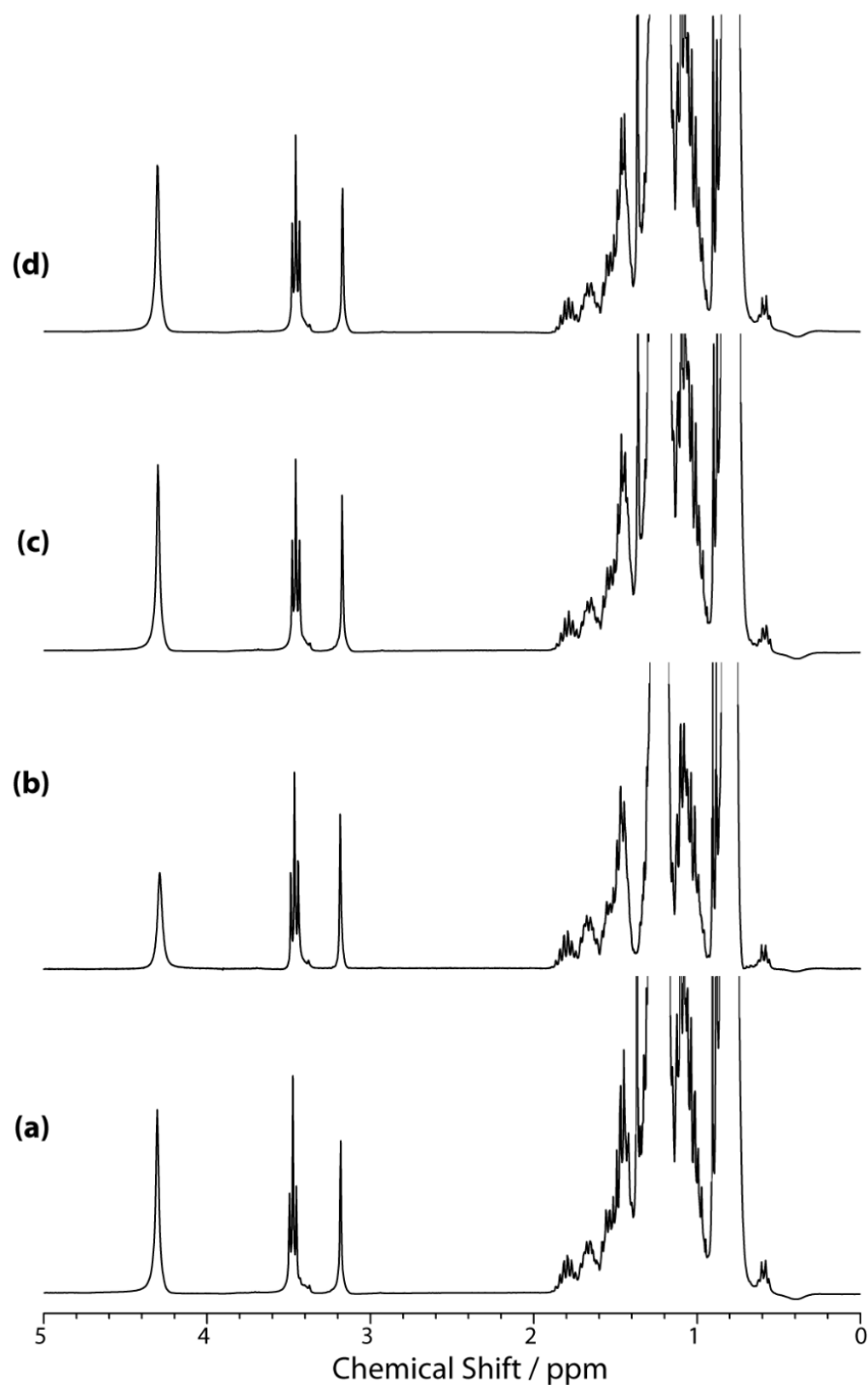
Figure A.6: ^{1}H NMR spectra for CTAB/alcohol/hexane/water system where the alcohol is (a) butanol, (b) pentanol, (c) hexanol and (d) heptanol. The signal intensity scale was limited to enable the signals of interest (the H_a resonance of CTAB, the H_g resonance of the alcohol and the alcohol hydroxyl resonance) to be easily viewed, they are too small without this limitation. As a result, the aliphatic resonances at low chemical shifts were cut off.

Appendix 4

The following shows all the steps involved in integrating Equation 5.7 to give Equation 5.8:

$$\frac{dN_{AB}}{dt} = k_{AB}N_A - N_{AB}(k_{AB} + k_{BA}) \qquad \text{Equation 5.7}$$

$$\int \frac{1}{k_{AB}N_A - N_{AB}(k_{AB} + k_{BA})}\, dN_{AB} = \int dt \qquad \text{Equation A.1}$$

If we say:

$$u = k_{AB}N_A - N_{AB}(k_{AB} + k_{BA}) \qquad \text{Equation A.2}$$

$$\frac{du}{dN_{AB}} = -(k_{AB} + k_{BA})$$

$$dN_{AB} = \frac{du}{-(k_{AB} + k_{BA})} \qquad \text{Equation A.3}$$

If Equation A.3 and Equation A.2 are substituted into Equation A.1:

$$\int_{N_{AB}^{t=0}}^{N_{AB}} \frac{1}{u} \times \frac{du}{-(k_{AB} + k_{BA})} = \int_0^t dt$$

$$\frac{1}{-(k_{AB} + k_{BA})} \int_{N_{AB}^{t=0}}^{N_{AB}} \frac{1}{u}\, du = \int_0^t dt$$

As:

$$\int \frac{1}{u}\, du = \ln(u)$$

Then:

$$\frac{\ln(k_{AB}N_A - N_{AB}(k_{AB} + k_{BA}))}{-(k_{AB} + k_{BA})} - \frac{\ln(k_{AB}N_A - N_{AB}^{t=0}(k_{AB} + k_{BA}))}{-(k_{AB} + k_{BA})} = t$$

$$\ln\left(k_{AB}N_A - N_{AB}(k_{AB} + k_{BA})\right) - \ln\left(k_{AB}N_A - N_{AB}^{t=0}(k_{AB} + k_{BA})\right) = -(k_{AB} + k_{BA})t$$

$$\ln\left(\frac{k_{AB}N_A - N_{AB}(k_{AB} + k_{BA})}{k_{AB}N_A - N_{AB}^{t=0}(k_{AB} + k_{BA})}\right) = -(k_{AB} + k_{BA})t$$

$$\frac{k_{AB}N_A - N_{AB}(k_{AB} + k_{BA})}{k_{AB}N_A - N_{AB}^{t=0}(k_{AB} + k_{BA})} = e^{-(k_{AB}+k_{BA})t}$$

As $N_{AB}^{t=0} = 0$:

$$\frac{k_{BA}N_A - N_{AB}(k_{AB} + k_{BA})}{k_{AB}N_A} = e^{-(k_{AB}+k_{BA})t}$$

$$k_{AB}N_A - N_{AB}(k_{AB} + k_{BA}) = k_{AB}N_A e^{-(k_{AB}+k_{BA})t}$$

$$-N_{AB}(k_{AB} + k_{BA}) = -k_{AB}N_A + k_{AB}N_A e^{-(k_{AB}+k_{BA})t}$$

$$N_{AB} = \frac{-k_{AB}N_A}{-(k_{AB} + k_{BA})} + \frac{k_{AB}N_A e^{-(k_{AB}+k_{BA})t}}{-(k_{AB} + k_{BA})}$$

$$N_{AB} = \frac{k_{AB}N_A}{(k_{AB} + k_{BA})} - \frac{k_{AB}N_A e^{-(k_{AB}+k_{BA})t}}{(k_{AB} + k_{BA})}$$

$$N_{AB} = \frac{k_{AB}N_A}{(k_{AB} + k_{BA})}\left(1 - e^{-(k_{AB}+k_{BA})t}\right)$$

As $\lambda^{AB} = k_{AB} + k_{BA}$:

$$N_{AB} = \frac{k_{AB}N_A}{\lambda^{AB}}\left(1 - e^{-\lambda^{AB}t}\right) \qquad \text{Equation 5.8}$$

Appendix 5

The following shows all the steps involved in integrating Equation 5.11 to give Equation 5.12:

$$\frac{dN_{BA}}{dt} = k_{BA}'N_B - N_{BA}(k_{AB}' + k_{BA}') \qquad \text{Equation 5.11}$$

$$\int \frac{1}{k_{BA}'N_B - N_{BA}(k_{AB}' + k_{BA}')} dN_{BA} = \int dt \qquad \text{Equation A.4}$$

If we say:

$$u = k_{BA}'N_B - N_{BA}(k_{AB}' + k_{BA}') \qquad \text{Equation A.5}$$

$$\frac{du}{dN_{BA}} = -(k_{AB}' + k_{BA}')$$

$$dN_{BA} = \frac{du}{-(k_{AB}' + k_{BA}')} \qquad \text{Equation A.6}$$

If Equation A.6 and Equation A.5 are substituted into Equation A.4:

$$\int_{N_{BA}^{t=0}}^{N_{BA}} \frac{1}{u} \times \frac{du}{-(k_{AB}' + k_{BA}')} = \int_0^t dt$$

$$\frac{1}{-(k_{AB}' + k_{BA}')} \int_{N_{BA}^{t=0}}^{N_{BA}} \frac{1}{u} du = \int_0^t dt$$

As:

$$\int \frac{1}{u} du = \ln(u)$$

Then:

$$\frac{\ln(k_{BA}'N_B - N_{BA}(k_{AB}' + k_{BA}'))}{-(k_{AB}' + k_{BA}')} - \frac{\ln(k_{BA}'N_B - N_{BA}^{t=0}(k_{AB}' + k_{BA}'))}{-(k_{AB}' + k_{BA}')} = t$$

$$\ln\left(k_{BA}'N_B - N_{BA}(k_{AB}' + k_{BA}')\right) - \ln\left(k_{BA}'N_B - N_{BA}^{t=0}(k_{AB}' + k_{BA}')\right) = -(k_{AB}' + k_{BA}')t$$

$$\ln\left(\frac{k_{BA}'N_B - N_{BA}(k_{AB}' + k_{BA}')}{k_{BA}'N_B - N_{BA}^{t=0}(k_{AB}' + k_{BA}')}\right) = -(k_{AB}' + k_{BA}')t$$

$$\frac{k_{BA}'N_B - N_{BA}(k_{AB}' + k_{BA}')}{k_{BA}'N_B - N_{BA}^{t=0}(k_{AB}' + k_{BA}')} = e^{-(k_{AB}'+k_{BA}')t}$$

As $N_{BA}^{t=0} = 0$:

$$\frac{k_{BA}'N_B - N_{BA}(k_{AB}' + k_{BA}')}{k_{BA}'N_B} = e^{-(k_{AB}'+k_{BA}')t}$$

$$k_{BA}'N_B - N_{BA}(k_{AB}' + k_{BA}') = k_{BA}'N_B e^{-(k_{AB}'+k_{BA}')t}$$

$$-N_{BA}(k_{AB}' + k_{BA}') = -k_{BA}'N_B + k_{BA}'N_B e^{-(k_{AB}'+k_{BA}')t}$$

$$N_{BA} = \frac{-k_{BA}'N_B}{-(k_{AB}' + k_{BA}')} + \frac{k_{BA}'N_B e^{-(k_{AB}'+k_{BA}')t}}{-(k_{AB}' + k_{BA}')}$$

$$N_{BA} = \frac{k_{BA}'N_B}{(k_{AB}' + k_{BA}')} - \frac{k_{BA}'N_B e^{-(k_{AB}'+k_{BA}')t}}{(k_{AB}' + k_{BA}')}$$

$$N_{BA} = \frac{k_{BA}'N_B}{(k_{AB}' + k_{BA}')}\left(1 - e^{-(k_{AB}'+k_{BA}')t}\right)$$

As $\lambda^{BA} = k_{AB}' + k_{BA}'$:

$$N_{BA} = \frac{k_{BA}'N_B}{\lambda^{BA}}\left(1 - e^{-\lambda^{BA}t}\right) \qquad \text{Equation 5.12}$$

Appendix 6

A total of six different phase cycles for the PGSTE DEXSY pulse sequence were tested. The phases of each rf pulse are shown in Figure A.7 where the phase of the acquisition channel is represented by ph31. The phase cycles give the phase of the rf pulses as X, Y, -X or –Y, and the acquisition channels as 0, 1, 2, 3 which determines which magnetisation is in channel 1 and channel 2, Table A.1.

Table A.1: A table to show how the phase of the acquisition channel effects the magnetisation in channel 1 and channel 2.

	Channel 1	Channel 2
0	Add I_x	Add I_y
1	Deduct I_y	Add I_x
2	Deduct I_x	Add I_y
3	Deduct I_y	Deduct I_x
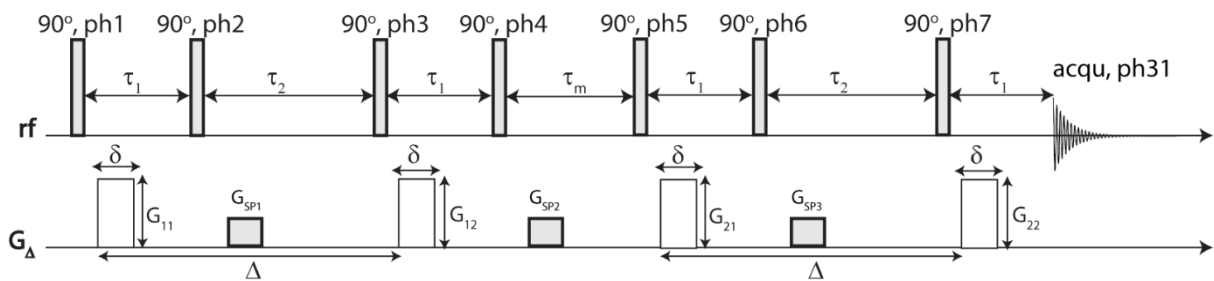
Figure A.7: PGSTE DEXSY pulse sequence showing the phases of the rf pulses and the acquisition channel.

The following gives the different phase cycles explored, and the associated product operators, where $\omega\tau$ is the phase angle as a result of precession in the transverse plane, θ is the phase angle produced as a result of application of a magnetic field gradient pulse, φ and φ_2 are the phase shifts as a result of diffusion before and after the mixing time, respectively.

1. Original Phase Cycle:

	Ph1	Ph2	Ph3	Ph4	Ph5	Ph6	Ph7	Ph31
a	X	X	Y	X	Y	X	Y	0
b	-X	X	Y	X	Y	X	Y	2
c	X	X	Y	X	Y	Y	X	0
d	-X	X	Y	X	Y	Y	X	2
e	X	X	Y	Y	X	X	Y	0
f	-X	X	Y	Y	X	X	Y	2
g	X	X	Y	Y	X	Y	X	0
h	-X	X	Y	Y	X	Y	X	2
i	X	Y	X	X	Y	X	Y	0
j	-X	Y	X	X	Y	X	Y	2
k	X	Y	X	X	Y	Y	X	0
l	-X	Y	X	X	Y	Y	X	2
m	X	Y	X	Y	X	X	Y	0
n	-X	Y	X	Y	X	X	Y	2
o	X	Y	X	Y	X	Y	X	0
p	-X	Y	X	Y	x	Y	X	2

a. $I_z \xrightarrow{90_x} I_y \xrightarrow{\text{Gradient}} I_y\cos(\omega\tau + \theta) + I_x\sin(\omega\tau + \theta) \xrightarrow{90_x} -I_z\cos(\omega\tau + \theta) + I_x\sin(\omega\tau + \theta) \xrightarrow{\text{Spoiler}} -I_z\cos(\omega\tau + \theta) \xrightarrow{90_y} I_x\cos(\omega\tau + \theta) \xrightarrow{\text{Gradient}} I_x\cos(\omega\tau + \theta)\cos(\omega\tau + \theta + \varphi) - I_y\cos(\omega\tau + \theta)\sin(\omega\tau + \theta + \varphi) \xrightarrow{90_x} I_x\cos(\omega\tau + \theta)\cos(\omega\tau + \theta + \varphi) + I_z\cos(\omega\tau + \theta)\sin(\omega\tau + \theta + \varphi) \xrightarrow{\text{Spoiler}} I_z\cos(\omega\tau + \theta)\sin(\omega\tau + \theta + \varphi) \xrightarrow{90_y} -I_x\cos(\omega\tau + \theta)\sin(\omega\tau + \theta + \varphi) \xrightarrow{\text{Gradient}} -I_x\cos(\omega\tau + \theta)\sin(\omega\tau + \theta + \varphi)\cos(\omega\tau + \theta) + I_y\cos(\omega\tau + \theta)\sin(\omega\tau + \theta + \varphi)\sin(\omega\tau + \theta) \xrightarrow{90_x} -I_x\cos(\omega\tau + \theta)\sin(\omega\tau + \theta + \varphi)\cos(\omega\tau + \theta) - I_z\cos(\omega\tau + \theta)\sin(\omega\tau + \theta + \varphi)\sin(\omega\tau + \theta) \xrightarrow{\text{Spoiler}} -I_z\cos(\omega\tau + \theta)\sin(\omega\tau + \theta + \varphi)\sin(\omega\tau + \theta) \xrightarrow{90_y} I_x\cos(\omega\tau + \theta)\sin(\omega\tau + \theta + \varphi)\sin(\omega\tau + \theta) \xrightarrow{\text{Gradient}} I_x\cos(\omega\tau + \theta)\sin(\omega\tau + \theta + \varphi)\sin(\omega\tau + \theta)\cos(\omega\tau + \theta + \varphi_2) - I_y\cos(\omega\tau + \theta)\sin(\omega\tau + \theta + \varphi)\sin(\omega\tau + \theta)\sin(\omega\tau + \theta + \varphi_2)$

If the same procedure is undertaken for the remaining phase cycle steps, the resultant magnetisation

is as follows:

b. $-I_x\cos(\omega\tau + \theta)\sin(\omega\tau + \theta + \varphi)\sin(\omega\tau + \theta)\cos(\omega\tau + \theta + \varphi_2) + I_y\cos(\omega\tau + \theta)\sin(\omega\tau + \theta + \varphi)\sin(\omega\tau + \theta)\sin(\omega\tau + \theta + \varphi_2)$

c. $-I_y\cos(\omega\tau + \theta)\sin(\omega\tau + \theta + \varphi)\cos(\omega\tau + \theta)\cos(\omega\tau + \theta + \varphi_2) - I_x\cos(\omega\tau + \theta)\sin(\omega\tau + \theta + \varphi)\cos(\omega\tau + \theta)\sin(\omega\tau + \theta + \varphi_2)$

d. $I_y\cos(\omega\tau + \theta)\sin(\omega\tau + \theta + \varphi)\cos(\omega\tau + \theta)\cos(\omega\tau + \theta + \varphi_2) + I_x\cos(\omega\tau + \theta)\sin(\omega\tau + \theta + \varphi)\cos(\omega\tau + \theta)\sin(\omega\tau + \theta + \varphi_2)$

e. $I_x\cos(\omega\tau + \theta)\cos(\omega\tau + \theta + \varphi)\cos(\omega\tau + \theta)\cos(\omega\tau + \theta + \varphi_2) - I_y\cos(\omega\tau + \theta)\cos(\omega\tau + \theta + \varphi)\cos(\omega\tau + \theta)\sin(\omega\tau + \theta + \varphi_2)$

f. $-I_x\cos(\omega\tau + \theta)\cos(\omega\tau + \theta + \varphi)\cos(\omega\tau + \theta)\cos(\omega\tau + \theta + \varphi_2) + I_y\cos(\omega\tau + \theta)\cos(\omega\tau + \theta + \varphi)\cos(\omega\tau + \theta)\sin(\omega\tau + \theta + \varphi_2)$

g. $I_y\cos(\omega\tau + \theta)\cos(\omega\tau + \theta + \varphi)\sin(\omega\tau + \theta)\cos(\omega\tau + \theta + \varphi_2) + I_x\cos(\omega\tau + \theta)\cos(\omega\tau + \theta + \varphi)\sin(\omega\tau + \theta)\sin(\omega\tau + \theta + \varphi_2)$

h. $-I_y\cos(\omega\tau + \theta)\cos(\omega\tau + \theta + \varphi)\sin(\omega\tau + \theta)\cos(\omega\tau + \theta + \varphi_2) - I_x\cos(\omega\tau + \theta)\cos(\omega\tau + \theta + \varphi)\sin(\omega\tau + \theta)\sin(\omega\tau + \theta + \varphi_2)$

i. $-I_x\sin(\omega\tau + \theta)\cos(\omega\tau + \theta + \varphi)\sin(\omega\tau + \theta)\cos(\omega\tau + \theta + \varphi_2) + I_y\sin(\omega\tau + \theta)\cos(\omega\tau + \theta + \varphi)\sin(\omega\tau + \theta)\sin(\omega\tau + \theta + \varphi_2)$

j. $I_x\sin(\omega\tau + \theta)\cos(\omega\tau + \theta + \varphi)\sin(\omega\tau + \theta)\cos(\omega\tau + \theta + \varphi_2) - I_y\sin(\omega\tau + \theta)\cos(\omega\tau + \theta + \varphi)\sin(\omega\tau + \theta)\sin(\omega\tau + \theta + \varphi_2)$

k. $I_y\sin(\omega\tau + \theta)\cos(\omega\tau + \theta + \varphi)\cos(\omega\tau + \theta)\cos(\omega\tau + \theta + \varphi_2) + I_x\sin(\omega\tau + \theta)\cos(\omega\tau + \theta + \varphi)\cos(\omega\tau + \theta)\sin(\omega\tau + \theta + \varphi_2)$

l. $-I_y\sin(\omega\tau + \theta)\cos(\omega\tau + \theta + \varphi)\cos(\omega\tau + \theta)\cos(\omega\tau + \theta + \varphi_2) - I_x\sin(\omega\tau + \theta)\cos(\omega\tau + \theta + \varphi)\cos(\omega\tau + \theta)\sin(\omega\tau + \theta + \varphi_2)$

m. $I_x\sin(\omega\tau + \theta)\sin(\omega\tau + \theta + \varphi)\cos(\omega\tau + \theta)\cos(\omega\tau + \theta + \varphi_2) - I_y\sin(\omega\tau + \theta)\sin(\omega\tau + \theta + \varphi)\cos(\omega\tau + \theta)\sin(\omega\tau + \theta + \varphi_2)$

n. $-I_x\sin(\omega\tau + \theta)\sin(\omega\tau + \theta + \varphi)\cos(\omega\tau + \theta)\cos(\omega\tau + \theta + \varphi_2) + I_y\sin(\omega\tau + \theta)\sin(\omega\tau + \theta + \varphi)\cos(\omega\tau + \theta)\sin(\omega\tau + \theta + \varphi_2)$

o. $I_y\sin(\omega\tau + \theta)\sin(\omega\tau + \theta + \varphi)\sin(\omega\tau + \theta)\cos(\omega\tau + \theta + \varphi_2)+I_x\sin(\omega\tau + \theta)\sin(\omega\tau + \theta + \varphi)\sin(\omega\tau + \theta)\sin(\omega\tau + \theta + \varphi_2)$

p. $-I_y\sin(\omega\tau + \theta)\sin(\omega\tau + \theta + \varphi)\sin(\omega\tau + \theta)\cos(\omega\tau + \theta + \varphi_2)-I_x\sin(\omega\tau + \theta)\sin(\omega\tau + \theta + \varphi)\sin(\omega\tau + \theta)\sin(\omega\tau + \theta + \varphi_2)$

This gives the total magnetisation in each channel as:

Channel 1: $2I_x(\cos\varphi\cos\varphi_2 - \sin\varphi\sin\varphi_2)$

Channel 2: 0

2. Phase Cycle reported by Callaghan et al.[1]:

Ph1	Ph2	Ph3	Ph4	Ph5	Ph6	Ph7	Ph31
X	X	Y	X	Y	X	Y	0
X	X	Y	X	Y	Y	X	1
X	X	Y	Y	X	X	Y	1
X	X	Y	Y	X	Y	X	0
X	Y	X	X	Y	X	Y	1
X	Y	X	X	Y	Y	X	0
X	Y	X	Y	X	X	Y	0
X	Y	X	Y	X	Y	X	1

Channel 1: $I_x(\cos\varphi\cos\varphi_2 - \sin\varphi\sin\varphi_2)$

Channel 2: $-I_y(\cos\varphi\sin\varphi_2 + \sin\varphi\cos\varphi_2)$

3. Phase cycle suggested by Klaus Zick at Bruker:

Ph1	Ph2	Ph3	Ph4	Ph5	Ph6	Ph7	Ph31
X	X	X	X	X	X	X	0
X	X	X	-X	X	X	X	2
X	Y	Y	Y	X	X	-X	3
X	Y	Y	-Y	X	X	-X	1
X	X	X	X	-X	X	X	2
X	X	X	-X	-X	X	X	0
X	Y	Y	Y	-X	X	-X	1
X	Y	Y	-Y	-X	X	-X	3

Channel 1:$-I_x(\cos\varphi\sin\varphi_2 - \sin\varphi\cos\varphi_2)$

Channel 2: $I_x(\cos\varphi\cos\varphi_2 - \sin\varphi\sin\varphi_2)$

4. Same phase cycle as in 3 but changed the acquisition channel:

Ph1	Ph2	Ph3	Ph4	Ph5	Ph6	Ph7	Ph31
X	X	X	X	X	X	X	2
X	X	X	-X	X	X	X	0
X	Y	Y	Y	X	X	-X	1
X	Y	Y	-Y	X	X	-X	1
X	X	X	X	-X	X	X	0
X	X	X	-X	-X	X	X	2
X	Y	Y	Y	-X	X	-X	1
X	Y	Y	-Y	-X	X	-X	1

Channel 1: $I_x(\cos\varphi\sin\varphi_2 - \sin\varphi\cos\varphi_2)$

Channel 2: 0

5. A phase cycle based on the phase cycle for 1D PGSTE sequence:

Ph1	Ph2	Ph3	Ph4	Ph5	Ph6	Ph7	Ph31
X	y	Y	-Y	X	Y	Y	0
X	X	X	-Y	X	X	X	2
-X	Y	Y	Y	-X	Y	Y	2
-X	X	X	Y	-X	X	X	0
Y	Y	Y	Y	Y	Y	Y	3
Y	X	X	-Y	Y	X	X	1
-Y	Y	Y	-Y	-Y	Y	Y	1
-Y	X	X	Y	-Y	X	X	3

Channel 1: 0

Channel 2: $-I_x(\cos\varphi\cos\varphi_2 + \sin\varphi\sin\varphi_2)$

6. Similar phase cycle as in 5 but acquisition channel changed:

Ph1	Ph2	Ph3	Ph4	Ph5	Ph6	Ph7	Ph31
X	y	Y	-Y	X	Y	Y	2
X	X	X	-Y	X	X	X	2
-X	Y	Y	Y	-X	Y	Y	0
-X	X	X	Y	-X	X	X	0
Y	Y	Y	Y	Y	Y	Y	1
Y	X	X	-Y	Y	X	X	3
-Y	Y	Y	-Y	-Y	Y	Y	3
-Y	X	X	Y	-Y	X	X	1

Channel 1: $I_x(\cos\varphi\cos\varphi_2 + \sin\varphi\sin\varphi_2)$

Channel 2: $I_x(\cos\varphi\cos\varphi_2 + \sin\varphi\sin\varphi_2)$

References

(1)   Khrapitchev, A. A.; Callaghan, P. T. *J. Magn. Reson.* **2001**, *152*, 259.

Appendix 7

The following shows the phase cycle and product operators for the 1D PGSTE sequence, Figure A.8.

The phase of the rf pulse and acquisition channels are written in the same way as demonstrated in

appendix 6, and $\omega\tau$ is the phase angle as a result of precession in the transverse plane, θ is the phase

angle produced as a result of application of a magnetic field gradient pulse, φ is the phase shift as a

result of diffusion.
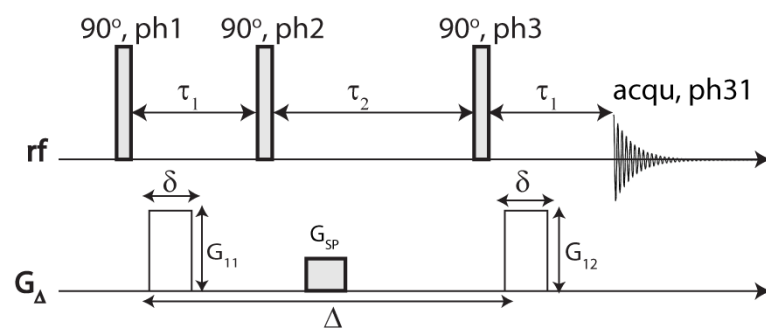
Figure A.8: 1D PGSTE pulse sequence showing the phases of the rf pulses and the acquisition channel.

	Ph1	Ph2	Ph3	Ph31
a	X	Y	Y	0
b	X	-Y	-Y	2
c	X	X	X	3
d	X	-X	-X	1
e	-X	Y	Y	2
f	-X	-Y	-Y	0
g	-X	X	X	1
h	-X	-X	-X	3
i	Y	Y	Y	0
j	Y	-Y	-Y	2
k	Y	X	X	3
l	Y	-X	-X	1
m	-Y	Y	Y	2
n	-Y	-Y	-Y	0
o	-Y	X	X	1
p	-Y	-X	-X	3

a. $I_z \xrightarrow{90_x} I_y \xrightarrow{Gradient} I_y \cos(\omega\tau + \theta) + I_x \sin(\omega\tau + \theta) \xrightarrow{90_y} I_y \cos(\omega\tau + \theta) + I_z \sin(\omega\tau + \theta) \xrightarrow{Spoiler} I_z \sin(\omega\tau + \theta) \xrightarrow{90_y} -I_x \sin(\omega\tau + \theta) \xrightarrow{Gradient} I_x \sin(\omega\tau + \theta)\cos(\omega\tau + \theta + \varphi) + I_y \sin(\omega\tau + \theta)\sin(\omega\tau + \theta + \varphi)$

If the same procedure is undertaken for the remaining phase cycle steps, the resultant magnetisation is as follows:

b. $I_x \sin(\omega\tau + \theta)\cos(\omega\tau + \theta + \varphi) + I_y \sin(\omega\tau + \theta)\sin(\omega\tau + \theta + \varphi)$

c. $-I_y \cos(\omega\tau + \theta)\cos(\omega\tau + \theta + \varphi) - I_x \cos(\omega\tau + \theta)\sin(\omega\tau + \theta + \varphi)$

d. $-I_y \cos(\omega\tau + \theta)\cos(\omega\tau + \theta + \varphi) - I_x \cos(\omega\tau + \theta)\sin(\omega\tau + \theta + \varphi)$

e. $I_x \sin(\omega\tau + \theta)\cos(\omega\tau + \theta + \varphi) - I_y \sin(\omega\tau + \theta)\sin(\omega\tau + \theta + \varphi)$

f. $I_x \sin(\omega\tau + \theta)\cos(\omega\tau + \theta + \varphi) - I_y \sin(\omega\tau + \theta)\sin(\omega\tau + \theta + \varphi)$

g. $I_y \cos(\omega\tau + \theta)\cos(\omega\tau + \theta + \varphi) + I_x \cos(\omega\tau + \theta)\sin(\omega\tau + \theta + \varphi)$

h. $I_y \cos(\omega\tau + \theta)\cos(\omega\tau + \theta + \varphi) + I_x \cos(\omega\tau + \theta)\sin(\omega\tau + \theta + \varphi)$

i. $I_x \cos(\omega\tau + \theta)\cos(\omega\tau + \theta + \varphi) - I_y \cos(\omega\tau + \theta)\sin(\omega\tau + \theta + \varphi)$

j. $I_x \cos(\omega\tau + \theta)\cos(\omega\tau + \theta + \varphi) - I_y \cos(\omega\tau + \theta)\sin(\omega\tau + \theta + \varphi)$

k. $-I_y \sin(\omega\tau + \theta)\cos(\omega\tau + \theta + \varphi) - I_x \sin(\omega\tau + \theta)\sin(\omega\tau + \theta + \varphi)$

l. $-I_y \sin(\omega\tau + \theta)\cos(\omega\tau + \theta + \varphi) - I_x \sin(\omega\tau + \theta)\sin(\omega\tau + \theta + \varphi)$

m. $-I_x \cos(\omega\tau + \theta)\cos(\omega\tau + \theta + \varphi) + I_y \cos(\omega\tau + \theta)\sin(\omega\tau + \theta + \varphi)$

n. $-I_x \cos(\omega\tau + \theta)\cos(\omega\tau + \theta + \varphi) + I_y \cos(\omega\tau + \theta)\sin(\omega\tau + \theta + \varphi)$

o. $I_y \sin(\omega\tau + \theta)\cos(\omega\tau + \theta + \varphi) + I_x \sin(\omega\tau + \theta)\sin(\omega\tau + \theta + \varphi)$

p. $I_y \sin(\omega\tau + \theta)\cos(\omega\tau + \theta + \varphi) + I_x \sin(\omega\tau + \theta)\sin(\omega\tau + \theta + \varphi)$

This gives the total magnetisation in each channel as:

Channel 1: $4I_x \sin \varphi$

Channel 2: $-4I_x \cos \varphi$

Appendix 8

The PGSTE DEXSY pulse sequence with timing modifications so that the start of acquisition coincides with the top of the echo is as follows. Any modifications are highlighted using red text.

This section of the pulse sequence shows the timings between the first two 90° pulses (denoted p1 in the sequence).

```
    p1:f1 ph1                ; (90 degree) excitation  hard pulse

     d2                      ; delay between pulse and gradient

    d16 grad{(0)|(0)|step(cnst11,10)+step(100,10)*r2d(cnst11)}
    d4
    d16 grad{(0)|(0)|(cnst11)+r2d(cnst11)-step(cnst11,10)-
step(100,10)*r2d(cnst11)}

    d2

    p1:f1 ph2                ; 90 degree excitation hard pulse
```

This section of the pulse sequence shows the timings between the last 90° pulse and acquisition. The delay d23 = d2 – de – 10u, where de is the time taken for acquisition to start, and 10u represents 10 μs. The delay d2 before d23 was removed to enable the period between the final 90° pulse and acquisition is equal to the period between the first two 90° pulses.

```
    p1:f1 ph7                           ; 90 degree excitation hard
pulse

    d2

    d16 grad{(0)|(0)|step(cnst11,10)+step(100,10)*r3d(cnst11)}
    d4
    d16 grad {(0)|(0)|(cnst11)+r3d(cnst11)-step(cnst11,10)-
step(100,10)*r3d(cnst11)}

    d2
    d23                                 ; gradient stabilization delay
Modified!! AJM d2 before d23 removed
    10u BLKGRAMP                        ; blank gradient amplifier
    ACQ_START(ph30,ph31)       ; !Modified!!start receiving, takes
DE
```

236

Appendix 9

A portion of the PGSTE DEXSY pulse sequence showing the modified blanking unit commands. This section shows the first magnetic field gradient pulse and spoiler gradient. The modifications are highlighted in red with any relevant comments. A delay of d20 replaced d6 to account for the addition 150 μs and 10 μs delays introduced as a result of the blanking unit commands.

```
"d20 = d6 - d2 - 10u - 150u"

p1:f1 ph1              ; (90 degree) excitation  hard pulse

  d2                   ; delay between pulse and gradient

     150u UNBLKGRAMP                        ; unblank gradient
amplifier
   d16 grad{(0)|(0)|step(cnst11,10)+step(100,10)*r2d(cnst11)}
   d4
   d16 grad{(0)|(0)|(cnst11)+r2d(cnst11)-step(cnst11,10)-
step(100,10)*r2d(cnst11)}
   d2
   10u BLKGRAMP                    ; blank gradient amplifier
   p1:f1 ph2           ; 90 degree excitation hard pulse
   d2
   d20                         ;modified to account for additional 150u
                              and 10u delay, originally this was d6
   150u UNBLKGRAMP          ; unblank gradient amplifier
   d17 grad {(0)|(0)|(0*cnst12)}
   d17 grad {(0)|(0)|(0.1*cnst12)}
   d17 grad {(0)|(0)|(0.2*cnst12)}
   d17 grad {(0)|(0)|(0.3*cnst12)}
   d17 grad {(0)|(0)|(0.4*cnst12)}
   d17 grad {(0)|(0)|(0.5*cnst12)}
   d17 grad {(0)|(0)|(0.6*cnst12)}
   d17 grad {(0)|(0)|(0.7*cnst12)}
   d17 grad {(0)|(0)|(0.8*cnst12)}
   d17 grad {(0)|(0)|(0.9*cnst12)}
   d5 grad {(0)|(0)|(1*cnst12)}
   d17 grad {(0)|(0)|(0.9*cnst12)}
   d17 grad {(0)|(0)|(0.8*cnst12)}
   d17 grad {(0)|(0)|(0.7*cnst12)}
   d17 grad {(0)|(0)|(0.6*cnst12)}
   d17 grad {(0)|(0)|(0.5*cnst12)}
   d17 grad {(0)|(0)|(0.4*cnst12)}
   d17 grad {(0)|(0)|(0.3*cnst12)}
   d17 grad {(0)|(0)|(0.2*cnst12)}
   d17 grad {(0)|(0)|(0.1*cnst12)}
   d17 grad {(0)|(0)|(0.0*cnst12)}
   d2
```

```
10u BLKGRAMP                              ; blank gradient amplifier
d2
```

Appendix 10

A portion of the PGSTE DEXSY pulse sequence (with the modified blanking unit commands) showing the movement of the magnetic field gradient pulses and spoiler gradients. This section shows the first magnetic field gradient pulse and spoiler gradient. The modifications are highlighted in red with any relevant comments. The delay d3 replaces d2 before the magnetic field gradient pulses and spoiler gradients; in doing so the sequence is shortened by d2 – d3 and hence d22 is inserted after the spoiler gradient to account for this and hence the total experiment time remains the same.

```
"d3 = 0.1m"                         ;modified AJM added a pulse
ringdown delay

"d22 = d6 - d3 - 10u - 150u + d2 - d3"       ;modified AJM d6 is
diffusion time


    p1:f1 ph1                   ; (90 degree) excitation  hard pulse

      d3                        ; delay between pulse and gradient
modified!AJM pulse ringdown delay (changed from d2)

          150u UNBLKGRAMP                        ; modified AJM
unblank gradient amplifier
    d16 grad{(0)|(0)|step(cnst11,10)+step(100,10)*r2d(cnst11)}
    d4
    d16 grad{(0)|(0)|(cnst11)+r2d(cnst11)-step(cnst11,10)-
step(100,10)*r2d(cnst11)}
    d2
    10u BLKGRAMP                            ; blank gradient amplifier
    p1:f1 ph2               ; 90 degree excitation hard pulse
    d3                      ; modified AJM pulse ringdown delay
(changed from d2)
          150u UNBLKGRAMP                        ; modified AJM
unblank gradient amplifier
    d17 grad {(0)|(0)|(0*cnst12)}
    d17 grad {(0)|(0)|(0.1*cnst12)}
    d17 grad {(0)|(0)|(0.2*cnst12)}
    d17 grad {(0)|(0)|(0.3*cnst12)}
    d17 grad {(0)|(0)|(0.4*cnst12)}
    d17 grad {(0)|(0)|(0.5*cnst12)}
    d17 grad {(0)|(0)|(0.6*cnst12)}
    d17 grad {(0)|(0)|(0.7*cnst12)}
    d17 grad {(0)|(0)|(0.8*cnst12)}
    d17 grad {(0)|(0)|(0.9*cnst12)}
    d5 grad {(0)|(0)|(1.0*cnst12)}
```

```
        d17 grad {(0)|(0)|(0.9*cnst12)}
        d17 grad {(0)|(0)|(0.8*cnst12)}
        d17 grad {(0)|(0)|(0.7*cnst12)}
        d17 grad {(0)|(0)|(0.6*cnst12)}
        d17 grad {(0)|(0)|(0.5*cnst12)}
        d17 grad {(0)|(0)|(0.4*cnst12)}
        d17 grad {(0)|(0)|(0.3*cnst12)}
        d17 grad {(0)|(0)|(0.2*cnst12)}
        d17 grad {(0)|(0)|(0.1*cnst12)}
        d17 grad {(0)|(0)|(0.0*cnst12)}
        d2
        10u BLKGRAMP                          ; modified AJM blank gradient
amplifier
        d20                     ;tau diffusion time
        d22                     ;tau diffusion time   ;modified AJM

        p1:f1 ph3               ; 90 degree excitation hard pulse
```

Appendix 11

The spoiler gradient modifications made to the PGSTE DEXSY sequence so that spoiler gradient

strength, **G,** and duration, δ, of each spoiler gradient is different.

Previously all three spoiler gradients were written as below:

```
d17 grad {(0)|(0)|(0*cnst12)}
d17 grad {(0)|(0)|(0.1*cnst12)}
d17 grad {(0)|(0)|(0.2*cnst12)}
d17 grad {(0)|(0)|(0.3*cnst12)}
d17 grad {(0)|(0)|(0.4*cnst12)}
d17 grad {(0)|(0)|(0.5*cnst12)}
d17 grad {(0)|(0)|(0.6*cnst12)}
d17 grad {(0)|(0)|(0.7*cnst12)}
d17 grad {(0)|(0)|(0.8*cnst12)}
d17 grad {(0)|(0)|(0.9*cnst12)}
d5 grad {(0)|(0)|(1.0*cnst12)}
d17 grad {(0)|(0)|(0.9*cnst12)}
d17 grad {(0)|(0)|(0.8*cnst12)}
d17 grad {(0)|(0)|(0.7*cnst12)}
d17 grad {(0)|(0)|(0.6*cnst12)}
d17 grad {(0)|(0)|(0.5*cnst12)}
d17 grad {(0)|(0)|(0.4*cnst12)}
d17 grad {(0)|(0)|(0.3*cnst12)}
d17 grad {(0)|(0)|(0.2*cnst12)}
d17 grad {(0)|(0)|(0.1*cnst12)}
d17 grad {(0)|(0)|(0.0*cnst12)}
```

Modifications were made to the second and third spoiler gradients. The modifications of the second

spoiler gradient pulse are as follows:

```
d17 grad {(0)|(0)|(-0.0*cnst12)}        ;modified AJM changed
spoiler amplitude
d17 grad {(0)|(0)|(-0.1*cnst12)}
d17 grad {(0)|(0)|(-0.2*cnst12)}
d17 grad {(0)|(0)|(-0.3*cnst12)}
d17 grad {(0)|(0)|(-0.4*cnst12)}
d17 grad {(0)|(0)|(-0.5*cnst12)}
d17 grad {(0)|(0)|(-0.6*cnst12)}
d17 grad {(0)|(0)|(-0.7*cnst12)}
d17 grad {(0)|(0)|(-0.8*cnst12)}
d17 grad {(0)|(0)|(-0.9*cnst12)}
d5 grad {(0)|(0)|(-1.0*cnst12)}
d17 grad {(0)|(0)|(-0.9*cnst12)}
d17 grad {(0)|(0)|(-0.8*cnst12)}
d17 grad {(0)|(0)|(-0.7*cnst12)}
d17 grad {(0)|(0)|(-0.6*cnst12)}
```

```
d17 grad {(0)|(0)|(-0.5*cnst12)}
d17 grad {(0)|(0)|(-0.4*cnst12)}
d17 grad {(0)|(0)|(-0.3*cnst12)}
d17 grad {(0)|(0)|(-0.2*cnst12)}
d17 grad {(0)|(0)|(-0.1*cnst12)}
d17 grad {(0)|(0)|(-0.0*cnst12)}
```

Finally, the modification made to the third spoiler gradient are:

```
d17 grad {(0)|(0)|(0*cnst12)}                    ;modified AJM
changed spoiler amplitude
d17 grad {(0)|(0)|(0.07*cnst12)}
d17 grad {(0)|(0)|(0.14*cnst12)}
d17 grad {(0)|(0)|(0.21*cnst12)}
d17 grad {(0)|(0)|(0.28*cnst12)}
d17 grad {(0)|(0)|(0.35*cnst12)}
d17 grad {(0)|(0)|(0.42*cnst12)}
d17 grad {(0)|(0)|(0.49*cnst12)}
d17 grad {(0)|(0)|(0.56*cnst12)}
d17 grad {(0)|(0)|(0.63*cnst12)}
d5 grad {(0)|(0)|(0.7*cnst12)}
d17 grad {(0)|(0)|(0.63*cnst12)}
d17 grad {(0)|(0)|(0.56*cnst12)}
d17 grad {(0)|(0)|(0.49*cnst12)}
d17 grad {(0)|(0)|(0.42*cnst12)}
d17 grad {(0)|(0)|(0.35*cnst12)}
d17 grad {(0)|(0)|(0.28*cnst12)}
d17 grad {(0)|(0)|(0.21*cnst12)}
d17 grad {(0)|(0)|(0.14*cnst12)}
d17 grad {(0)|(0)|(0.07*cnst12)}
d17 grad {(0)|(0)|(0.0*cnst12)}
```

NMR and Molecular Dynamics Study of the Size, Shape, and Composition of Reverse Micelles in a Cetyltrimethylammonium Bromide (CTAB)/n-Hexane/Pentanol/Water Microemulsion

Amanda J. Mills, John Wilkie, and Melanie M. Britton*

School of Chemistry, University of Birmingham, Edgbaston, B15 2TT, United Kingdom

Ⓢ Supporting Information

ABSTRACT: The size, shape, and composition of reverse micelles (RMs) in a cetyltrimethylammonium bromide (CTAB)/pentanol/n-hexane/water microemulsion were investigated using pulsed gradient stimulated echo (PGSTE) nuclear magnetic resonance (NMR) measurements and molecular modeling. PGSTE data were collected at observation times (Δ) of 10, 40, and 450 ms. At long observation times, CTAB and pentanol exhibited single diffusion coefficients. However, at short ($\Delta \leq 40$ ms) observation times both CTAB and pentanol exhibited slow and fast diffusion coefficients. These NMR data indicate that both CTAB and pentanol molecules reside in different environments within the microemulsion and that there is exchange between regions on the millisecond time scale. Molecular dynamic simulations of the CTAB RM, in a solvent box containing n-hexane and pentanol, produced an ellipsoid shaped RM. Using structural parameters from these simulations and the Stokes−Einstein relation, the structure factor and dimensions of the reverse micelle were determined. Analysis of the composition of the interphase also showed that there was a variation in the ratio of surfactant to cosurfactant molecules depending on the curvature of the interphase.
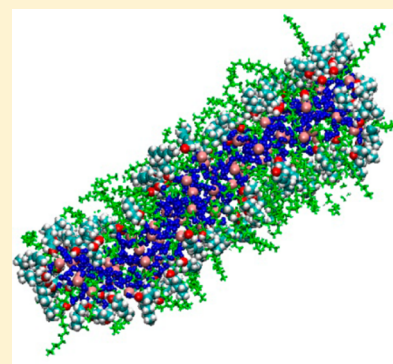
INTRODUCTION

Reverse micelles (RMs), formed in water-in-oil microemulsions, tend to be nanosized water droplets surrounded by a layer (interphase) of surfactant molecules in a continuous organic phase.[1] RMs have a broad range of applications and are frequently used as templates in the synthesis of nanoparticles,[2−5] drug delivery and biomolecule carriers,[6−8] and reactors for chemical and enzymatic reactions.[9−12] As a consequence, there is significant interest in their microstructure, size, and chemical properties. A variety of techniques have been used to probe these properties including fluorescence spectroscopy,[13−17] conductivity measurements,[15,18] dynamic light scattering (DLS),[19,20] small-angle X-ray scattering (SAXS),[21] and nuclear magnetic resonance (NMR).[22−28]

Although the literature is dominated by studies of RMs formed with sodium bis(2-ethylhexyl) sulfosuccinate (AOT), there is interest in RMs formed with other surfactants, particularly cetyltrimethylammonium bromide (CTAB). CTAB is of increasing interest because the headgroup is a good model for the lipid phosphatidylcholine.[29] CTAB RMs are therefore able to mimic cell membranes and consequently help determine the microenvironment of enzymes and proteins within the cellular environment.[30] CTAB RMs have also been found to possess an increased water solubilization capacity compared to AOT RMs,[3,31] which is important in the synthesis of nanoparticles, leading to an increase in their use in this area.[3] In nanoparticle synthesis, the use of RMs has been promoted as a method for controllably producing uniformly sized

nanoparticles.[2] CTAB RMs are frequently utilized, not only because of their confined water core, but also for additional advantages associated with an increased interphase fluidity, leading to greater intermicellar exchange,[5,31,32] and the presence of a cosurfactant.[2,5,29,32] Unlike RMs formed with AOT, CTAB requires the presence of a cosurfactant, typically a medium chain alcohol, in order to form stable RMs.[29,32] When the continuous oil phase acts as the cosurfactant, tertiary microemulsions are possible (e.g., CTAB/hexanol/water).[33] Quaternary microemulsions are formed when the cosurfactant is different from the continuous phase (e.g., CTAB/heptanol/cyclohexane/water).[13] The presence of the cosurfactant in quaternary microemulsions provides a useful additional parameter by which the size, shape, and interphase rigidity of the RM can be controlled,[2] as well as aid the stability of nanoparticles.[34]

CTAB RM droplet sizes have been characterized in only a few papers using electron microscopy,[3] conductance measurements,[35] fluorescence spectroscopy[36,37] and NMR.[27] Electron microscopy measurements[3] have determined droplet diameters between 10 and 150 nm for the CTAB/hexanol/water system. Conductance measurements[35] on the CTAB/heptane/butanol/water system gave droplet radii of 4.8−5.3 nm. Measurements by fluorescence spectroscopy have found droplet radii of 4.0−4.5 nm for CTAB RMs in chloroform/iso-octane mixtures.[36,37]

NMR measurements of diffusion[27] for the CTAB/pentanol/hexane/water system measured droplet radii of 1–5 nm over a range of ω_0 values. Although dynamic light scattering is frequently used to determine the sizes of RMs, it appears to be less utilized with CTAB RMs, which could be due to problems associated with the effect of dilution[18,37] on the composition of the RMs or index matching.[18,38,39]

Whereas the presence of a cosurfactant offers useful advantages for RM stability and nanoparticle synthesis, its presence and distribution gives rise to microemulsions of greater complexity, making characterization more difficult. Indeed, there remain many questions surrounding the role of the cosurfactant in RM formation, and how the cosurfactant is dispersed between the reverse micelle and continuous phase. Some of these questions were investigated by Palazzo and co-workers using NMR measurements of diffusion[18,27,40] on the CTAB/pentanol/hexane/water quaternary microemulsion. Through analysis of NMR diffusion data, they[18,27,40] showed that the pentanol was distributed between the RM interphase and continuous phase and that exchange between these regions was fast compared to the PGSE observation time, Δ. As only an average diffusion coefficient was measured for the pentanol (D_{obs}), the proportion of pentanol in the RM, P_{mic}, was determined by fitting D_{obs} to the Lindman equation[41,42] (eq 1), using a priori knowledge of the diffusion of pentanol in the continuous phase, D_{bulk}, and using the diffusion coefficient of CTAB as a measure of the RM diffusion coefficient, D_{mic}.

$$D_{obs} = P_{mic}D_{mic} + (1 - P_{mic})D_{bulk} \tag{1}$$

From the values of D_{mic}, RM sizes of 1–5 nm were determined[18,27,40] using the Stokes–Einstein equation (eq 2). A spherical shape was assumed (giving a value of 6 for the shape factor, f) and the viscosity was corrected for the amount of pentanol remaining in the continuous phase, as determined from P_{mic}.

$$D = \frac{k_B T}{f \pi \eta R_h} \tag{2}$$

In this paper, we investigate the CTAB/pentanol/n-hexane/water RM system using pulsed gradient stimulated echo (PGSTE) measurements and molecular simulations. A range of PGSTE observation times (Δ = 10–450 ms) was used, which included times shorter than those previously reported.[40] We observe that both pentanol and CTAB are distributed between RM and continuous phases. At short observation times ($\Delta \leq 40$ ms) both CTAB and pentanol exhibit two diffusion coefficients which are then averaged to a single value at Δ = 450 ms. Molecular simulations were performed for a CTAB RM in a solvent box containing n-hexane and pentanol. During the simulations, pentanol and CTAB molecules were distributed between RM and continuous phases and were observed to exchange between these two environments. The simulations showed that RMs are oblate in shape. By combining the structural parameters determined from simulation with the experimentally determined diffusion coefficients and P_{mic}, it was possible to determine the dimensions of CTAB RMs in this system.

■ EXPERIMENTAL SECTION

Sample Preparation. Cetyltrimethylammonium bromide (CTAB, Sigma-Aldrich, 98%), pentanol (Sigma-Aldrich, 99%), n-hexane (Fisher-Scientific, reagent grade), and water (Nano-pure filtered, resistivity 18 MΩ cm) were used to produce the CTAB/pentanol/n-hexane/water quaternary microemulsion. Microemulsions were prepared by dissolving 0.2 g CTAB in 8.394 mL of n-hexane, 0.487 mL of pentanol, and 0.068 mL of water and shaking for approximately 2 min. This gives a water/CTAB molar ratio, ω_0, of 6.9, a pentanol/CTAB molar ratio, P_0, of 8.2 and a volume fraction, ϕ, of 0.05. NMR measurements were taken approximately 1 h after sample preparation.

NMR Measurements. NMR experiments were performed on a Bruker DMX300 spectrometer equipped with a 7 T superconducting magnet, operating at a proton resonance frequency of 300.13 MHz. Samples were placed in a 5-mm NMR tube, inside a 5-mm ^{1}H resonator of a Bruker Diff30 probe. The variable temperature control unit was calibrated using a methanol standard,[43] by measuring the difference in chemical shift of the OH and CH$_3$ resonances at regular temperature intervals. Gradient strengths were calibrated by measuring the diffusivity of a n-octane sample at 289 K and compared with literature values.[44] The ^{1}H NMR spectrum of the CTAB/pentanol/n-hexane/water microemulsion is shown in Figure 1, with the structures, and proton numbering schemes, for CTAB and pentanol in Figure 2 and peak assignments listed in Table 1.
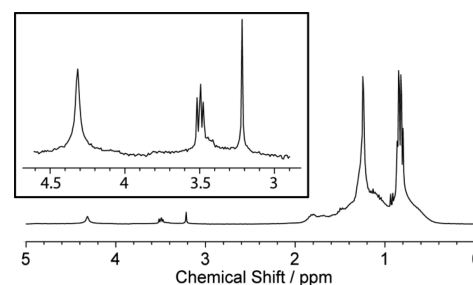
Figure 1. ^{1}H NMR spectra of CTAB/pentanol/n-hexane/water reverse micelle with inset showing an expanded region.
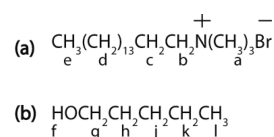
Figure 2. Molecular structure and numbering scheme for (a) CTAB and (b) pentanol.

Spin–spin (T_2) relaxation times for CTAB (H$_a$) and pentanol (H$_g$) were measured using ^{1}H NMR Carr Purcell Meiboom Gill (CPMG) experiments, $[90 - (\tau - 180 - \tau)_m - acq]_n$ at 298 ± 0.3 K. A repetition time of 15 s was used to

Table 1. ^{1}H NMR Peak Assignments for CTAB/Pentanol/n-Hexane/Water Reverse Micelle

δ/ppm	peak assignment
4.32	H$_f$ and water
3.52	H$_g$
3.45	H$_b$
3.22	H$_a$
1.80	H$_c$
1.50	H$_h$
1.35–1.16	H$_d$, H$_i$, H$_j$, H$_k$
0.95–0.8	H$_e$, H$_l$

collect four signal averages, n, with 16 echoes, m, varied from 0 to 1024 with a delay of $\tau = 2$ ms. An inversion recovery experiment, $[180° - \tau - 90° - acq]_n$, was used to measure the T_1 relaxation times of CTAB (H_a) and pentanol (H_g) at 298 ± 0.3 K. A series of $n = 33$ experiments was performed with logarithmically spaced time delays, τ, ranging from 5×10^{-6} s to 15 s.

Diffusion coefficients for the H_a resonance of CTAB and H_g of pentanol were measured using ^1H NMR pulsed gradient stimulated echo with bipolar pulse pairs (BPP−STE) experiments[43,45,46] at 298 ± 0.3 K. Data were collected at three observation times ($\Delta = 10$, 40, and 450 ms) using 32 gradient steps and $\delta = 3$ ms, $\Delta = 40$ ms, and $G_{max} = 0.9$ T m^{-1}; $\delta = 2$ ms, $\Delta = 450$ ms, and $G_{max} = 0.4$ T m^{-1}; or $\delta = 3$ ms, $\Delta = 10$ ms and $G_{max} = 1.9$ T m^{-1}. A repetition time of 6 s was used, which was between 3 and $5 \times T_1$ (depending on the proton), with two dummy scans. A comparison was made between data collected with a T_R of 6 and 12 s (which was $\geq 5T_1$ for all resonances), and no differences were observed. Hence, the shorter T_R was used to minimize the experiment time and limit the effect of changes in the system with time. Previous studies have used pulsed gradient spin echo[27] (PGSE) and stimulated echo[47] (PGSTE) measurements, whereas we utilize a bipolar pulse pair stimulated echo (BPP−STE) sequence, to access shorter observation times. To ensure there were no effects from the increased gradient strengths used with short observation times, the gradient stabilization delay was checked using a high-molecular-weight polydimethylsiloxane (PDMS) sample.[48] PGSTE sequences have a number of advantages over PGSE sequences, which are sensitive to J-coupling[49] and T_2 relaxation.[45,50] The issue with J-coupling can be avoided if only singlet peaks are selected. This is the case for the H_a proton in CTAB, but only the hydroxyl (H_f) proton in pentanol is a singlet, which is susceptible to exchange with water in the core of the RM.[51] The issue associated with T_2 becomes a factor when the observation time of the PGSE experiment is comparable with the T_2 relaxation time of the molecule of interest. In PGSTE sequences, spin relaxation during the observation time depends on T_1 rather than T_2, which is significantly longer than T_2 in the systems of interest here. However, stimulated echo sequences can be sensitive to the effects of cross-relaxation[52] where $\Delta > 20$ ms. A comparison of data acquired using PGSE, PGSTE, and BPP−STE experiments was made, to ensure observations are not a consequence of pulse sequence artifacts, and can be found in the Supporting Information (SI). Average diffusion coefficients were determined using the Stejskal−Tanner equation (eq 3). Where a monoexponential fit was poor, a biexponential fit was performed (see SI). The data were fitted to the minimum number of components necessary.

$$\frac{S(\boldsymbol{G})}{S(0)} = \exp\left[-\gamma^2\delta^2\boldsymbol{G}^2D\left(\Delta - \frac{\delta}{3}\right)\right] \tag{3}$$

Viscosity Measurements. Kinematic viscosity measurements of solutions of pentanol in n-hexane, over the concentration range of 0−1 M, were performed at 298 K using an Ubbelohde size 0 viscometer. Density measurements of the pentanol/n-hexane solutions were determined by weighing 10 mL of the sample, which had been kept at 298 ± 0.1 K. The dynamic viscosity (η) was calculated using the kinematic viscosity (v) and density (ρ) data (eq 4).

$$v = \frac{\eta}{\rho} \tag{4}$$

Molecular Mechanics and Molecular Dynamics (MD) Calculations. Molecular mechanics and molecular dynamics (MD) calculations were carried out using combined ff03[53] and gaff[54] force fields within AMBER v12.[55] Unless stated otherwise, all dynamic simulations were run at 300 K and constant volume with periodic boundaries, and with a EWALD nonbonded cutoff of 12 Å. Sampling of geometries, and velocities every 10 ps (5000 steps) were conducted during the data-gathering phase.

Droplet Construction for Calculations. Initially, a water droplet was constructed by solvation of a single water molecule with the *solvateshell* command within AMBER LEaP with a thickness of 25 Å. A layer of CTAB surfactant molecules was constructed around the water droplet with the CTAB headgroup close to the water and the hydrophobic chains pointing away. Once the CTAB layer was complete, a second layer of pentanol was constructed around the droplet with the hydroxyl group pointing away and the tails pointing toward the center of the droplet. Orientation and distributions of the CTAB and pentanol molecules were arranged randomly using a purpose-built code.[56] CTAB and pentanol placement around the droplet was performed using the same method as previously reported.[57] Sufficient bromide ions were added using the *addion* option on LEaP to ensure an overall neutral charge of the droplet. This process gave a ω_0 value similar to the experimental ω_0 value employed. A minimization was performed with no periodic box boundaries for a maximum of 100 000 cycles so the RMS gradients were <2 and had a G_{max} < 10^2. The minimization closes any gaps that may be present in the CTAB and pentanol layers constructed.

Solvent Box Preparation. The required number of n-hexane molecules for a cubic box, 100 Å in each dimension, was determined from the density of n-hexane (4624 molecules for a density of 0.6617 g/mL). The n-hexane molecules were added to the box in an ordered periodic array with a spacing of approximately 6 Å to give the correct number of n-hexane molecules. The ordered box of n-hexane was subjected to minimization for a maximum of 100 000 cycles at constant volume. The minimized box was subjected to 1 ns of equilibration dynamics at constant volume to randomize the positions of the n-hexane molecules. The result was saved as an off file using the *saveoff* command in AMBER, and the box boundaries offset at 100 Å.

Droplet Solvation. The optimized droplet was solvated using the n-hexane box off file prepared using the *loadoff* and *solvatebox* commands in LEaP with at least 20 Å of n-hexane around the optimized droplet. The solvated droplet was minimized for a maximum of 20 000 cycles so the RMS gradients were <2 and had a G_{max} <10^2 at constant volume. The optimized solvated droplet was then equilibrated using constant pressure of 1 atm, isotropic position scaling, compressibility of 44.6×10^{-6} bar^{-1}, and a pressure relaxation time of 1 ps, until the box size remained constant. Once the box size was constant, the equilibration was carried out at constant volume with no pressure scaling. Molecular dynamic calculations were run on the droplet for a total of 45 ns, which includes the time for equilibration, 200 ps.

■ RESULTS

Diffusion data for the H_g proton (pentanol) and H_a proton (CTAB), in the CTAB/pentanol/n-hexane/water microemulsion, are given in Tables 2 and 3, respectively. For both CTAB

Table 2. Diffusion Coefficients for the H_g Resonance in Pentanol at Observation Times of 450, 40, and 10 ms at 298 K

observation time / ms	D / 10^{-9} m^2 s^{-1}
450	1.55 ± 0.1
40	0.404 ± 0.02 (7.7%); 1.65 ± 0.1 (92.3%)
10	0.237 ± 0.02 (4.4%); 1.62 ± 0.1 (95.6%)

Table 3. Diffusion Coefficients for the H_a Resonance in CTAB at Observation Times of 450, 40, and 10 ms at 298 K

observation time / ms	D / 10^{-9} m^2 s^{-1}
450	0.374 ± 0.03
40	0.243 ± 0.02 (92.3%); 1.54 ± 0.3 (7.7%)
10	0.224 ± 0.02 (85.8%); 1.20 ± 0.1 (16.2%)

and pentanol, the diffusion data can be fitted to a single diffusion coefficient at long observation times (Δ = 450 ms), but a fit to two diffusion coefficients is necessary (see SI) at short observation times (Δ = 40 and 10 ms). The diffusion data indicate both the pentanol and CTAB molecules are distributed between two different regions, and that there is exchange between these two regions which leads to a weighted-average of D at long Δ. The distribution of CTAB and pentanol between two environments is also supported by the T_2 relaxation decays for protons H_g (pentanol) and H_a (CTAB), which also required biexponential fits, giving T_2 relaxation times of 0.837 s (60.6%) and 0.027 s (39.4%) for pentanol and T_2 = 0.783 s (45.6%) and 0.246 s (54.4%) for CTAB. T_1 relaxation times for protons H_g (pentanol) and H_a (CTAB) were 2 and 0.44 s, respectively. Figure 3 shows a plot of viscosity against pentanol
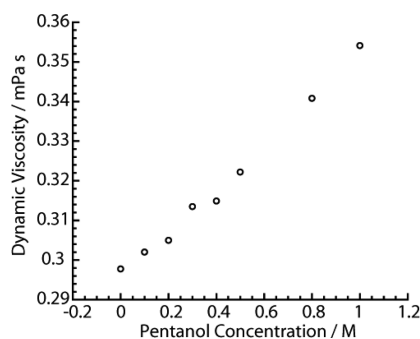

Figure 3. Dynamic viscosity of different concentrations of pentanol in n-hexane at 298 K.

concentration for a range of solutions of pentanol in n-hexane. The diffusion coefficients for pentanol in these solutions are shown in Figure 4. A table of these data can be found in the SI.

Figure 5 gives a graphical view of the MD simulated RM in a CTAB/n-hexane/pentanol/water microemulsion at different simulation times. The RM was initially constructed from a spherical droplet of water surrounded by a layer of surfactant molecules, followed by a layer of pentanol molecules, which were solvated with n-hexane molecules (Figure 5a). During the MD simulation, the RM distorts into an oblate structure from
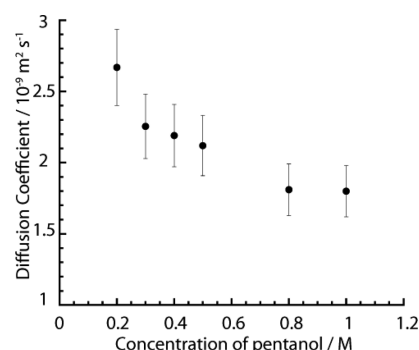

Figure 4. Plot of the diffusion coefficient of pentanol in n-hexane at various concentrations at 298 K.

its initial spherical form. Distributions of the hydrodynamic radius, R_h, of the simulated RM, measured as the distance from the RM center to the terminal carbon of each CTAB molecule, is shown in Figure 6. Figure 7 gives the distributions of the water core radius, R_w, measured as the distance from the RM center to each CTAB headgroup nitrogen atom.

As the simulation progresses, there is a redistribution of pentanol molecules between the RM and continuous phase. The number of pentanol molecules in the RM was followed over time and was determined by calculating the number of pentanol molecules that were within 8 Å, the equilibrated interphase thickness, of any CTAB nitrogen atoms in the RM. A plot of the pentanol to CTAB ratio during the simulation is given in Figure 8 and shows a plateau in the number of pentanol molecules in the RM after 6 ns. While the number of pentanol molecules in the RM reaches an equilibrium, the shape and size of the RM reaches steady-state after 15 ns. After 45 ns, 42.3% of the pentanol molecules are in the reverse micelle and 57.7% are in the continuous phase. During the length of the simulation, pentanol molecules exchange between the continuous phase and reverse micelle. In addition to exchange of the pentanol molecules, an individual CTAB molecule was also observed to exchange between the RM and continuous phase.

■ DISCUSSION

At long observation time (Δ = 450 ms), only a single diffusion coefficient is observed, as had been previously reported for this system at Δ = 140 ms.[18,27,40] However, when Δ is decreased, slow (ca. 10^{-10} m^2 s^{-1}) and fast (ca. 10^{-9} m^2 s^{-1}) diffusion coefficients are observed for pentanol, confirming the cosurfactant is distributed between the RM and continuous phase and suggesting slow exchange between these two environments at Δ = 10 ms. As the slow diffusion coefficients for pentanol and CTAB are similar, at 2.37 × 10^{-10} m^2 s^{-1} and 2.24 × 10^{-10} m^2 s^{-1}, respectively, it suggests the slow diffusion coefficient is associated with the RM (D_{mic}) and the fast diffusion coefficient corresponds to pentanol in the continuous phase (D_{bulk}). If only pentanol in the RM contributes to D_{slow} and pentanol in the bulk contributes to D_{fast}, a two-component fit of eq 3, for the data at Δ = 10 ms, will determine the proportions of pentanol in the RM interphase (P_{mic}) and continuous phase. However, this direct interpretation of the data gives a value of P_{mic} = 0.05, which is significantly lower than the value previously reported by Palazzo et al.[27] (P_{mic} = 0.3). P_{mic} values around 0.3 have also been determined for comparable systems by Schulmann titration and conductivity
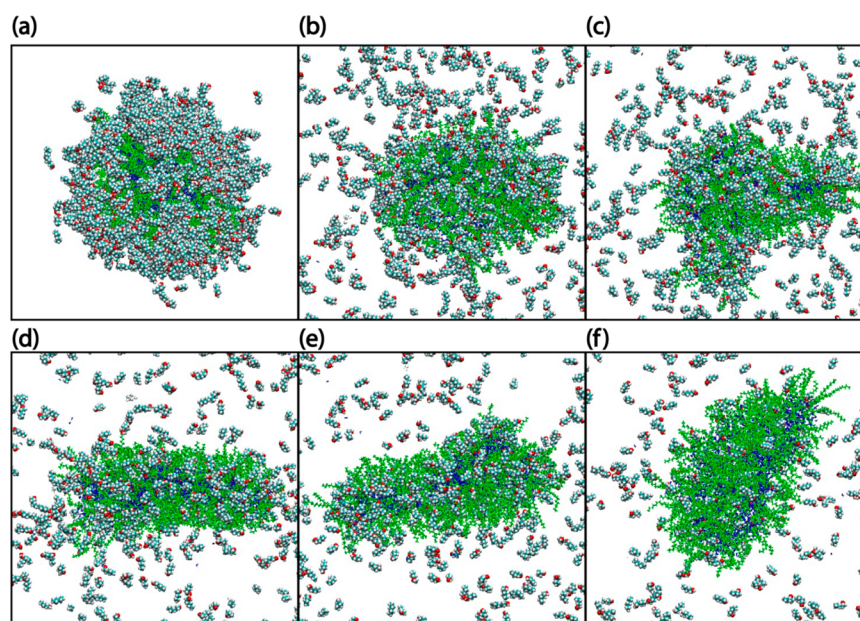
Figure 5. Molecular dynamic snapshots of a RM in the CTAB/*n*-hexane/pentanol/water microemulsion at simulations times of (a) 200 ps, (b) 5 ns, (c) 10 ns, (d) 15 ns, (e) 20 ns, and (f) 45 ns. The hexane molecules have been removed and only the RM is displayed with CTAB molecules shown in green and water in blue. Pentanol is colored by atom, with white for hydrogen, blue for carbon, and red for oxygen.
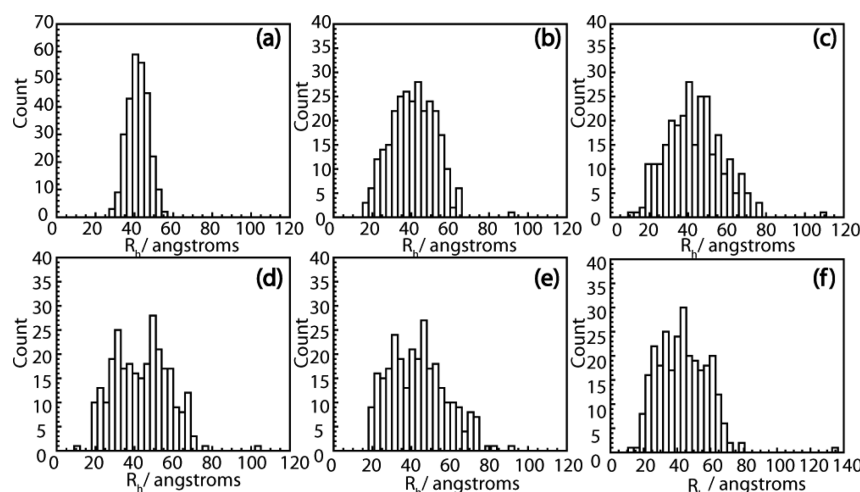

Figure 6. Distributions of the root-mean-square of the distance (R_h) between the center of the droplet and each terminal CTAB carbon at the following time points (a) 200 ps, (b) 5 ns, (c) 10 ns, (d) 15 ns, (e) 20 ns, and (f) 45 ns.

measurements, where P_{mic} values of 0.46 (CTAB/pentanol/hexane/water)[47] and 0.31 (CTAB/butanol/heptane/water at 303 K)[35] have been reported, respectively. A P_{mic} value higher than 0.05 is also supported by our molecular modeling, where an interphase ratio of pentanol/CTAB of $r = 1.93 \pm 0.05$ is determined, while $r = 0.48$ is expected for $P_{mic} = 0.05$.

These factors, therefore, indicate our initial interpretation of the diffusion data must be too simplistic and that some exchange during the 10-ms observation time occurs, skewing the relative proportions of pentanol for the two environments. As D_{slow} for pentanol is comparable with D_{slow} for CTAB, it suggests that the pentanol molecules giving rise to this component are diffusing as part of the RM and their exchange is slow at $\Delta = 10$ ms. However, fast exchange for a proportion of pentanol molecules from the RM with the continuous phase will lead to a weighted average of D_{fast} and an underestimation of P_{mic}. It appears that only a proportion of pentanol in the

interphase is exchanging on a time scale typically expected for molecular exchange in these systems[58,59] and the rest are exchanging significantly slower, on a millisecond time scale. This unexpected observation is also supported by the relaxation time data for pentanol, where two relaxation times are observed, rather than an averaged value.[60] Analysis of the T_2 relaxation data for pentanol shows that it is biexponential with T_2 relaxation times of 0.837 s (60.6%) and 0.027 s (39.4%). It is expected that pentanol in the interphase will have the shorter relaxation time, due to reduced motional freedom.[61]

As the proportion of D_{slow} cannot be used to determine P_{mic} directly, an alternative approach has been taken. Using the weighted average of D at $\Delta = 450$ ms, a value of P_{mic} was determined using eq 1 and a similar approach to Palazzo et al.[27] Using D_{slow} for CTAB as the value for D_{mic}, P_{mic} was determined by using a value of D_{bulk} for pentanol in hexane (Figure 4, with data given in the SI), where initially all the

10771

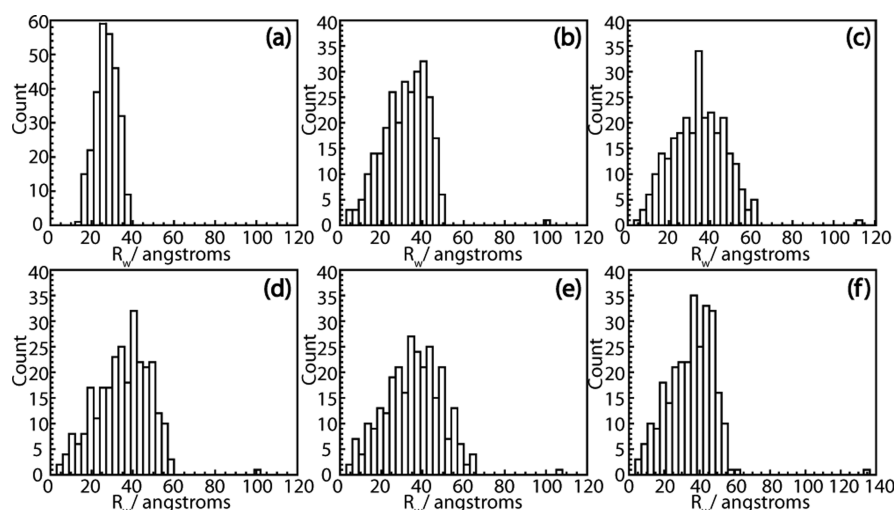dx.doi.org/10.1021/jp504585k | *J. Phys. Chem. B* 2014, 118, 10767−10775

Figure 7. Root mean square distributions of the distance (R_w) between the center of the droplet and each nitrogen of the CTAB headgroup at the following time points (a) 200 ps, (b) 5 ns, (c) 10 ns, (d) 15 ns, (e) 20 ns, and (f) 45 ns.
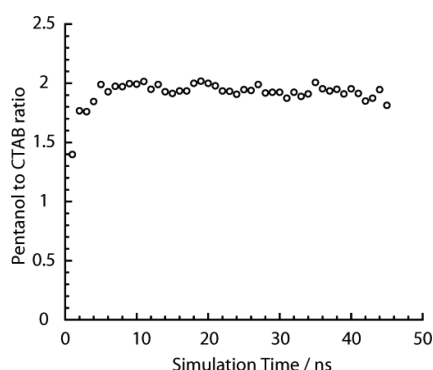

Figure 8. Plot of the pentanol to CTAB ratio in the interphase of the simulated RM as a function of simulation time.

pentanol was assumed to be in the continuous phase. From this calculation, a value for P_{mic} was determined which indicated an amount of pentanol in the continuous phase and hence a modified value for D_{bulk}. Using this corrected D_{bulk}, a corrected P_{mic} value was obtained, and then the process was repeated until the values for P_{mic} converged, giving a value of $P_{mic} = 0.43$. This value is more in line with the values that have been previously determined, though it is higher than the value determined by Palazzo and co-workers for this system. A primary difference between the studies is that a slower value for D_{mic} is used in our analysis, as previously only a single weighted-average value for D_{CTAB} was observed. Also, in our analysis we do not assume, as was previously done, that $D_{bulk}\eta$ is a constant, and use experimental values for D_{bulk} from solutions of pentanol in hexane. Both studies assume the diffusivity of pentanol in hexane is unaffected by the presence of the RMs.

Our interpretation indicates the behavior of the cosurfactant is not uniform throughout the interphase and that only a proportion of the pentanol molecules are in fast exchange with the continuous phase. This observation raises the question— what actually constitutes the interphase? Where the interphase is defined as the region within the chain length of the surfactant, there are two pools of cosurfactant molecules exchanging on different time scales. The MD simulations suggest that these slower exchanging pentanol molecules are

those that are closest to the water core. While exchange of these "core" pentanol molecules appears slow at $\Delta = 10$ ms, they do exchange with the continuous phase at longer times. This is shown in the measurements at $\Delta = 450$ ms, where only a single weighted average diffusion coefficient is observed.

The NMR data also show that CTAB is distributed between two environments, with exchange also on the millisecond time scale. This is a surprising observation, as CTAB has negligible solubility in n-hexane and typically requires the presence of water in order to be solubilized. However, the observation of fast and slow diffusion coefficients suggests the CTAB is indeed distributed between reverse micelles and the continuous phase, either as monomers, or, as has been observed in CTAB/water/i-octane/n-hexanol RMs containing $[Ru(bpy)_3]^{2+}$, small ($\omega_0 \sim 0$) micelles.[62] CTAB molecules are in relatively slow exchange between these different environments, as indicated by the diffusion data at long observation time ($\Delta = 450$ ms). Application of the Lindman equation, using the data at $\Delta = 10$ ms, returns a weighted-average of $D_{av} = 3.74 \times 10^{-10}$ m^2 s^{-1}, which compares well to the value $D = 3.63 \times 10^{-10} \pm 0.1$ m^2 s^{-1} measured at $\Delta = 450$ ms. A distribution of CTAB between micelles of different sizes was not observed in the NMR study by Palazzo et al.[27,40] However, their Δ and δ values were relatively long[63] ($\Delta = 140$ ms, $G = 0.07$ T m^{-1}, and δ ranging from 14 to 32 ms) which could explain why CTAB outside the RM was not observed. Evidence of smaller CTAB micelles has been reported by Rack et al.[62] from lifetime decay data for excited state $[Ru(bpy)_3]^{2+}$. The partitioning of CTAB between different regions is also observed in our MD simulations, where, after 2.1 ns, a CTAB molecule escapes the RM and then hovers near the interphase, briefly entering the RM again 1 ns later, before finally diffusing further away into the continuous phase, where it remained for the rest of the simulation. Our simulations suggest that the CTAB is stabilized by pentanol molecules in the continuous phase, with only pentanol molecules within a radius of 15 Å of the CTAB and n-hexane molecules located further away.

Using the slow CTAB diffusion coefficient as a measure of the diffusion of the RM, D_{mic}, and a corrected viscosity of $\eta = 0.311$ mPa s for the continuous phase (where $P_{mic} = 0.43$ gives a solution of 0.28 M pentanol in hexane), a hydrodynamic radius of the RM was determined at 3.13 ± 0.28 nm, via the

Stokes–Einstein equation (eq 2). Although this size is consistent with previous reports of droplet size by Palazzo et al.[27,40] and Lang et al.,[37] there is a problem with this analysis. This is because the shape of the RMs had previously been assumed to be spherical, whereas our molecular simulations show the RM is oblate rather than spherical (Figure 5). A quantitative description of the shape of the micelle is possible by measuring the lengths of the three semiaxes a, b, and c and determining the eccentricity, e, value.[64] The three semiaxes were calculated using the principle moments of inertia, and using the following equations:[64,65]

$$I_1 = \frac{1}{5}M(a^2 + b^2) \tag{5}$$

$$I_2 = \frac{1}{5}M(a^2 + c^2) \tag{6}$$

$$I_3 = \frac{1}{5}M(b^2 + c^2) \tag{7}$$

where M is the total mass and the major semiaxis is a, the minor semiaxis is c, and b is the axis that is perpendicular to both a and c. Where structures are spherical: $a \approx b \approx c$, where structures are oblate: $a \approx b > c$. The three semiaxes are plotted in Figure 9a as a function of simulation time. This plot shows
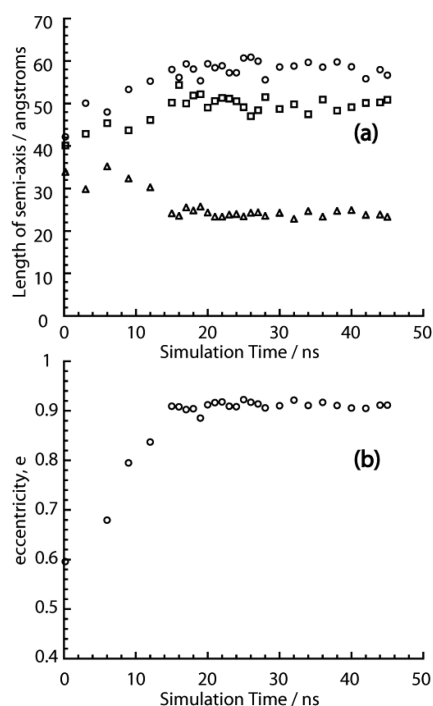

Figure 9. Plot (a) shows the lengths of the three semiaxes a, b, and c in angstroms as a function of simulation time represented as circles (semiaxis a), squares (semiaxis b), and triangles (semiaxis c). Plot (b) gives the eccentricity value, e, as a function of simulation time.

that the shape of the reverse micelle appears to stabilize after 15 ns simulation time. Average values, and standard deviations, for the semiaxes were determined to be 5.82 ± 0.16 nm (a), 5.01 ± 0.16 nm (b), and 2.41 ± 0.074 nm (c) over the final 30 ns period of the simulation, which shows that $a \approx b > c$, indicating an oblate structure. Using these values for a and c in eq 8, the eccentricity value was determined.

$$e = \sqrt{1 - \frac{c^2}{a^2}} \tag{8}$$

Spherical structures have a value of zero, when $e \to 1$ a disc or rod-like shape is found.[65] Figure 9b shows a plot of the eccentricity value over simulation time, which approaches 0.9 after 15 ns. As the RM is oblate, it is necessary to use a modification of the Stokes–Einstein equation for nonspherical structures,[66] using the shape factor, f, for an oblate ellipsoid (eq 9):

$$f_{\text{oblate}} = \frac{\sqrt{\left(\frac{1}{p}\right)^2 - 1}}{\left(\frac{1}{p}\right)^{2/3} \arctan\left(\sqrt{\left(\frac{1}{p}\right)^2 - 1}\right)} \tag{9}$$

where $p = c/a$. Using eq 9 and eq 10, R_H can be determined.

$$R_H = \frac{k_B T}{6\pi \eta D_{\text{mic}} f_{\text{oblate}}} \tag{10}$$

Using the average values of a and c obtained from the MD simulation, giving $p = 0.41$, a value of $f_{\text{oblate}} = 1.068$ is obtained and hence a R_H value of 2.93 nm. By using this value for p and assuming that the volume of the spherical droplet ($V = (4/3)\pi R_H^3$) equals that of the corresponding oblate droplet ($V = (4/3)\pi a^2 c$), the reverse micelle dimensions were determined to be $a = 3.95 \pm 0.10$ nm and $c = 1.61 \pm 0.05$ nm.

Further analysis of the MD simulations also shows that there is a variation in the composition of the interphase of the RM depending on the curvature of the region probed. Where the RM has highest curvature (Figure 10a), a higher concentration of pentanol molecules is observed, with a pentanol/CTAB ratio of $r = 4.3$. In regions of lowest curvature (Figure 10b), the ratio is lower at $r = 1.6$.
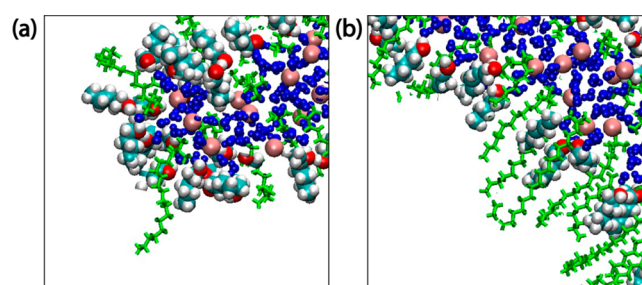

Figure 10. Molecular dynamic snapshots of the CTAB/n-hexane/pentanol/water RM interphase at 45 ns showing (a) high curvature region and (b) low curvature region. CTAB molecules are shown in green, bromide in pink, water in dark blue, and pentanol is colored by atom, with white for hydrogen, blue for carbon, and red for oxygen.

■ CONCLUSION

By measuring the diffusion coefficients for pentanol and CTAB at short and long observation times, it was possible to determine the distribution of CTAB and pentanol between the RM interphase and continuous phase. Exchange of both pentanol and CTAB were observed between the interphase and continuous phase, on the millisecond time scale, and at longer observation times resulted in an averaged diffusion coefficient. Molecular modeling showed that the shape of CTAB RMs is oblate, rather than the previously assumed spherical shape, and

that there is a variation in the ratio of surfactant to cosurfactant in the interphase depending on the curvature of the interphase. The use of a solvent box in the MD simulations allowed the distribution of the CTAB and pentanol molecules to be mapped. Both the simulations and experiments showed that the pentanol molecules move between the interphase and continuous phase, as do the CTAB molecules.

■ ASSOCIATED CONTENT

Ⓢ Supporting Information

Comparison of diffusion data acquired using PGSE, PGSTE, and BPP-STE pulse sequences for CTAB and pentanol at observation time, Δ, of 40 and 140 ms; comparisons between mono- and biexponential fits for these diffusion data. This material is available free of charge via the Internet at http://pubs.acs.org.

■ AUTHOR INFORMATION

Corresponding Author
*E-mail: m.m.britton@bham.ac.uk.

Notes
The authors declare no competing financial interest.

■ ACKNOWLEDGMENTS

■ REFERENCES

(1) Correa, N. M.; Silber, J. J.; Riter, R. E.; Levinger, N. E. Nonaqueous Polar Solvents in Reverse Micelle Systems. *Chem. Rev.* **2012**, *112*, 4569−4602.

(2) Capek, I. Preparation of Metal Nanoparticles in water-in-oil (w/o) Microemulsions. *Adv. Colloid Interface Sci.* **2004**, *110*, 49−74.

(3) Fang, X.; Yang, C. An Experimental Study on the Relationship between the Physical Properties of CTAB/Hexanol/Water Reverse Micelles and ZrO$_2$−Y$_2$O$_3$ Nanoparticles Prepared. *J. Colloid Interface Sci.* **1999**, *212*, 242−251.

(4) Pileni, M. P. The Role of Soft Colloidal Templates in Controlling the Size and Shape of Inorganic Nanocrystals. *Nat. Mater.* **2003**, *2*, 145−150.

(5) Uskokovic, V.; Drofenik, M. Synthesis of Materials within Reverse Micelles. *Surf. Rev. Lett.* **2005**, *12*, 239−277.

(6) Kogan, A.; Garti, N. Microemulsions as Transdermal Drug Delivery Vehicles. *Adv. Colloid Interface Sci.* **2006**, *123*, 369−385.

(7) Luisi, P. L. Enzymes Hosted in Reverse Micelles in Hydrocarbon Solution. *Angew. Chem., Int. Ed.* **1985**, *24*, 439−450.

(8) Sharon, M.; Ilag, L. L.; Robinson, C. V. Evidence for Micellar Structure in the Gas Phase. *J. Am. Chem. Soc.* **2007**, *129*, 8740−8746.

(9) Fendler, J. H. Interactions and Reactions in Reversed Micellar Systems. *Acc. Chem. Res.* **1976**, *9*, 153−161.

(10) McIlwaine, R. E.; Fenton, H.; Scott, S. K.; Taylor, A. F. Acid Autocatalysis and Front Propagation in Water-in-Oil Microemulsions. *J. Phys. Chem. C* **2008**, *112*, 2499−2505.

(11) Miyake, Y. Enzymatic Reaction in Water-in-Oil Microemulsions. *Colloids Surf., A* **1996**, *109*, 255−262.

(12) Pileni, M. P. Reverse Micelles as Microreactors. *J. Phys. Chem.* **1993**, *97*, 6961−6973.

(13) Corbeil, E. M.; Levinger, N. E. Dynamics of Polar Solvation in Quaternary Microemulsions. *Langmuir* **2003**, *19*, 7264−7270.

(14) Levinger, N. E. Ultrafast Dynamics in Reverse Micelles, Microemulsions, and Vesicles. *Curr. Opin. Colloid Interface Sci.* **2000**, *5*, 118−124.

(15) Mays, H. Dynamics and Energetics of Droplet Aggregation in Percolating AOT Water-in-Oil Microemulsions. *J. Phys. Chem. B* **1997**, *101*, 10271−10280.

(16) Rodenas, E.; Dolcet, C.; Valiente, M.; Valeron, E. C. Physical Properties of Dodecyltrimethylammonium Bromide (DTAB) Micelles in Aqueous Soultion and their Behaviour as the Reaction Medium. *Langmuir* **1994**, *10*, 2088−2094.

(17) Rodenas, E.; Perez-Benito, E. Sizes and Aggregation Numbers of SDS Reverse Micelles in Alkanols obtained by Fluorescence Quenching Measurements. *J. Phys. Chem.* **1991**, *95*, 4552−4556.

(18) Giustini, M.; Palazzo, G.; Colafemmina, G.; Della Monica, M.; Giomini, M.; Ceglie, A. Microstructure and Dynamics of the Water-in-Oil CTAB/n-Pentanol/n-Hexane/Water Microemulsion: A Spectroscopic and Conductivity Study. *J. Phys. Chem.* **1996**, *100*, 3190−3198.

(19) Baruah, B.; Roden, J. M.; Sedgwick, M.; Correa, N. M.; Crans, D. C.; Levinger, N. E. When is Water not Water? Exploring Water Confined in Large Reverse Micelles using a Highly Charged Inorganic Molecular Probe. *J. Am. Chem. Soc.* **2006**, *128*, 12758−12765.

(20) Schatzel, K. Light-Scattering - Diagnostic Methods for Colloidal Dispersions. *Adv. Colloid Interface Sci.* **1993**, *46*, 309−332.

(21) Hirai, M.; Kawai-Hirai, R.; Sanada, M.; Iwase, H.; Mitsuya, S. Characteristics of AOT Microemulsion Structure Depending on Apolar Solvents. *J. Phys. Chem. B* **1999**, *103*, 9658−9662.

(22) Angelico, R.; Balinov, B.; Ceglie, A.; Olsson, U.; Palazzo, G.; Soderman, O. Water Diffusion in Polymer-like Reverse Micelles. 2. Composition Dependence. *Langmuir* **1999**, *15*, 1679−1684.

(23) Halliday, N. A.; Peet, A. C.; Britton, M. M. Detection of pH in Microemulsions, without a Probe Molecule, Using Magnetic Resonance. *J. Phys. Chem. B* **2010**, *114*, 13745−13751.

(24) Law, S. J.; Britton, M. M. Sizing of Reverse Micelles in Microemulsions using NMR Measurements of Diffusion. *Langmuir* **2012**, *28*, 11699−11706.

(25) Maitra, A. Determination of Size Parameters of Water Aerosol OT Oil Reverse Micelles from their Nuclear Magnetic-Resonance Data. *J. Phys. Chem.* **1984**, *88*, 5122−5125.

(26) Packer, K. J.; Rees, C. Pulsed NMR Studies of Restricted Diffusion. I. Droplet Size Distributions in Emulsions. *J. Colloid Interface Sci.* **1972**, *40*, 206−218.

(27) Palazzo, G.; Lopez, F.; Giustini, M.; Colafemmina, G.; Ceglie, A. Role of the Cosurfactant in the CTAB/Water/n-Pentanol/n-Hexane Water-in-oil Microemulsion. 1. Pentanol Effect on the Microstructure. *J. Phys. Chem. B* **2003**, *107*, 1924−1931.

(28) Söderman, O.; Stilbs, P.; Price, W. S. NMR Studies of Surfactants. *Concepts Magn. Reson., Part A* **2004**, *23A*, 121−135.

(29) Crans, D. C.; Schoeberl, S.; Gaidamauskas, E.; Baruah, B.; Roess, D. A. Antidiabetic Vanadium Compound and Membrane Interfaces: Interface-facilitated Metal Complex Hydrolysis. *J. Biol. Inorg. Chem.* **2011**, *16*, 961−972.

(30) Marhuenda-Egea, F. C.; Piera-Velazquez, S.; Cadenas, C.; Cadenas, E. Reverse Micelles in Organic Solvents: A Medium for the Biotechnological use of Extreme Halophilic Enzymes at Low Salt Concentration. *Archaea* **2002**, *1*, 105−111.

(31) López-Quintela, M. A.; Tojo, C.; Blanco, M. C.; García Rio, L.; Leis, J. R. Microemulsion Dynamics and Reactions in Microemulsions. *Curr. Opin. Colloid Interface Sci.* **2004**, *9*, 264−278.

(32) Eastoe, J.; Hollamby, M. J.; Hudson, L. Recent Advances in Nanoparticle Synthesis with Reversed Micelles. *Adv. Colloid Interface Sci.* **2006**, *128*, 5−15.

(33) Rodenas, E.; Valiente, M. The Determination of some Physical Properties of Reverse CTAB Micelles in 1-Hexanol. *Colloids Surf.* **1992**, *62*, 289−295.

(34) Curri, M. L.; Agostiano, A.; Manna, L.; Della Monica, M.; Catalano, M.; Chiavarone, L.; Spagnolo, V.; Lugara, M. Synthesis and Characterization of CdS Nanoclusters in a Quarternary Microemulsion: The Role of the Cosurfactant. *J. Phys. Chem. B* **2000**, *104*, 8391−8397.

(35) Bisal, S.; Bhattacharya, P. K.; Moulik, S. P. Conductivity Study of Microemulsions - Dependance of Structural Behaviour of Water/Oil

Systems on Surfactant, Cosurfactant, Oil and Temperature. *J. Phys. Chem.* **1990**, *94*, 350−355.

(36) Atik, S. S.; Thomas, J. K. Photoprocesses in Cationic Microemulsion Systems. *J. Am. Chem. Soc.* **1981**, *103*, 4367−4371.

(37) Lang, J.; Mascolo, G.; Zana, R.; Luisi, P. L. Structure and Dynamics of Cetyltrimethylammonium Bromide Water-in-Oil Microemulsions. *J. Phys. Chem.* **1990**, *94*, 3069−3074.

(38) *ASTM Standard E2490. Standard Guide for Measurement of Particle Size Distribution of Nanomaterials in Suspension by Photon Correlation Spectroscopy (PCS)*. ASTM International: West Conshocken, PA, 2009; DOI: 2410.1520/E2490-2409; www.astm.org.

(39) Langevin, D. Microemulsions. *Acc. Chem. Res.* **1988**, *21*, 255−260.

(40) Palazzo, G.; Carbone, L.; Colafemmina, G.; Angelico, R.; Ceglie, A.; Giustini, M. The Role of the Cosurfactant in the CTAB/Water/*n*-Pentanol/*n*-Hexane System: Pentanol Effect on the Phase Equilibria and Mesophase Structure. *Phys. Chem. Chem. Phys.* **2004**, *6*, 1423−1429.

(41) Nilsson, P. G.; Lindman, B. Water Self-diffusion in Nonionic Surfactant Solutions. Hydration and Obstruction Effects. *J. Phys. Chem.* **1983**, *87*, 4756−4761.

(42) Nilsson, P. G.; Lindman, B. Mixed Micelles of Nonionic and Ionic Surfactants: A Nuclear Magnetic Resonance Self-diffusion and Proton Relaxation Study. *J. Phys. Chem.* **1984**, *88*, 5391−5397.

(43) Claridge, T. D. W. *High-Resolution NMR Techniques in Organic Chemistry*, 2nd ed.; Elsevier: Oxford, 2009; Vol. 27.

(44) Tofts, P. S.; Lloyd, D.; Clark, C. A.; Barker, G. J.; Parker, G. J. M.; McConville, P.; Baldock, C.; Pope, J. M. Test Liquids for Quantitative MRI Measurements of Self-diffusion Coefficient in vivo. *Magn. Reson. Med.* **2000**, *43*, 368−374.

(45) Callaghan, P. T. *Translational Dynamics & Magnetic Resonance: Principles of Pulsed Gradient Spin Echo NMR*; Oxford University Press: Oxford, 2011.

(46) Wu, D. H.; Chen, A. D.; Johnson, C. S. An Improved Diffusion-Ordered Spectroscopy Experiment Incorporating Bipolar-Gradient Pulses. *J. Magn. Reson. A* **1995**, *115*, 260−264.

(47) Giustini, M.; Murgia, S.; Palazzo, G. Does the Schulman's Titration of Microemulsions Really Provide Meaningful Parameters? *Langmuir* **2004**, *20*, 7381−7384.

(48) Price, W. S.; Hayamizu, K.; Ide, H.; Arata, Y. Strategies for Diagnosing and Alleviating Artifactual Attenuation Associated with Large Gradient Pulses in PGSE NMR Diffusion Measurements. *J. Magn. Reson.* **1999**, *139*, 205−212.

(49) Torres, A. M.; Zheng, G.; Price, W. S. J-compensated PGSE: An Improved NMR Diffusion Experiment with fewer Phase Distortions. *Magn. Reson. Chem.* **2010**, *48*, 129−133.

(50) Tanner, J. E. Use of the Stimulated Echo in NMR Diffusion Studies. *J. Chem. Phys.* **1970**, *52*, 2523−2526.

(51) Halliday, N. Magnetic Resonance Investigations of pH in Microemulsions. Ph.D. Thesis, University of Birmingham, 2011.

(52) Chen, A.; Shapiro, M. Nuclear Overhauser Effect on Diffusion Measurements. *J. Am. Chem. Soc.* **1999**, *121*, 5338−5339.

(53) Duan, Y.; Wu, C.; Chowdhury, S.; Lee, M. C.; Xiong, G. M.; Zhang, W.; Yang, R.; Cieplak, P.; Luo, R.; Lee, T.; et al. A Point-charge Force Field for Molecular Mechanics Simulations of Proteins Based on Condensed-phase Quantum Mechanical Calculations. *J. Comput. Chem.* **2003**, *24*, 1999−2012.

(54) Wang, J. M.; Wolf, R. M.; Caldwell, J. W.; Kollman, P. A.; Case, D. A. Development and Testing of a General Amber Force Field. *J. Comput. Chem.* **2004**, *25*, 1157−1174.

(55) Case, D. A.; Darden, T. A.; Cheatham, T. E.; Simmerling, C. L.; Wang, J.; Duke, R. E.; Luo, R.; Walker, R. C.; Zhang, W.; Merz, K. M. et al. AMBER 12; 2012; University of California, San Francisco, CA.

(56) Wilkie, J., Programme available from the author (J.W) on request j.wilkie@bham.ac.uk.

(57) Binks, D. A.; Spencer, N.; Wilkie, J.; Britton, M. M. Magnetic Resonance Studies of a Redox Probe in a Reverse Sodium Bis(2-ethylhexyl)sulfosuccinate/Octane/Water Microemulsion. *J. Phys. Chem. B* **2010**, *114*, 12558−12564.

(58) Hansen, J. R. High-resolution and Pulsed Nuclear Magnetic Resonance Studies of Microemulsions. *J. Phys. Chem.* **1974**, *78*, 256−261.

(59) Barreleiro, P. C. A.; Alexandridis, P. C-13-NMR Evidence on Amphiphile Lifetime in Reverse (water-in-oil) Micelles Formed by a Poloxamer Block Copolymer. *J. Colloid Interface Sci.* **1998**, *206*, 357−360.

(60) Soderman, O.; Jonstromer, M.; Vanstam, J. Nonspherical Micelles in the Sodium Dodecyl-Sulfate Brine System - a Fluorescence Quenching and Nuclear Magnetic Resonance Study. *J. Chem. Soc.-Faraday Trans.* **1993**, *89*, 1759−1764.

(61) Guo, W.; Fung, B. M.; Orear, E. A. Exchange of Hybrid Surfactant Molecules Between Monomers and Micelles. *J. Phys. Chem.* **1992**, *96*, 10068−10074.

(62) Rack, J. J.; McCleskey, T. M.; Birnbaum, E. R. Perturbing the Sequestered Water-Pool in Microemulsions: The Role of the Probe in Affecting Reverse Micelle Equilibria. *J. Phys. Chem. B* **2002**, *106*, 632−636.

(63) Palazzo, G. Personal communication via e-mail for experimental parameters.

(64) Abel, S.; Sterpone, F.; Bandyopadhyay, S.; Marchi, M. Molecular Modeling and Simulations of AOT-Water Reverse Micelles in Isooctane: Structural and Dynamic Properties. *J. Phys. Chem. B* **2004**, *108*, 19458−19466.

(65) Martinez, A. V.; Dominguez, L.; Malolepsza, E.; Moser, A.; Ziegler, Z.; Straub, J. E. Probing the Structure and Dynamics of Confined Water in AOT Reverse Micelles. *J. Phys. Chem. B* **2013**, *117*, 7345−7351.

(66) Willis, S. A.; Dennis, G. R.; Zheng, G.; Price, W. S. Hydrodynamic Size and Scaling Relations for Linear and 4 Arm Star PVAc Studied using PGSE NMR. *J. Mol. Liq.* **2010**, *156*, 45−51.